



HAL
open science

Metallic oxide nano-clusters synthesis by ion implantation in high purity Fe₁₀Cr alloy

Ce Chris Zheng

► **To cite this version:**

Ce Chris Zheng. Metallic oxide nano-clusters synthesis by ion implantation in high purity Fe₁₀Cr alloy. Materials Science [cond-mat.mtrl-sci]. Université Paris Saclay (COMUE), 2015. English. NNT : 2015SACLS091 . tel-01242211

HAL Id: tel-01242211

<https://theses.hal.science/tel-01242211v1>

Submitted on 11 Dec 2015

HAL is a multi-disciplinary open access archive for the deposit and dissemination of scientific research documents, whether they are published or not. The documents may come from teaching and research institutions in France or abroad, or from public or private research centers.

L'archive ouverte pluridisciplinaire **HAL**, est destinée au dépôt et à la diffusion de documents scientifiques de niveau recherche, publiés ou non, émanant des établissements d'enseignement et de recherche français ou étrangers, des laboratoires publics ou privés.

NNT : 2015SACLS091

THESE DE DOCTORAT
DE
L'UNIVERSITE PARIS-SACLAY
PREPAREE A
L'UNIVERSITE PARIS-SUD

ÉCOLE DOCTORALE N°576
Particules, Hadrons, Énergie, Noyau, Instrumentation,
Imagerie, Cosmos et Simulation

Spécialité de doctorat : Energie Nucléaire

Par

Monsieur Ce ZHENG

Synthèse de nano-amas d'oxyde métallique par implantation ionique
dans un alliage Fe10Cr de haute pureté

Thèse présentée et soutenue à Orsay, le 12 Novembre 2015 :

Composition du Jury :

Mme Odile STEPHAN	Professeure, Université Paris-Sud, LPS	Présidente
Mme Maylise NASTAR	Chercheure, CEA, DEN/DANS/DMN/SRMP	Rapporteur
M. Michel PEREZ	Professeur, INSA & Université Lyon, MATEIS	Rapporteur
M. Jean-Luc BECHADE	Chercheur, CEA, DEN/DANS/DMN/SRMP	Examineur
M. Frédéric DELABROUILLE	Ingénieur, EDF R&D, MMC, Les Renardières	Examineur
M. Frédéric GARRIDO	Professeur, Université Paris-Sud, CSNSM	Directeur de thèse
Mme Aurélie GENTILS	Chargée de Recherche, CNRS, CSNSM	Co-directeur de thèse
M. Joël RIBIS	Chercheur, CEA, DEN/DANS/DMN/SRMA	Encadrant

NNT : 2015SACLS091

DOCTORAL THESIS
OF
UNIVERSITY PARIS-SACLAY
PREPARED AT
UNIVERSITY PARIS-SUD

DOCTORAL SCHOOL N°576
Particles, Hadrons, Energy, Nucleus, Instrumentation,
Imagery, Cosmos and Simulation

Discipline : Nuclear Energy

By

Mr Ce ZHENG

Metallic nano-oxide clusters synthesis by ion implantation
in high purity Fe₁₀Cr alloy

PhD thesis defended at Orsay, on 12 November 2015 :

Composition of the Jury :

Mme Odile STEPHAN	Professor, Université Paris-Sud, LPS, France	President
Mme Maylise NASTAR	Researcher, CEA, DEN/DANS/DMN/SRMP, France	Referee
M. Michel PEREZ	Professor, INSA & Université Lyon, MATEIS, France	Referee
M. Jean-Luc BECHADE	Researcher, CEA, DEN/DANS/DMN/SRMP, France	Examiner
M. Frédéric DELABROUILLE	Engineer, EDF R&D, MMC, Les Renardières, France	Examiner
M. Frédéric GARRIDO	Professor, Université Paris-Sud, CSNSM, France	PhD director
Mme Aurélie GENTILS	Researcher, CNRS, CSNSM, France	PhD supervisor
M. Joël RIBIS	Researcher, CEA, DEN/DANS/DMN/SRMA, France	PhD co-supervisor

Acknowledgements

Time always flies fast. The journey of my seven years study in France is about to come to an end. A thesis is the result of very many events and very many interactions that can hardly be summarized in a few pages. I am sincerely grateful to everyone who has helped and supported me along this long, tough, but fulfilling road to complete my doctoral dissertation. The list of people who gave small but sometimes very important contributions to my work would be quite long, and I would also probably forget many names. This is why I am going to name a few important people, hoping for forgiveness if I will leave someone out.

This thesis has been carried out at the Centre de Sciences Nucléaires et de Sciences de la Matière (CSNSM, UMR 8609, former Centre de Spectrométrie de Nucléaire et de Spectrométrie de Masse), a joint research unit of the Université Paris-Sud and CNRS (IN2P3 Institut). I am grateful to Jean-Antoine Scarpaci, the Director of the lab, to be able to do my work here in good conditions.

I wish to express my sincere thanks to the members of my thesis defence jury: the reviewers: Prof. Michel Perez and Dr. Maylise Nastar; and the examiners: Prof. Odile Stephan, Dr. Jean-Luc Béchade and Dr. Frédéric Delabrouille, for accepting to judge my work and for their constructive comments which enhanced the manuscript to its present shape.

I express my deep gratitude to my thesis supervisor, Dr. Aurélie Gentils, who has given me the opportunity to work with her for firstly a six-months internship during the second year of Master Nuclear Energy and then a three-years thesis. She provided me lots of valuable guidance, assistance, and expertise during the past three years. Her patience and encouragement always give me confidence during my work. She taught me the ability to do independent the research. It has been an honor to be her Ph.D student.

I am very much grateful to my co-supervisor Dr. Joël Ribis for his help, support and cooperation to complete my thesis work. He and Aurélie introduced me to the field of Transmission Electron Microscopy, and taught me how to prepare and analyze the TEM samples using various TEM techniques. I am very grateful for his constant encouragement, and I am always amazed at his reduction of complex problems to its simplest. I give him all my deepest respect and gratitude.

I convey my special thanks and gratitude to my thesis director, Prof. Frédéric Garrido, who introduced me to the field of materials for nuclear application, and made it attract successfully

my interest. He was always available for scientific discussions and provided assistance to me during my work. I enjoyed his help, guidance, insight and humor all these years.

Huge thanks to Dr. Vladimir A. Borodin, who were always available for scientific discussions as well as to give me a lot of interesting, important and useful advices on my research and experiments.

My special thanks to the SEMIRAMIS group members with whom ion implantation and TEM examination were performed. Additionally, I express here my sincere thanks to Odile Kaïtasov and Cédric Baumier for their support and cooperation especially for helping me to get familiarized with the use of TEM. I could not have nice TEM images without careful TEM thin foils preparation and the help of Lucie Delauche (Instrumentation group). I would like to express my thanks to Benoît Arnal, from CEA/DEN/DANS/DMN/SRMA, who prepared for me a FIB TEM sample.

Many thanks to Marion Descoins and Dominique Mangelinck with whom I built good collaboration for APT measurements and analyses along the past three years. Thanks for their welcome in Marseille and spending good times in fruitful discussions. I also give me my special thanks to France Dalle (CEA/DEN/DANS/DMN/SRMA) for her help doing analyses of APT data and fruitful discussions.

I extend my special thanks to members of the team Matière Condensée et Irradiation (PS2): Franck Fortuna, Aurélie Gentils, Stéphanie Jublot-Leclerc, Olivier Plantevin, Andres F. Santander-Syro, Emmanouil Frantzeskakis, Alice Defresne, Tobias Rödel, Cédric Bareille, Dzung-Han Tsai, Monika Güttler, Xiaoqiang Li, for the good times spent at lunches and also for putting a large effort in hearing and correcting my French. Thank them to bringing joys and humor to me and to everyone else in the team.

My special thanks to Réjane, Sonia, Patricia, Kim, Christine and Nicolas for their indispensable aide concerned with mail, travel and administration during my stay.

I acknowledge the former Doctoral School 534 MIPEGE (Université Paris-Sud, Orsay, France) for the support of my Ph.D funding.

I pay respect to my family, especially my parents who always give me great supports and confidence. Finally, I give my great thanks to my girlfriend Hao Yao who gives me all her love.

Contents

Contents	1
Résumé	3
Summary	3
List of abbreviations	5
Introduction	7
Chapter 1 Bibliographic review	9
1. Generation IV nuclear reactors	10
2. Promising candidates for the fuel cladding of SFR	12
2.1. Austenitic steels.....	12
2.2. Ferritic/Martensitic (F/M) steels	13
2.3. Oxide Dispersion Strengthened (ODS) steels	14
2.3.1 Effect of chromium.....	15
2.3.2 Effect of alloying elements.....	17
2.3.3 Effect of yttria.....	17
2.3.4 Effect of titanium.....	18
2.3.5 Effect of excess oxygen	20
3. The manufacture of ODS steels	21
3.1. Conditions of synthesis	22
3.2. Mechanisms of synthesis of nano-oxide particles.....	22
3.3. Synthesis of ODS steels: alternative processes	23
4. Characterization of dispersed oxide particles	23
4.1. The different families of identified nano-oxide particles.....	23
4.2. The nature of Y-, Ti-enriched nano-oxides	25
4.2.1 Stoichiometric Y-, Ti-, O-enriched particles.....	25
4.2.2 Non-stoichiometric Y-, Ti-, O-enriched clusters.....	27
4.3. Mechanisms of nucleation of nano-oxide particles.....	30
5. Ion irradiation-induced defects: formation, diffusion and effects	32
5.1. Principle of ion irradiation	32
5.2. Properties of irradiation-induced defects	34
5.2.1 Interstitials and interstitial-impurity complexes.....	34
5.2.2 Vacancies and solute/impurity-vacancies clusters	35
5.3. Diffusion of point defects.....	36
5.4. Radiation-enhanced diffusion (RED).....	38
5.5. Radiation-induced segregation (RIS) and radiation-induced precipitation (RIP).....	39
5.6. Precipitation induced by irradiation	41
Chapter 2 Experimental techniques	43
1. Transmission electron microscopy	44
1.1. Conventional methods: SAED, BF, DF and WBDF	44
1.1.1 Selection Area Electron Diffraction (SAED).....	44
1.1.2 Bright Field (BF) and Dark Field (DF) imaging	45
1.1.3 Two-beam condition and Weak Beam Dark Field (WBDF) imaging.....	45
1.2. Analytical methods for chemical compositions: EDX, EELS and EFTEM	46
1.2.1 Energy Dispersive X-ray spectroscopy (EDX)	46
1.2.2 Electron Energy Loss Spectrometry	48
1.2.3 Comparison between EDX and EELS.....	50
1.2.4 Energy Filtered TEM (EFTEM):.....	51
1.3. Analytical methods for crystallographic structure: HRTEM	53
1.4. TEM specimen preparation	56
1.5. Thermal annealing performed in TEM.....	57

2. Introduction of the as-received material: high-purity Fe10Cr alloy	58
3. Ion implantation.....	61
3.1. Instrument.....	61
3.2. Two-stage ion implantation at RT: Al ⁺ ions then O ⁺ ions.....	62
4. Atom probe tomography (APT)	64
4.1. APT specimen preparation	65
4.2. Principle of APT.....	65
4.3. APT measurements	67
4.4. APT data treatment.....	68
4.5. Common artifacts: Trajectory aberrations & Local magnification effects.....	70
Chapter 3 Results.....	73
1. Introduction of the as-implanted material	74
2. Precipitate size and number density evolution	77
2.1. Comparison between as-implanted thin foils and FIB lamina	77
2.2. Comparison between as-implanted and annealed thin foils	78
3. Chemical compositions of precipitates.....	80
3.1. Chemical composition using EFTEM	80
3.1.1 As-implanted thin foils and FIB lamina	80
3.1.2 Annealed thin foils	84
3.2. APT analyses of as-implanted samples.....	85
3.2.1 Compositional measurements.....	85
3.2.2 Cluster analyses	88
3.2.2.1 Number density, spatial distribution and size distribution of clusters	88
3.2.2.2 Chemical compositions of clusters.....	91
3.3. APT analyses of annealed samples	95
3.3.1 Compositional measurements.....	95
3.3.2 Cluster analysis.....	98
3.3.2.1 Number density, spatial distribution and size distribution of clusters	99
3.3.2.2 Chemical compositions of clusters.....	102
4. Crystallographic structure of precipitates	105
4.1. Measurements of SAED and HRTEM obtained in as-implanted samples.....	105
4.2. Measurements of SAED obtained in annealed samples.....	113
5. Preferential precipitation in point defects sinks	115
5.1. Elements enrichment at grain boundaries	115
5.2. Precipitation on dislocation lines and loops.....	116
Chapter 4 Discussion	119
1. Room temperature material transport	120
2. Physical mechanisms involved in precipitate synthesis.....	124
Conclusion and perspectives.....	129
Annexes.....	133
Annexe A: APT and TEM sample preparation by Focused Ion Beam.....	135
Annexe B: (Fe,Cr)- and Cr-rich oxides.....	139
Annexe C: Precipitation in dislocation loops in annealed specimens.....	143
Annexe D: The effect of sample thickness on particle precipitation	145
Annexe E: TEM characterizations of single Al implanted samples	151
Annexe F: Scientific communications	157
Annexe G: Résumé en français de la thèse	159
References	163

Résumé

Les aciers ODS (Oxide Dispersed Strengthened Steels), renforcés par des dispersions de nano-oxydes métalliques (à base d'éléments Y, Ti et O), sont des matériaux prometteurs pour les réacteurs nucléaires de génération IV. La compréhension fine des mécanismes mis en jeu lors de la précipitation de ces nano-oxydes permettrait d'améliorer la fabrication et les propriétés mécaniques de ces aciers ODS, avec un fort impact économique en vue de leur industrialisation. Pour étudier expérimentalement ces mécanismes, une approche analytique par implantation ionique est utilisée dans cette étude, permettant de contrôler différents paramètres de synthèse de ces précipités comme la température et leur concentration. Ce projet a permis de démontrer la faisabilité de cette méthode et d'étudier le comportement d'alliages modèles (à base d'oxyde d'aluminium) sous recuit thermique. Des alliages Fe-10Cr de haute pureté ont été implantés avec des ions Al et O à température ambiante. Les observations de microscopie électronique en transmission ont montré que des nano-oxydes apparaissent dans la matrice de Fe-10Cr dès l'implantation à température ambiante, sans recuit subséquent. Les défauts créés lors de l'implantation ionique sont à l'origine de la mobilité des éléments introduits, permettant la nucléation de ces nanoparticules, de quelques nm de diamètre. Ces nanoparticules sont composées d'aluminium et d'oxygène, et également de chrome. Les examens en haute résolution montrent que leur structure cristallographique correspond à celle d'un composé hors équilibre de l'oxyde d'aluminium (de type $\gamma\text{-Al}_2\text{O}_3$). Les traitements thermiques effectués après implantation induisent une croissance de la taille de ces nano-oxydes, et un changement de phase qui tend vers la structure d'équilibre (de type $\alpha\text{-Al}_2\text{O}_3$). Ces résultats sur des alliages modèles s'appliquent entièrement aux matériaux industriels : en effet l'implantation ionique reproduit les conditions du broyage, et les traitements thermiques sont à des températures équivalentes à celles des traitements d'élaboration thermo-mécaniques. Un mécanisme de la précipitation de nano-oxydes dispersés dans des alliages ODS est proposé dans ce manuscrit.

Summary

ODS (Oxide Dispersed Strengthened) steels, which are reinforced with metal dispersions of nano-oxides (based on Y, Ti and O elements), are promising materials for future nuclear reactors. The detailed understanding of the mechanisms involved in the precipitation of these nano-oxides would improve manufacturing and mechanical properties of these ODS steels, with a strong economic impact for their industrialization. To experimentally study these mechanisms, an analytical approach by ion implantation is used, to control various parameters of synthesis of these precipitates as the temperature and concentration. This study demonstrated the feasibility of this method and concerned the behavior of alloys models (based on aluminum oxide) under thermal annealing. High purity Fe-10Cr alloys were implanted with Al and O ions at room temperature. Transmission electron microscopy observations showed that the nano-oxides appear in the Fe-10Cr matrix upon ion implantation at room temperature without subsequent annealing. The mobility of implanted elements is caused by the defects created during ion implantation, allowing the nucleation of these nanoparticles, of a few nm in diameter. These nanoparticles are composed of aluminium and oxygen, and also chromium. The high-resolution experiments show that their crystallographic structure is that of a non-equilibrium compound of aluminum oxide (cubic $\gamma\text{-Al}_2\text{O}_3$ type). The heat treatment performed after implantation induces the growth of the nano-sized oxides, and a phase change that tends to balance to the equilibrium structure (hexagonal $\alpha\text{-Al}_2\text{O}_3$ type). These results on model alloys are fully applicable to industrial materials: indeed ion implantation reproduces the conditions of milling and heat treatments are at equivalent temperatures to those of thermo-mechanical treatments. A mechanism involving the precipitation of nano-oxide dispersed in ODS alloys is proposed in this manuscript based on the obtained experimental results, and the existing literature.

List of abbreviations

APT	Atom Probe Tomography
BF	Bright Field
bcc	body-centered cubic (structure)
CTF	Contrast Transfer Function (in HRTEM)
DF	Dark Field
EDX	Energy Dispersive X-ray spectroscopy
EFTEM	Energy Filtered Transmission Electron Microscopy
fcc	face centered cubic (structure)
FFT	Fast Fourier Transform
HAADF	High-Angle Annular Dark Field
hcp	hexagonal close packed (structure)
HRTEM	High Resolution Transmission Electron Microscopy
MA	Mechanical Alloying
ODS	Oxide Dispersed Strengthened Steel
RED	Radiation-Enhanced Diffusion
RIP	Radiation-Induced Diffusion
RIS	Radiation-Induced Segregation
SANS	Small Angle Neutron Scattering
SAXS	Small-Angle X-ray Scattering
SFR	Sodium-cooled Fast Reactor
SIA	Self-Interstitial Atom
STEM	Scanning Transmission Electron Microscopy
TEM	Transmission Electron Microscopy
XRD	X Ray Diffraction
WBDF	Weak Beam Dark Field

Introduction

While the worldwide growth of nuclear energy slowed during the 2008-2009 global economic recession and the aftermath of the Fukushima-Daiichi nuclear accident, the World Energy Outlook projects a minimum of 40% increase in nuclear electricity production by 2035. Taking into account the responsibilities of reducing carbon emission and preventing global warming, doubling of nuclear electricity would be required¹. To respond the energy evolution requirement, the Generation IV international forum established initially by nine countries in January 2000, is now leading multinational collaboration on research and development for advanced nuclear energy systems². Generation IV nuclear energy systems are expected to have good performance in four broad areas: sustainability, economics, safety & reliability and proliferation resistance & physical protection³. France government has chosen sodium-cooled fast neutron reactor (SFR) as the priority concept among six promising advanced reactor concepts due to the abundant experience already gained from the development of prototypes Phénix (1973-2009) and Super Phénix (1983-1997). This decision imposes to develop advanced materials that can stand up to extreme operation temperatures (i.e. from 400 to 600°C) and high radiation fields (i.e. up to 200 displacements per atom) of SFR⁴.

ODS (Oxide Dispersed Strengthened) steels, which are reinforced with metal dispersions of nano-oxides (based on Y, Ti and O elements), are promising candidates for not only the application of fuel cladding of SFR but also the structural materials (e.g. first wall) of fusion reactors. The presence of high densities of nano-oxide particles is known to significantly improve the mechanical properties of ODS steels⁵. ODS are also used in other applications such automotive industry thanks to these reinforced mechanical properties. However, the fabrication of ODS steels, currently based on a co-grinding of metallic powders and thermomechanical treatments, is not optimized. The detailed understanding of the mechanisms involved in the precipitation of these nano-oxide particles would improve manufacturing and mechanical properties of these ODS steels, with a strong economic impact for their industrialization.

¹ World Energy Outlook 2012 International Energy Agency, IEA/OCED (2012)

² John E. Kelly, Progress in Nuclear Energy, **77** (2014), 240

³ https://www.gen-4.org/gif/jcms/c_9502/generation-iv-goals

⁴ J. G. Marques, energy conversion and management, **51** (2010) 1774

⁵ P. Yvon, F. Carre, Journal of Nuclear Materials, **385** (2009) 217

The mechanisms involved in the precipitation of nano-oxide particles have recently been studied and suggested by numerous researchers. Marquis *et al.*⁶ and Murali *et al.*⁷ demonstrated that nano-oxide particles formed preferentially a core/shell structure since the presence of a shell would decrease the interfacial energy, favoring the nucleation of the oxide particles. Fu *et al.*⁸ suggested yet a different mechanism obtained from first-principles studies: oxygen shows an exceptionally high affinity for vacancies. If vacancies preexist, the O-vacancy pair formation energy essentially vanishes. This O-vacancy mechanism enables the unusual high O solubility and the nucleation of O-enriched nanoclusters, which attract solutes with high O affinities (Ti and Y) in order to form Y, Ti-enriched nano-particles in ODS steels. Xu *et al.*⁹ confirmed the suggestion of Fu *et al.* by experiments of positron-lifetime spectroscopy.

Face to this uncertainty, the main objective of this PhD study is to study experimentally the mechanisms involved in the precipitation of nano-oxide particles in high purity FeCr model alloys. An analytical approach by ion implantation and subsequent thermal annealing is used, to synthesize nano-oxide precipitates under well-controlled conditions. The morphology (e.g. size, density, distribution), crystal structure and chemical composition of precipitates before and after thermal annealing are characterized by conventional and analytical transmission electron microscopy (TEM) observations combining with atom probe tomography (APT) analyses. A mechanism involving the precipitation of nano-oxide dispersed in ODS alloys is proposed in this manuscript based on the obtained experimental results, and the existing literature.

This manuscript includes four Chapters. Firstly, a summary of research background and review of typical results of ODS steels shown in the existing literature is given in Chapter 1. Experimental information including sample preparation, ion implantation, thermal annealing and characterization methods of TEM and APT are introduced in Chapter 2. The results described in Chapter 3 correspond to the morphology, chemical compositions and crystal structure of precipitates before and after thermal annealing. Finally, we discuss some non-evident features of the experimental observations and demonstrate how they contribute to the physical understanding of the oxide precipitation kinetics in Chapter 4. The conclusion & perspectives is given at the end, along with some annexes.

⁶ E.A. Marquis, Applied Physics Letter, **93** (2008) 181904

⁷ D. Murali, B.K. Panigrahi, M.C. Valsakumar, Sharat Chandra, C.S. Sundar, Journal of Nuclear Materials, **403** (2010) 113

⁸ C.L. Fu, Maja Krčmar, G. S. Painter, Xing-Qiu Chen, Physical Review Letters, **99** (2007) 225502

⁹ J. Xu, C.T. Liu, M.K. Miller, Hongmin Chen, Physical Review B, **79** (2009) 020204

Chapter 1 Bibliographic review

1. Generation IV nuclear reactors	10
2. Promising candidates for the fuel cladding of SFR.....	12
2.1. Austenitic steels.....	12
2.2. Ferritic/Martensitic (F/M) steels	13
2.3. Oxide Dispersion Strengthened (ODS) steels.....	14
2.3.1 Effect of chromium:	15
2.3.2 Effect of alloying elements:	17
2.3.3 Effect of yttria:	17
2.3.4 Effect of titanium:	18
2.3.5 Effect of excess oxygen:	20
3. The manufacture of ODS steels.....	21
3.1. Conditions of synthesis.....	22
3.2. Mechanisms of synthesis of nano-oxide particles	22
3.3. Synthesis of ODS steels: alternative processes.....	23
4. Characterization of dispersed oxide particles.....	23
4.1. The different families of identified nano-oxide particles	23
4.2. The nature of Y-, Ti-enriched nano-oxides	25
4.2.1 Stoichiometric Y-, Ti-, O-enriched particles	25
4.2.2 Non-stoichiometric Y-, Ti-, O-enriched clusters	27
4.3. Mechanisms of nucleation of nano-oxide particles.....	30
5. Irradiation-induced defects: formation, diffusion and effects	32
5.1. Principle of Irradiation	32
5.2. Properties of irradiation-induced defects.....	34
5.2.1 Interstitials and interstitial-impurity complexes	34
5.2.2 Vacancies and solute/impurity-vacancies clusters	35
5.3. Diffusion of point defects	36
5.4. Radiation-enhanced diffusion (RED)	38
5.5. Radiation-induced segregation (RIS) and radiation-induced precipitation (RIP).....	39
5.6. Precipitation induced by irradiation	41

1. Generation IV nuclear reactors

While the worldwide growth of nuclear energy slowed during the 2008-2009 global economic recession and the aftermath of the Fukushima-Daiichi nuclear accident, the World Energy Outlook projects a minimum of 40% increase in nuclear electricity production by 2035 [world energy outlook, 2012]. With the responsibilities of reducing carbon emission and preventing global warming, doubling of nuclear electricity would be required. To respond the energy evolution requirement, the Generation IV international forum established initially by nine countries in January 2000, is now leading multinational collaboration on research and development for advanced nuclear energy systems [Kelly, 2014]. Technology goals have been defined for Generation IV systems in four broad areas [GIF, website link]:

- ***Sustainability:*** Generation IV nuclear energy systems need provide long-term available energy generation and effective fuel utilization for worldwide energy production. The nuclear waste should also be minimized, thereby improving protection for the public health and the environment.
- ***Economics:*** Generation IV nuclear systems will have a reduced life-cycle cost comparing to other energy sources. Their financial risk level is comparable to other energy projects.
- ***Safety and reliability:*** Generation IV nuclear energy systems perform obligatorily at least as well in terms of safety and reliability as current nuclear reactors. In particular, these systems should have a very low degree of reactor core damage and eliminate the need for offsite emergency response.
- ***Proliferation resistance and physical protection:*** Generation IV nuclear energy systems will increase the assurance that they are very unattractive and the least desirable route for diversion or theft of weapons-usable materials, and provide increased physical protection against acts of terrorism.

Six promising advanced reactor concepts have been selected for development from among 130 proposals [Kelly, 2014]:

- ***Molten salt reactor (MSR)*** is a neutron reactor. In this concept, nuclear fuels dissolve into the molten fluoride that serves as a coolant. The mixed fluid arrives at critical condition in a graphite core, which serves also as moderator.
- ***Supercritical-Water-Cooled Reactor (SCWR)*** is a thermal neutron reactor. It uses the supercritical water (water at a temperature and pressure above its critical point, containing both properties of the liquid and the gas) as moderator and coolant.

- **Very-High-Temperature Reactor (VHTR)** is also a thermal reactor that uses graphite as moderator. The outlet temperature reaches to $\sim 1000^{\circ}\text{C}$ according to the concept.
- **Gas-Cooled Fast Reactor (GFR)** is a fast neutron helium-cooled reactor with outlet temperature of 850°C . Radiation to high doses does not make helium radioactive in comparison to other possible coolants.
- **Lead-Cooled Fast Reactor (LFR)** is a fast neutron reactor with molten lead or lead bismuth eutectic coolant.
- **Sodium-cooled fast reactor (SFR)** is fast neutron sodium-cooled reactor with closed fuel cycle for efficient management of actinides and conversion of fertile uranium.

Schematic overview and relevant characteristics of above six reactors are shown in Fig. 1.1.

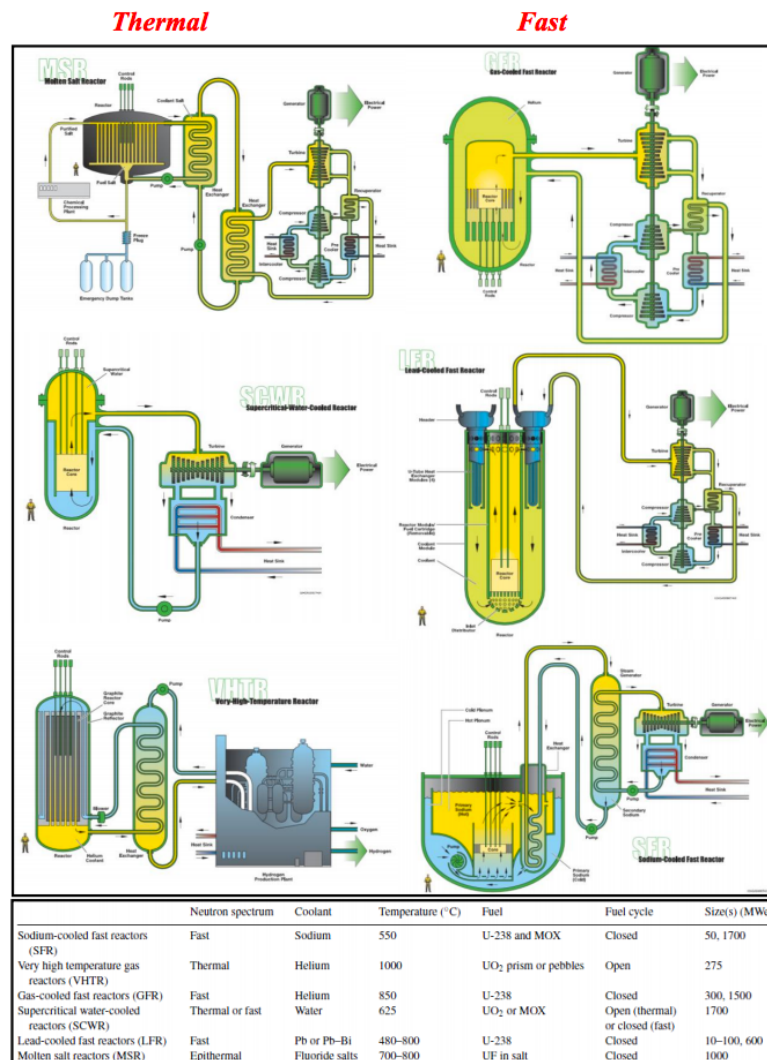


Fig. 1.1 The six generation IV reactor systems and their characteristics [Kelly, 2014].

The operating temperatures and the displacement damage doses of six promising Generation IV concepts are shown in Fig. 1.2. The values for Generation II-III concepts are given as a benchmark. To compete economically with Generation II-III concepts, Generation IV nuclear

energy systems all operate at higher temperatures that enable to improve the thermodynamic efficiency. In addition, higher displacement damage doses than in Generation II-III concepts, are expected for some of Generation IV systems (LFR, MSR, SFR).

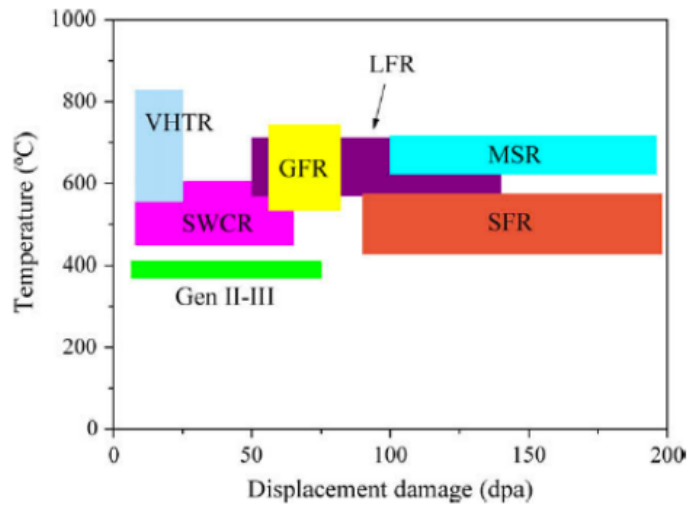


Fig. 1.2 Overview of operating temperatures and displacement damage dose regimes for structural materials in current (generation II) and proposed future (Generation IV) fission energy systems. The six Gen IV fission systems are Very High Temperature Reactor (VHTR), Super Critical Water Reactor (SCWR), Lead Fast Reactor (LFR), Gas Fast Reactor (GFR), Sodium Fast Reactor (SFR) and Molten Salt Reactor (MSR). [Marques, 2010].

Among six Generation IV concepts, SFR is chosen as a priority concept by France government because this concept benefits to its closed fuel cycle and excellent potential for actinide management, including resource extension [Capus, 2007]. Furthermore, significant experience was already gained from the development of SFR prototypes Phénix (1973-2009) and Super Phénix (1983-1997).

The fuel cladding of SFR keeps fuel pins and products of fission reaction isolating from the coolant (liquid sodium), which is a strongly corrosive reactant to metals. In addition, the cladding is subjected to temperatures from 400 to 600°C and fast neutron-induced irradiation doses up to 200 dpa [Marques, 2010]. Therefore, developing advanced materials that can stand up to extreme temperature, high radiation fields, and repeated thermal shocks over periods of years to decades is a huge challenge for SFR. The three promising candidates for the fuel cladding of SFR are described in the following section.

2. Promising candidates for the fuel cladding of SFR

2.1. Austenitic steels

304 and 316 austenitic steels were applied to for the first generation of fast reactors [Cheon, 2009 and Shibahara, 1994]. The selection is based on their good corrosion and thermal creep

resistance. The high temperature mechanical strength, good fabrication technology and abundant experience are also among their advantages. However, they are subjected to significant void swelling induced by radiation [Garner, 2000]. This disadvantage has been improved by adding stabilizing elements, varying chemical composition and applying cold work.

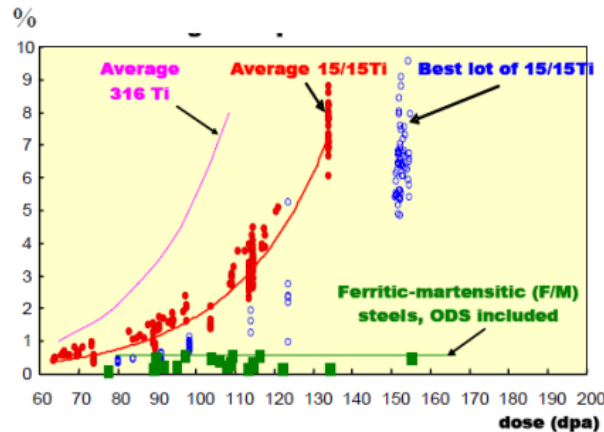


Fig. 1.3 Hoop deformation of different grades of austenitic Phénix claddings and ferritic/martensitic (F/M) materials versus dose at temperatures between 675 and 825 K after [Yvon, 2009].

As shown in Fig. 1.3, austenitic 15/15Ti steels exhibit better swelling resistance than 316 steels. However, the use of austenitic 15/15Ti steels is limited in the range of relatively low doses. In addition, the depletion of Cr at grain boundaries under high doses irradiation is suspected to play a role in irradiation-assisted stress corrosion cracking [Okamoto, 1979; Bruemmer, 1999].

2.2. Ferritic/Martensitic (F/M) steels

Ferritic/Martensitic (F/M) steels offer more advantages and are potential candidates for fuel claddings of SFR as well as for other Gen IV designs [Cheon, 2009; Shibahara, 1994]. Commercial F/M steels based on 9-12%Cr exhibit the highest swelling resistance in comparison with austenitic steels (Fig. 1.3). The high void swelling resistance is a generic property of ferritic alloys [Little, 2006]. In addition these materials have high thermal conductivity and low thermal expansion [Little, 1979]. The limitation to the use of F/M steels is their creep resistance at temperatures (400-600°C) desired in the Gen IV systems. One approach to improve the creep resistance is reinforcing the F/M steels by stable dispersion of nano-particles. The reinforced steels are introduced below.

2.3. Oxide Dispersion Strengthened (ODS) steels

Oxide Dispersion Strengthened (ODS) steels are F/M steels reinforced by a stable dispersion of nano-oxide particles. The thermally stable nano-oxide particles dispersed in the matrix improve the radiation resistance and creep resistance at high temperature. As a result, ODS steels are promising candidates for not only the application of fuel cladding of SFR but also the structural materials (e.g. first wall) of fusion reactors. In addition, ODS steels are also used in other applications such automotive industry thanks to these reinforced mechanical properties.

The first ODS steels for nuclear applications, the ODS DY and DT were developed by CEN-SCK Mol and fabricated by Dour Metal in Belgium [Bremaecker, 2012]. Meanwhile, the ODS steels MA956 were developed by International Nickel Company (INCO) in United Kingdom, and PM2000 alloys were developed by Metallwerk Plansee, a company from Austria [Klueh, 2005]. MA956 and PM2000 are 20% Cr-ODS steels containing 5% Al, which exhibit superior resistance than DY and DT to oxidation and corrosion in hot gases at high temperature. Products made from these alloys are commercially used in turbines, combustion chambers and so on. These commercialized alloys constitute the first group (also called 1st generation) of ODS steels.

The second group is devoted to the application of fuel cladding for SFR reactors, anticipating its superior resistance to radiation, and its excellent creep strength and dimensional stability at an elevated temperature. The development of ODS steels in the R&D stage has been engaged since 1990 firstly in Japan then in United States and Europe. Numerous laboratories and research groups joined the workshop or collaboration project: fabrication and microstructure are again optimized, tested, examined and reported step by step up to the ideal properties [de Carlan, 2009].

The design of ODS steels for the application of fuel cladding is based on either the martensitic or the ferritic steels, reinforced by dispersion of nano-oxides. Ytria is chosen as the dispersoid due to its good thermal stability. As an example, Y_2O_3 has the highest free energy of formation, in comparison to other oxides such as Al_2O_3 , TiO_2 and ZrO_2 at a temperature until to 2500 K [Smithells Metals Reference Book, 2004]. In addition, iron and yttrium are immiscible, so it is also in favor of the stability of Y_2O_3 in iron chromium alloys [Li, 1993]. The dispersoid Y_2O_3 serves as a block for mobile dislocation to improve the high-temperature strength and as a sink of point defects induced by radiation displacement to maintain superior radiation resistance. Presently, different ODS steels are being developed in Japan, in Europe and in United States. These ODS steels contain different amounts of Cr, and major part of them contains other alloying elements (Ti, W, Mo, Ni, Al, Mn, V, C...). Chemical

compositions of principal ODS steels are listed in the Table 1.1. The effect and function of each element is discussed below:

ODS steels	Y ₂ O ₃	Cr	Ti	W	Addition
DY [Monnet, 2004]	0,5	13	2,2	-	1,5 Mo
MA956 [Chao, 1998]	0,5	20	0,5	-	5 Al
MA957 [Miller, 2004]	0,25	14	0,9	-	0,1 Al + 0,3 Mo
PM 2000 [Sporer, 1992]	0,5	20	0,5	-	5,5 Al
12YWT [Larson, 2001]	0,25	12	0,4	3	-
14YWT [Miller, 2006]	0,25	14	0,4	3	-
K1 [Kasada, 2007]	0,37	18	0,3	0,3	-
K3 [Yutani, 2007]	0,3	16	0,3	2	4 Al
K4 [Kasada, 2007]	0,37	19	0,3	1,8	4,6 Al
M93 [Ukai, 2002]	0,35	9	0,2	2	0,12 C
F94 [Ukai, 2000]	0,24	12	0,3	2	0,06 C
F95 [Yamashita, 2004]	0,25	12	0,3	2	0,06 C
1DK [Yamashita, 2002]	0,34	13	0,6	2,8	0,05 C
1DS [Yamashita, 2002]	0,63	11	0,4	2,7	0,09 C
ODS-Eurofer97 [Schaublin, 2002]	0,3	9	-	1,1	0,5 Mn + 0,2 V + 0,11 C
Fe-14Cr-Y2O3 (J05 CEA) [Steckmeyer, 2010]	0,3	14	0,3	1,1	0,3 Mn + 0,3 Si + 0,15 Ni

Table 1.1: nominal chemical compositions (wt%) of principal ODS steels

2.3.1 Effect of chromium

Due to the content of Cr, ODS steels are distinguished into three categories: (i) martensitic ODS steels (e.g. M93 and ODS-Eurofer 97); (ii) ferritic ODS steels (e.g. MA957, 12YWT and 14YWT); (iii) high Cr content ferritic ODS steels (e.g. K1, K3, K4 and PM2000). Ferritic/martensitic ODS steels containing 9–12 wt.% chromium have been developed as the fuel cladding material of SFR because of their high creep strength at elevated temperatures and enough resistance to neutron irradiation embrittlement.

However, the application of ferritic/martensitic ODS steels to the cladding in SCWR and LFR is limited because of insufficient corrosion resistance of the steel. Thus, high Cr content ferritic ODS steels are developed for the application to SCWR and LFR, of which the most critical issue is to improve their corrosion resistance.

It is well known that the corrosion resistance of ODS steels increases with chromium concentration. However, the effect of Al on corrosion resistance depends on Cr concentration (e.g. it has been reported the addition of 4 wt.% Al did not remarkably influence the corrosion resistance. However, in 16Cr-ODS steel, the addition of Al improved corrosion resistance.). For this reason, high Cr (up to 22%) ODS steels with Al additives (up to 4.5%) have been considered for the application to structural materials used in the high corrosive environment [Kimura, 2011].

On the other hand, high Cr concentration is often subjected to increase aging embrittlement in the temperature region around 475 °C, through the formation of Cr-rich secondary phase. The demixion between Fe-rich phase and Cr-rich phase induces an increase of ductile-brittle transition temperature (DBTT) [Lee, 2007]. Kimura *et al.* [Kimura, 2009] have investigated the aging effects of ODS steels with different Cr content by measuring their impact fracture energy at RT after aging at 500 °C up to 10kh (Fig. 1.4). The results show that the fracture energy decreases with increasing Cr content before and also after aging. In addition, aging causes a significant reduction in the fracture energy.

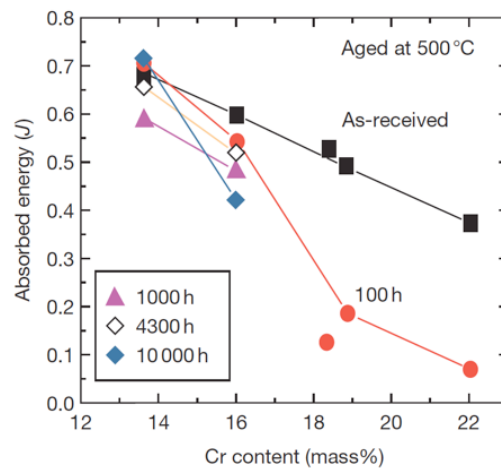


Fig. 1.4 Ageing embrittlement of high Cr-ODS steels with respect to Cr content [Kimura, 2009].

Moreover, ferritic ODS steels have a strong strength anisotropy due to the extremely elongated “bamboo” structure grains (Fig. 1.5(a)) in the matrix. These grains, created during the manufacturing step (hot extrusion), are parallel to the rolling direction and lead to the strength degradation in other direction. A possible approach to overcome this hurdle is to apply the recrystallization processing [Ukai, 1997; Ukai, 2002] for ferritic ODS steels. Fig. 1.5(c) represents the TEM micrograph showing recrystallized grains: recrystallization heat-treatment was applied to break the “bamboo” structure elongated grains and to produce more equi-axed grains. The anisotropy of strength is thus reduced. Up to now, this issue is still being studied since the recrystallization processing is very difficult to achieve.

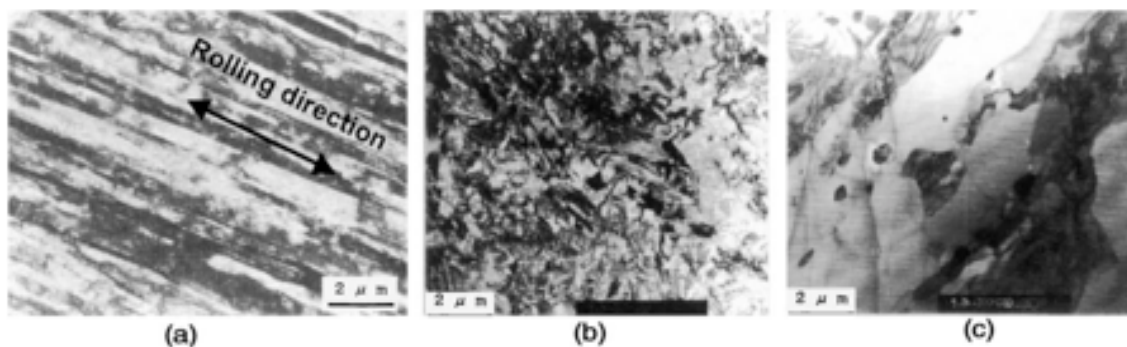


Fig. 1.5 TEM micrographs of thin foils: (a) in cold-rolled cladding; (b) tempered martensitic structure of 9Cr-ODS; (c) recrystallized structure of 12Cr-ODS [Ukai, 2002].

From that point of view, martensitic ODS steels are more attractive since the structure would be composed of more equi-axed grains (see Fig. 1.5(b)) due to the reversible α - γ phase transformation in the hot-extrusion and the subsequent heat treatment [Ohtsuka, 2004]. Hence, the choice of Cr content is a compromise among the corrosion resistance, ductility property and strength isotropy.

2.3.2 Effect of alloying elements

A series of alloying elements are available to be introduced into ODS steels. Each of them has proper function. The general rule is to avoid formation of long life radioactive nuclides. So normally, low activation elements are preferably used. That is why Mo (high activation) is replaced by W (low activation) in some of ODS steels. In addition, W is a more effective solid solution strengthener than Mo. As a familiar element in steels, C with a relative low or high content is added into some ODS steels. The reason is to ensure ODS materials as 100% martensitic or 100% ferritic steels. Other minor elements in ODS steels are restricted strictly at low amounts.

2.3.3 Effect of yttria

Ukai *et al.* [Ukai, 1993] have investigated the effects of Y_2O_3 contents (up to 0,56 wt%) on tensile properties and creep rupture strength of ODS steels. As shown Fig. 1.6(a), the tensile strength along the extruded direction increases consistently with an increase in Y_2O_3 content, whereas the total elongation decreases. From Fig. 1.6(b), the creep rupture strength (resistance of creep) at 973 K is saturated at about 0,4 wt% content.

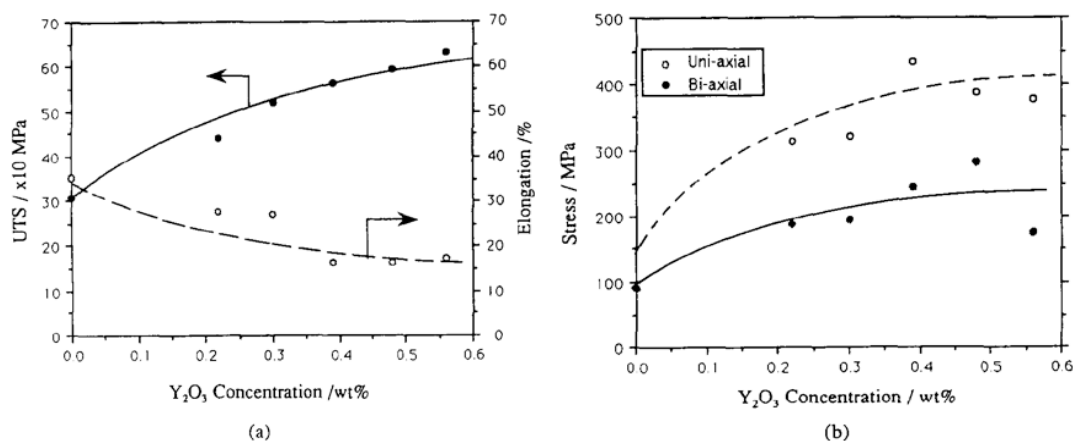


Fig. 1.6 Effect of addition of Y_2O_3 in 13Cr-3W-0,5Ti on tensile properties (a) and creep rupture strength (b) at 923 K (5 specimens) [Ukai, 1993].

In addition, Ukai *et al.* [Ukai, 1997] demonstrated the degree of recrystallization depends on the content of Y_2O_3 . The content should be restricted below the appropriate amount (0,25 wt%) for attaining the recrystallized structure in ODS steels.

Ohtsuka *et al.* [Ohtsuka, 2004] reported that 9Cr-ODS martensitic steels with Y_2O_3 shows a peculiar transformation behavior comparing with base steels without Y_2O_3 . The presence of particles suppresses partially the reverse transformation from α to γ phase during hot extrusion, thereby forming not only equi-axed martensitic grains but also elongated residual- α phase grains. This phenomenon was also observed by Yamamoto *et al.* [Yamamoto, 2010] via dilatometric measurement. It suggested that the possible mechanism of formation process of residual- α phase grains is a competition between the driving force (ΔG) and pinning force (F), where the driving force is evaluated in terms of Gibbs energy versus carbon content at each temperature, and the pinning force is due to the presence of oxide particles respectively. Residual- α phase grains contain ultra-fine oxide particles and close oxide particles distribution, which are responsible for apparent improvement of creep resistance at high temperature. The content of Y_2O_3 added in ODS steels, is thus a compromise between mechanical properties and creep resistance.

2.3.4 Effect of titanium

The effects of addition of elements such as Ti, Nb, V, Zr in ferritic ODS steels were investigated and are shown in Fig. 1.7(a). An addition of small amounts of Ti or Zr sufficiently reduces the size of oxide particles. But the effectiveness of Zr is weaker than that of Ti. Ukai *et al.* [Ukai, 1993] compared the efficiency of the addition of Ti and TiO_2 . He suggested that the formation of ultra-fine oxide particles is better achieved by the addition of Ti than by TiO_2 . With adding Ti up to 0,55 wt%, the resistance of creep is also increased in ferritic ODS steels as shown in Fig. 1.7(b).

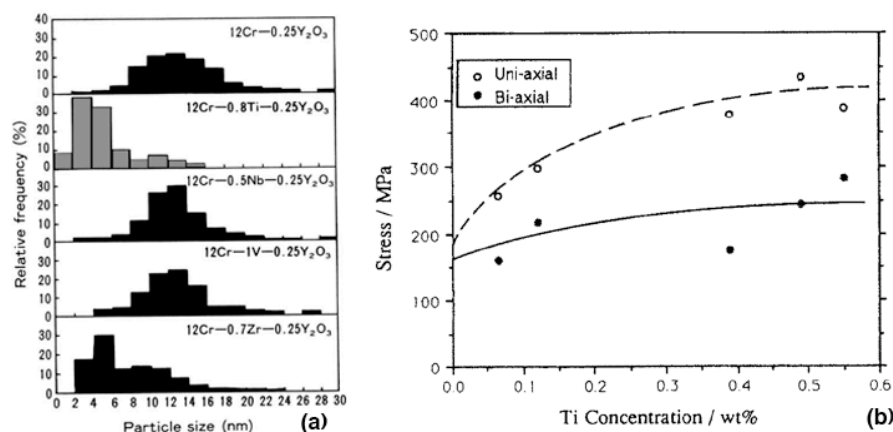


Fig. 1.7: (a) Size distribution of oxide particles determined by TEM in 12Cr-ODS steels in various elements addition [S. Ukai, JNM, 2002]; (b) Effect of addition of Ti in 13Cr-3W-0,5Y₂O₃ ODS steels on creep rupture strength at 923K (5 specimens) [Ukai, 1993].

Further study of Ukai [Ukai, JNST, 2002] confirmed Ti plays an important role in reducing the oxide particle size and improving creep resistance. Based on TEM micrographs and EDX analyses, he revealed that Y_2O_3 particles are chemically changed to $Y_2Ti_2O_7$ ($Y_2O_3-2TiO_2$) or

Y_2TiO_5 (Y_2O_3 - TiO_2). The reduction of the average particle radius and the average inter-distance between particles happen at the same time. The improvement of creep resistance is attributed to the drastic reduction of oxide particles size.

Different works confirmed this result. Ramar *et al.* [Ramar, 2009] investigated the microstructure of ODS Eurofer 97 (with or without Ti) by TEM. After comparing the distribution of particles, he concluded that the addition of Ti results in the reduction of size of particles (about 20 nm and 7 nm, respectively without and with Ti). Klimiankou *et al.* [M. Klimiankou, 2004] characterized particles in ODS (Ti-containing) steels by HRTEM (High Resolution TEM) and EFTEM (Energy Filter TEM). The analysis of HRTEM picture combined with EFTEM results show definitely that there is not any formation of pure Y-O particles, and formed oxide particles have $Y_2Ti_2O_7$ composition. Miller *et al.* [Miller, 2003], using APT, compared the distribution of oxide particles in as-processed 12YW and 12YWT (Ti-containing) ODS steels (see Fig. 1.8). The results indicated that the size of particles in 12YWT is slightly smaller than the one in 12YW (2 nm instead of 2,4 nm), but the number density of particles in 12YWT is higher than the one in 12YW ($1,4 \times 10^{24} m^{-3}$ instead of $3,9 \times 10^{23} m^{-3}$). It proves the effect of the addition of Ti in ODS steels.

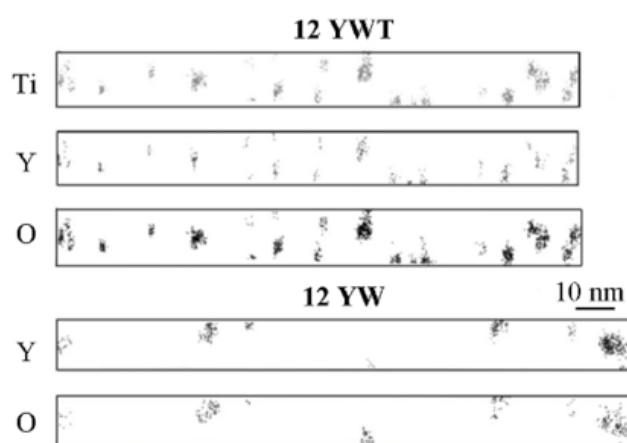


Fig. 1.8 Atom maps of the 12YW (without Ti) and 12YWT (with Ti) ODS steels showing the presence of fine Y+Ti+O-enriched particles. The number density of particles is higher in the 12YWT [Miller, 2003].

In addition, several analyses were carried out on powders of ODS steels after different milling conditions and heat treatment by Ratti *et al.* [Ratti, 2009] via SANS (small angle neutron scattering). This study shows Ti is available to refine the precipitation in ODS steels, and the nano-phases formed in ODS steels, which contain the element of Ti, are much more resistant to coarsening than the phases without Ti.

The generation of elongated residual- α phase grains is enhanced due to the solute carbon shortage through increasing Ti contents and forming TiC precipitates [Ohtsuka, 2004]. If Ti is added to excess, however, it creates too much strength, which negatively impacts cold rolling

and cold workability. To achieve a balance between strength and workability, a compromised value of Ti should be selected.

2.3.5 Effect of excess oxygen

Excess oxygen is defined as subtracting oxygen contents in Y_2O_3 from total O contents in steel. Since it is easy to be mixed in steels during the manufacturing process, the contamination of excess oxygen should be studied. In 1993, Ukai *et al.* [Ukai, JNM, 1993] examined the effect of the excess oxygen content varying from 0,05 to 0,15 wt% in 13Cr-0,5Ti-0,5Y $_2O_3$ steels. They concluded that ultra-fine (Y, Ti, O) oxide particles could not be formed without any excess oxygen. And the creep rupture strength of these steels increases with excess oxygen content and saturates at around 0,08 wt%. Their latter study [Ukai, ISIJ, 2002] shown that the degradation of creep strength exists if excess oxygen content is too small.

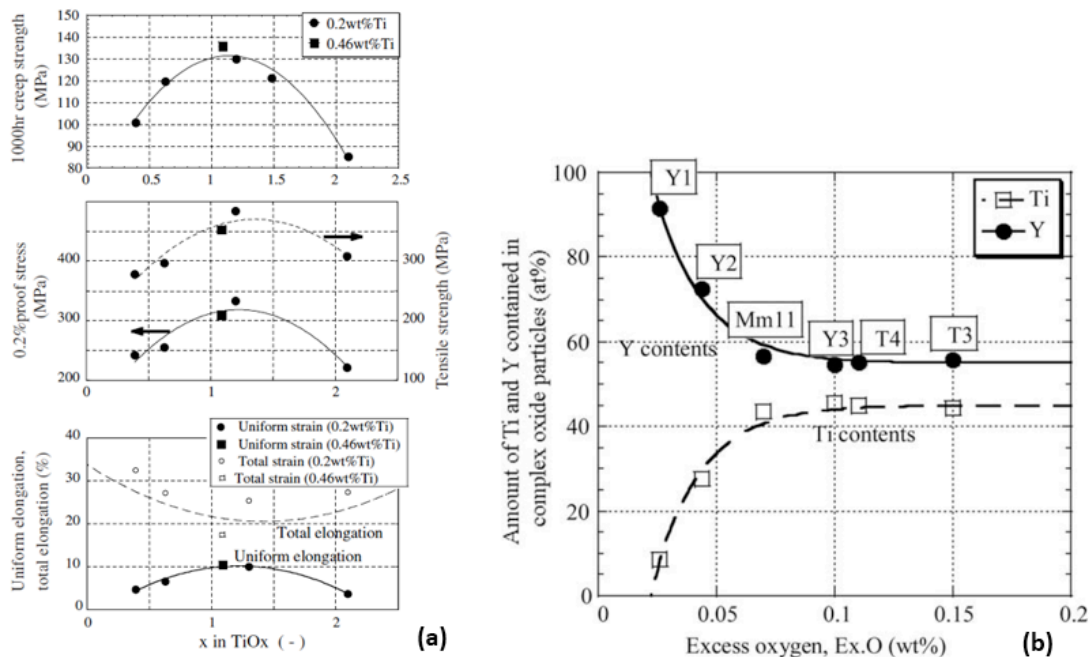


Fig. 1.9: (a) mechanical properties versus atomic ratio of Ex.O/Ti, x in TiO_x ; (b) EDX analysis result of oxide particles in transformed α -grain by extracted replica [Ohtsuka, 2004].

Ohtsuka *et al.* [Ohtsuka, 2004] studied the effect of excess oxygen content combining with the content of Ti. The excess oxygen and Ti contents were varied from 0,026 to 0,17 and from 0,18 to 0,46 wt% respectively in the study. They revealed that when the atomic ratio between excess oxygen and Ti (x in TiO_x) is around 1,0, the formation of elongated residual- α phase grains, which possess ultra-fine and close oxide particles distribution, are promoted. The number density of oxide particles in equi-axed grains would be maximum at the same time. Therefore, superior mechanical properties as shown in Fig. 1.9(a) are achieved, when x in TiO_x is around 1,0. Higher excess oxygen-containing steels than 0,07 wt% have the Y/Ti ratio

close to 1,0 (see Fig. 1.9(b)) in oxide particles. It is inferred that oxide particles may be similar to $Y_2Ti_2O_7$. The subsequent study [Ohtsuka, 2006] demonstrated that excess oxygen plays relatively a more important role than Ti for making fine and dense oxides particles as well as improving mechanical properties.

In summary, the choice of chemical components of ODS steels results from a compromise among different properties (such as corrosion resistance, creep strength, ductility and workability). It is the reason why the chemical compositions of ODS steels vary from one to the other one. It should be noticed that the properties of ODS steels depend on also fabrication processes and conditions.

3. The manufacture of ODS steels

The first elaboration of ODS materials (nickel-base superalloy) was achieved by Benjamin in 1970 [Benjamin, 1970] via mechanical alloying. This method, still being used to obtain a fine distribution of nano-oxide particles in the matrix until today, proves its absolute adaptability for the manufacture of ODS steels. The manufacture of ODS steels consist of a series of processes: mechanical alloying (MA), consolidation and additional heat treatment (Fig. 1.10).

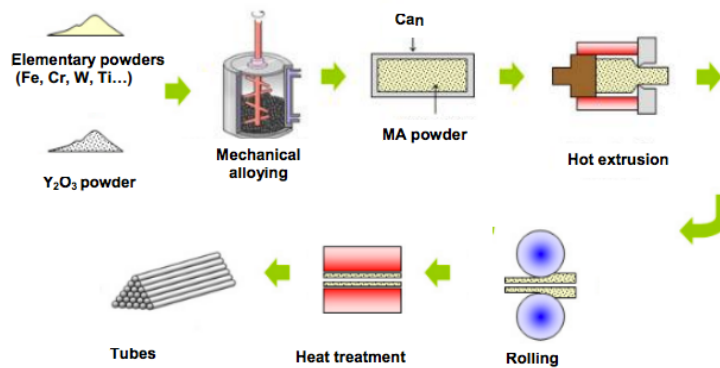


Fig. 1.10 Basic scheme of ODS production: mechanical alloying and subsequent heat treatment [Ukai, 2000].

During MA, the element powders and yttria powder are mechanically alloyed in an argon gas atmosphere using either a planetary ball mill or an attrition type ball mill. The mechanically alloyed powders are sealed in hollow-shaped cans and degassed in several hours. Then, the hollow shape of the bars is consolidated by powder metallurgical processes, such as Hot Isostatic Pressing (HIP) or Hot Extrusion (HE). In order to match the final dimension of fuel cladding, different recrystallization and cold/warm heat treatments are applied to produce final shape such as tube [Odette, 2008; Ukai, 2000].

3.1. Conditions of synthesis

The nature of nano-oxide structures highly depends on conditions of synthesis. For MA, the conditions of synthesis include: atmosphere, temperature, time of MA, the weight ratio of ball to powder and type of milling equipments, etc [Surgyanarayana, 2001]. For the consolidation, the key parameter is temperature. Although numerous of ODS steels were successfully synthesized by either planetary ball milling [Hsiung, 2011; Williams, 2010; Couvrat, 2011] or attrition type ball milling [Couvrat, 2011; Unifantowicz, 2011], the conditions of synthesis are still far away from being fully understood.

Klimenkov *et al.* [Klimenkov, 2009] studied two lots of ODS steels named as UE and FZK, which are produced by the same processes. The presence of complex oxide particles was observed in the UE, whereas this was not the case in the FZK. In addition, Hoelzer *et al.* [Hoelzer, 2007] synthesized the 14 YWT ODS steels, of which the measured DBTT temperature is 81 °C. This value has a huge difference with the value obtained by McClintock *et al.* [McClintock, 2009], which is -188 °C for 14 YWT ODS steels. Therefore, understanding of mechanisms controlling the processes of synthesis becomes a major object for studies of ODS steels.

3.2. Mechanisms of synthesis of nano-oxide particles

The mechanism of synthesis of nano-oxide particles was widely proposed as the dissolution of Y₂O₃ during ball milling followed by precipitation of oxide during annealing [Miller, 2006; Alinger, 2004]. This mechanism was supported by the study of Okuda *et al.* [Okuda, 1995] who synthesized and characterized an ODS steel containing high content of Ti and Y₂O₃. The characterization after MA by XRD and TEM confirmed no any oxide existed. Small Angle X-Ray Scattering (SAXS) revealed that most of objects after MA are nanoclusters smaller than 1 nm. On the contrary, nano-oxide particles precipitated in the ODS steel after the thermal annealing at 1000 °C. Studies by Larson *et al.* [Larson, 2001] and Miller *et al.* [Miller, 2006] are also in the same direction. It should be reminded that APT investigations in their studies are performed only in the final state of the manufacture of ODS steels. Therefore, APT investigations were not achieved in the state just after MA.

However, Laurent-Brocq *et al.* [Laurent-Brocq, 2012] proposed a different mechanism based on the study in a Fe-Y₂O₃ model ODS alloy processed by reactive ball milling and annealing. According to their study, reactants are dissolved into the iron matrix until an oversaturated solid solution is formed, and the nucleation of nanoclusters can thus begin during MA.

Subsequent thermal annealing at 800 °C induces a great enhancement of NC nucleation which stops after few minutes without any coarsening occurring. The unexpected nucleation occurring at MA stage is owned to numerous vacancies created by MA. The relation between vacancies and nano-oxide particles in ODS steels will be talked later.

3.3. Synthesis of ODS steels: alternative processes

Several alternative processes replacing MA in the synthesis of ODS steels were reported: Laurent-Brocq *et al.* [Laurent-Brocq, 2010] adopted YFe_3 and Fe_2O_3 as reactants, and applied them to the reactive ball milling since this method usually promotes the formation of nanoclusters [Legendre, 2007]. It was shown that reactive ball milling and thermal annealing were efficient in synthesizing a ODS steel. Liu *et al.* [Liu, 2010] melted firstly some alloying elements (Fe, Cr, W, Fe-Ti and Fe-Y) to form a base alloy. Oxygen was then introduced by importing an atmosphere of Argon and Oxygen. The objective is forming a homogeneous Y-Ti-O dispersion in matrix only by heat treatments without MA. Both large (100 nm) Ti-rich and fine (10-20 nm) Y-Ti-rich oxides were observed after a thermal annealing at 1300 °C. Schneibel *et al.* [Schneibel, 2008] proposed an internal oxidation of intermetallics (Fe_{17}Y_2 or Fe_{11}YTi) at 700 °C. Y-Fe-rich and Y-Ti-rich oxide particles (20-40 nm) were observed. Further thermal annealing at 1100 °C induced the coarsening of particles until to 200 nm. Finally, Sakuma *et al.* [Sakuma, 2004] replaced MA by a co-implantation of Y^+ and O^+ ions. The co-implantation into the ferritic steel induced an oversaturated solid solution of implanted ions. Then, subsequent thermal annealing induced Y-rich oxide precipitation and a homogeneous distribution of precipitates. The disadvantage about the cost cannot cover the importance of this method since it offers an experimental approach to better understand the mechanism of synthesis of ODS steels.

4. Characterization of dispersed oxide particles

4.1. The different families of identified nano-oxide particles

Microstructure of ODS steel has been characterized mainly by TEM and APT. According to these characterizations, the smallest size of particles is about 1-2 nm, whereas the biggest size can reach 50 nm. Moreover, the chemical compositions are not uniform. In fact, the nature of oxide particles strongly depends on conditions of fabrication and components of alloys.

Fig. 1.11(a) shows a BF TEM image of extraction replica obtained from MA957 ODS steels [Sakasegawa, 2009]. Further analysis of XRD and EDX indicated that there are at least three types of phases (Fig. 1.11(b)): (1) non-stoichiometric Y-, Ti-, O-enriched clusters with a size of 2-10 nm; (2) stoichiometric $Y_2Ti_2O_7$ that have a larger particle size of 10-35 nm; and (3) aggregated oxides (> 100 nm) such as Ti-enriched oxides and Al-enriched oxides.

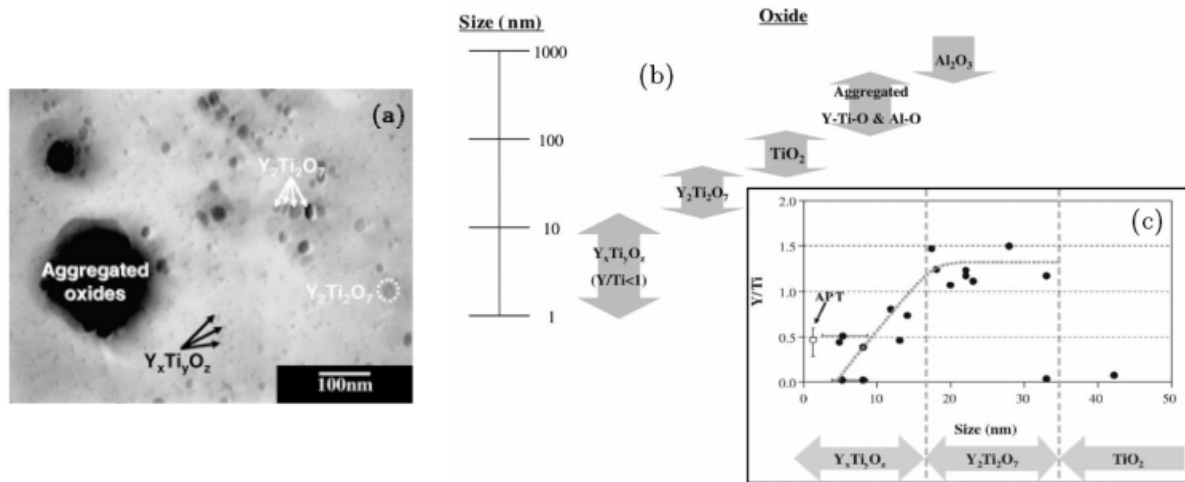


Fig. 1.11 Analysis of particles identified in the ODS MA957: (a) TEM image of extraction replica; (b) size distribution of oxides; (c) correlation between chemical composition and size of oxide particles [Sakasegawa, 2009].

The presence of TiO_2 at grain boundaries in ODS steels was reported by Kasada *et al.* [Kasada, 2011]. The study shows the evidence that not all Ti atoms associate with Y atoms in order to form Y-, Ti-, O-enriched clusters. Complex carbide $M_{23}C_6$ were also observed in ODS steels with 9 at.% [Ramar, 2009], 14 at.% [Olier, 2012] and 19 at.% [Kasada, 2007] Cr. Precipitates of carbide $M_{23}C_6$ exist principally at grain boundaries of these ODS steels. The presence of carbon is believed to be the reason for the formation of these carbides. And carbon seems to come from the contamination during MA. Klimiankou *et al.* [Klimiankou, 2007] demonstrated that the presence of carbide $M_{23}C_6$ can be eliminated if an adequate heat treatment is applied to ODS steels.

The formation of aggregated Ti-enriched oxides and complex carbide $M_{23}C_6$ suppress the nucleation of nano-size Y-, Ti-, O-enriched particles and lead to the segregation of minor elements. They are thus considered as non-desirable nano-particles in ODS steels. So subsequent introduction will only focus on the nature of stoichiometric Y-, Ti-, O-enriched particles and non-stoichiometric Y-, Ti-, O-enriched clusters.

4.2. The nature of Y-, Ti-enriched nano-oxides

4.2.1 Stoichiometric Y-, Ti-, O-enriched particles

For stoichiometric Y-, Ti-, O-enriched particles, chemical compositions of particles were also investigated intensively by several different methods. According these studies, stoichiometric Y-, Ti-, O-enriched particles have not only $Y_2Ti_2O_7$ as reported by Sakasegawa *et al.* [Sakasegawa, 2009], but also Y_2TiO_5 or even Y_2O_3 in both Ti-added ODS steels and ODS steels without Ti addition. The XRD analysis of extracted replica dissolved from the matrix of Ti-added ODS steels revealed the diffraction peaks corresponding to two crystallographic structures: $Y_2Ti_2O_7$ and Y_2TiO_5 [Ukai, 1993; Okuda, 1995]. With applying EDX analysis to large size Y-, Ti-, O-enriched particles, Ohtsuka *et al.* [Ohtsuka, 2004] found two different ratios of Y/Ti, and thus distinguished to $Y_2Ti_2O_7$ (Y/Ti = 1) and Y_2TiO_5 (Y/Ti = 2). The investigations of Small Angle X-ray Scattering (SAXS) combined with Small Angle Neutron Scattering (SANS) allowed Ohnuma *et al.* [Ohnuma, 2009] to identify the presence of $Y_2Ti_2O_7$ particles in 9Cr-ODS steels. Alinger *et al.* [Alinger, 2009] confirmed the presence of $Y_2Ti_2O_7$ particles in MA957 and 12YWT ODS steels with using the same technique. In addition, Alinger *et al.* also observed the presence of Y_2TiO_5 .

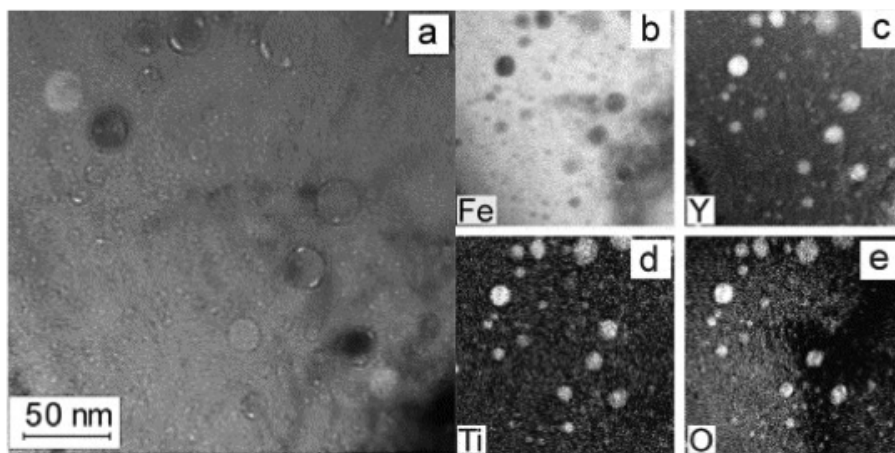


Fig. 1.12 Conventional bright field (a) and EFTEM images (b)–(e) of $Y_2Ti_2O_7$ ODS particles in reduced-activation ferritic–martensitic steel. The bright field image was taken slightly defocused in order to enhance the particle contrast. The EFTEM mapping images were acquired using Fe $L_{2,3}$, Y $M_{5,6}$, Ti $L_{2,3}$, and O K EELS edges [Klimiankou, 2004].

Energy-Filtred TEM (EFTEM) and High-Resolution TEM (HRTEM) are also adequate techniques which allow us to identify chemical compositions of nano-particles, and determine their crystallographic structures.

Klimiankou *et al.* [Klimiankou, 2004] investigated RAFM-ODS alloys by EFTEM and HRTEM. EFTEM mapping images acquired using Fe $L_{2,3}$, Y $M_{5,6}$, Ti $L_{2,3}$, and O K edges are shown in Fig. 1.12(b-e). The dark spots on the Fe $L_{2,3}$ image (Fig. 1.12(b)) show the local Fe deficiency, whereas the bright spots on the Y $M_{5,6}$, Ti $L_{2,3}$, and O K images (Fig. 1.12(c-e))

show the local Y, Ti, O enrichment. Moreover, bright spots are consistent with the contrasts shown in the BF image (Fig. 1.12(a)) and the dark spots shown in the Fe $L_{2,3}$ image (Fig. 1.12(b)). This suggests that nano-particles have the Y-Ti-O compositions.

Fig. 1.13(a) shows a HRTEM micrograph from an ODS particle in which two atomic planes are visible simultaneously. A combination of the interplanar distance and the angle between the systems of planes is given in Fig. 1.13(b) for the (0 0 4) and (2 -2 2) atomic planes of $Y_2Ti_2O_7$ cubic phases with the [1 1 0] zone axis. Actually, the measured data are equal to the following data calculated from the $Y_2Ti_2O_7$ structure. The analysis of HRTEM picture combined with above EFTEM results show definitely that ODS particles have $Y_2Ti_2O_7$ composition.

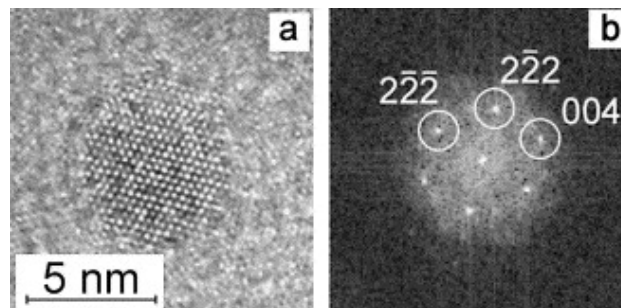


Fig. 1.13 HRTEM micrograph of a $Y_2Ti_2O_7$ particle (a) and FFT image of this micrograph (b). The diffraction spots from $Y_2Ti_2O_7$ particle of $\{2\ 2\ 2\}$ and $\{0\ 0\ 4\}$ types are marked with circles [Klimiankou, 2004].

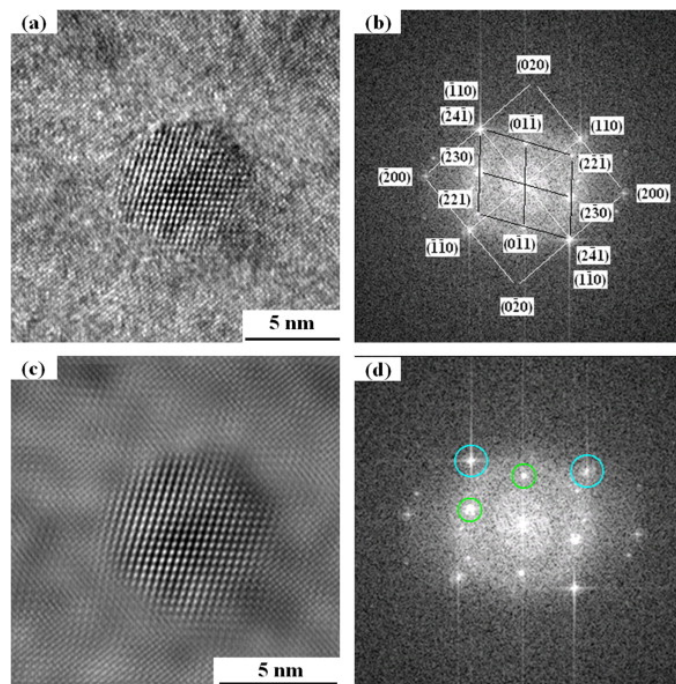


Fig. 1.14 (a) HRTEM micrograph of a semi-coherent orthorhombic Y_2TiO_5 oxide and the surrounding matrix, (b) FFT diagram of the micrograph in (a), (c) FFT filtered image of the lattice image in (a), and (d) diffraction spots used to reconstruct the IFFT image (c) [Dou, 2014].

Dou et al. [Dou, 2014] characterized the nano-particles in an Al-alloyed high-Cr ODS alloy with Zr addition by HRTEM. Semi-coherent orthorhombic Y_2TiO_5 oxides were observed.

Fig. 1.14 shows the HRTEM image of an Y_2TiO_5 oxide (about 7.4 nm) and the surrounding matrix lattice. The measured interplanar distances and angles are consistent with the reference values. However, some authors [Bhattacharryya, 2012; Cayron, 2010] reported the observation of structures of nano-particles, which are quite similar to Y_2TiO_5 or $Y_2Ti_2O_7$, but correspond not to any known Y-, Ti-enriched oxides.

Klimiankou *et al.* [Klimiankou, 2003] observed the correlation of orientation between nano-particles of Y_2O_3 and the matrix lattice in the ODS Eurofer alloy without Ti addition. Ramar *et al.* [Ramar, 2009] confirmed that it exists the orientation relation between nano-particles of Y_2O_3 and the matrix in the ODS Eurofer alloy without Ti addition. But the relation is not fully coherent but semicoherent. On the contrary, Yamashita *et al.* [Yamashita, 2004] suggested that there is no any particular coherence between nano-particles of Y_2O_3 and the matrix in the 12Cr ODS steel.

Ribis *et al.* [Ribis, 2012] studied the interfacial strained structure and orientation relationships of the nano-particles in a Fe-14Cr-W-Ti after a thermal annealing at 1573 K and 1h. The thermal annealing induced the coarsening of nano-particles. Most of the coarsened phases found are $Y_2Ti_2O_7$ particles, which have a cubical shape and embedded with a cube-on-cube orientation relationship with the matrix. The lattice misfit calculated is about 12.6% which suggests that particles are semicoherent. The interfacial structure revealed by using Moiré fringes concluded that $8d\{110\}Fe$ equals to $9d\{440\}Y_2Ti_2O_7$, there is thus common planes existing. And every $8d\{110\}Fe$ a misfit dislocation is potentially introduced to relax the interfacial strain.

It was reported that the recrystallization [Yazawa, 2004] and phase transformation [Yamamoto, 2011] induce the loss of interface coherence between nano-particles and the matrix in ODS steels. It means the interface coherence is susceptible to processes of the fabrication of ODS steels.

4.2.2 Non-stoichiometric Y-, Ti-, O-enriched clusters

The APT method is ideal to investigate the compositions of non-stoichiometric Y-, Ti-, O-enriched clusters since their size is quite small (< 5 nm) for conventional TEM investigations. Several results of APT investigations are summarized in the Table 1.2.

ODS steels	Fe	Cr	W	Y	Ti	O	Y/Ti	(Y+Ti)/O
MA957 [Miller, 2004]	10.1 ± 4.1	1.7 ± 1.7	-	15.4 ± 7.3	32.9 ± 5.3	39.9 ± 6.9	0.5	1.2
Ma957 [Miller, 2011]	-	-	-	9.1 ± 0.6	49.5 ± 1.4	37.5 ± 1.2	0.18	1.4
14YWT [Miller, 2006]	5.5 ± 4.6	1.2 ± 1.1	-	7.5 ± 4.3	42.2 ± 5.6	43.5 ± 5.3	0.18	1.1
14YWT [He, 2014]	57.7 ± 8.5	19.5 ± 1.8	0.53	3.7 ± 1.8	8.6 ± 4.3	9.8 ± 4.2	0.43	1.25
12YWT [Miller, 2003]	-	7.0 ± 4.3	0.21	9.22 ± 7.8	19.9 ± 8.7	23.6 ± 10.6	0.46	1.27
12YWT [Miller, 2005]	4.1 ± 4.1	0.8 ± 0.8	0.13	8.1 ± 5.2	42 ± 5.6	44.4 ± 8.2	0.19	1.13
Fe18Cr-Y ₂ O ₃ [Ribis, 2014]	63.6 ± 4.3	24.4 ± 3.1	0.43	2.8 ± 0.3	5.1 ± 1.3	1.6 ± 0.8	0.6	4.9

Table 1.2: Nano-oxides (2-5 nm) compositions (at.%) and standard deviation of different ODS steels reported in the literature.

The compositions reported in each study are highly sensitive to ODS steels chemistry, processing conditions, and choice of APT parameters. For same 14 YWT ODS, Miller *et al.* [Miller, 2006] reported T-, Ti-, O-enriched nanoclusters contain 5.5 at.% Fe and 1.2 Cr at.%. The ratio of Y/Ti and (Y+Ti)/O are 0.18 and 1.1, respectively. However, He *et al.* [He, 2014] reported the nnaoclusters contain huge amount of Fe (57.7 at.%) and Cr (19.5 at.%). In addition, the ratio of Y/Ti is 0.43, which is almost three times more than the value obtained by Miller *et al.* Even for the same 12 YWT ODS and the same research group, the compositions of nanoclusters reported in 2003 by Miller *et al.* [Miller, 2003] are not the same with the one reported in 2005 [Miller, 2005].

The presence of elements belonging to matrix, such as Fe was suggested to be an artifact due to the lower evaporation field of oxygen-rich phases [Marquis, 2008]. The difference of evaporation field could induce local magnification effects and leads to aberrations at reconstructed interface over distances. Williams *et al.* [Williams, 2010] suggested an approach to reduce the contribution of this artifact, with the use of simple corrections to the APT data during the analysis. With applying this approach to the existing data, Miller *et al.* [Miller, 2011] reported the corrected compositions of nanoclusters in MA957 ODS, which are only contain the values of Y, Ti and O.

Because the non-stoichiometric nanoclusters are very small (2-5 nm), embedded in the Fe matrix, and may have a coherent relation with the matrix, it is thus extremely difficult to obtain the structural information by conventional TEM, which is limited by a low spatial resolution and the lack of capability for atomic-scale chemical analysis. Thanks to the evolution of TEM instruments and techniques, the characterization of crystallographic structure for non-stoichiometric nanoclusters is feasible.

Bhattacharryya *et al.* [Bhattacharryya, 2012] confirmed that the crystallographic structure of non-stoichiometric nanoclusters conserve $Y_2Ti_2O_7$ pyrochlore structure even if they are quite small than 4 nm. On the contrary, Brandes *et al.* [Brandes, 2012] indicated the crystallographic structure of non-stoichiometric nanoclusters is hard to identify since the structure is strongly disordered and looks to be amorphous.

Recently, more and more TEM microscopes are equipped with double Cs-correctors. Double Cs-corrected TEM can attain a resolution below to 1 Å in STEM mode, which allows us to well understand the structure and chemical feature of the non-stoichiometric nanoclusters. Hirata *et al.* [Hirata, 2011] achieved the atomic scale characterization of the nanoclusters with using Cs-corrected TEM. The experimental HAADF-STEM image of a nanocluster shown in Fig. 1.15(e) reveals the nanocluster has a NaCl structure with a lattice coherency with the *bcc*-Fe matrix. To understand the atomic structure of the nanoclusters, Hirata *et al.* constructed three possible structural models in which a Ti(Y, Fe, Cr)O nanocluster is embedded in the *bcc*-Fe matrix (Fig. 1.15(a)).

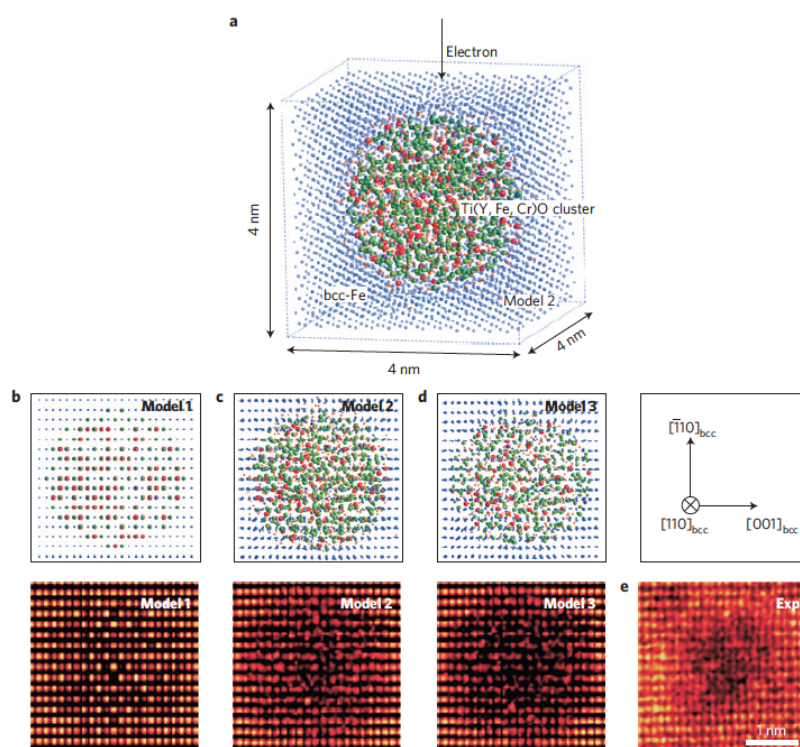


Fig. 1.15 Structure modeling of the nanocluster from $[110]_{bcc}$ direction: (a). 3D external view of a structure model (Model 2) where a 3 nm (Ti, Y, Fe, Cr)O nanocluster is embedded in the *bcc* matrix. The projections of Model 1, Model 2 and Model 3 are depicted, respectively, in (b), (c) and (d), where green, red, blue, purple and orange circles denote Ti, Y, Fe, Cr and O atoms respectively. The corresponding simulated HAADF-STEM images from the three models are shown in the lower panels of (b)-(d). (e). The experimental HAADF-STEM image. Model 2 is the structure model which is most consistent with the experimental data [Hirata, 2011].

The nanocluster in ‘Model 1’ shown in Fig. 1.15(b) is an unrelaxed perfect NaCl structure that is coherent with the *bcc* matrix. The ‘Model 2’ (Fig. 1.15(c)) and ‘Model 3’ (Fig. 1.15(d))

are relaxed defective NaCl structures that are coherent and incoherent with the bcc matrix, respectively. Both ‘Model 2’ and ‘Model 3’ are phenomenologically consistent with the experimental one in contrast variation of the atomic image (Fig. 1.15 (e)). However, the FFT analysis for ‘Model 3’ fails to explain the experimental data, provides compelling evidence that defective NaCl structure with a high lattice coherency with the bcc matrix (‘Model 2’) are the most dependable structure model of the nanoclusters. The defective NaCl structure is capable of accommodating a large number of vacancies, which seems to be the most important reasons for the unusual stability of the clusters at high temperature and in intensive neutron irradiation condition.

4.3. Mechanisms of nucleation of nano-oxide particles

Although field evaporation and reconstruction of the precipitates suffer from artefacts, a core/shell structure was still found for both small nanoclusters and large nano-particles in three ODS alloys: MA957 (Fig. 1.16(a)), ODS Fe-12 wt%Cr (Fig. 1.16(b)) and ODS Eurofer-97 (Fig. 1.16(c)) by APT investigations [Marquis, 2008]. The left column of Fig. 1.16 illustrates the case of the nanoclusters with sizes less than 4 nm, while the right column of Fig. 1.16 illustrates the case for larger nano-particles (> 8 nm). The shell structure is visible all around the core. The compositions profiles corresponding to each nanoclusters and nano-particles reveal that cores are Y and O rich while shell regions are enriched in O, Ti, Cr or V depending on alloy compositions.

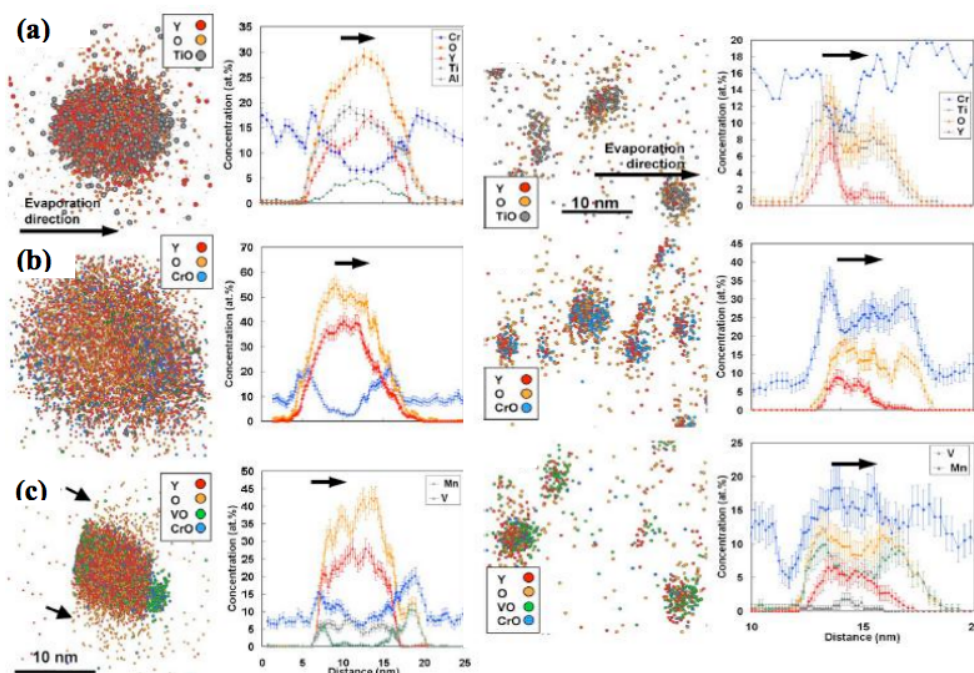


Fig. 1.16 Slices through 3D reconstructions showing the evaporation structures of large oxide particles (left column) and small oxide nanoclusters (right column) in (a) MA957, (b) ODS Fe-12Cr alloy, and (c) ODS Eurofer 97 alloy. All samples were analyzed in laser pulsing mode [Marquis, 2008].

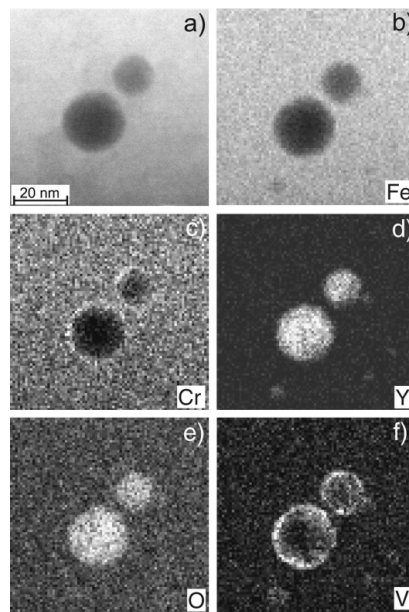


Fig. 1.17 EDX elemental mapping of an area with two ODS particles: (a) HAADF image, (b)–(f) elemental maps obtained using Fe-K α , Cr-K α , Y-L, O-K, and V-K α EDX lines, respectively [Klimenkov, 2009].

The core/shell structure was also identified by TEM. Klimenkov *et al.* [Klimenkov, 2009] observed the nano-particles in ODS Eurofer97 alloy have the core/shell structure. Two particles, 24 and 14 nm in diameter, show a darker contrast in the HAADF image (Fig. 1.17(a)) as well as in Fe and Cr maps (Fig. 1.17(b)-(c)). A brighter contrast is shown in Y and O maps (Fig. 1.17 (d)-(e)). The V-rich shell around both particles is clearly visible in the V map (Fig. 1.17(f)). A slight increase of the Cr concentration around particles can be observed in the Cr map. These measurements reveal the formation of a thin V-Cr-O shell of 0.5-1.5 nm thickness around the core of particles containing Y and O.

Both two experiments confirmed that the minor alloying elements contained in the matrix influence the chemical compositions of nano-particles in different types of ODS steels via forming a minor elements-rich shell. Therefore, Marquis *et al.* [Marquis, 2008] suggested a mechanism to explain the existence of the core/shell structure: the Y₂O₃ oxide, as the most stable of the Cr, V, Ti, Y oxides with the highest free energy of formation, may have a high nucleation barrier. The presence of a shell, however, would decrease the interfacial energy, favoring the nucleation of the oxide particles. Note that a similar mechanism was described for the formation of Cu-Mn-Ni rich precipitates in RPV steels [Liu, 1997]. D. Murali *et al.* [Murali, 2010] did atomistic simulations based on density functional theory (DFT). They found that both Y and Ti atoms show strong affinity towards oxygen in bcc Fe. In fact, binding energies increase when Ti or Y is added to the O-v cluster. In contrast, the negative binding energies of Cr with Y and Ti suggest that they interact repulsively in bcc Fe. The repulsive interaction of Cr with Y and Ti would suggest depletion of Cr in the core of the nanoclusters. In addition, it has been identified that the Cr atoms have a negligible interaction

with vacancy, O-V, Y-V-O and repulsive interaction with the Y-V-O-Ti clusters that suggest that the energetics of cluster formation least favors the presence of Cr atom in the core of the nanoclusters. Therefore, a core/shell structure is expected for the nanoclusters in ODS steels.

Fu *et al.* [Fu, 2007] suggested yet a different mechanism obtained from first-principles studies: oxygen shows an exceptionally high affinity for vacancies. If vacancies preexist, the O-vacancy pair formation energy essentially vanishes. This O-vacancy mechanism enables the unusual high O solubility and the nucleation of O-enriched nanoclusters, which attract solutes with high O affinities (Ti and Y) in order to form Y, Ti-enriched nano-particles in ODS steels. Xu *et al.* [Xu, 2009] confirmed the suggestion of Fu *et al.* by an experimental approach: Positron-lifetime spectroscopy. Xu *et al.* found vacancy clusters containing four to six vacancies coexisted with nanoclusters (2-4 nm in diameter) containing Ti, Y and O exist in a mechanically alloyed ferritic steel. In contrast, no vacancy clusters were detected in similar alloys containing no nanoclusters. They thus indicated that vacancies are a vital component of the nanoclusters in these alloys.

As already mentioned, a great number of vacancies can be created by MA during the first stage of the synthesis of ODS steels. So the mechanism suggested by Fu *et al.* seems to be reasonable, and some authors [Laurent-Brocq, 2010; Laurent-Brocq, 2012; Hirata, 2011] adopted this mechanism to explain the nucleation of small nanoclusters and large nano-particles observed in their study.

5. Ion irradiation-induced defects: formation, diffusion and effects

5.1. Principle of ion irradiation

In this paragraph, we review effects of ion irradiation. As ion implantation is one of irradiation cases, we will take this case as an example to show general effects of irradiation. Ion implantation is a process by which ions of a material are accelerated in an electrical field and impacted into a solid. The interaction between ions and the solid are divided into two different parts:

- (1). the interaction between ions and atoms of solid (nuclear stopping power: $(\frac{dE}{dx})_n$);
- (2). the interaction between ions and electrons of solid (electron stopping power: $(\frac{dE}{dx})_e$).

The first interaction is considered as an elastic collision between ions and atoms of the solid, whereas the second one is considered as an inelastic collision between bound electrons in the solid and the ions moving through it. The inelastic collision may result both in excitations of

bound electrons of the solid, and in excitations of the electron cloud of the ion as well. The total stopping power is therefore the sum of two terms:

$$\frac{dE}{dx} = \left(\frac{dE}{dx}\right)_n + \left(\frac{dE}{dx}\right)_e$$

Fig. 1.18 shows the evolution of nuclear stopping power as a function of incident energy of ions. If the incident energy of ions is low enough, the nuclear stopping power is dominant. This is the case for heavy ions with low energy. If the incident energy of ions is high enough, the electron stopping power becomes the dominant term. And this case is true for light ions with high energy.

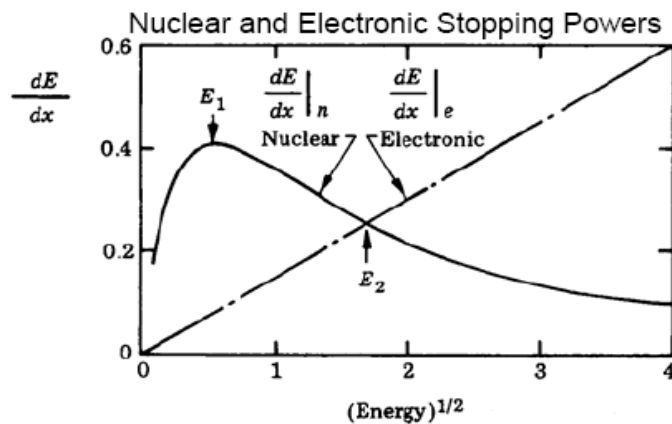


Fig. 1.18 Evolution of nuclear and electron stopping power as a function of incident energy of ions

Coming back to the interaction between ions and the solid, Kinchin *et al.* [Kinchin, 1955] has summarized all possible relation conditions among incident energy of ions E_0 and the threshold energy E_d , which is the minimum energy to displace an atom from its lattice site, leaving behind a vacant site or vacancy.

- If $E_0 < E_d$, the implanted ion can't displace any atoms of the solid. It loses its kinetic energy by the vibration of matrix of the solid. Finally, it is stopped inside matrix and becomes an interstitial.
- If $E_d < E_0 < 2E_d$, the knocked atom leaves its lattice site, leaving behind a vacant site or a vacancy. The knocked atom becomes an interstitial or is recombined with a vacancy created by other atoms.
- If $2E_d < E_0$, the kinetic energy transferred to the atom is sufficient, it travels through the crystal, colliding with its neighbors and displacing them from their sites. In return, they may repeat such events, leading to a collision cascade.
- If $2E_d \ll E_0$, the electron stopping power is dominant, so the loss of energy is achieved by inelastic collision. Therefore, there is no atomic displacement.

For collision cascade, every displaced atom leaves behind a vacancy, and every displaced atom will eventually be wedged into the interstices of the lattice. Frenkel pairs are thus formed since the number of interstitials is equal to the number of vacancies. Both vacancies and interstitials are belonging to irradiation-induced point defects, and they will be reviewed in the next paragraph.

5.2. Properties of irradiation-induced defects

Irradiation-induced defects existing in the crystalline lattice are various. They can be listed by the order of dimension:

- ⇒ Point defects (0D): vacancies and interstitials
- ⇒ Liner defects (1D): dislocation
- ⇒ Planar defects (2D): dislocation loops
- ⇒ Volume defects (3D): voids, bubbles, stacking fault

Point defects (vacancies and interstitials) are essential for both physical and mechanical effects of irradiation in materials. Here, we only describe point defects in details.

5.2.1 Interstitials and interstitial-impurity complexes

An interstitial is an atom that is located in a position of a crystal that is not a regular lattice site. Typically, there are two possible interstitial sites in cubic crystal lattices: octahedral sites and tetrahedral sites. Considering the material studied in our case, a *bcc* FeCr alloy, we only briefly review interstitial in this case.

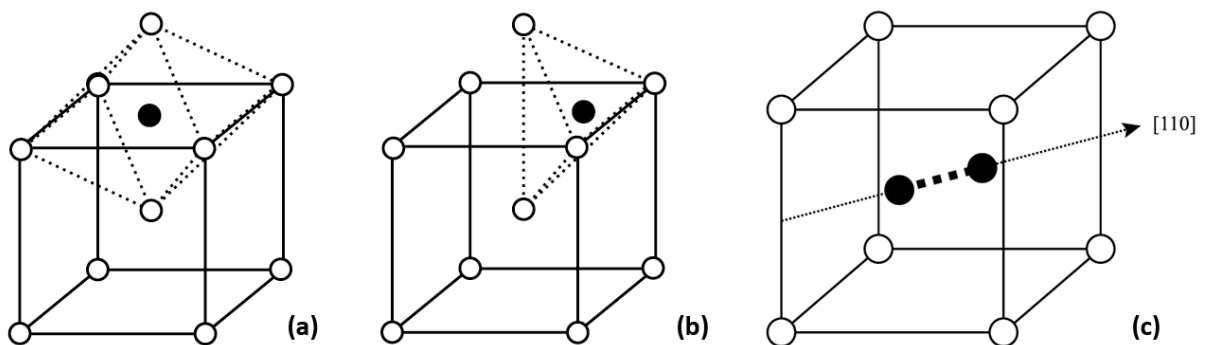


Fig. 1.19 In the *bcc* unit cell: (a) octahedral sites for interstitials; (b) tetrahedral sites for interstitials; (c) dumbbell configuration of self-interstitial atoms (SIAs) [Was, 2007].

The *bcc* lattice is cubic with unit cell of length a (lattice constant) and with atoms located at the corners of the unit cell and the center of the cell. Each corner atom is shared by eight unit cells and the center atom is occupied only by one unit cell, so the total number of atoms per unit cell is two atoms per unit cell.

Octahedral sites are interstitial positions that are surrounded by an octahedron where the lattice atoms make up the six vertices of an octahedron. In the *bcc* lattice, octahedral

interstitial sites are located on the faces and the edge of the unit cell giving $6 \text{ faces} \times \frac{1}{2} \text{ site per face} + 12 \text{ edges} \times \frac{1}{4} \text{ sites per edge} = 6 \text{ sites per unit cell}$ (Fig. 1.19(a)) [Was, 2007].

Tetrahedral sites are interstitial positions in which the atom is located inside a tetrahedron formed by lattice atoms. Tetrahedral interstitial sites in the bcc lattice are located on the faces and in the corners of the faces. There are $6 \text{ faces} \times 4 \text{ locations per face} \times \frac{1}{1} \text{ sites per face} = 12 \text{ tetrahedral sites}$ (Fig. 1.19(b)) [Was, 2007].

In fact, the stable configuration of self-interstitial atoms (SIAs) in metals is the dumbbell configuration where two atoms are associated with a single lattice site (Fig. 1.19(c)). The repulsion among the atom cores induces the atoms arrange themselves in the energy orientation, of which the $\langle 110 \rangle$ direction is the lowest for bcc metals.

Impurity atoms in metals play a crucial role in the trapping for SIAs, and their trapping efficiency depends on the size of atoms (oversized or undersized). Undersized atoms and interstitials constitute stable interstitial-impurity complexes whose configuration is the mixed dumbbell where one of the dumbbell atoms is replaced by the impurity atom. The impurity can jump between the indicated positions of the central octahedron, forming a new mixed dumbbell with the adjacent host atom. The dumbbell interstitial mechanism for the diffusion will be introduced in the next chapter.

5.2.2 Vacancies and solute/impurity-vacancies clusters

The vacancy is the simplest point defect in metal lattices. The single vacancy structure is a missing lattice atom with the nearest neighbors relaxing toward the vacancy. Comparing to SIAs, vacancies have lower formation energies but higher migration energy. Therefore, they are much less mobile than SIAs [Ullmaier, 1980]. Even though multiple vacancies have small binding energies compared to interstitial clusters but are often observed in irradiated metals.

Vacancies can bind to solute and impurity atoms in order to form solute/impurity-vacancies clusters. These solutes or impurities can act as efficient traps for vacancies in the lattice. Amara *et al.* [Amara, 2010] studied the interaction between Al atoms and vacancies (V) in α -iron by the first-principle calculations. His study indicates that the formation of small $V_n Al_m$ complexes ($n, m = 0-4$) is energetically favorable. Their stability is mainly driven by strong Al-V attractions whereas Al-Al interactions are repulsive. Fu *et al.* [Fu, 2007] reported the results of first-principle studies about the interaction between O atoms and vacancies in iron. Oxygen atoms confined as an interstitial, shows an exceptionally high affinity for vacancies. If vacancies preexist, the O-vacancy pair formation energy essentially vanishes. A two-steps O-vacancy mechanism is then given to explain the formation of Y-Ti-O enriched nanoclusters

in the ODS steels: firstly, the nucleation of O-enriched nanoclusters; secondly, O-enriched clusters attract other solutes with high O affinities (Ti and Y). A similar result was also reported by Barouh *et al.* [Barouh, 2014], which shows the formation of small V_nO_m complexes is energetically favorable until to the 8th nm configuration. In addition, their study shows vacancies can weakly attract Cr atoms in iron. However, another study [Chen, 2010] reported that vacancies are transparent to Cr atoms.

5.3. Diffusion of point defects

Macroscopic description of diffusion is governed by two fundamental laws developed by Fick in 1880. The first law is about the relationship between the flux and the concentration gradient. For diffusion in one dimension, this law can be simplified to:

$$J = -D\nabla C = -D\frac{\partial C}{\partial x}$$

where J is the flux, D is the diffusion coefficient and C is the composition concentration. The minus sign indicates that diffusion takes place toward the direction of decreasing concentration of the diffusion specie.

The second law gives a relation between the concentration gradient and the rate of change of concentration caused by diffusion. In one dimension and if D is not a function of the concentration, the equation can be simplified to:

$$\frac{\partial C}{\partial t} = -\nabla \cdot J = -D\frac{\partial^2 C}{\partial x^2}$$

Fick's laws provide a description of diffusion on the macroscopic scale, while sometimes we prefer to obtain a description of diffusion on the microscopic level. The detailed demonstration of diffusion equation on the microscopic level can be found elsewhere. In general, the diffusion coefficient has a uniform expression:

$$D = D_0 \exp\left(\frac{-Q}{kT}\right)$$

where D_0 is the temperature independent term, Q is the activation energy, k is the Boltzmann constant and T is the temperature.

The activation energy is not uniform and depends on mechanisms of diffusion. There are several mechanisms of lattice diffusion, some requiring the presence of defects, others not. The classification and description of all types of mechanisms can be found here [Mrowec, 1980]. In next part, we only review the mechanisms requiring the presence of defects.

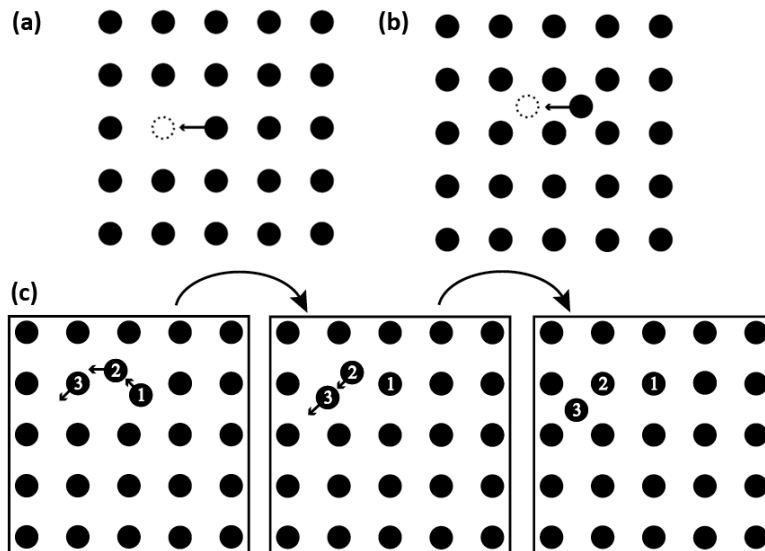


Fig. 1.20 Mechanisms of diffusion in one dimension: (a) Vacancy mechanism; (b) Interstitial mechanism; (c) Dumbbell interstitial mechanism [Was, 2007].

Vacancy mechanism: Diffusion occurs by the jump of an atom from its lattice site to a vacant site (Fig. 1.20(a)). The movement of the atom requires the presence of a neighboring vacancy. The vacancy mechanism is regarded as either a movement of the atom or the opposite movement of the vacancy. For pure vacancy diffusion, the activation energy $Q_V = E_m^V$, where E_m^V is the energy for vacancy migration. Therefore, the pure vacancy diffusion coefficient can be written as:

$$D = D_0 \exp\left(\frac{-E_m^V}{kT}\right)$$

Before continuing, it should be pointed out that the pure vacancy diffusion is not equal to the atom diffusion via a vacancy mechanism (also called as vacancy self-diffusion). In the latter case, the energy that a vacancy can be created should be added into the activation energy, so $Q_V = E_f^V + E_m^V$, where E_f^V is the vacancy formation energy and E_m^V is the energy for vacancy migration. Therefore, the vacancy self-diffusion coefficient is given as:

$$D = D_0 \exp\left(\frac{-(E_m^V + E_f^V)}{kT}\right)$$

Interstitial mechanism: This mechanism involves the movement of an atom from one interstitial to another (Fig. 1.20(b)). Pushing an atom through the barrier atoms needs considerable energy, so this mechanism occurs more possibly when the diffused atom is smaller than the host lattice atoms. For interstitial diffusion, the activation energy $Q_V = E_m^i$, where E_m^i is the energy for interstitials migration. Therefore, the pure interstitial diffusion coefficient can be written as:

$$D = D_0 \exp\left(\frac{-E_m^i}{kT}\right)$$

For the same reason, the interstitial self-diffusion (atom diffusion via an interstitial mechanism) coefficient is given as:

$$D = D_0 \exp\left(\frac{-(E_m^i + E_f^i)}{kT}\right)$$

where E_f^i is the interstitial formation energy and E_m^i is the energy for interstitials migration.

Dumbbell interstitial mechanism: The dumbbell is consisted of an interstitial and a lattice atom. The mechanism involves the symmetrical placement of the interstitial and the lattice atom. In addition, the interstitial atom and the lattice atom share the same lattice site (Fig. 1.20(c)). The dumbbell is a very stable configuration for the interstitial, and it can move along the preferred directions.

5.4. Radiation-enhanced diffusion (RED)

In the absence of irradiation, the diffusion in a pure metal is driven by thermally activated motion of equilibrium concentration of vacancies. The thermal diffusion coefficient D_{th} can be written as

$$D_{th} = C_v^0 D_v$$

where C_v^0 is equilibrium concentration of vacancies and D_v is their diffusion coefficient.

Because the concentration of irradiation-induced point defects (interstitials and vacancies) are much greater than those produced thermally, the diffusion under irradiation is accelerated comparing to thermal diffusion [Picraux, 1978]. The diffusion coefficient under irradiation in a pure metal is thus given by:

$$D_{rad} = D_v C_v + D_i C_i$$

where D_v and D_i are the vacancy and interstitial diffusion coefficient, respectively. C_v and C_i are the vacancy and interstitial concentration, respectively. If $C_v \gg C_v^0$ with high enough mobility, then RED will be the dominant process. So $D_{rad} \gg D_{th}$ is true, which indicates the diffusion is enhanced by irradiation.

Irradiation creates excess point defects in materials, which can be eliminated by mutual recombination or by reaction with a defect sink, such as surfaces, grain boundaries, dislocations, dislocation loops or precipitates. So the concentration of point defects at any point and time of the solid is a balance between the production rate and the loss rate of point

defects, and is described by non-equilibrium thermodynamics diffusion equations:

$$\frac{dC_v}{dt} = K_0 - RC_iC_v - K_{vs}C_vC_s \quad (1)$$

$$\frac{dC_i}{dt} = K_0 - RC_iC_v - K_{is}C_iC_s \quad (2)$$

where K_0 is the point defect production rate proportional to the radiation flux, R is the vacancy-interstitial recombination rate, C_s is the sink concentration, and K_{vs} and K_{is} are vacancy-sink and interstitial-sink reaction rate coefficients for all common sinks, respectively.

Analytical solutions to these two equations have been developed and described for four different regimes [Was, 2007]. Briefly, the defect concentrations initially increase linearly with $C_v = C_i = K_0t$. Depending on the temperature and sink density, the evolution of defect concentrations will undergo different regimes, such as mutual recombination, interstitial annihilation contributed by sinks, vacancy annihilation also contributed by sinks. Finally, the defect concentrations become time independent constants at the steady state. The time independent property of solutions to Eq. (1) and (2) at the steady state provides an approach to simplify these two equations to:

$$0 = K_0 - RC_iC_v - K'_{vs}D_vC_vC_s \quad (3)$$

$$0 = K_0 - RC_iC_v - K'_{is}D_iC_iC_s \quad (4)$$

where $K_{vs} \propto D_v$ and $K_{is} \propto D_i$, and the K terms can be written as $K = K'D$.

The physic meaning of Eq. (3) and (4) is that vacancies and interstitials contribute to atom mobility to the same extent, so Eq. (3) and (4) at steady state is symmetric with regard to D_vC_v and D_iC_i . If $K'_{vs} \approx K'_{is}$, then $D_vC_v = D_iC_i$, which is an approximation when vacancies and interstitials contribute equally to atom mobility. Moreover, Fortuna *et al.* [Fortuna, 2011] explored one-dimensional steady-state diffusion equation, and gave another approximation to estimate the value of D_XC_X ($X = i$ or v) under ion implantation case:

$$D_vC_v = D_iC_i \approx \gamma\Omega L\phi v_F$$

where γ is a numerical factor of the order of unity, Ω is the matrix atomic volume, L is the thickness of the implanted material, ϕ is the flux of implanted ions and v_F is the average number of Frenkel pairs produced by an incident ion.

5.5. Radiation-induced segregation (RIS) and radiation-induced precipitation (RIP)

Radiation-enhanced diffusion (RED) clarifies how irradiation can increase the atomic mobility of atoms in the material. Here, radiation-induced segregation will show how the

coupling between the point defect and the solute or impurity atoms fluxes toward point defect sinks can lead to enrichment or depletion of solute atoms at these sinks.

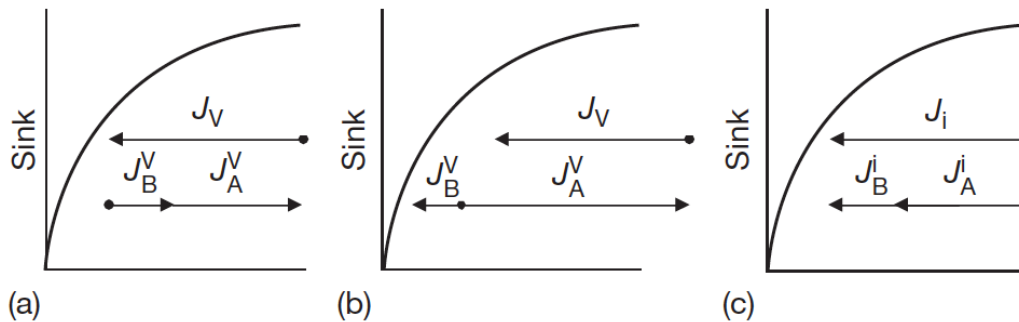


Fig. 1.21 Radiation-induced segregation mechanisms due to coupling between point defect and solute fluxes in a binary A-B alloy: (a) An enrichment of B occurs if $d_{BV} < d_{AV}$ and a depletion if $d_{BV} > d_{AV}$; (b) When the vacancies drag the solute, an enrichment of B occurs; (c) An enrichment of B occurs when $d_{Bi} > d_{Ai}$ [Nastar, 2012].

Okamoto *et al.* [Okamoto, 1973] observed strain contrast around voids in an austenitic stainless steel during irradiation in a high voltage electron microscope. They attributed this contrast to the radiation-induced segregation (RIS). This is the first time the evidence of RIS was observed experimentally. Typically, RIS mechanisms due to coupling between point defect and solute fluxes in a binary A-B alloy are classified in three cases:

In Fig. 1.21(a), both A and B fluxes are in the opposite direction to the vacancy flux, so if $d_{BV} < d_{AV}$, an enrichment of B is expected; in the opposite case ($d_{BV} > d_{AV}$), a depletion of B will occur. This mechanism is called as inverse Kirkendall (IK) effect, which was coined by Marwick *et al.* [Marwick, 1978]. The IK effect is often more useful to explain RIS in concentrated alloys.

In Fig. 1.21(b), A and B fluxes are not necessarily in the same direction. If B solute atoms have a high binding energy with vacancies and if formed vacancy-solute clusters can drag B atoms toward to point defect sinks, the vacancy and solute fluxes can be in the same direction. In such a case, an enrichment of B will occur regardless the values of d_{AV} and d_{BV} . In this case, RIS is owed to drag effects or migration of vacancy-solute clusters. The mechanism was proposed by Aust *et al.* [Aust, 1968].

In Fig. 1.21(c), both A and B fluxes are in exactly the same direction to the interstitial flux. If the A and B solute atoms are strongly bound to the interstitials and if $d_{Bi} > d_{Ai}$, an enrichment of B is expected due to the migration of interstitial-solute clusters. The mechanism was proposed by Rehn *et al.* [Rehn, 1979].

More generally, these three mechanisms of RIS are not mutually exclusive. Each mechanism can either occur individually or combine with each other. Enrichment or depletion of elements

due to RIS is difficult to predict because RIS effects depend on various parameters, such as segregating elements, the sink structure, radiation particles dose and temperature. The modeling of mechanisms relevant to RIS can be found in Wharry *et al.* [Wharry, 2014].

When the local solute concentration in the vicinity of a point defect sink reaches the solubility limit, radiation-induced precipitation (RIP) will occur instead of RIS. Both RIS and RIP can be thought as a consequence of RED.

As we mentioned before, the evolution of concentration profiles of point defects can be described by non-equilibrium thermodynamics diffusion equations. In the case of the problem of RIS, the concentration profile of chemical elements α need to be considered. Therefore, diffusion equations are given by:

$$\frac{\partial C_V}{\partial t} = -\text{div}J_\alpha + K_0 - RC_iC_V - K_{VS}C_VC_S \quad (5)$$

$$\frac{\partial C_i}{\partial t} = -\text{div}J_\alpha + K_0 - RC_iC_V - K_{iS}C_iC_S \quad (6)$$

$$\frac{\partial C_\alpha}{\partial t} = -\text{div}J_\alpha \quad (7)$$

where C_α is the concentration of element α , and J_α is the flux of element α . The solution of these equations requires the knowledge of how the flux J_α is related to the concentrations. This problem relies on the theory of thermodynamics of irreversible processes. The final description of J_α can be written in terms of the phenomenological coefficients of diffusion and the driving forces.

5.6. Precipitation induced by irradiation

Irradiation can induce the formation of precipitates in an alloy. The nucleation and growth of precipitates can be expressed as an effect of point defects (vacancies and interstitials) due to high levels of solute supersaturation under irradiation. The supersaturation then provides the driving force for the reaction. The nucleation of precipitates is divided into incoherent and coherent conditions. The distinction between these two cases lies in the behavior of point defects at the precipitate surface. Incoherent precipitates behave like voids in which defects can be absorbed and emitted. However, the interface of coherent precipitates acts as a defect trap so that the defect retains itself [Was, 2007].

In order to understand the incoherent nucleation of precipitates, Maydet *et al.* [Maydet, 1977] and Russel *et al.* [Russel, 1979] developed a model based on the number of solutes and the number of excess vacancies. In their opinion, precipitates with greater atomic volume than the matrix must have excess vacancies to relieve the strain energy. On the contrary, undersized precipitates should not contain excess vacancies since these vacancies destabilize the

undersized precipitate phase. Finally, Russel *et al.* [Russel, 1979] showed the effect of irradiation on the stability of incoherent precipitates by a schematic phase diagram (Fig. 1.22)

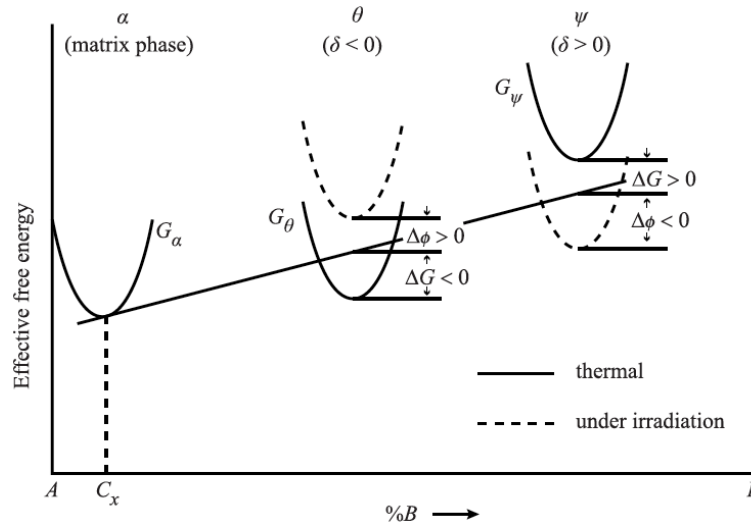


Fig. 1.22 Schematic phase diagram showing the effect of irradiation on the stability of incoherent precipitates in the case where the precipitates is thermally stable (θ) and thermally unstable (metastable ψ) [Russel, 1979].

In this phase diagram, the θ phase is thermally stable and the ψ phase is not thermally stable (metastable) by the sign of δ , where $\delta = \frac{(\Omega - \Omega_m)}{\Omega_m}$, Ω and Ω_m are the atomic volume of the precipitate and the matrix, respectively. The stable θ phase has a lower free energy than the metastable ψ phase under thermal condition. Therefore, the precipitation of the θ phase is more favorable than the ψ phase. However, the order of stability is reversed by irradiation so that the θ phase would dissolve and the ψ phase would precipitate under irradiation condition. The precipitation of the metastable phase is an evidence that irradiation would induce precipitation in an undersaturated solid solution.

Chapter 2 Experimental techniques

1. Transmission electron microscopy.....	44
1.1. Conventional methods: SAED, BF, DF and WBDF	44
1.1.1 Selection Area Electron Diffraction (SAED).....	44
1.1.2 Bright Field (BF) and Dark Field (DF) imaging.....	45
1.1.3 Two-beam condition and Weak Beam Dark Field (WBDF) imaging	45
1.2. Analytical methods for chemical compositions: EDX, EELS and EFTEM.....	46
1.2.1 Energy Dispersive X-ray spectroscopy (EDX).....	46
1.2.2 Electron Energy Loss Spectrometry	48
1.2.3 Comparison between EDX and EELS	50
1.2.4 Energy Filtered TEM (EFTEM):	51
1.3. Analytical methods for crystallographic structure: HRTEM.....	53
1.4. TEM specimen preparation.....	56
1.5. Thermal annealing performed in TEM.....	57
2. Introduction of the as-received material: high-purity Fe10Cr alloy	58
3. Ion implantation	61
3.1. Instrument.....	61
3.2. Two-stage ion implantation at RT: Al⁺ ions then O⁺ ions.....	62
4. Atom probe tomography (APT).....	64
4.1. APT specimen preparation.....	65
4.2. Principle of APT	65
4.3. APT measurements	67
4.4. APT data treatment.....	68
4.5. Common artifacts: Trajectory aberrations & Local magnification effects	70

1. Transmission electron microscopy

The characterizations of nano-particles in both as-implanted and annealed specimens were performed by Transmission Electron Microscopy (TEM). Three TEM microscopes used are:

- **FEI Tecnai G² 20 twin** LaB₆ filament operating at 200 kV, equipped with EDX spectrometer and Gatan Image Filter (GIF) at CSNSM/JANNuS Orsay, France [CSNSM/TEM, Website]
- **JEOL 2010F** field emission gun (FEG) operating at 200 kV, equipped with EDX spectrometer and EEL spectrometry at CEA-SRMA, Saclay, France.
- **JEOL 2100** LaB₆ filament operating at 200 kV, equipped with EDX spectrometer and Gatan Image Filter (GIF) at CEA-SRMA, Saclay, France.

In the microscope *FEI Tecnai G² 20 twin*, both conventional and analytical methods (except HRTEM) were applied to the characterization. Analytical methods (except HRTEM) were also applied in the microscope *JEOL 2100*. High-resolution TEM (HRTEM) imaging was undertaken by the microscope *JEOL 2010F*.

1.1. Conventional methods: SAED, BF, DF and WBDF

1.1.1 Selection Area Electron Diffraction (SAED)

When incident beam of electrons traverses TEM thin foils, the beam becomes either transmitted (direct) or diffracted (indirect). The spots corresponding to both transmitted and diffracted beams constitute diffraction pattern. To view the diffraction pattern from a specimen, the imaging-system lenses of the microscope are adjusted such that the back focal plane of the objective lens acts as the object plane for the intermediate lens. This causes the diffraction pattern to be projected onto the viewing screen. Selected area electron diffraction (SAED) patterns can be obtained by inserting a selected area aperture. The diffraction pattern is studied by using the Bragg equation:

$$d_{hkl} \times D = \lambda \times L$$

where d_{hkl} is the interplanar distance of the (h, k, l) plane, D is distance between the transmitted spot and the diffracted spot (g_{hkl}), λ is the wavelength of electron beam and L is the camera length. $\lambda \times L$ is the camera length that depends on the configuration of TEM microscope. And D can be measured directly on the diffraction pattern. Therefore, the value of d_{hkl} can be obtained for any (h, k, l) plane.

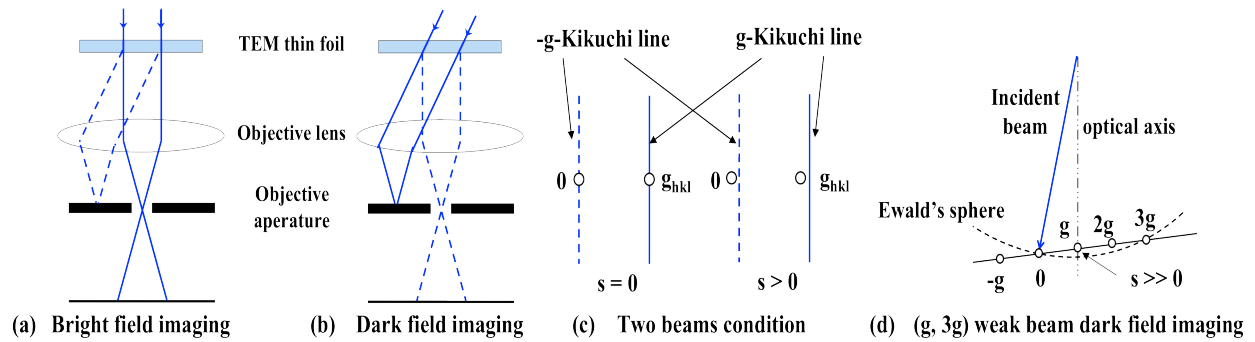


Fig. 2.1 Schemes of conventional TEM methods: (a) Bright field imaging; (b) Dark field imaging; (c) Two-beam condition: exact Bragg condition (left) and excitation error slightly positive condition (right); (d) (g, 3g) weak beam dark field imaging.

1.1.2 Bright Field (BF) and Dark Field (DF) imaging

Bright field (BF) TEM images are formed, if we use an adequate objective aperture to select only the transmitted beam of electrons (Fig. 2.1(a)). In this case, the BF image results from a weakening of the direct beam by its interaction with the specimen. On the contrary, the direct beam is blocked by the aperture while only one diffracted beam is allowed to pass the objective aperture. In order to avoid a deterioration of image by aberrations (particularly chromatic), we keep the objective aperture centered on the optical axis and tilt the incident beam so that the scattering angle between the incident beam and the diffracted beam is not changed (Fig. 2.1(b)). Since diffracted beams have strongly interacted with the specimen, very useful information is present in dark field (DF) images such as defects (dislocation, dislocation loops) or nano-particles.

The size of nano-particles is defined by several criteria: the morphology of nano-particles, the histogram of the size distribution, the equivalent diameter d_{eq} and the density ρ (number of particles in the unit volume). The equivalent diameter d_{eq} is given as:

$$d_{eq} = 2 \times \sqrt{\frac{S}{\pi}}$$

where S is the surface of nano-particles measured in this study by the softwares *Photoshop* and *Image J*.

1.1.3 Two-beam condition and Weak Beam Dark Field (WBDF) imaging

For good image contrast, the specimen is normally tilted to get rid of almost all other diffraction beams with the exception of the transmitted beam and the chosen diffracted beam. Therefore, only the chosen diffraction beam is excited. This is referred to as a two-beam condition (exact Bragg condition without excitation error ($s=0$)). If the region is thick, Kikuchi lines are normally visible as the diffraction pattern at the same time. In this case, the

dark Kikuchi line intersects the transmitted spot and the corresponding bright Kikuchi line intersects the diffracted spot g_{hkl} (left case in Fig. 2.1(c)). In the real manipulation, we will tilt the specimen to approach the two-beam condition but having a slightly positive excitation error (right case in Fig. 2.1(c)). Two-beam condition is an efficient way to enhance the image contrast and is an essential step to achieve the weak beam dark field (WBDF) imaging.

With increasing the value of excitation error, defects observed on the DF image are much sharper, whereas the contrast of the DF image is weaker. The weak beam dark field (WBDF) images are formed if we use a diffracted beam with large excitation error ($s \gg 0$). The whole manipulation for the WBDF imaging is: firstly, we tilt the specimen to approach two-beam condition. Then, the next step is tilting to the so-called (\mathbf{g} , $3\mathbf{g}$) condition (Fig. 2.1(d)). The (\mathbf{g} , $3\mathbf{g}$) condition means, the \mathbf{g} reflection we want to use for the WBDF image is in the optical axis, whereas the Bragg condition for the $3\mathbf{g}$ reflection is exactly satisfied. Then we get a relatively large excitation error ($s \gg 0$) for the \mathbf{g} reflection. With the help of WBDF method, the defect free specimen area appears dark because of the weak diffraction intensity. Moreover, dislocations and dislocation loops can be visualized as sharp bright line and bright loops, respectively.

1.2. Analytical methods for chemical compositions: EDX, EELS and EFTEM

1.2.1 Energy Dispersive X-ray spectroscopy (EDX)

Energy Dispersive X-ray spectroscopy (EDX) is a qualitative and quantitative X-ray microanalytical technique that can provide information on the chemical composition of a specimen. When the beam of electrons penetrate the specimen and interact with the atoms of the specimen in TEM microscope, two types of X-rays result from these interactions: Bremsstrahlung X-rays, which are also referred to as background X-rays, and Characteristic X-rays.

Bremsstrahlung X-rays: Bremsstrahlung X-rays are produced by slowing down of the incident beam by the electric field surrounding the nuclei of the atoms in the specimen. Electrons of the incident beam lose energy and change direction due to inelastic scattering in the specimen. Some of the lost energy is converted to Bremsstrahlung X-rays.

Characteristic X-rays: Characteristic X-rays result from electron transition between inner orbits, which are normally full (Fig. 2.2(a)). The production of Characteristic X-rays is two-stages process: Firstly, an electron is removed from one of the inner shells of the atom by inelastic scattering with an electron of the incident beam. Therefore, the atom losing an

electron is ionized and in an unstable state. Then, the atom regains stability when an electron from an outer shell fills the inner shell vacancy and an X-ray photon is emitted. The x-rays emitted are characteristic in energy, which is equal to the difference between the ionization energies of the electrons involved in the transition. As ionization energies for each shell of each element are specific, so each element has Characteristic X-ray lines that allow a specimen's elemental composition to be identified by a nondestructive technique, while the intensities of the Characteristic X-ray peaks allow the concentration of the elements to be quantified. The spectrum displayed in the EDX systems (Fig. 2.2(b)) comprises Characteristic X-ray peaks superimposed on the continuum background (Bremsstrahlung X-rays).

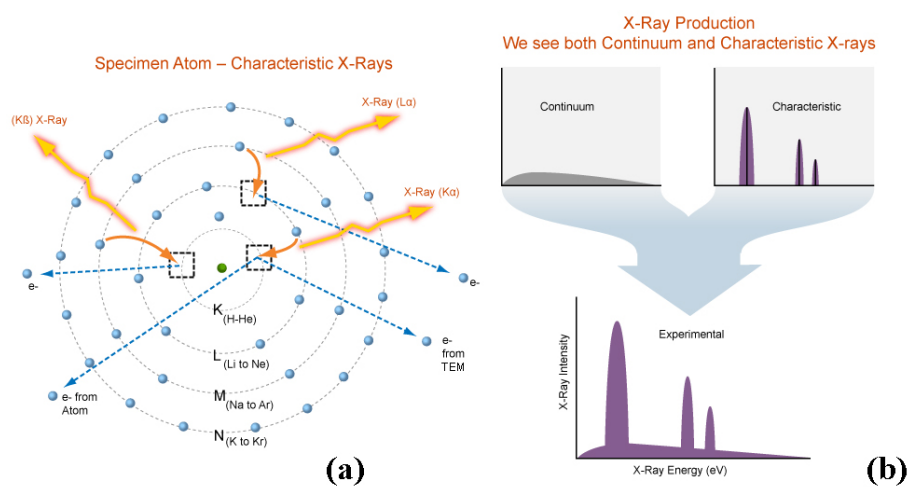


Fig. 2.2(a) Specimen atom- Characteristic X-rays: the electron transition involved in generating the K α , K β and L α X-ray photons; (b) The X-ray spectrum displayed by the EDX system comprises Characteristic X-ray peaks superimposed on the continuum (Bremsstrahlung X-rays) [siteweb: ammr.org].

The operating principle: The operating principle is the same for either Si(Li) or Si drift (SDD) EDX detector : the energy of incoming X-ray is dissipated by the creation of a series of electron-hole pairs in the semiconductor crystal inside the EDX detector. The number of pairs created is directly proportional to the energy of X-rays. A high bias voltage applied across the crystal causes electron-hole pairs to move to electrodes on opposite sides of the crystal, which forms a charge pulse. The charge pulse is then amplified by a sensitive preamplifier. Final output pulses proportional in height to the incoming X-ray energy.

Qualitative and quantitative analysis: In performing qualitative analysis, the spectrum can be acquired in a short time (10-100s). The information of the specific energy of the Characteristic X-ray peaks for each element is available as detector database. This information allows us to identify elements belonging to the specimen. It is noted that the separation of the members of X-ray lines below 3 keV becomes so small that the peaks are

not easily resolved. Owing to the relatively poor resolution in this energy range, the O K α peak usually overlaps the Cr L $_{\alpha,\beta}$ peak. It is thus hard to identify the presence of oxygen in our case by EDX qualitative analysis. Quantitative analysis can be performed in different approaches. One popular approach is to consider background in the spectrum as an undesirable signal. The effect of background is removed by mathematical filtering during the process of quantification. When background is removed from the spectrum, the intensities of remaining Characteristic X-ray peaks is compared in order to obtain the quantification of each element.

1.2.2 Electron Energy Loss Spectrometry

Electron Energy Loss Spectrometry (EELS) is the analysis of the energy distribution of the electrons that have passed through a thin specimen and interacted with it inelastically. It is a powerful tool capable of providing both compositional and chemical information of the specimen.

Egerton [Egerton, 2009] described TEM-EELS as instrumentation based on the magnetic prism, in which a uniform magnetic field is generated by an electromagnet with shaped polepieces (Fig. 2.3(a)).

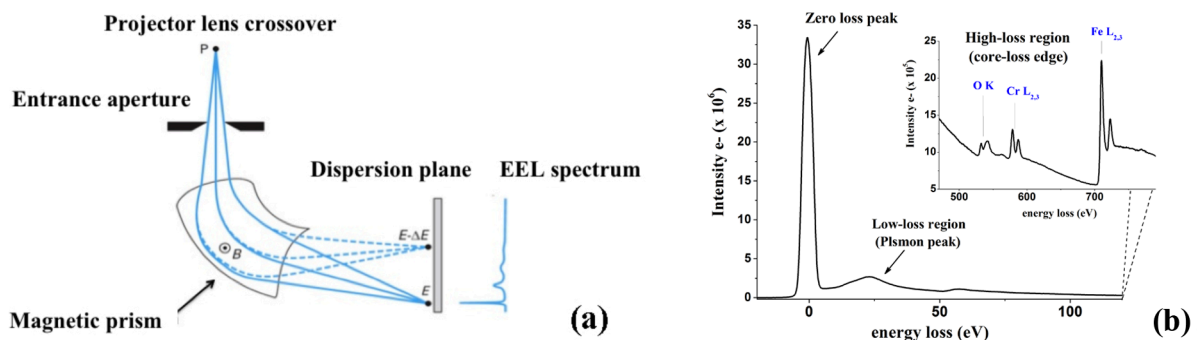


Fig. 2.3 EEL spectrometer and EEL spectrum: (a) Dispersive and focusing properties of a magnetic prism in a plane perpendicular to the magnetic field. Solid lines represent zero-loss electrons (E), and dashed lines represent those that have lost energy (ΔE) during transmission through the specimen [Karlik]; (b) A typical EEL spectrum consist of zero-loss peak, low-loss region and high-loss region.

Within this field, electron follow circular paths and are deflected through an angle of typically 90° due to Lorentz force. The description of Lorentz force is given as:

$$F = evB = \frac{mv^2}{R}$$

where e , v and m are the electron charge, speed and relativistic mass, giving a bend radius that depends on speed and therefore on electron energy:

$$R = \left(\frac{m}{e} \right) Bv$$

If the entrance beam originates from a point object, electrons of a given energy are returned to a signal image point. Solid lines shown in Fig. 2.3(a) represent the trajectory of zero-loss electrons (with an energy E). And dashed lines represent those that have lost energy (ΔE) during transmission through the specimen. The existence of different electron energies results in a focused spectrum displayed in the dispersion plane. This spectrum is referred to as electron energy loss (EEL) spectrum, which can be divided into three parts that depend on various scattering processes that occur within the specimen (Fig. 2.3(b)):

Zero-loss peak at 0 eV: The peak at 0 eV, known as the zero-loss peak, contains electrons that still have the original beam energy. These electrons only interacted elastically or not at all with the atomic nucleus of the specimen. The intensity of the zero-loss peak is so high that dominates the EEL spectrum if the specimen is reasonably thin thanks to the specimen preparation. The advantage of the zero-loss peak can be used to assess the local thickness of the specimen. The most common procedure is the *log-ratio* method, based on the measurement of the integrated intensity I_0 of the zero-loss peak relative to the integral I_t of the whole spectrum [Egerton, 2009]. The equation of *log-ratio* method is given as:

$$\frac{t}{\lambda} = \ln\left(\frac{I_t}{I_0}\right)$$

where t is the local thickness and λ is the electron mean free path for the low energy loss. The *log-ratio* thickness $\frac{t}{\lambda}$ can be converted to the absolute thickness if the exact value of λ is known.

Low-loss region (< 100 eV): The electrons corresponding to this region interact inelastically with the atoms of the specimen under the form of Plasmon excitation. This phenomenon is a result of weakly bound valence electrons of the material in the specimen collectively interacting with the electron beam [Egerton, 1996]. Since the Plasmon generation is the most frequent inelastic interaction of electron with the specimen, the intensity in this region is relatively high but still quite lower than the zero-loss peak. Most of elements have their characteristic edges in the low-loss region, however, the element such as oxygen do not have the peak in this region.

High-loss region (> 100 eV): During the inelastic scattering process, a specific minimum energy, also called as ionization threshold, must be transferred from the electrons of the incident beam to the inner-shell electron, which leads to ionization. These energy-loss electrons appear as an edge in the high-loss region of the EEL spectrum and are referred to as

the ionization edge (also called as core-loss edge) of the element in the specimen [Brydson, 2001]. Thus, EELS is complementary to EDX, and it can be utilized for qualitative and quantitative element analysis as well. In particular, the availability of detecting light elements is the main advantage of EELS.

The amount of inelastically scattered electrons drastically decreases with increasing energy loss, thus small peaks are superimposed on a strongly decreasing background in the high-loss region. Therefore, the background to a particular core-loss edge needs to be extrapolated and subtracted before EELS quantification. After subtraction, the remaining intensity of core-loss edge provides a quantitative estimate of the concentration of the corresponding element. The elemental-ratio between two elements A and B is given as:

$$\frac{N_A}{N_B} = \frac{I_A(\alpha, \Delta E) \times \sigma_B(\alpha, \Delta E)}{I_B(\alpha, \Delta E) \times \sigma_A(\alpha, \Delta E)}$$

where N_i is the atomic concentration of the element i , $I_i(\alpha, \Delta E)$ is the integrated intensity of core-loss edge of the element i after subtracting the extrapolated background over an energy range ΔE and $\sigma_i(\alpha, \Delta E)$ is the partial cross section, calculated for core-loss scattering up to an angle α and energy range ΔE .

For the EEL spectra in the range of [400 eV–1000 eV], the intensity has been collected inside an energy range of [507 eV–557 eV] for O, [573 eV–594 eV] for Cr and [705 eV–740 eV] for Fe with 0.3 eV/Channel. The intensity of Al has been collected inside energy ranges of [70 eV–85 eV] and [1540 eV–1575 eV]. The data has been collected inside a convergence semi-angle α (equal to 4.85 mrad) and a collection semi-angle β (equal to 11.81 mrad). All the ionization cross section have been calculated using a Hartree-Slater model.

1.2.3 Comparison between EDX and EELS

When the electron beam is incident on the specimen, the X-ray photons carrying the elemental information propagate along all directions in space. In practice, only a fraction of these X-ray photons are collected by the X-ray detector because of the difficulties in inserting a large detector in an electron beam column without affecting other capabilities of the TEM. The EEL spectrometer does not have this problem because it is introduced in the path of the electron beam that has gone through the specimen or it is attached to the bottom of the TEM column. A significantly high percentage of electrons carrying elemental information from the area of interest can be directed into the spectrometer. As a result, EELS offers better signal collection efficiency to detect elements from a very limited volume of material at the area of interest. The X-ray energy resolution achieved by standard X-ray detectors is approximately 2

orders of magnitude worse than the energy resolution of an EEL spectrometer [Subramanian, 2011].

1.2.4 Energy Filtered TEM (EFTEM):

EELS method allows to form EEL spectra in the TEM. Alternatively, it is possible to insert a narrow slit at the spectrum plane, which can remove all electrons except those within a small chosen energy window and reform an Energy Filtered TEM (EFTEM) image.

The benefit of EFTEM method comes from elemental mapping, using the energy loss electrons contributing to the characteristic edges of elements of interest in either the low-loss region or the high-loss region. Elemental map provides the information of elemental chemical composition, which is a very useful method for the characterization of nano-particles.

As we mentioned in the description of high-loss region, the ionization edges (or core loss edges) are usually several orders of magnitude weaker than zero-loss or Plasmon peaks. For this reason, the background signal under the ionization edge of elements of interest in the EEL spectrum must be subtracted in order to achieve elemental mapping. The background will dominate the EEL spectrum and limit any meaningful extraction of element maps if the investigated region of the specimen is too thick. Therefore, it is very important to estimate the thickness of the region. The thickness map, which contains the information of *log-ratio* thickness $\frac{t}{\lambda}$ of the region, is a useful way to estimate the feasibility of EFTEM elemental mapping. The measurement of thickness is also based on the *log-ratio* method already shown in the description of the zero-loss peak. In general, $\frac{t}{\lambda} < 0.4$ is the threshold for elemental mapping.

In thin specimens, elemental mapping can be obtained by either the *jump-ratio* or *three-window* methods [Brydson, 2001]. In the *jump-ratio* method, two images are recorded by selecting an energy window before and after characteristic edge of the element of interest. Dividing core loss intensity by that of the preceding background gives the ratio of these two images showing the elemental distribution in only a qualitative way but with a better signal/noise ratio than *three-window* method [Hofer, 1995; Crozier, 1995]. Furthermore, *jump-ratio* images are particularly susceptible to artifacts as a result of their sensitivity to changes in the preceding background arising from thickness change of the specimen or from preceding core loss edges [Ahn, 2006].

In the *three-window* method (see Fig. 2.4), background is recorded in two pre-edge images by selecting two energy windows (pre-edge 1 and 2) simultaneously before the core loss edge of the element of interest. The core loss signal plus background is then recorded in a post-edge image by selecting an energy window (post-edge) after the core loss edge. Background after the core loss edge is extrapolated according to two pre-edge images. Finally, the elemental map is obtained by subtracting the extrapolated background from the post-edge image. The background subtraction algorithm should account for specimen drift that may occur during the collection process because the pre- and post- edge images are acquired sequentially [Subramanian, 2011]. This approach offers better background subtraction but may fail when the images are noisy.

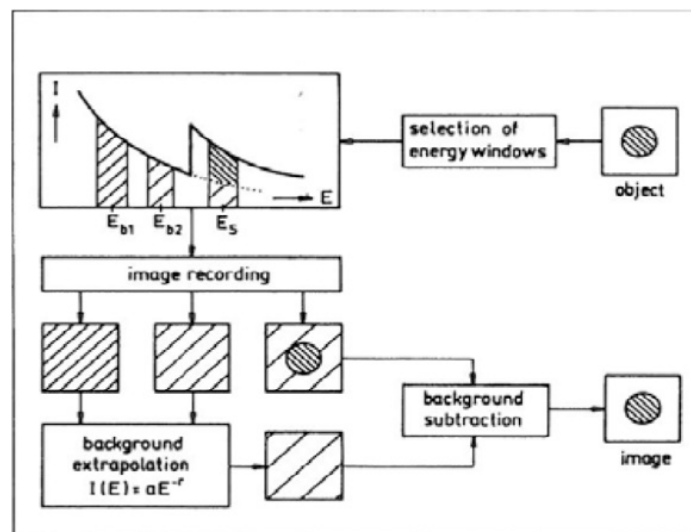


Fig. 2.4 Scheme of elemental maps by employing the *three-window* method [Ribis, 2010].

In our study, the energy-filtered images were recorded using a binning of 2×2 thus resulting in 512×512 pixels. Elemental maps were acquired by using both *jump-ratio* and *three-window* methods. Elemental maps obtained by the *jump-ratio* method were compared with those obtained by the *three-window* method before being considered as real elemental maps due to the presence of artifacts.

Energy windows of elements of interest for the jump-ratio method: For iron, the relevant peak in the low-loss region is 54 eV (Fe-M_{2,3}). Correspondingly, the window for the pre-edge acquisition started at 44 eV, and the window for the post-edge acquisition started at 60 eV. The width of each window was 8 eV. For chromium, the relevant peak in the low-loss region is 42 eV (Cr-M_{2,3}), so the window for the pre-edge acquisition started at 32 eV, while the window for the post-edge acquisition started at 48 eV. The width of each window was 8 eV. For aluminium, which has the peak at 73 eV (Al-L_{2,3}), the window for the pre-edge acquisition started at 63 eV, while the window for the post-edge acquisition started at 78 eV.

The width of each window was 10 eV.

Energy windows of elements of interest for the three-window method: For iron, the relevant edge energy threshold is 708 eV (Fe-L_{2,3}). Correspondingly, two windows for the pre-edge acquisition started at 625 eV and 665 eV, respectively, and the window for the post-edge acquisition started at 720 eV. The width of each window was 30 eV. For chromium, the relevant edge energy threshold is 575 eV (Cr-L_{2,3}), so two windows for the pre-edge acquisition started respectively at 522 eV and 547 eV, while the window for the post-edge acquisition started at 577 eV. The width of each window was 20 eV. For aluminium, which has the edge energy threshold at 1560 eV (Al-K), the windows for the pre-edge acquisition started respectively at 1445 eV and 1495 eV, while the window for the post-edge acquisition started at 1550 eV. The width of each window was 50 eV. Finally, for the oxygen edge energy threshold of 532 eV (O-K), the windows for the pre-edge acquisition started respectively at 469 eV and 499 eV and the window chosen for the post-edge acquisition started at 532 eV. The width of each window was 30 eV.

1.3. Analytical methods for crystallographic structure: HRTEM

High-resolution TEM (HRTEM) images are formed by using a large objective aperture to select multiple beams (Fig. 2.5). Selected beams are reconstructed to yield contrast that can frequently be interpreted in terms of the projected crystal potential, which is directly related to the atomic structure of materials.

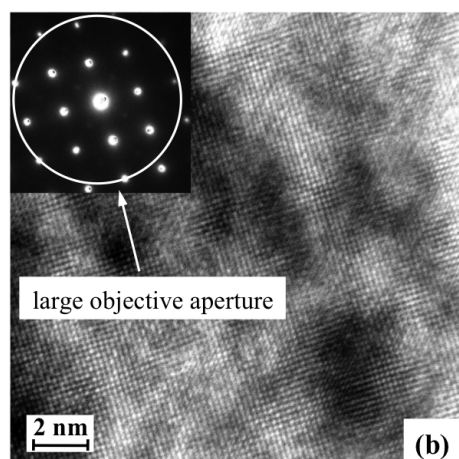


Fig. 2.5 High-resolution TEM image showing the matrix FeCr. The inset is the diffraction pattern oriented along $\langle 100 \rangle$. The shape of the large objective aperture is marked by the white circle.

To obtain ideal high-resolution TEM images, the specimen should be thin enough, and crystals of the specimen need to be pre-aligned close a zone-axis orientation. The objective aperture should be large enough and be well centered. In very thin specimens, the amplitude of incoming electrons is unaffected, so there can be no amplitude contrast. However, the

phases of the transmitted electrons will change and these phase changes appear as differences in phase contrast. The contrast formation in HRTEM images is based on the weak phase-object approximation if the specimen is very thin. The detailed description of this approximation can be found somewhere else [Williams, 2009]. Here we only focus on the influence of parameters relevant to the Contrast Transfer Function (CTF) because it decides which microscope can be applied to the HRTEM imaging.

Contrast Transfer Function (CTF): It describes the imperfections in the TEM lens system that result in modifications of the amplitudes and phases of the electron beam (wave) as it passes through the lenses to the image plane. It is frequently used to evaluate and compare performances of TEM microscopes for HRTEM. The function can be described as:

$$T(k) = -\sin\left[\frac{\pi}{2}C_s\lambda^3k^4 + \pi\Delta f\lambda k^2\right]$$

where k is the spatial frequency (nm^{-1}), C_s is the spherical aberration coefficient depending on the objective lens quality, λ is the wavelength defined by accelerating voltage and Δf is the defocus value. The important features of the function CTF($T(k)$) are shown in Fig. 2.6.

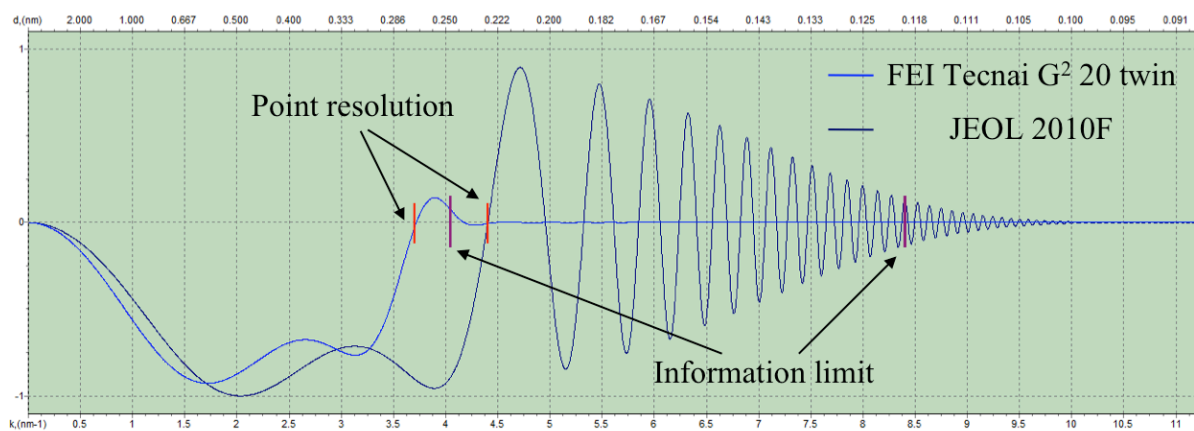


Fig. 2.6 Capabilities for high resolution TEM imaging of two different TEM microscopes: Two curves of the contrast transfer function (CTF) were drawn by the simulation software *Contrast Transfer Function Explorer* with using Scherzer defocus ($df = -86.7 \text{ nm}$ and -61.3 nm for FEI and JEOL, respectively) and the same magnification. Both two curves are modified by envelope functions: the temporal coherency envelope and the spatial coherency envelope.

The function starts at 0 and decreases. Then it stays almost constant and constant and close to 1. After firstly crossing the spatial frequency k -axis, it repeatedly crosses the k -axis as k increases.

The function can continue forever but, in reality, it is modified by envelope functions and eventually dies off. The exact mathematical form of these envelope functions is complex. In general, the result is described by multiplying the function by both the temporal coherency

envelope E_c and the spatial coherence envelope E_a to yield an effective transfer function $T_{eff}(k)$:

$$T_{eff}(k) = T(k)E_cE_a = -\sin\left[\frac{\pi}{2}C_s\lambda^3k^4 + \pi\Delta f\lambda k^2\right]E_cE_a$$

where the temporal coherency envelope E_c is caused by chromatic aberrations, focal and energy spread, instabilities in the high tension and objective lens current; the spatial coherence envelope E_a is caused by the finite incident beam convergence.

Effect of the defocus Δf : The presence of zeros in the function means that we have gaps in the output signal. Obviously, the best function is the one with the fewest zeros and with the broadest band of good transmittance (where CTF is close to -1). Back in 1949, Scherzer suggested an optimum defocus that occurs at:

$$\Delta f_{Sch} = -1.2 \times (C_s\lambda)^{1/2}$$

At this optimum defocus (also called as Scherzer defocus), all the beams will have nearly constant phase out to the first crossover of the spatial frequency k -axis. This crossover point is defined as the point resolution (marked in Fig. 2.6), which is expressed as:

$$\delta = 0.66 \times C_s^{1/4} \lambda^{3/4}$$

Up to the point resolution, phase-contrast images are directly interpretable. In other words, this is not the information limit but it is the limit where we can use nearly intuitive arguments to interpret what we see [Williams, 2009].

Effect of the aberration coefficient C_s : The value of C_s is proportional to the value of the point resolution δ . A smaller value of C_s means a better point resolution. Therefore, TEM microscopes equipped a high quality objective lens or a C_s corrector, have a better point resolution.

Effect of the accelerating voltage: the wavelength is another parameter that contributes to the value of the point resolution. In TEM microscopes, the wavelength of electrons is decided by the accelerating voltage. A high accelerating voltage (ex: 300 kV rather than 200 kV) allows us to achieve a higher point resolution.

Effect of the spatial coherence envelope E_a : The effect of the envelope functions is to impose a virtual aperture in the back focal plane of the objective lens, regardless of the setting of focus. The presence of this virtual aperture means that high-order passbands are simply not

accessible. This cut-off thus imposes a new resolution limit on the microscope [Williams, 2009]. This is what we called the information limit (marked in Fig. 2.6).

Between two envelope functions, the spatial coherence envelope E_a is one major factor that influences the information limit. The spatial coherency is defined by the convergence of the incoming electrons that can be expressed as:

$$\alpha^2 = \frac{M^2 j}{\pi B t}$$

where M is magnification; j is charge density; B is brightness and t is exposure time. For a given TEM microscope, the information limit can be improved by lowering magnification, increasing the exposure time, using smaller size and condenser aperture. The convergence also depends on the brightness of the electron source. At this point of view, TEM microscopes equipped Field Emission Gun (FEG) has a good advantage than those equipped LaB₆ filament since the brightness of an FEG is at least 100 times higher than a LaB₆ source [Williams, 2009]. This high brightness decreases the convergence angle, and increases the signal-to-noise ratio. In addition, FEG reduces the instrumental contribution to chromatic aberrations that also improves temporal coherency envelope E_c .

As shown in Fig. 2.6, Contrast transfer functions of *JEOL2010F* equipped FEG and *FEI Tecnai G² 20 twin* equipped LaB₆ filament were drawn with using Scherzer defocus and the same magnification. Both microscopes are operated at 200 kV. The comparison shows the convergence angles obtained are 1 mrad and 0.1 mrad for *FEI* and *JEOL*, respectively. The smaller convergence angle of *JEOL* indicates it has not only a smaller information limit but also a better spatial coherency than *FEI*. This explains why we chosen to use *JEOL2010F* for HRTEM imaging.

The information limit is usually beyond the point resolution, so full interpretation of high-resolution images requires extensive computer simulation because the high-resolution image loses phase information when it is recorded. In our study, the evaluation of high-resolution TEM (HRTEM) images was performed by means of fast Fourier transformation (FFT). In addition, HRTEM images were simulated by *JEMS* program [Stadelmann, 1987] and compared with experimental images. The TEM operation energy of 200 kV, the spherical aberration constant of 1 mm, the chromatic aberration of 1.4 mm, the defocus of -63 nm⁻¹, and 0 – 0.1 mrad beam convergence angle were used as input parameters for the simulation.

1.4. TEM specimen preparation

The as-received bulk material is a high-purity FeCr (10.54 at.% Cr) alloy supplied by Ecole Nationale Supérieure des Mines, Saint-Etienne, France. It has a shape as stick of 1.4 cm in

diameter. The stick was cut into a series of thin plates with a thickness of approximately 1 mm. These plates were mechanically ground down to 60 ~ 100 μm with the help of abrasive papers containing carbide/diamond abrasives. The mechanically polished plates were punched into discs of 3 mm in diameter (Fig. 2.7(a)).

To obtain as-received TEM thin foils, the punched discs were perforated by using a twin jet electro-polisher (Struers© Tenupol-5) with 10% perchloric acid and 90% ethanol solution at -10°C. The perforated discs were rinsed by pure ethanol at -10°C then desiccated on the filter paper.

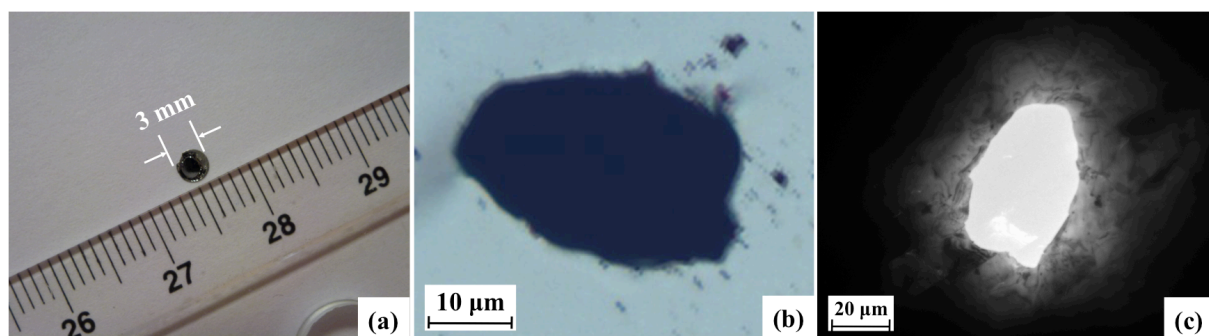


Fig. 2.7 (a) Photo of the punched disc of 3mm in diameter taken by Nikon® digital camera; (b) Photo of the hole existing in centre of the as-received thin foil taken by Olympus® optical microscope; (c) BF TEM image of the as-received thin foil, showing the hole and the surrounding transparent area.

The photo taken by Olympus® optical microscope (Fig. 7(b)) shows the perforation hole is quite small and irregular. The BF TEM image (Fig. 7(c)) reveals that only the edges near the hole are thin enough ($< 150 \text{ nm}$) to electron transparency, which can thus be directly examined by TEM. The perforated discs, also called as-received TEM thin foils are ready for ion implantation.

In order to facilitate TEM observations (eliminate the magnetism and limit the contribution of the matrix), the lamina was extracted from the as-implanted thin foil by an in-situ lift-out technique in an instrument called Focused Ion Beam (FIB). For the detail of this method, readers are invited to read Annexe A. The FIB lamina preparation has been performed by Benoît Arnal at CEA/DEN/DANS/DMN/SRMA.

1.5. Thermal annealing performed in TEM

Thermal annealing was carried out inside the microscope of *FEI Tecnai G² 20 twin* with using the *FEI* TEM heating specimen holder. The maximum allowed temperature for this specimen holder is about 700 °C. The annealing temperature was set at 500 °C with a duration ~3 hours.

For each in-situ thermal annealing, one as-implanted TEM thin foil was mounted on the heating specimen holder. The holder was connected with the controller (see Fig. 2.8(a)) and

inserted into the microscope (Fig. 2.8(b)). The vacuum condition inside the column of TEM was 1.2×10^{-5} Pa.

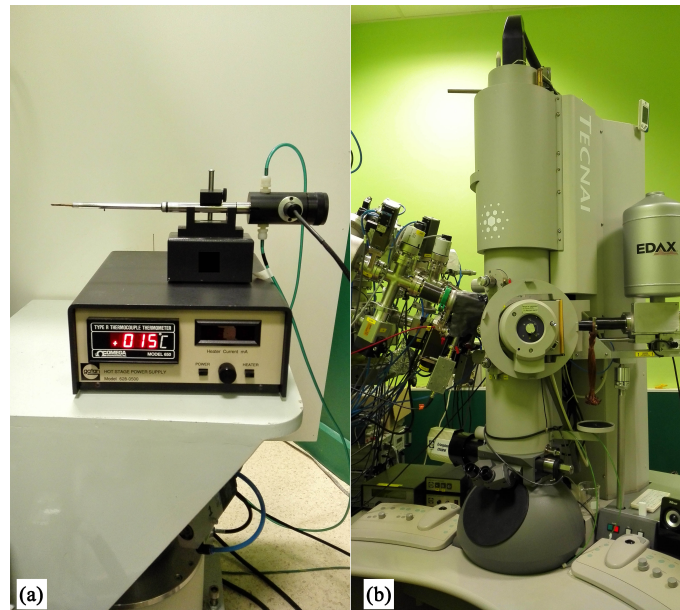


Fig. 2.8 (a) FEI heating TEM specimen holder (up) connecting with the controller (below). The pipes of cooling (in green color) water connect with the holder during thermal annealing; (b) TEM FEI Tecnai G^2 20 twin.

The controller can display the actual temperature of the holder and allow us to adjust the electrical current passing through the heating holder. The temperature increases with the current density. To stabilize at 500 °C, the current intensity was set to 418 mA. The duration for reaching 500 °C was shorter than 5 minutes. Obviously, it is negligible comparing to the total duration of thermal annealing.

Cooling water kept passing through the heating holder during and after thermal annealing. The holder was held inside the microscope until the actual temperature returned to room temperature. Annealed specimens are stocked under vacuum condition.

2. Introduction of the as-received material: high-purity Fe10Cr alloy

The as-received bulk material is a high-purity FeCr (10.54 at.% Cr) alloy supplied by Ecole Nationale Supérieure des Mines, Saint-Etienne, France. Fig. 2.9 shows a panorama of BF TEM images of the as-received TEM thin foil. The morphology of grains is non-equiaxial. The average lengths of grains measured by the software *Image J* are 3 μm and 4 μm along horizontal and vertical directions, respectively.

Nominal compositions of the as-received material based on the supplier report are listed in Table 2.1. Concentrations of major elements were found to be 90.14 wt.% (89.46 at.%) for Fe

and 9.86 wt.% (10.54 at.%) for Cr, respectively. Minor impurities e.g. Carbon, Nitrogen, Oxygen and Sulfur, were found to be less than 0.001 wt.%.

Elements	Fe	Cr	C	N	O	S
wt.%	90.14	9.86	≤ 0.001	≤ 0.001	≤ 0.001	≤ 0.001
at.%	89.46	10.54	-	-	-	-

Table 2.1 Nominal compositions of high purity FeCr alloy, based on the supplier report.

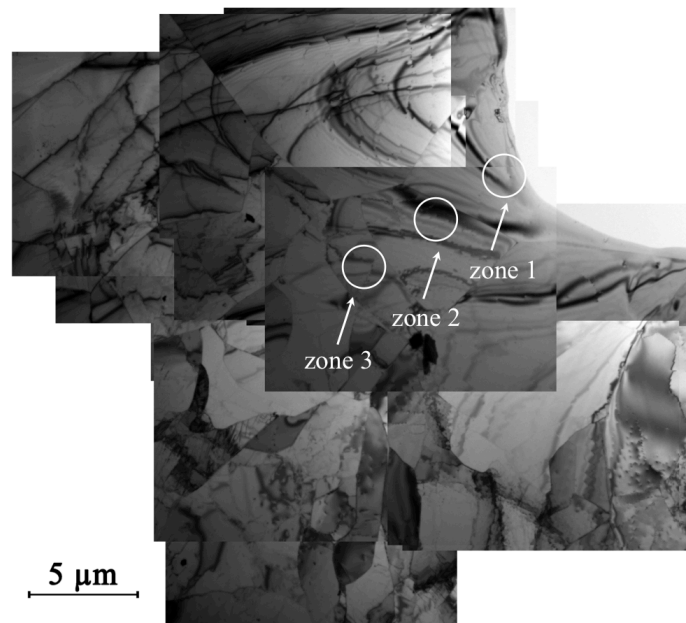


Fig. 2.9 Panorama of bright field (BF) TEM images of the as-received TEM thin foil: 3 zones encircled by white circles were selected for Energy Dispersion X-ray (EDX) investigations. Electron Energy Loss Spectrometry (EELS) investigation was also applied in the zone 1. Since the specimen was prepared by mechanical and electrolytic polishing, a hole could be seen on the upper right corner in the panorama.

In order to verify chemical compositions of the as-received material, both Energy Dispersive X-ray spectroscopy (EDX) and Electron Energy Loss Spectrometry (EELS) were applied to three different zones encircled in Fig. 2.9.

The resulting EDX spectra are drawn in Fig. 2.10. Spectra are normalized with the Fe $K\alpha$ peak. Major peaks (e.g. Cr $K\alpha$, Cr $K\beta$, Fe $K\alpha$ and Fe $K\beta$) are clearly visible, whereas the O $K\alpha$ peak overlaps the Cr $L_{\alpha,\beta}$ peak. No other potential impurities were observed from EDX spectra. The Cr concentration measured by EDX quantification is 8~9 at.%, which is less than the reference value (10.54 at.%) shown in Table 2.1.

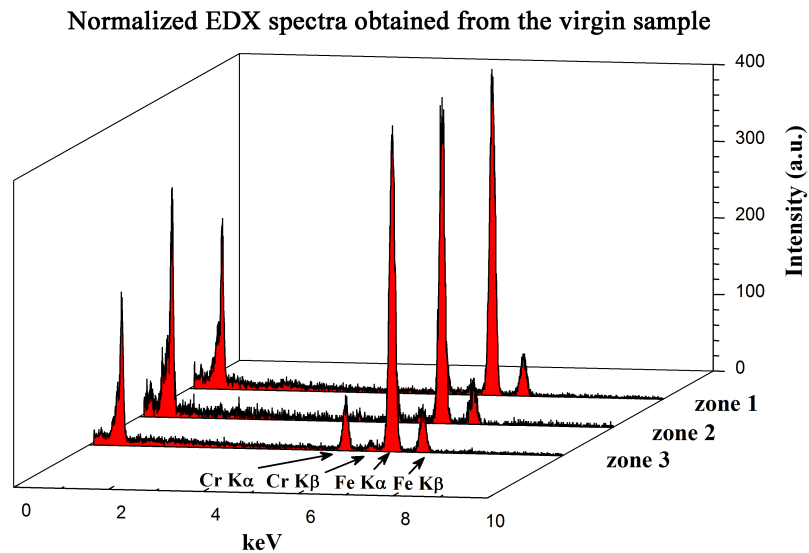


Fig. 2.10 EDX spectra obtained from three zones marked in Fig. 2.9. Spectra are normalized with the Fe K α peak.

The resulting EEL spectrum in the range of [475 eV-900 eV] is shown in Fig. 2.11. Cr L_{2,3} and Fe L_{2,3} edges are directly observed from the spectrum. Although O K edge is less visible, one can still confirm the presence of O K edge. The presence of oxygen in the as-received material is suggested due to oxidation on the material surface.

Signal and background of Cr L_{2,3} and Fe L_{2,3} edges were obtained with selecting energy window to relevant ranges of energy loss. The Cr concentration measured by EELS quantification is ~10.9 at.%, which is more closer to the reference value (10.54 at.%) shown in Table 2.1.

The comparison between measured concentrations of Cr reveals that the quantification effected by EELS is much more precise that effected by EDX. This result is consistent with the previous description (section 1.2.3 in Chapter 2). Furthermore, EDX and EELS analyses confirm that the as-received material examined is high-purity FeCr alloy (10.54 at.% Cr).

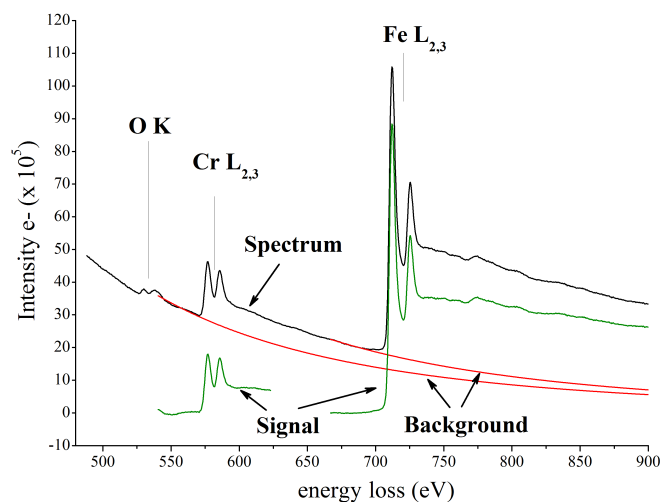


Fig. 2.11 EEL spectrum obtained from the zone 1 marked in Fig. 2.9: signal and background spectra of Cr L_{2,3} and Fe L_{2,3} peaks are extracted and drawn in green and red colors, respectively.

The crystallographic structure of the matrix was also verified by high resolution TEM. Fig. 2.12(a) shows a high resolution TEM image taken in the as-received TEM thin foil. Corresponding FFT analysis shown in Fig. 2.12(b) reveals that the matrix has a *bcc* lattice structure oriented along $\langle 100 \rangle$. The lattice structure and orientation are consistent with those identified in the diffraction pattern inserted in Fig. 2.12(a). The lattice parameter was found to be 2.85 Å and 2.9 Å according to the FFT analysis and the diffraction pattern using the Bragg equation, respectively. Both two values are quite close to the reference lattice parameter of *bcc* FeCr alloy (2.876 Å [Villars, 1985]).

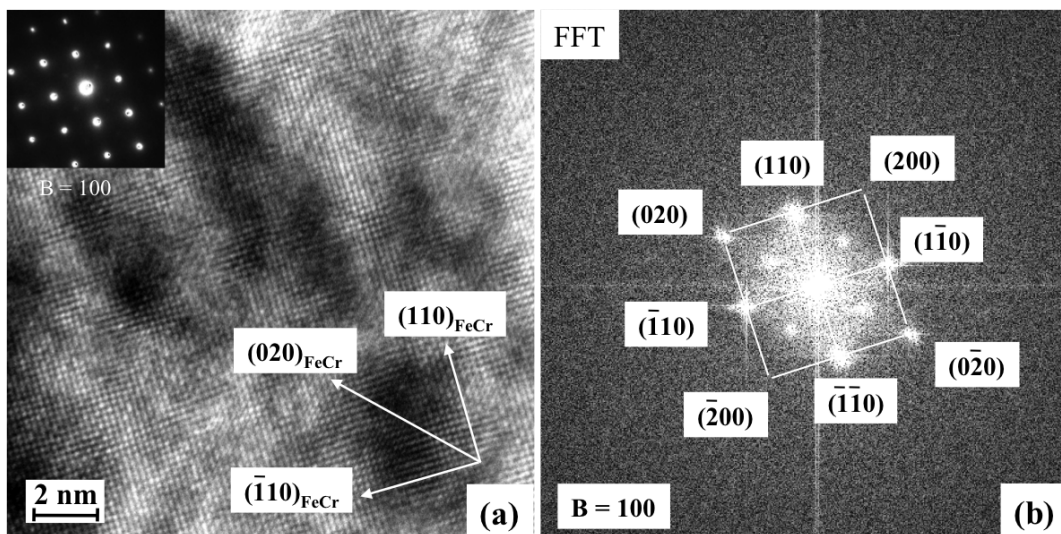


Fig. 2.12 Microstructure of the as-received TEM thin foil: (a) High resolution TEM image of the matrix FeCr. The corresponding electron diffraction pattern ($B=100$) is inserted in (a); (b) FFT analysis showing a *bcc* structure oriented along $\langle 100 \rangle$. FFT analysis correlates well with the inserted electron diffraction pattern.

In conclusion, the examined material is high-purity FeCr (9.86 wt.%) alloy, which has a *bcc* lattice structure with the lattice parameter of ~ 2.876 Å.

3. Ion implantation

3.1. Instrument

The ion implantation was carried out at Centre de Sciences Nucléaires et de Sciences de la Matière (CSNSM/JANNuS-Orsay, France) with JANNuS-Orsay facility [JANNuSOrsay, web site], where a 2 MV ARAMIS accelerator and 190 kV IRMA implanter are coupled with a 200 kV FEI TECNAI G² 20 TWIN transmission electron microscope to allow simultaneous co-irradiation and *in-situ* observations (Fig. 2.13(a)).

In this study, ex-situ ion implantation was carried out directly at 190 kV IRMA implanter (Fig. 2.13(b)) in order to obtain abundant as-implanted specimens at the beginning of this PhD study.

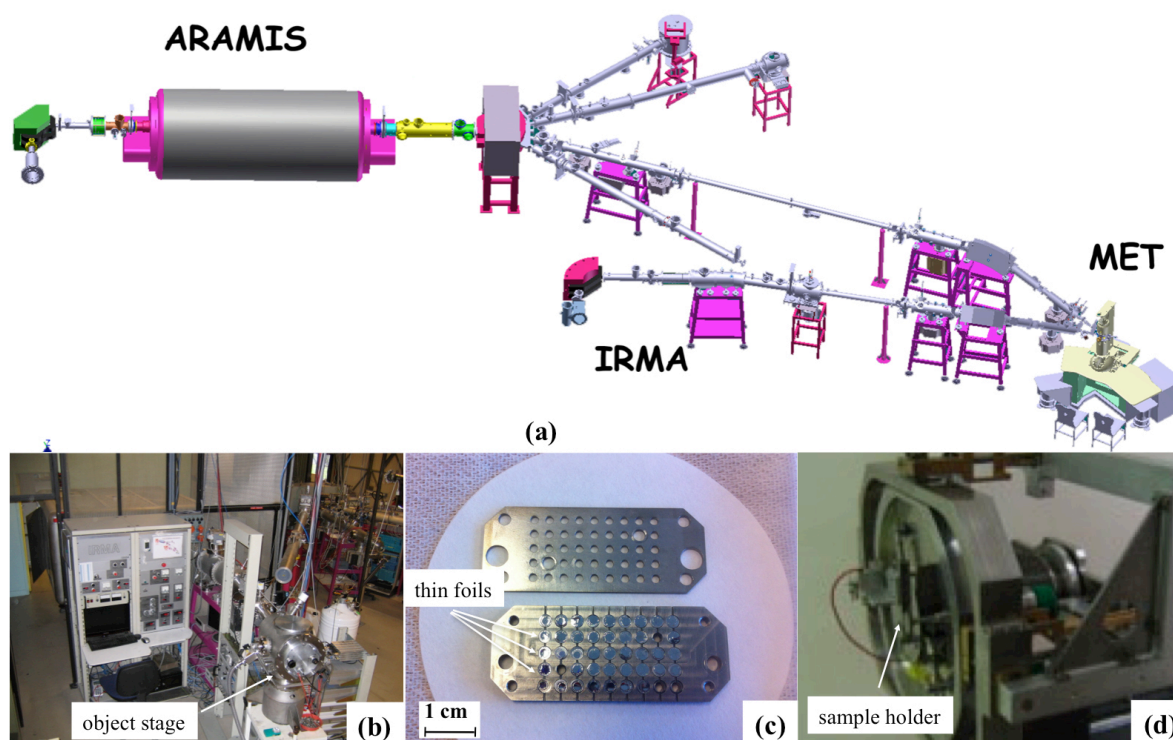


Fig. 2.13 (a) Scheme of JANNuS Orsay facilities: 2 MV ARAMIS accelerator and 190 kV IRMA implanter are coupled with a 200 kV FEI TECNAI G² 20 TWIN transmission electron microscope to allow simultaneous co-irradiation and *in-situ* observation; (b) Photo of 190 kV IRMA implanter of which the beam line is removed in order to insert the object stage for *ex-situ* ion implantation; (c) Photo of the specimen holder in which thin foils are embedded; (d) Photo of the object stage on which the specimen holder is mounted.

Fig. 2.13(c) shows the specimen holder used for *ex-situ* ion implantation. It offers at most 43 available positions for thin foils at the same time. Once most of the positions are occupied by specimens, the holder is then mounted on the object stage (Fig. 2.13(d)), which is inserted in the chamber of IRMA implanter during ion implantation.

3.2. Two-stage ion implantation at RT: Al⁺ ions then O⁺ ions

Al⁺ ions were chosen instead of Y⁺ or another metallic ions because: firstly, Al has a bigger diffusion coefficient (than Y or Ti in FeCr) [Hirvonen, 1982 ; Campbell, 1980], and we thus expect the oxide precipitates to form more easily, at lower temperature. Secondly, Al is known as one of important alloying elements. Its content can reach to 5.5 wt.% in several commercial ODS alloys such as MA956 [Chao, 1998], MA957 [Miller, 2004] and PM2000 [Sporer, 1992]. Thirdly, it was recently reported that the Al-Cr-O system has a thermodynamically metastable phase, which has a NaCl-like structure with 33% vacancies on the metal sites [Khatibi, 2011]. This metastable (Al, Cr, O) solid solution was synthesized in films grown onto Si substrates using reactive radio frequency magnetron sputtering, which is a non-equilibrium technique as ion implantation. In total, it is moreover a model case to be able to better experimentally study the early stages of precipitation. Therefore, we choose to

implant 3 %wt Al_2O_3 , ten times more than the industrial composition (0.3%wt of Y_2O_3), to be in the most probable conditions of precipitation. In order to observe by TEM, ions should be located at the position where the thicknesses are between 0 and 100 nm. So we chose the ion energy to obtain an ion distribution with a maximum implantation peak at 50 nm.

Two-stage ion implantation was carried out at room temperature with firstly 70 keV Al^+ ions to the fluence of $2 \times 10^{16} \text{ cm}^{-2}$ and then with 37 keV O^+ ions to the fluence of $3 \times 10^{16} \text{ cm}^{-2}$. The ion flux was $6.8 \times 10^{12} \text{ cm}^{-2} \cdot \text{s}^{-1}$ for both Al^+ and O^+ implantations. The specimen holder was inclined perpendicularly to the ion beam. The interval between each implantation required in order to change the ion source lasted for $\sim 2\text{-}3$ hours; during this time the foils remained in vacuum. No deliberate heating of the specimens was applied during ion implantation, while the specimen temperature increase caused by the ion beam is estimated to be less than 50 K.

The concentration profiles of implanted ions and created vacancies due to ion implantation were simulated using Monte Carlo code Stopping and Range of Ions in Matter (SRIM) [Ziegler, 1996], assuming the displacement energy of iron atoms of 40 eV [Juslin, 2007].

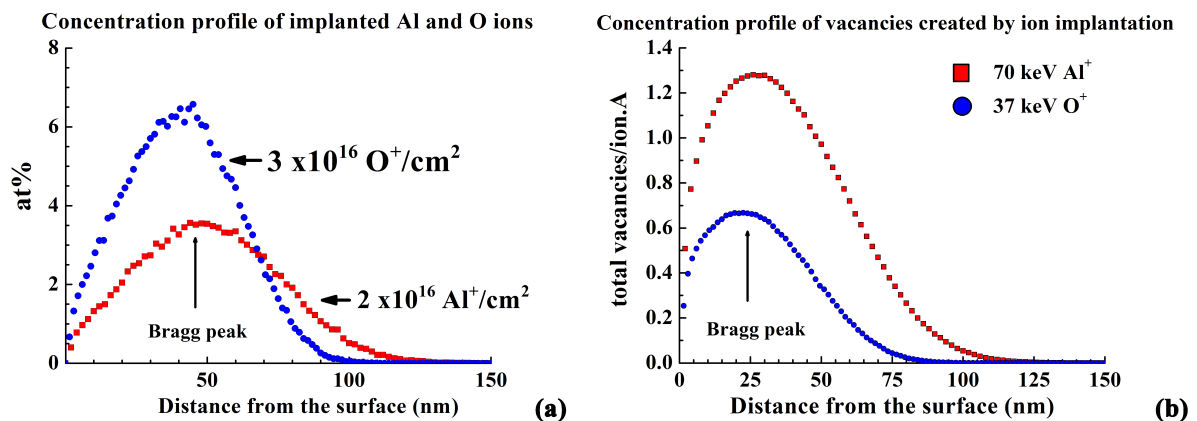


Fig. 2.14 Concentration profiles predicted by SRIM (displacement energy of 40 eV): (a) The concentration profiles of implanted ions. The concentration peak of both Al^+ and O^+ ions is predicted at 50 nm; (b) The concentration profile of vacancies created due to ion implantation. The concentration peak is predicted at 25 nm rather than 50 nm.

Fig. 2.14(a) shows that for both Al^+ and O^+ ions the concentration profile peaks are at approximately 50 nm from the specimen surface facing the beam. The nominal (i.e. without the account of the profile diffusional spreading) peak concentrations are 3.5 at.% for Al and 6.4 at.% for O atoms. Fig. 2.14(b) shows that for vacancies created by both Al^+ and O^+ ion implantation. The concentration profile peaks are at approximately 25 nm rather than 50 nm. The nominal (without considering recombination) peak concentrations are 1.28 vacancies per incident ion per Angström ($\text{ion}^{-1} \cdot \text{\AA}^{-1}$) for Al^+ ion implantation and 0.67 vacancies per incident ion per Angström ($\text{ion}^{-1} \cdot \text{\AA}^{-1}$) for O^+ ion implantation. In terms of displacements per atom

(dpa), the value of dpa was derived from the concentration of vacancies per incident ion per Angström according to the equation:

$$dpa = \frac{\phi \times n \times 1.10^8}{\rho}$$

where ϕ is the ion flux ($\text{cm}^{-2} \cdot \text{s}^{-1}$), n is the number of vacancies created at a distance from the surface ($\text{ion}^{-1} \cdot \text{\AA}^{-1}$) and ρ is the atomic density ($\text{at} \cdot \text{cm}^{-3}$).

The calculated numbers of atomic displacements are ~ 780 per incident Al^+ ion and ~ 320 per O^+ ion. The calculated damage production rates in the damage peak (at ~ 25 nm distance from the surface) are 1.027×10^{-2} and 5.35×10^{-3} $\text{dpa} \cdot \text{s}^{-1}$ for Al^+ and O^+ ions, respectively.

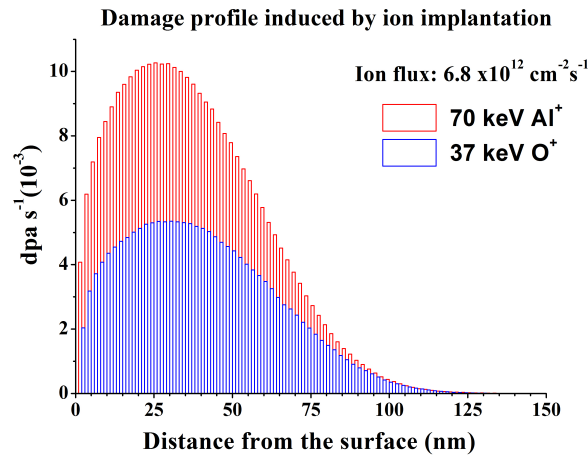


Fig. 2.15 Damage profiles predicted by SRIM (displacement energy of 40 eV): Damage profiles of 70 keV Al^+ (red color) and 37 keV O^+ (blue color) ions for the flux $6.8 \times 10^{12} \text{ cm}^{-2} \text{ s}^{-1}$.

In addition, damage profiles shown in Fig. 2.15 reveal that the damage due to both Al^+ and O^+ ion implantation is not homogeneous in the range of distance from the surface between 0 and 150 nm. After ion implantation, all as-implanted specimens were examined immediately by TEM observations. Only the specimens that still retain electron transparent regions were stored under vacuum condition and characterized by TEM.

4. Atom probe tomography (APT)

The results of APT analyses were observed in close collaboration with Dr. Marion Descoins, Dr. Dominique Mangelinck (IM2NP, Marseille, France) and Dr. France Dalle (CEA/DEN/DANS/DMN/SRMA). The specimen preparation, APT measurements and data analysis were carried out at IM2NP through the support of METSA network (2014) and NEEDS-Matériaux (2013). Data analysis was also partially made at CEA, Saclay.

4.1. APT specimen preparation

The bulk discs of 3 mm in diameter were obtained after mechanical polishing and punching. These processes are the same as those already introduced in TEM specimen preparation (section 1.4 in Chapter 2). The bulk discs were then jet-electropolished for a few seconds in a Tenupol-5 thinning device at -10 °C, to obtain dimpled discs. During electropolishing, one face of bulk discs was protected, resulting in a mirror-finished surface dimple (Fig. 2.16(a)) formed on the etched face of dimpled discs. The protected face shown in Figure 2.16(b) is still coarse since it was not etched.

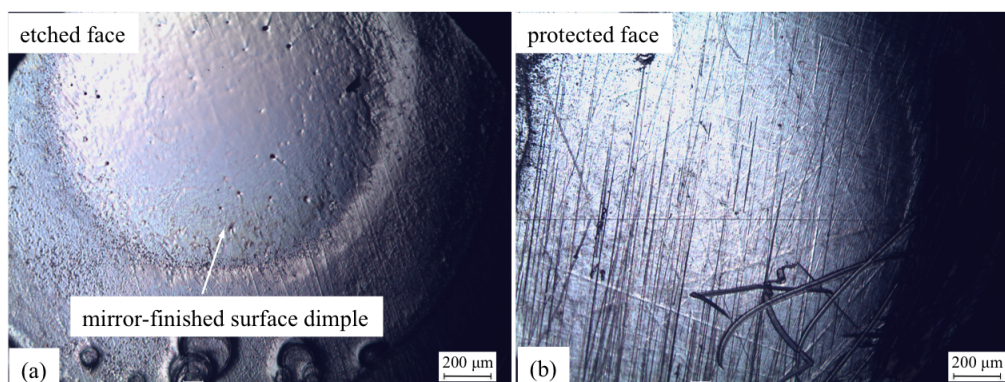


Fig. 2.16 Photos of the as-implanted dimpled disc taken by Olympus[®] optical microscope: (a) The etched face showing a mirror-finished surface dimple; (b) The protected face showing coarse surface.

Al⁺ and O⁺ ions were consecutively implanted into polished dimpled discs at room temperature. The parameters (energy, fluence, temperature...) used for dimpled discs are the same ones used for TEM thin foils. Implanted ions were projected perpendicularly toward the mirror-finished surface dimple during ion implantation. Subsequent thermal annealing was applied to some of as-implanted dimpled discs at 500 °C and 3 hours, to obtain annealed dimpled discs.

The next step is use as-implanted and annealed dimpled discs to fabricate needle-shaped tips, which are ideal for APT analyses. The tips were produced by an in-situ lift-out method using a FEI Helios 600 NanoLab 2-30 kV focused ion beam (FIB) at IM2NP, Marseille, France. A detail description of the lift-out method can be found in Annexe A.

4.2. Principle of APT

Atom probe is described as a field ion microscope equipped with a time-of-flight mass spectrometer and position sensitive detector.

In Fig. 2.17, a sharp cryogenically-cooled tip is introduced into an ultrahigh vacuum chamber. A positive voltage V_0 (5-20 kV) is then applied to the tip. In the presence of such a high electric field, atoms at the surface of a tip are ionized.

The ions are then accelerated by the surrounding electric field towards the detector along the electric field lines. As each ion is detected, its time-of-flight is converted into a mass-to-charge ratio by using a formula derived from simple potential and kinetic-energy considerations.

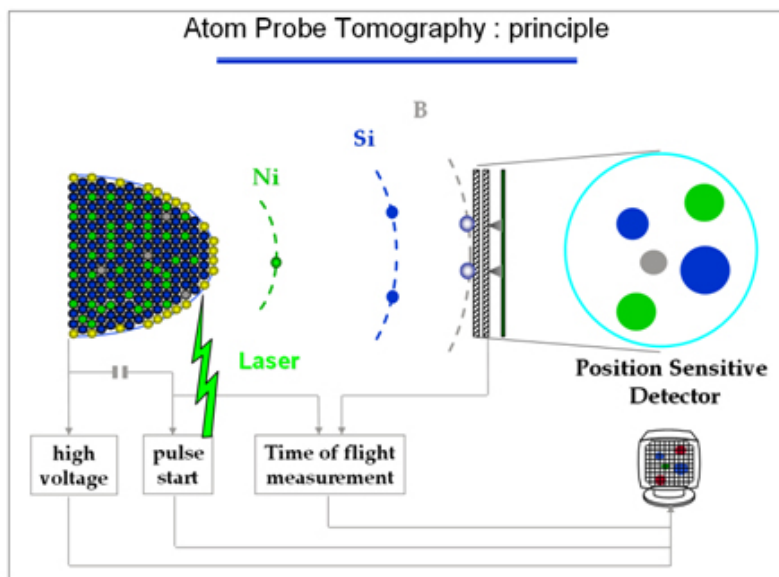


Fig. 2.17 Schematic representation of Atom Probe Tomography (APT) [IM2NP, website].

The mass-over-charge ratio $\frac{m}{n}$ is deduced from the applied voltage, $V_{total} = V_0 + V_p$ (with V_0 and V_p standing electric and pulse voltages, respectively) and the measured time of flight, t by using the energy balance relationship:

$$\frac{m}{n} = 2e \times (V_0 + V_p) \times \left(\frac{t}{L}\right)^2$$

where m is the ion mass; n is the ion charge state (1^+ , 2^+ ...); e is the elementary charge and L is the length between the tip and the detector.

The mass-to-charge ratios of the detected ions are generally represented in the form of a histogram, also called mass spectrum. The ability to distinguish the different isotopes, combined with the mass-to-charge ratio, enables unambiguous identification of the chemical nature of the ions associated with each mass peak. Therefore, The peaks appeared in the mass spectrum could be identified and associated to the corresponding element or its isotopes or even combination (molecular ions).

4.3. APT measurements

APT measurements were carried out using an atom probe (LEAP 3000TM XHR, Imago Scientific Instruments) equipped with a pulsed laser (Pulse Width = 10 ps, wavelength = 532 nm) at IM2NP in Marseille, France. This LEAP is equipped with a mass reflectron, which improves the mass resolution (Flight Path = 382 mm). In our measurements, the atom probe was operated in the laser-pulsing mode. Detail conditions of each run are listed in Table 2.2.

During the analysis, the specimen base temperature was maintained between 53 and 87 K in ultra-high vacuum conditions ($< 1.7 \times 10^{-11}$ Torr). In addition, the laser energy varied from 0.5 to 1.2 nJ under laser pulsing mode. Only runs collecting at least 10 millions ions were considered in order to reduce the statistical error.

	N° run	N° tip	Laser energy (nJ)	Pulse frequency (kHz)	T (K)	Pressure (Torr)	Detection rate (%)	Total ions (Million)
As-implanted	R30_03984	M15	0.8	100	86.9	9.5×10^{-11}	0.8 – 1	20.8
Annealed 500°C & 3hours	R30_05508	M20	0.8	100	86.1	10^{-11}	0.7 – 1	11.8
	R30_05509	M13	0.8	100	86.5	9.7×10^{-12}	0.5 – 1.2	53.9
	R30_05510	M21	0.6 – 1.1	100	54.1	9.6×10^{-12}	0.5	5.3
	R30_05511	M22	0.8	100	53.2	9.2×10^{-12}	0.5 – 1.2	48.8
	R30_05514	M29	0.8	100	86.5	1.7×10^{-11}	0.7	115.3

Table 2.2 Conditions of APT analysis for both as-implanted and annealed tips (500 °C and 3h)

The background, mass resolution and percentage of good hits of each run are listed in Table 2.3. Background of each run is negligible and do not influence the definition of characteristic peaks shown in mass spectrum. The quality of a mass spectrum is generally assessed by the mass resolution, which is defined as $\frac{M}{\Delta M}$, where ΔM is the width of the peak at 50% of peak height (full-width at half-maximum (FWHM)).

In our study, all of runs have a mass resolution higher than 1000 FWHM in laser-pulsing mode, which reveal the high quality of APT measurements. In laser-pulsing mode, the threshold of good hits is 50 - 60% [Miller, 2014]. As can be seen in Table 2.3, the good hits percentage of all runs is over this threshold.

In total, the run R30_03984 (as-implanted) and the run R30_05514 (annealed) have not only a good mass resolution but also excellent good hits. The cluster analysis was carried out in these two runs in order to characterize the nature (size, number density, distribution, chemical compositions) of precipitates prior and after thermal annealing.

	N° run	N° tip	Background (ppm/nsec)	Mass resolution FWHM (⁵⁶ Fe ²⁺)	Good hits (%)
As- implanted	R30_03984	M15	2.4	1170	92.1
Annealed 500°C & 3hours	R30_05508	M20	3.62	1103	84.3
	R30_05509	M13	12.50	1145	87.3
	R30_05510	M21	5.97	1060	80.0
	R30_05511	M22	5.57	1158	86.2
	R30_05514	M29	9.67	1174	87.8

Table 2.3 Quality of APT runs for both as-implanted and annealed tips (500 °C and 3h)

4.4. APT data treatment

The three-dimensional reconstruction of the sharp tip from APT data was done according to the methodology described in Refs. [Mangelinck, 2014; Gault, 2011], using a commercial software (IVASTM). Nano-clusters were identified using clustering algorithm approach based on the idea that nano-clusters are local regions enriched in solute atoms. This algorithm also known as maximum separation method depends on several parameters:

- **d_{max} (nm):** The algorithm groups solute atoms separated by a distance d_{max}. If two solute atoms p and q have a distance d(p, q) between each other, and if d(p, q) is inferior or equal to d_{max}, solute atoms p and q are thus associated in the same nanocluster.
- **N_{min} (number of atoms):** In order to avoid the misinterpretation of occasional density fluctuations of random solid solution as clusters, all small clusters with the number of solute atoms below a threshold N_{min} are taken out of consideration.

- **L_{enveloppe} (nm)**: Nanoclusters are constructed on the remaining solute groups by adding all the atoms within some distance $L \sim d_{\max}$ from the solutes atoms in each group.
- **D_{erode} (nm)**: The previous step induces an artificial layer existing on the surface of nanocluster, which the erosion method helps to eliminate.

The principal parameters used in the maximum separation method are d_{\max} and N_{\min} . They are determined for each particular set of APT data using statistic analysis of the nearest neighbor and clusters count distributions.

Once nano-clusters are identified, they are subjected to further characterization in terms of size, number density and chemical compositions.

Cluster size: the estimation of feature size is made from the radius of gyration (R_g), that is the average distance between each cluster atom and the centre of mass of the cluster. The full description of the radius of gyration can be found in [Miller, 2014]. In APT experiments, the radius of gyration (R_g) is normally determined for the 3-D from

$$R_g = \sqrt{\frac{\sum_{i=1}^n [(x_i - \bar{x})^2 + (y_i - \bar{y})^2 + (z_i - \bar{z})^2]}{n}}$$

The radius of gyration provides a parameter that is slightly smaller than the actual size of the feature. Therefore, it is common to convert the radius of gyration to an alternative parameter, the Guinier radius, R_G , which represents the actual size of the feature with the use of the

following equation: $R_G = \sqrt{\frac{5}{3}} R_g$

The cluster size represented by the Guinier radius is comparable with the size estimated by other analysis techniques such as the TEM characterization [Williams, 2010].

Cluster number density: the number density of a distribution of discrete clusters may be calculated from the number of clusters observed (N_p) in the volume analyzed. In principle, the volume could be estimated from the products of the extents of the x, y and z directions of the analyzed volume. However, the extents of the x and y dimensions of these data generally increase during the analysis due to the blunting of the specimen, making a reliable estimate difficult [Miller, 2014].

Alternatively, the volume may be estimated from the total number of atoms detected in the volume, N_{vol} , the average atomic volume, Ω , and the detection efficiency of the single-ion detector, ξ . Therefore, the number density is given by: $\rho = \frac{N_p \xi}{N_{vol} \Omega}$

Chemical compositions of clusters: the concentration of an element i , in the analyzed volume can be expressed as: $C_i(at.\%) = \frac{N_i}{N_t} \times 100$

where N_i is the number of atoms of the element i and N_t is the total number of atoms in the volume. Considering only statistical variation, the precision of the composition measurement

is given by: $\sigma_i = \sqrt{\frac{C_i(1 - C_i)}{N_t}}$

4.5. Common artifacts: Trajectory aberrations & Local magnification effects

Discrepancies between reconstructed atomic data and the original structure result not only from imperfections in the reconstruction procedure, but also from artifacts that induce deflections in the flight of the ions. The evaporation of multiphase materials is complicated due to the chemical dependence of the evaporation field. Phases with higher evaporation fields than the matrix will tend to protrude on the surface leading to a local higher curvature. According to the principle of APT data reconstruction, image magnification depends on tip radius, and local change in curvature of the tip induces variations in magnification [Rose, 1956]. A major consequence of the field difference is the trajectory overlap between precipitates and matrix atoms near the interface, which results in interface smearing and inaccurate concentration measurements [Marquis, 2010].

Gault *et al.* [Gault, 2012] illustrated this phenomenon in the cases of low field and high field precipitates. When the field required to field evaporate the precipitate is lower or higher than that required for the matrix, these are referred to as, respectively, low field or high field precipitates. In Fig. 2.18, the dashed lines correspond to the expected trajectories of the ions, and the solid lines to the actual trajectories.

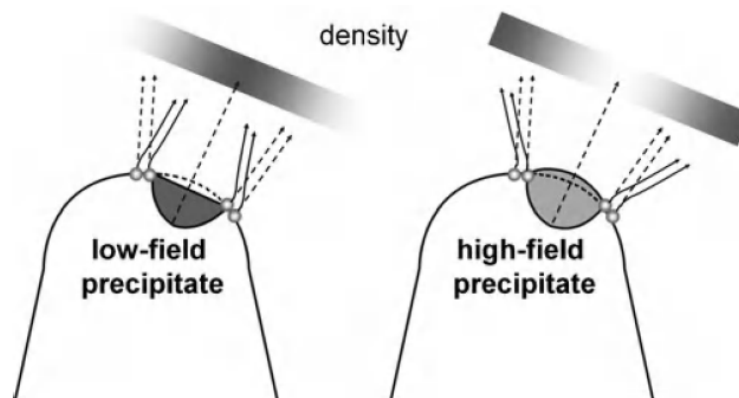


Fig. 2.18 Trajectory aberrations and impact on the density due to a change in the surface curvature in the case of low- and high-field precipitate. The dashed lines correspond to the expected trajectories of the ion, and the solid lines to the actual trajectories [B. Gault, 2012].

In the case of low field precipitates, the variation in the evaporation field leads to an apparent increase in the density of hits (left schema in Fig. 2.18). On the contrary, in the case of high field precipitates, the variation leads to an apparent decrease in the density of hits.

This artifact was already observed by Williams *et al.* [Williams, 2010] and Marquis [Marquis, 2008] in the case of precipitates in ODS steels, leading to trajectory overlaps up to a few nanometers near the particle/matrix interface. In Chapter 3, we introduce a simple matrix-correction for APT data obtained by the cluster analysis. This simple correction helps us to better understand element contents in the clusters prior and after the thermal annealing.

Chapter 3 Results

1. Introduction of the as-implanted material.....	74
2. Precipitate size and number density evolution.....	77
2.1. Comparison between as-implanted thin foils and FIB lamina.....	77
2.2. Comparison between as-implanted and annealed thin foils.....	78
3. Chemical compositions of precipitates.....	80
3.1. Chemical composition using EFTEM.....	80
3.1.1 As-implanted thin foils and FIB lamina.....	80
3.1.2 Annealed thin foils.....	84
3.2. APT analyses of as-implanted samples.....	85
3.2.1 Compositional measurements.....	85
3.2.2 Cluster analyses.....	88
3.2.2.1 Number density, spatial distribution and size distribution of clusters.....	88
3.2.2.2 Chemical compositions of clusters.....	91
3.3. APT analyses of annealed samples.....	95
3.3.1 Compositional measurements.....	95
3.3.2 Cluster analysis.....	98
3.3.2.1 Number density, spatial distribution and size distribution of clusters.....	99
3.3.2.2 Chemical compositions of clusters.....	102
4. Crystallographic structure of precipitates.....	105
4.1. Measurements of SAED and HRTEM obtained in as-implanted samples.....	105
4.2. Measurements of SAED obtained in annealed samples.....	113
5. Preferential precipitation in point defects sinks.....	115
5.1. Elements enrichment at grain boundaries.....	115
5.2. Precipitation on dislocation lines and loops.....	116

1. Introduction of the as-implanted material

The energy-dispersive X-ray (EDX) analysis applied on the as-implanted material confirms the presence of both Al and O atoms (see Fig. 3.1). In order to compare the spectra recorded on both as-received (blue line) and as-implanted (red line) thin foils, the spectra were normalized with the Fe $K\alpha$ peak. The estimated content of aluminum ($\sim 1.85 \pm 0.2$ at.%) is in good agreement with the implanted number of Al^+ ions (~ 1.91 at.%). The quantification of the amount of oxygen is, however, impossible because the O peak strongly overlaps with a nearby Cr peak in the EDX spectrum.

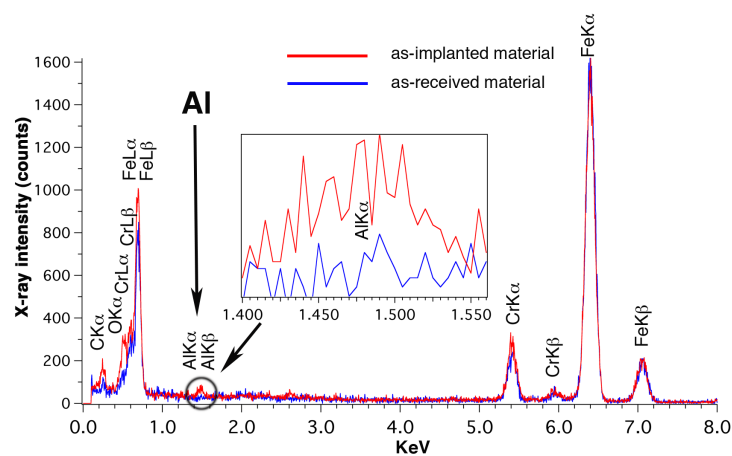


Fig. 3.1 EDX spectra recorded on both as-received (blue line) and as-implanted (red line) Fe-Cr thin foils. The spectra are normalized with the Fe $K\alpha$ peak.

EEL spectrum with energy loss 475 to 800 eV has been obtained and drawn in Fig. 3.2(a). O K, Cr $L_{2,3}$ and Fe $L_{2,3}$ core loss edges are all evidently visible in the spectrum. In addition, the O K edge is much more comparable to the Cr $L_{2,3}$ edge in the case of the as-implanted thin foil than that in the case of as-received thin foil. Signal (green) and background (red) spectra of these three edges were extracted from the spectrum (Fig. 3.2 (a)) in order to quantify elemental concentrations. The quantification of oxygen by EELS is easier than that by EDX since O K edge does not overlap with Cr $L_{2,3}$ edge. The estimated O content ($\sim 3.2 \pm 0.15$ at.%) is slightly higher than the implanted number of O^+ ions (~ 2.8 at.%). The difference is possibly due to the occurrence of the oxidation, which has already been reported in as-received thin foils.

For aluminum, it has two characteristic edges in the EEL spectrum: Al $L_{2,3}$ (73 eV) edge in the low-loss region (Fig. 3.2(b)) and Al K (1560 eV) edge in the high-loss region (Fig. 3.2(c)). The signals of Al edges extracted from the spectra confirm the presence of Al in as-implanted thin foils. However, it is hard to achieve a precise quantification of Al content due to weak intensity of Al signals.

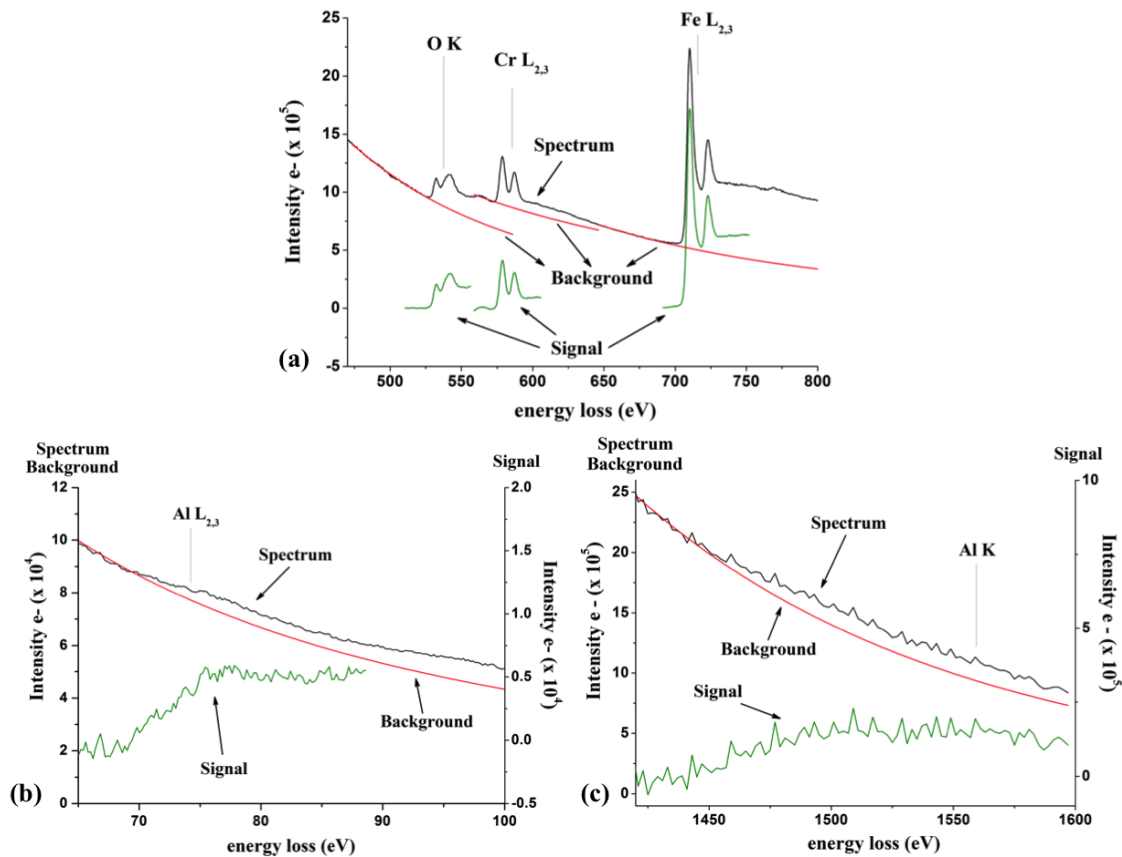


Fig. 3.2 EEL spectrum obtained from the as-implanted Fe-Cr thin foil: (a) Spectrum in the range of 475 to 800 eV for O K, Cr $L_{2,3}$ and Fe $L_{2,3}$ peaks; (b) Spectrum in the range of 65 to 100 eV for Al $L_{2,3}$ edge; (c) Spectrum in the range of 1500 to 1650 eV for Al K edge. Both signal and background spectra of O K, Cr $L_{2,3}$, Fe $L_{2,3}$, Al $L_{2,3}$ and Al K peaks are extracted and drawn in green and red colors, respectively.

In total, EDX and EELS characterization confirm that both Al and O atoms were successfully introduced into the high purity FeCr thin foils by ion implantation at room temperature.

Fig. 3.3 shows the bright field micrograph of the as-implanted FIB lamina and its corresponding high angular dark field (HAADF) micrograph obtained under scanning TEM (STEM) mode.

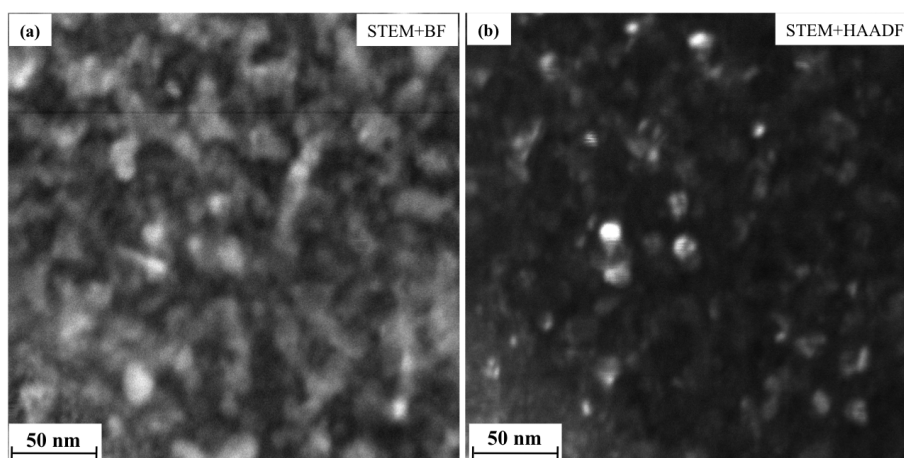


Fig. 3.3 The microscope operated under scanning TEM (STEM) mode: (a) Bright Field (BF) micrograph; (b) Corresponding High Angular Dark Field (HAADF) micrograph.

HAADF images are also called as Z-contrast images because contrasts are proportional to Z^2 (Z is the atomic number). The white spots shown in Fig. 3.3(b) reveal that precipitates were synthesized in as-implanted samples due to ion implantation.

Since all metallic elements (Fe, Cr and Al) Therefore, the precipitates observed in the HAADF-STEM image (Fig. 3.3(b)) are probably a mix of multiple nano-oxides.

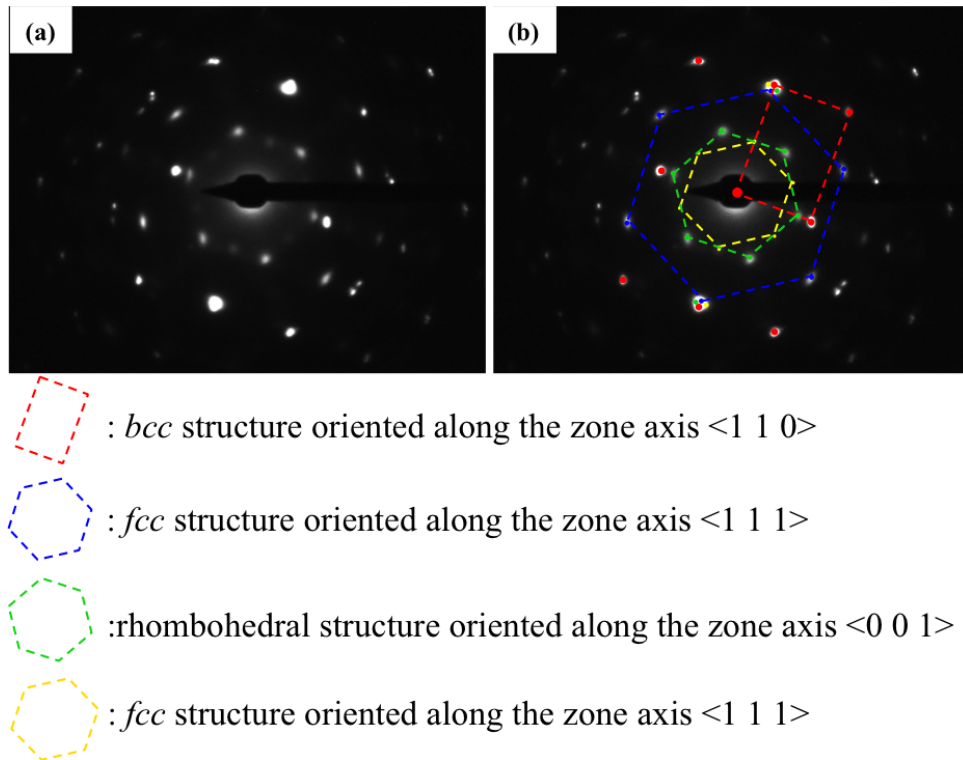


Fig. 3.4 (a) Selective Area Electron Diffraction (SAED) pattern oriented along $\langle 1\ 1\ 0 \rangle$ Fe-Cr lattice direction on a region of the as-implanted thin foil; (b) The colorful shapes represent different sets of diffraction spots. Each set of diffraction spots correspond to either the Fe-Cr matrix or one of nano-oxides.

The co-existence of multiple nano-oxides was identified in the diffraction pattern (Fig. 3.4(a)) oriented along $\langle 1\ 1\ 0 \rangle$ Fe-Cr lattice direction on a region of the as-implanted thin foil. The colorful shapes drawn in Fig. 3.4(b) represent different sets of diffraction spots that correspond to the Fe-Cr matrix and multiple nano-oxides. An overview of the crystallographic structure of multiple nano-oxides was listed below Fig. 3.4. The *bcc* structure (red rectangular) corresponds to the Fe-Cr matrix oriented along $\langle 1\ 1\ 0 \rangle$ direction. Beside this, the rest of structures correspond to multiple nano-oxides oriented in different direction. The nature (size, density, chemical composition and structure...) of different nano-oxides will be fully introduced later. Here, we only give simply a summary of results. In general, the rhombohedral structure (green hexagonal) and the *fcc* structure (yellow hexagonal) have been found to correspond to Cr-rich oxides and (Fe, Cr)-rich oxides, respectively. In contrast, another *fcc* structure (blue hexagonal) belongs to (Al, Cr)-rich oxides.

Obviously, the (Al, Cr)-rich oxides are the most interesting precipitates in our study, since the atoms implanted are Al and O. Thus, only the results relevant to (Al, Cr)-rich oxides are introduced in Chapter III. Other results corresponding to (Fe, Cr)-rich and Cr-rich oxides are put in Annexe B.

2. Precipitate size and number density evolution

2.1. Comparison between as-implanted thin foils and FIB lamina

The diffraction spots were properly selected so that only precipitates corresponding to (Al, Cr)-rich oxides could be observed in DF TEM images. As described in the section 1.4 of Chapter 2, most of as-implanted samples are as-implanted thin foils prepared by mechanical and electrolytic polishing. Others were prepared by *in-situ* lift-out technique with the help of Focus Ion Beam (FIB). This kind of samples is thus called as as-implanted FIB lamina.

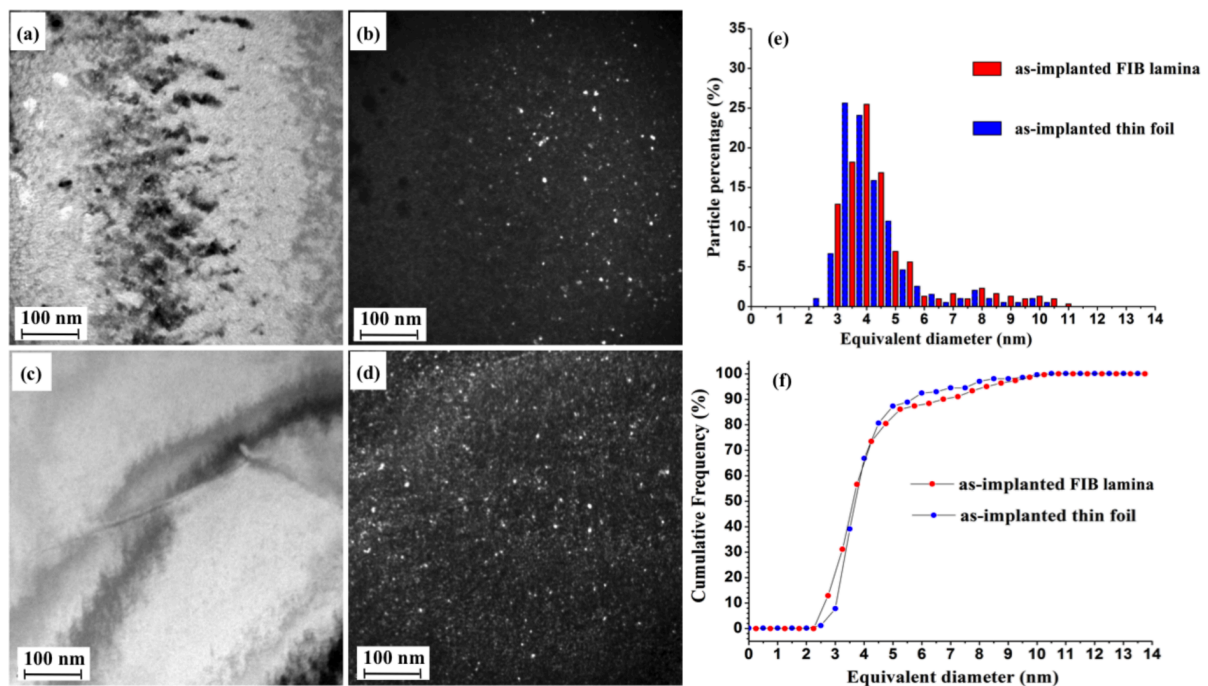


Fig. 3.5 As-implanted thin foil: (a) Bright Field (BF) TEM image; (b) Corresponding Dark Field (DF) TEM image. As-implanted FIB lamina: (c) BF TEM image; (d) Corresponding DF TEM image. (e) Comparison of size (equivalent diameter) of the precipitates identified in (b) and (d); (f) Cumulative frequency as a function of size of precipitates corresponding to (e).

Fig. 3.5(a) and (c) show BF TEM images taken on the as-implanted thin foil and FIB lamina, respectively. The corresponding DF TEM images are shown in Fig. 3.5(b) and (d). Bright spots corresponding to precipitates can be observed in both micrographs. Obviously, the distributions of precipitates are heterogeneous in both two kinds of as-implanted samples. Another spatial effect observed in our study – not detailed here – is the sensitivity of precipitation to the thickness of TEM samples (please see Annexe D).

The measurement of the surface of bright spots allows us to estimate the size of precipitates, which is defined by the equivalent diameter d_{eq} :

$$d_{eq} = 2 \times \sqrt{\frac{S}{\pi}}$$

where S is the surface of precipitates identified in the DF TEM image.

Fig. 3.5(e) shows the corresponding histogram of precipitate size. The precipitate size (equivalent diameter) ranges from 2 to 10.5 nm centered on 4.3 nm and 4.4 nm for the as-implanted thin foil and FIB lamina, respectively. Obviously, the distribution of size of precipitates is independent to the sample preparation method. The cumulative frequency corresponding to Fig. 3.5(e) is drawn in Fig. 3.5(f) as a function of the equivalent diameter. In the range of 3 to 5 nm, the two curves drawn in Fig. 3.5(f) almost overlap each other, whereas the curve of the as-implanted FIB lamina is under the one of the as-implanted thin foil in the large size region. It means that most of precipitates are in the range of 3 to 5 nm. But the number of large size precipitates in the as-implanted FIB lamina is slightly higher than that in the as-implanted thin foil. The number density of precipitates has the same order of magnitude ($\sim 10^{22} \text{ m}^{-3}$) for both two kinds of as-implanted samples.

2.2. Comparison between as-implanted and annealed thin foils

Comparing to the as-implanted state in Fig. 3.6(a) and (b), the microstructure of oxide precipitates after thermal annealing at 500 °C and 3 hours is presented in Fig. 3.6(d) and (e) for after 1 hour and in Fig. 3.6(g) and (h) for after 3 hours. The precipitates have evolved during thermal annealing: their sizes become larger and larger. The histograms presented on Fig. 3.6 highlight this evolution of the size of precipitates from 0 to 3 hours at 500 °C. Before thermal annealing, the precipitate size ranges from 2 to 10.5 nm centered on 4.3 nm (see Fig. 3.6(c)). After 1 hour of thermal annealing, the center of the histogram shifts to 6.5 nm (see Fig. 3.6(f)). Finally, the histogram presents a wider distribution of precipitates, centered on 7.7 nm. The distributions of precipitates are still heterogeneous after thermal annealing. On the contrary, a decrease in the number density was measured with increasing the duration of thermal annealing. The number density is initially $(1 \pm 0.3) \times 10^{22} \text{ m}^{-3}$ in the as-implanted state, then decreases to $(7 \pm 2) \times 10^{21} \text{ m}^{-3}$ after the thermal annealing at 500 °C and 3 hours.

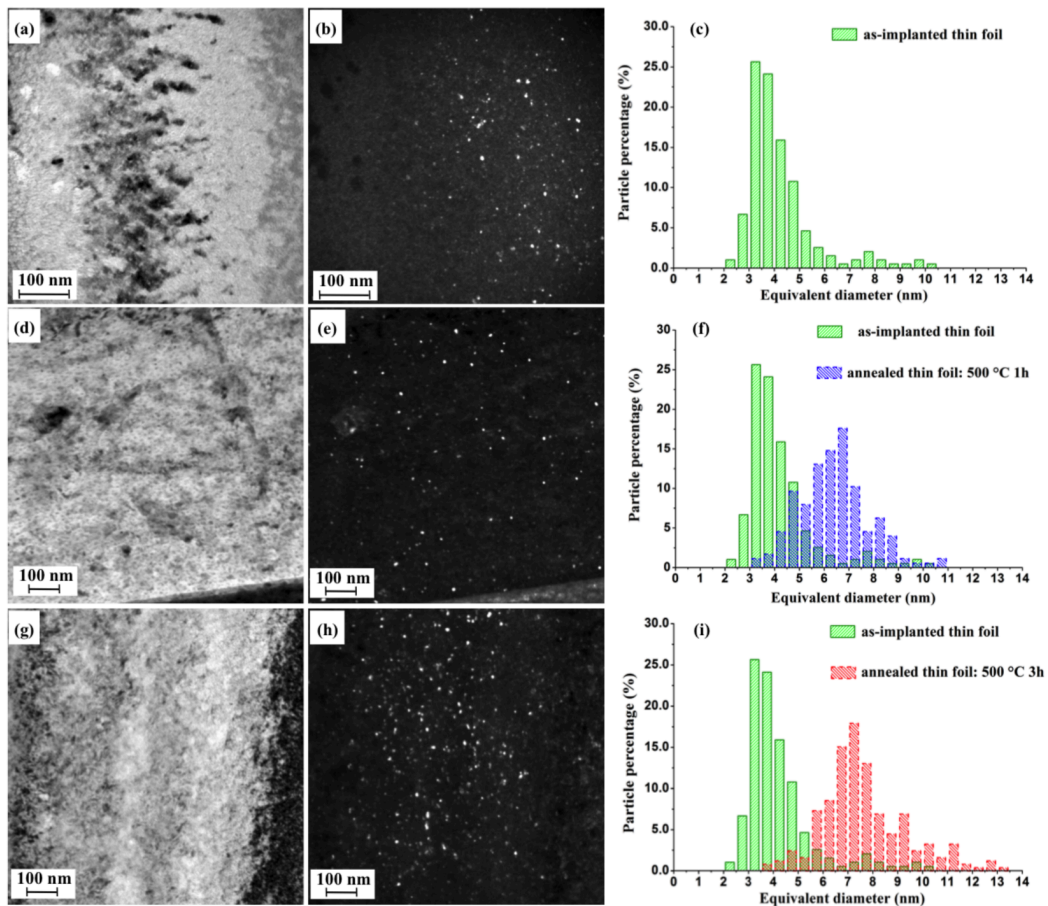


Fig. 3.6 As-implanted thin foil: (a) Bright Field (BF) TEM image; (b) Corresponding Dark Field (DF) TEM image; (c) Distribution of size (equivalent diameter) of the precipitates identified in (b). Annealed thin foil at 500 °C and 1 hour: (d) BF TEM image; (e) Corresponding DF TEM image; (f) Comparison of size (equivalent diameter) of the precipitates identified in (b) and (e). Annealed thin foil at 500 °C and 3 hours: (g) BF TEM image; (h) Corresponding DF TEM image; (i) Comparison of size (equivalent diameter) of the precipitates identified in (b) and (h).

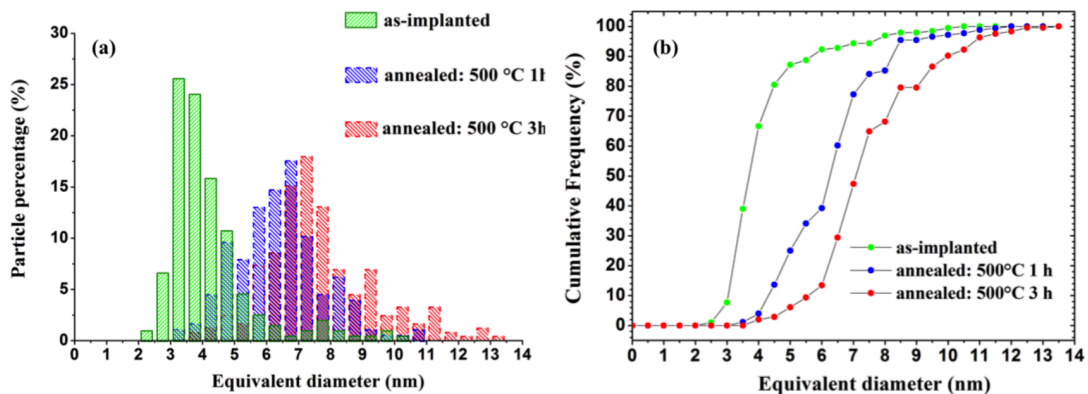


Fig. 3.7 (a) Evolution of size (equivalent diameter) of precipitates: in the as-implanted thin foil, the annealed one at 500 °C and 1 hour and the annealed one at 500 °C and 3 hours; (b) Cumulative frequency as a function of size of precipitates corresponding to (a).

Fig. 3.7 summarizes the evolution of precipitate size during thermal annealing. Comparing to the average precipitate size of the annealed sample in 1 hour, the average precipitate size of the annealed sample in 3 hours still increases slightly. The curves of the cumulative frequency as a function of the equivalent diameter (see Fig. 3.7(b)) tend to shift toward high equivalent diameters, which also confirms the increase of precipitate size due to thermal annealing.

Beside TEM characterization, the precipitate size and number density were also studied by APT analysis. A comparison between results obtained by these two different methods can be found in the section of APT analysis.

3. Chemical compositions of precipitates

The chemical composition of the precipitates has been studied using Energy-Filtered TEM (paragraph 3.1) and using Atom Probe Tomography (paragraphs 3.2 and 3.3) in both as-implanted and annealed samples.

3.1. Chemical composition using EFTEM

Precipitates chemical analyses have been performed using EFTEM imaging in both as-implanted and annealed samples. Before each EFTEM investigations, the foil thicknesses were calculated from EFTEM thickness maps (also known as $\frac{L}{\lambda}$ maps, where L is the local absolute specimen thickness and λ is the inelastic electron mean free path) by using the log-ratio method [Williams, 1996]. The inelastic mean free path was estimated from the equation derived by Malis *et al.* [Malis, 1988]. The EFTEM thickness map is an efficient tool to verify the feasibility of EFTEM analyses. All signal and background setup parameters for EFTEM elemental mapping can be found in the section 1.2.4 of Chapter 2). In addition, the resulting EFTEM elemental maps are superimposed with each other in order to form a false color image (color overlay), which reflects the spatial relationships and distributions of the elements investigated. This image processing method was firstly derived by Hofer *et al.* [Hofer, 1997]. However, the color image is not sufficient for ascribing quantitative information to intensity values, and can only offer qualitative information for the chemical composition.

3.1.1 As-implanted thin foils and FIB lamina

EFTEM analyses were firstly applied to as-implanted TEM thin foils. Four precipitates located in the zone where the thickness of the thin foil is approximately 50 nm ($\frac{L}{\lambda} \sim 0.45$ and $\lambda \sim 110$ nm). The resulting energy-filtered images are shown in Fig. 8(a)-(d). The dark contrasts in the Fe-L_{2,3} elemental map (Fig. 3.8(a)) indicates the local Fe depletion at four positions that, according to EFTEM observation, correspond to precipitated clusters. Contrariwise, the bright contrasts in the Al-K elemental map (Fig. 3.8(c)) and O-K elemental map (Fig. 3.8(d)) show the local Al and O enrichment at the same positions. The contrasts in the Cr-L_{2,3} elemental map are not sufficiently obvious to verify if these positions are locally

enriched or not. This issue may result from the thickness of the zone, which is not thin enough to achieve perfect EFTEM analyses.

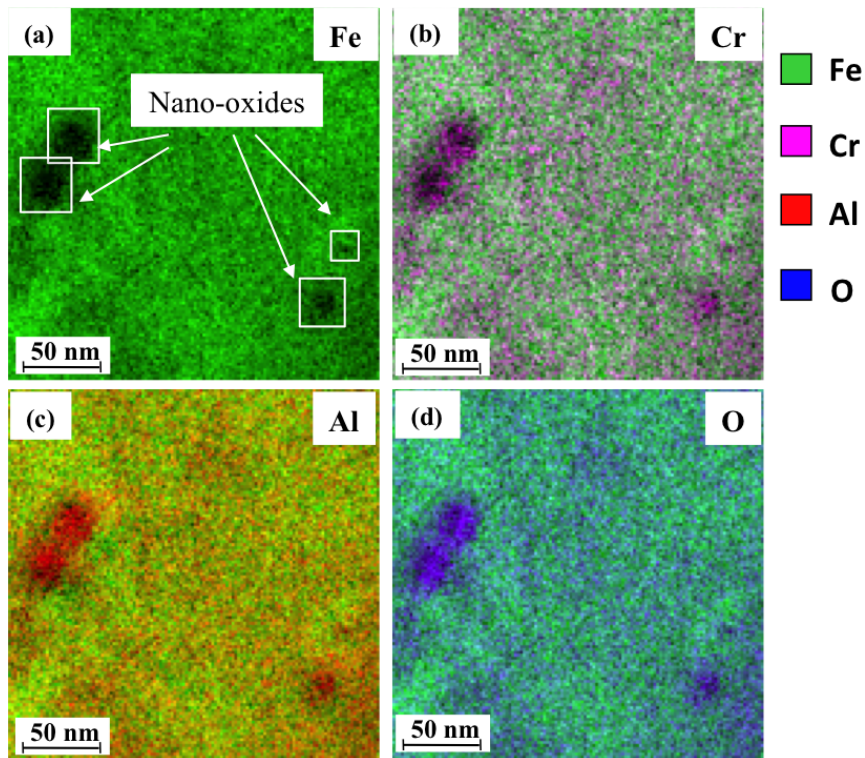


Fig. 3.8 Energy-filtered TEM (EFTEM) characterization of typical precipitates in the as-implanted thin foil: The panels show three-window EFTEM elemental maps of Fe- $L_{2,3}$ edge (a), Cr- $L_{2,3}$ edge (b), Al-K edge (c) and O-K edge (d). The colors indicate the elements as marked in the legend.

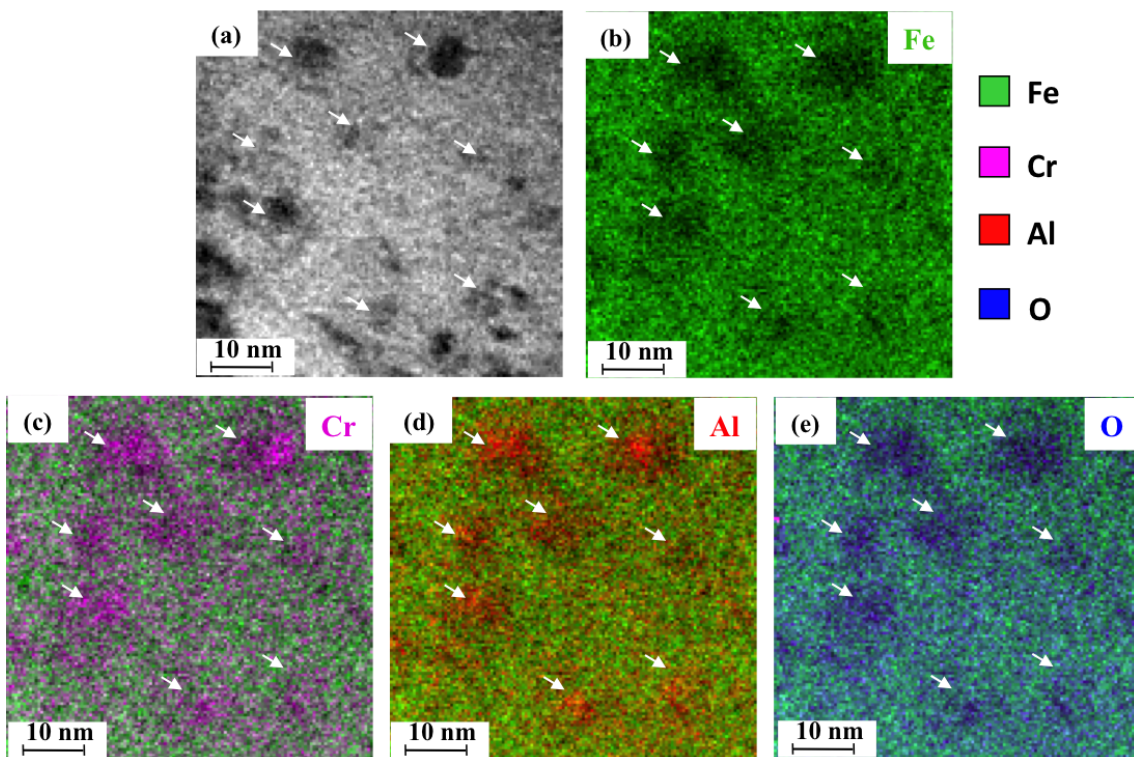


Fig. 3.9 Energy-filtered TEM (EFTEM) characterization of typical precipitates in the as-implanted FIB lamina: (a) Bright Field (BF) TEM image of region of interest for EFTEM characterization. The panels show jump ratio images of Fe- $M_{2,3}$ edge (b), Cr- $M_{2,3}$ edge (c), Al- $L_{2,3}$ edge (d) and three-window EFTEM elemental map of O-K edge (e). The colors indicate the elements as marked in the legend.

Comparing to TEM thin foils, the samples prepared by FIB (also called as FIB lamina) is usually much more thinner. The thickness advantage of the FIB lamina contributes to overcome the previous issue. The thickness of the FIB lamina equals to approximately 25 nm ($\frac{L}{\lambda} \sim 0.22$ and $\lambda \sim 110$ nm) regarding Fig. 3.9-3.10. As a consequence, the FIB lamina is well suitable for EFTEM investigations.

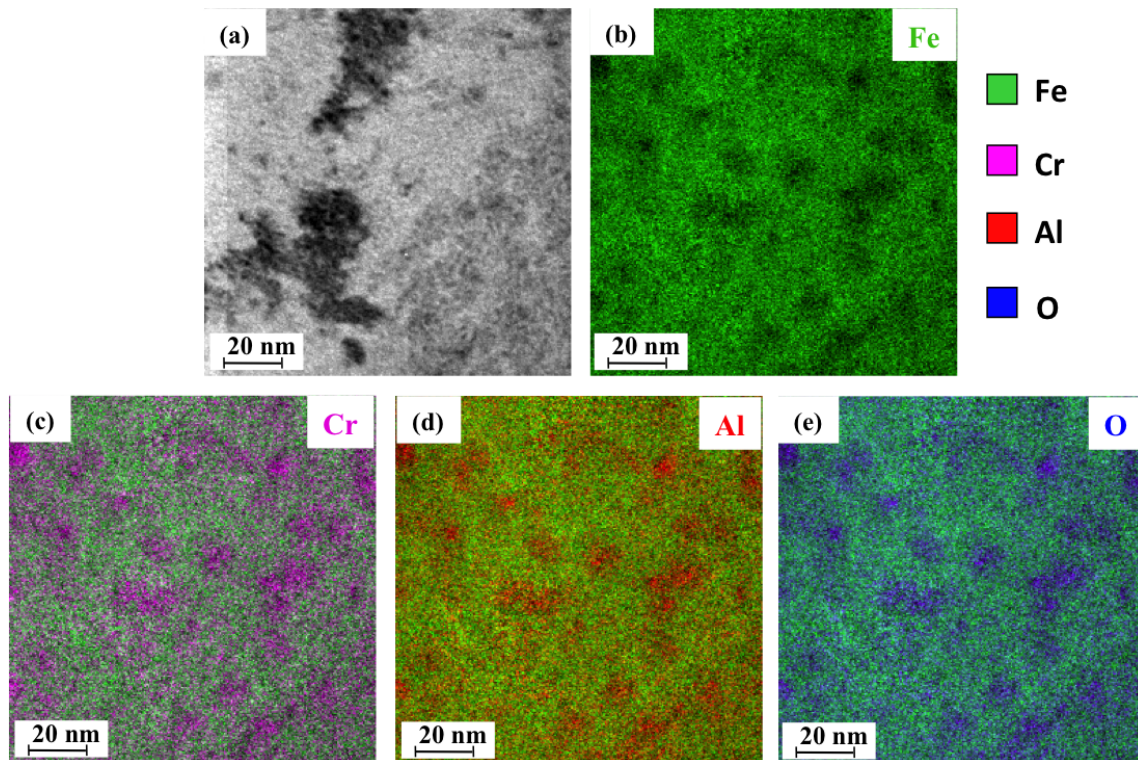


Fig. 3.10 Energy-filtered TEM (EFTEM) characterization of typical precipitates in the as-implanted FIB lamina: (a) Bright Field (BF) TEM image of region of interest for EFTEM characterization. The panels show jump-ratio images of Fe-M_{2,3} edge (b), Cr-M_{2,3} edge (c), Al-L_{2,3} edge (d) and three-window EFTEM elemental map of O-K edge (e). The colors indicate the elements as marked in the legend.

Fig. 3.9(a) is a BF TEM image of the FIB lamina, which shows a typical spatial distribution of precipitates in the matrix. The dark contrasts are supposed to be precipitates and highlighted by the arrows. Fig. 3.9(b) presents a Fe-M_{2,3} elemental map showing the local Fe depletion. The positions of the Fe depletion are consistent with those of the dark contrasts presented on Fig. 3.9(a). This confirms that the location of precipitates is inside the matrix. Fig. 3.9(c)-(e) present respectively the Cr-M_{2,3}, Al-L_{2,3} and O-K elemental maps showing the local Cr, Al and O enrichment. The correlation between the Fe depletion and the (Cr, Al, O) enrichment reveals that the precipitates formed in as-implanted samples are (Al, Cr)-rich oxides, even if their quantitative chemical compositions are not yet possibly determined by EFTEM analyses.

Fig. 3.10(a) shows another BF TEM image, in which precipitates are not clearly visible due to

the presence of defects and the low contrast between the matrix and precipitates. Combining Fe-M_{2,3} elemental map with Cr-M_{2,3}, Al-L_{2,3} and O-K elemental maps, one can see that Fe depletion correlate to the enrichment of Cr, Al and O. This confirms again that the precipitates formed in the as-implanted samples are (Al, Cr)-rich oxides. Moreover, the signal-to-noise ratio of the energy-filtered TEM images is better than that on the BF image and thus allows the detection of precipitates, which are not clearly visible on the BF image. For the precipitates identified in Fig. 3.8-3.10, they have sizes ranging between 3 and 30 nm, although most of them are below 10 nm. The results are consistent with those obtained by the measurement on DF TEM images.

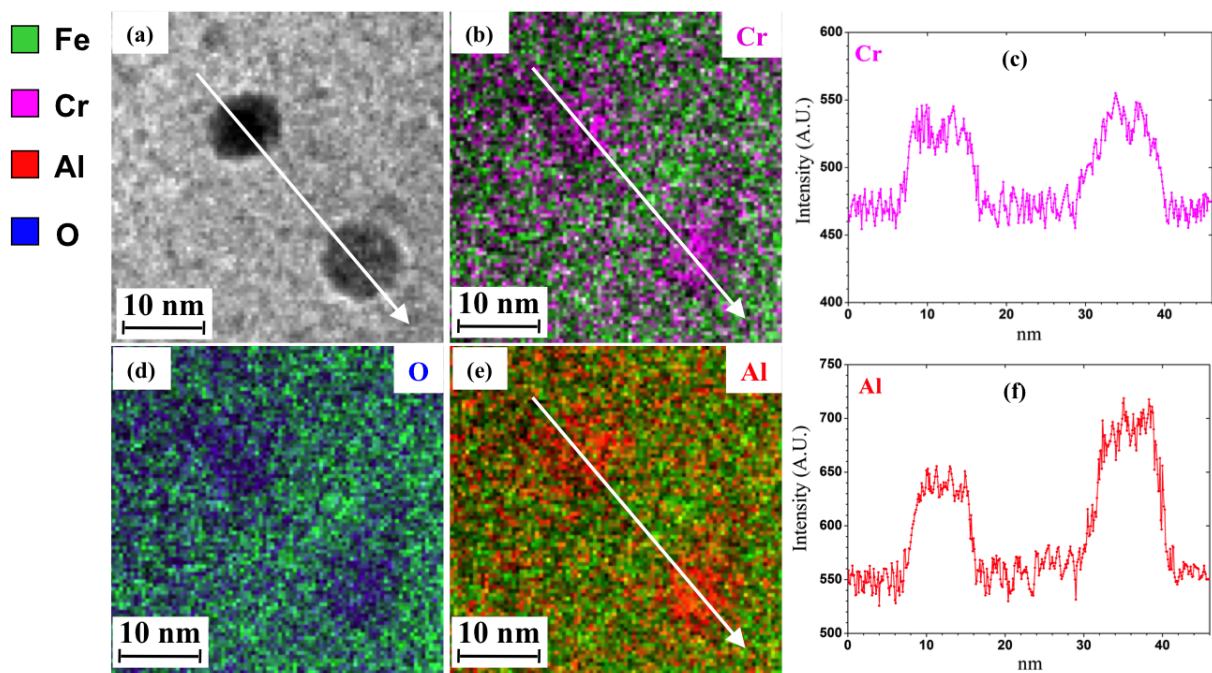


Fig. 3.11 Energy-filtered TEM (EFTEM) series showing (Al, Cr, O) precipitates with homogeneous (not core-shell) structure in the as-implanted FIB lamina. (a) BF image; (b) Cr-M_{2,3} jump-ratio image and (c) Cr intensity profile across the precipitates along the direction of the white arrow; (d) O-K three-window EFTEM elemental map; (e) Al-L_{2,3} jump-ratio image and (f) Al intensity profile across the precipitates along the direction of the white arrow.

Fig. 3.11(a) is a BF TEM image containing two precipitates, of which the shape is clearly visible due to the dark contrasts in the micrograph. The precipitate chemistry was investigated by EFTEM. Elemental maps of Cr, O and Al (Fig. 3.11 (b), (d) and (e)) show the studied precipitates are (Al, Cr)-rich oxides. Cr and Al intensity profiles across two precipitates along the arrow direction are drawn in Fig. 3.11(c) and (e), respectively. The intensity profiles reveal that Cr signal does not extend further than the Al signal. As a consequence, the precipitates prefer a homogeneous structure rather than the core-shell structure. The sizes of precipitates measured from the intensity profiles are approximately 9 and 11 nm, respectively.

3.1.2 Annealed thin foils

As mentioned above, thermal annealing at 500 °C and 3 hours induced the increase of precipitate size. In Fig. 3.12(a), a big size precipitate ($d_{eq} \sim 20$ nm) is marked by the arrow and reflected by the BF micrograph of the annealed thin foil. The EFTEM investigation was applied to this precipitate located in the zone where the thickness of the thin foil was found to be approximately 35 nm ($\frac{L}{\lambda} \sim 0.32$ and $\lambda \sim 110$ nm).

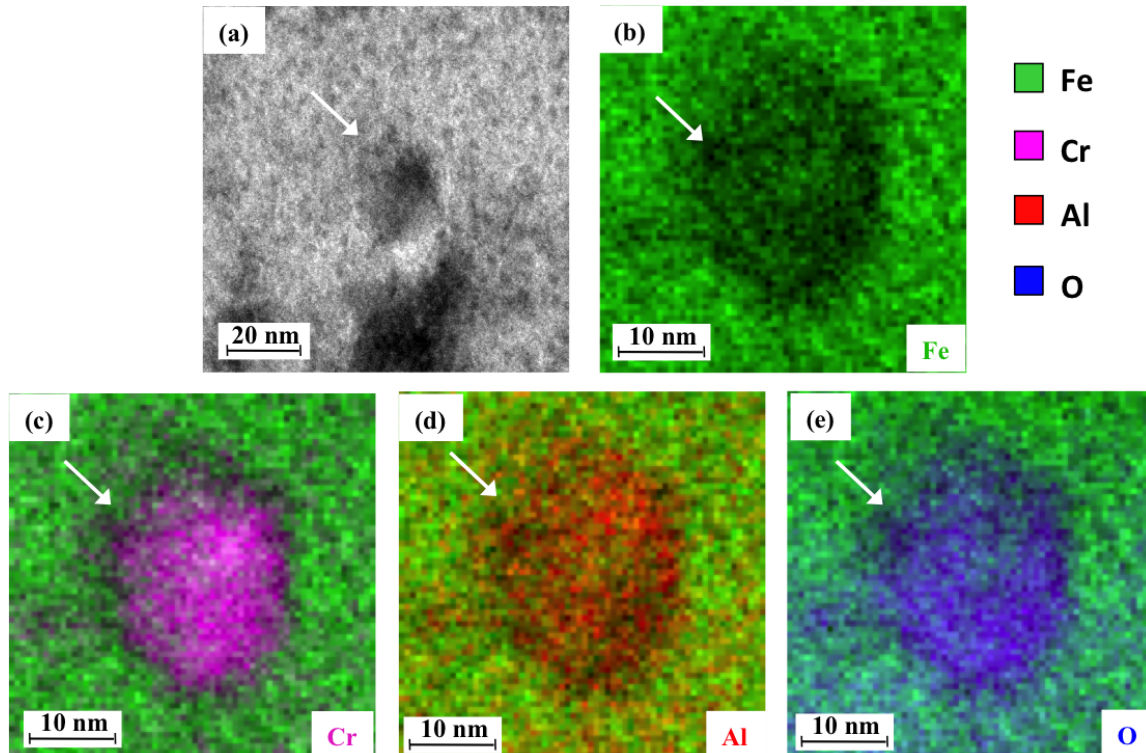


Fig. 3.12 Energy-filtered TEM (EFTEM) characterization of typical precipitates in the annealed thin foil at 500 °C and 3 hours: (a) Bright Field (BF) TEM image of region of interest for EFTEM characterization. The panels show jump-ratio images of Fe- $M_{2,3}$ edge (b), Cr- $M_{2,3}$ edge (c), Al- $L_{2,3}$ edge (d) and three-window EFTEM elemental map of O-K edge (e). The colors indicate the elements as marked in the legend.

The resulting energy-filtered images are presented in Fig. 3.12(b)-(e). The dark contrast on the Fe- $M_{2,3}$ elemental map (Fig. 3.12(b)) show the local Fe deficiency. The Fe elemental map gives a clear view of this precipitate in the matrix. The other three elemental maps (Fig. 3.12(c)-(e)) acquired by the filtering of the Cr- $M_{2,3}$, Al- $L_{2,3}$ and O-K edges exhibit the same pattern of bright contrasts which correspond to the precipitate observed on the BF and Fe elemental map. This suggests that the precipitate has the same Al-Cr-O compositions after thermal annealing at 500 °C and 3 hours.

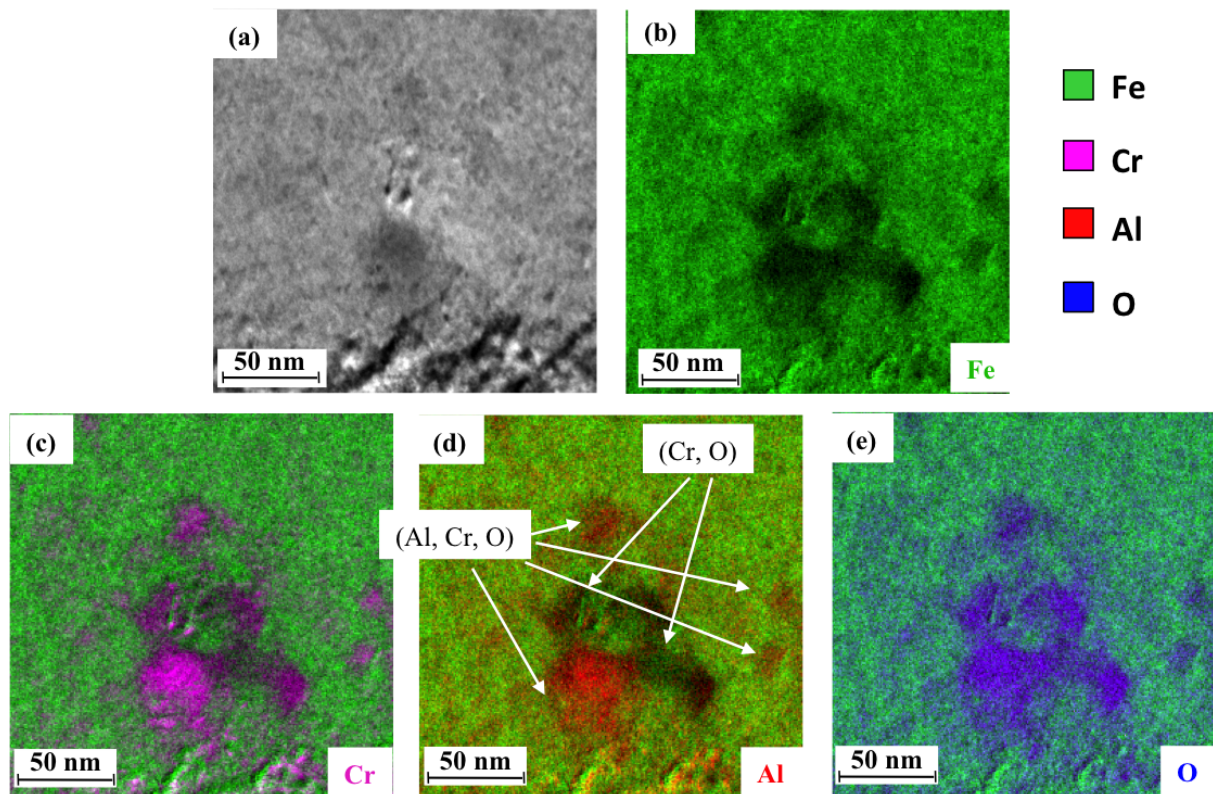


Fig. 3.13 Energy-filtered TEM (EFTEM) characterization of typical precipitates in the annealed thin foil at 500 °C and 3 hours: (a) Bright Field (BF) TEM image of region of interest for EFTEM characterization. The panels show jump-ratio images of Fe- $M_{2,3}$ edge (b), Cr- $M_{2,3}$ edge (c), Al- $L_{2,3}$ edge (d) and three-window EFTEM elemental map of O-K edge (e). The colors indicate the elements as marked in the legend.

The EFTEM investigation was also performed on another region of the annealed thin foil. Similar energy-filtered images are presented in Fig. 3.13(b)-(e). The Fe depletion combining with the Cr and O enrichment are consistent with the previous results of Fig. 3.12. However, two types of oxides instead of one uniform oxide can be distinguished in the Al elemental map (Fig. 3.13(d)): (Al, Cr)-rich oxides and Cr-rich oxides in accordance with the bright and dark contrasts appeared in the Al elemental map. The synthesis of Cr-rich oxides is probably owed to the oxidation.

3.2. APT analyses of as-implanted samples

3.2.1 Compositional measurements

Fig. 3.14 shows 1-D elemental atomic concentration profiles along the z-axis of the reconstructed volume. The APT data used for the 3-D reconstruction was obtained from the as-implanted tip (R30_03984). The mass spectrum of sputtered atoms measured on the as-implanted tip demonstrated numerous peaks corresponding not only to single elements (Fe, Cr, Al and O) but also to small metal-oxygen fragments M_xO_y (with $x = 1$ to 2 and $y = 1$ to 3) as well. Small metal-oxygen fragments M_xO_y were decomposed into two separate elements

during the count of elemental content. The overall elemental content of the studied volume was found to correspond to 86.41 ± 0.03 at.% Fe, 9.77 ± 0.09 at.% Cr, 0.56 ± 0.09 at.% Al and 2.71 ± 0.12 at.% O. The overall content of oxygen atoms in the studied volume corresponds to the amount of oxygen implanted in the volume (2.77 at.%), as estimated using SRIM code. However, the number of aluminum atoms is only 30 % of that implanted (1.91 at.%).

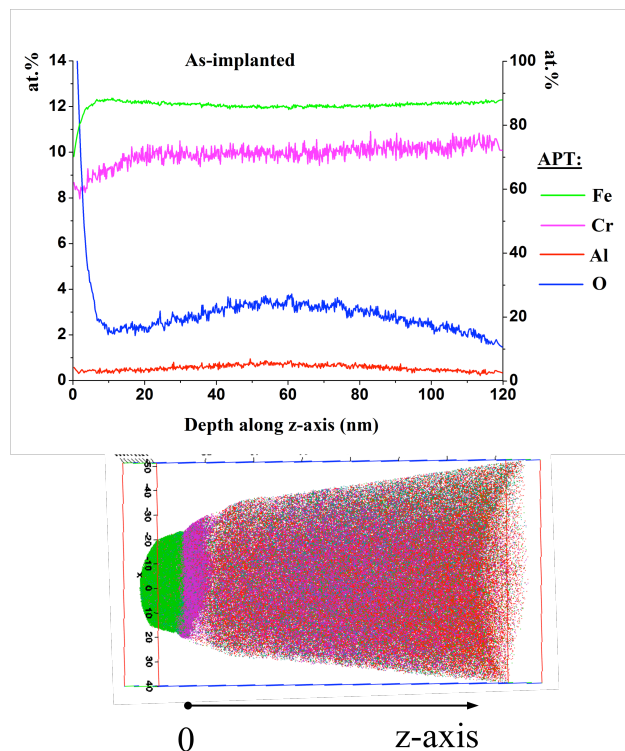


Fig. 3.14 3-D reconstruction of the APT data obtained from the as-implanted tip (R30_03984) and 1-D elemental atomic concentration profiles along the z-axis of the reconstructed volume: The origin of the z-axis for 1-D concentration profiles starts at the interface between the protective layer of Ni and the real matrix of the as-implanted tip. The left y-axis (0-14 at.%) is for profiles of Cr, Al and O, and the right one (0-100 at.%) is only for the profile of Fe.

Significant content of Ni was detected on the top of the as-implanted tip. The presence of Ni in the as-implanted tip arises from the remaining protective layer of Ni after the APT tip preparation. Here, the origin of the z-axis for 1-D concentration profiles starts at the interface between the protective layer of Ni and the real matrix of the as-implanted tip. The profiles of Fe and Cr are almost independent of the depth along z-axis, whereas the profiles of Al and O depend on the depth. In the region near the surface of the tip (0-10 nm), a huge variation of the concentration of O indicates the oxidation occurred at the region near the surface of the as-implanted tip (without considering the protective layer). The maximum concentrations of Al and O in Fig. 3.14 were found to correspond to 0.91 at.% and 3.87 at.% at the depth of 46 nm, respectively. The depth of maximum peaks corresponds well to the profiles of Al and O simulated using SRIM code. However, the maximum concentration values obtained from the concentration profiles are only 26 % and 60 % of that simulated for Al and O, respectively.

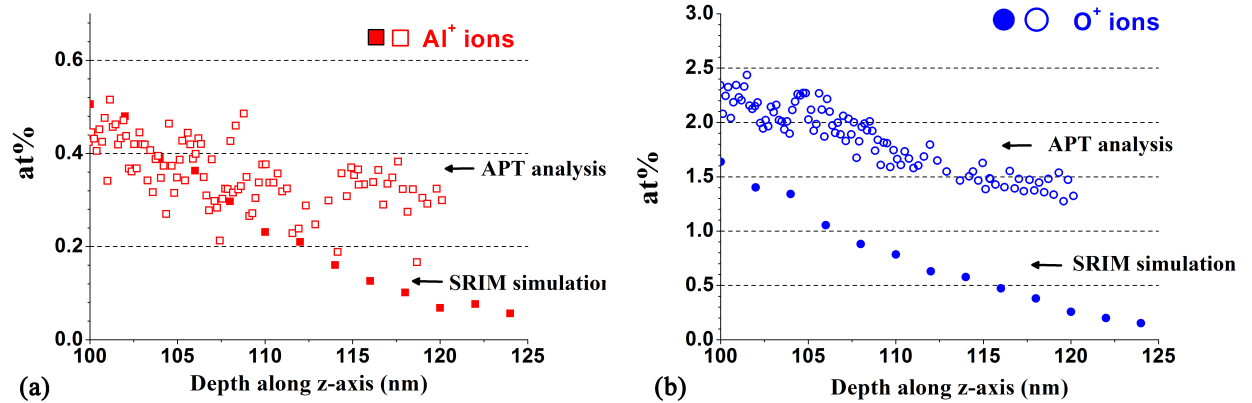


Fig. 3.15 Comparison of 1-D elemental atomic concentration profiles obtained from the APT analysis of the as-implanted tip (R30_03984) and the SRIM simulation: (a) the profiles of Al in the range of 100 to 125 nm; (b) the profiles of O in the range of 100 to 125 nm.

In the region ranged of 100 to 125 nm, the concentration of Al obtained from the APT analysis is slightly larger than the one obtained from the SRIM simulation (see Fig. 3.15(a)). On the contrary, the difference of concentration profiles of O is much more significant (see Fig. 3.15(b)). In total, the concentrations of Al and O obtained from the APT analysis are relatively larger than those obtained from the SRIM simulation in the deeper region. This is the evidence for the high mobility of implanted Al and O ions.

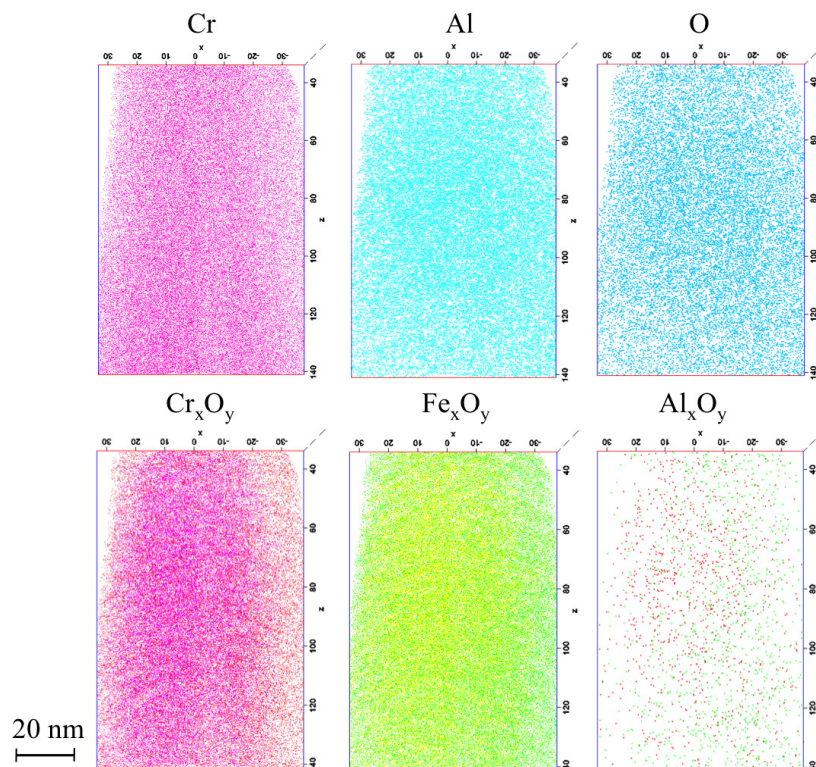


Fig. 3.16 3-D APT reconstruction from the as-implanted tip (R30_03984): the distributions of evaporated elements and molecular ions.

A sub-volume (approximately $40 \times 60 \times 80 \text{ nm}^3$) was selected from the 3-D reconstructed volume shown in Fig. 3.14. The top of sub-volume was chosen to start at 40 nm along the z-axis so that the influence of the oxidation near the surface was eliminated. Fig. 3.16 shows

the distributions of evaporated elemental species (Cr, Al, O) and molecular ions corresponding to oxides (Cr_xO_y , Fe_xO_y , Al_xO_y) in this sub-volume. For elemental species, their distributions are almost homogeneous in the sub-volume, although the cases in Al and O are less homogeneous than that in Cr. For molecular ions, the distributions of chromium oxide and iron oxide are much more intense than that of aluminum oxide. As a consequence, the dispersion of nano-clusters can't derive from the distributions of elemental species and molecular ions.

3.2.2 Cluster analyses

In order to get more information about nano-clusters, the cluster analysis algorithm (as described in the section 4.4 of Chapter 2) was applied to this sub-volume (approximately $40 \times 60 \times 80 \text{ nm}^3$). Both elemental species (Al, O) and molecular species corresponding to aluminum oxide contribution (Al_2O , AlO_2 , AlO and O_2) were selected to define the clusters. These species are called 'core' species. Core species were selected using a maximum separation distance $d_{\text{max}}=1 \text{ nm}$. The value for d_{max} was determined from the nearest-neighbor distribution for all the selected species, which exhibits two distinct peaks, one at small distances for the clusters and one for the dilute matrix with larger average distances between the species. The local minimum between the two peaks was selected as a d_{max} value. Clusters were defined as a group of at least and $N_{\text{min}}=20$ core atoms within d_{max} . In addition, clusters smaller than a critical value of N_{min} were considered as random clusters in the matrix solid solution and were removed from the analysis. The remaining atoms were included in a cluster if they are positioned within a surround distance $L = d_{\text{max}} = 1 \text{ nm}$ of a core atom defining the cluster. The atoms at the interface were then eroded if they are within $d_{\text{erosion}} = 0.5d_{\text{max}} = 0.5 \text{ nm}$ from a matrix atom.

3.2.2.1 Number density, spatial distribution and size distribution of clusters

The obtained three-dimensional atom map of extracted clusters is shown in Fig. 3.17(a)-(b). There were 151 clusters identified in the sub-volume, so the estimated density is $9.45 \times 10^{23} \text{ m}^{-3}$ with using the number density equation described in the section 4.4 of Chapter 2. The number density estimated by APT has a higher order of magnitude with the number density obtained by TEM characterization ($1 \times 10^{22} \text{ m}^{-3}$).

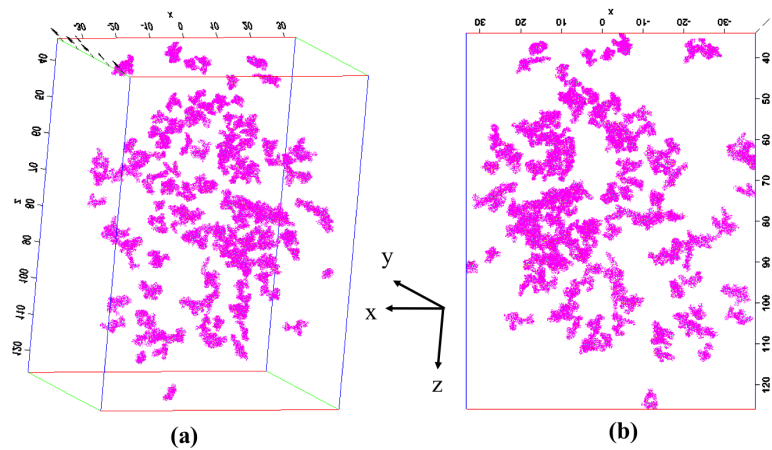


Fig. 3.17 (a) 3-D distribution of zones enriched in Al, O atoms and Al-O molecular ions in the selected sub-volume obtained by the application of cluster processing to the APT data. The depth direction is along the z-axis direction. (b) The projection of the sub-volume along the y-axis direction.

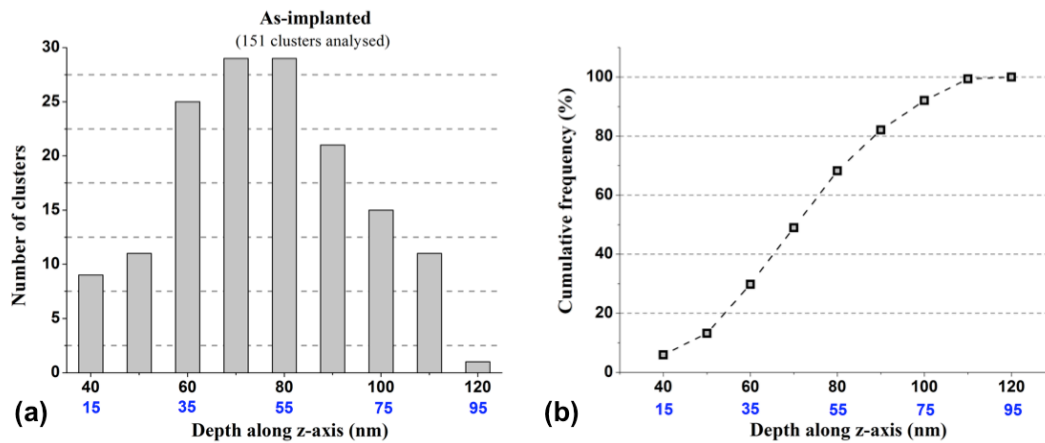


Fig. 3.18 (a) The depth distribution histogram of cluster centre positions with taking the bin width as 10 nm; (b) Cumulative frequency of the depth distribution histogram. The depth direction is along the z-axis. For the depth values written in black color, the origin of the depth is the same as the origin of the depth for the total reconstructed volume. The thickness of the protective layer of Ni was estimated as 25 nm according to the concentration profile of Ni. So the depth values written in blue color were obtained by subtracting the thickness of the layer.

The number of clusters with respect to the depth coordinate of clusters is shown in Fig. 3.18(a), and the cumulative frequency corresponding to Fig. 3.18(a) is shown in Fig. 3.18(b). The bin width of the histogram was set to 10 nm. For the depth values written in black color, the origin of the depth is the same as the origin of the depth for the total reconstructed volume. The thickness of the protective layer of Ni was estimated as 25 nm according to the concentration profile of Ni. So the depth values written in blue color were obtained by subtracting the thickness of the layer. With subtracting the thickness of the protective layer, the depth profile of the cluster number density became to be comparable with 1-D elemental atomic concentration profiles of Al and O. Obviously, The depth distribution of clusters is heterogeneous, and the depth coordinate (between 45-55 nm) corresponding to the maximum peak of the histogram is consistent with the one (~50 nm) corresponding to the profiles of implanted Al and O ions.

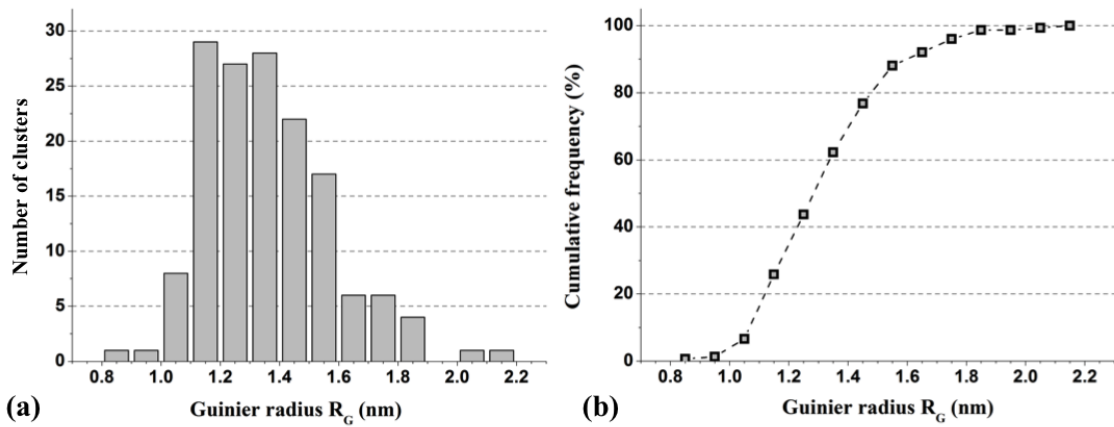


Fig. 3.19 (a) The size distribution histogram of clusters with taking the bin width as 0.1 nm; (b) Cumulative frequency of the size distribution histogram. The Guinier radius R_G was adopted to represent the size of cluster.

An estimation of feature size is made from the Guinier radius R_G , which is related to the radius of gyration R_g by:

$$R_G = \sqrt{\frac{5}{3}} R_g$$

The full description of the Guinier radius and the radius of gyration can be found in the section 4.4 of Chapter 2.

Fig. 3.19 (a) shows the size distribution histogram of clusters as a function of the Guinier radius R_G . The bin width of the histogram was set to 0.1 nm. For 151 clusters, the Guinier radius ranges from 0.8 to 2.2 nm centered on 1.4 nm. Furthermore, the curve of cumulative frequency shown in Fig. 3.19(b) reveals that 81.4% of clusters has the Guinier radius in the range of 1.1 to 1.6 nm.

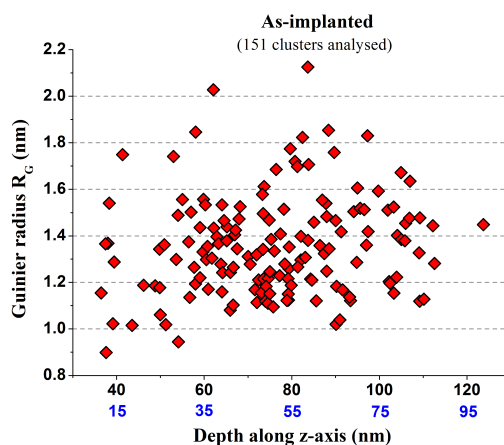


Fig. 3.20 The size distribution of clusters as a function of the depth coordinate of clusters: The Guinier radius R_G described in the section 4.4 of Chapter 2 was adopted to represent the size of cluster. The depth direction is along the z-axis. For the depth values written in black color, the origin of the depth is the same as the origin of the depth for the total reconstructed volume. The depth values written in blue color were obtained by subtracting the thickness of the protective layer of Ni.

The size distribution was also drawn as a function of the depth coordinate of clusters (see Fig. 3.20). In fact, Fig. 3.20 is considered as a combination of Fig. 3.18(a) and Fig. 3.19(a). It reveals that most of clusters are located in the range of 35 to 55 nm with the Guinier radius of 1.1 to 1.6 nm. The distribution of clusters correlate with 1-D elemental atomic concentration profiles of Al and O (maximum peak at 46 nm).

3.2.2.2 Chemical compositions of clusters

Elemental compositions in each of 151 clusters obtained from cluster analysis were drawn in Fig. 3.21. Cross symbols with different colors represent atomic compositions of Fe, Cr, Al and O in the clusters. And elemental compositions in the matrix were represented by colorful lines.

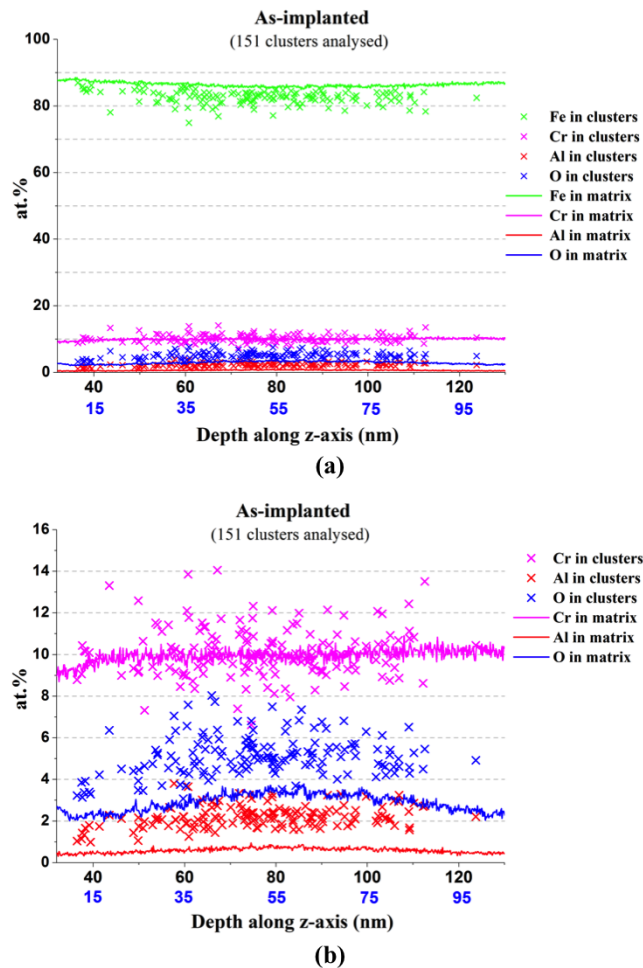


Fig. 3.21 (a) The evolution of elemental contents (including Fe) in the matrix and 151 clusters as a function of the depth coordinate of clusters; (b) The same evolution of elemental contents without Fe. The depth direction is along the z-axis direction. For the depth values written in black color, the origin of the depth is the same as the origin of the depth for the total reconstructed volume. The depth values written in blue color were obtained by subtracting the thickness of the protective layer of Ni.

In Fig. 3.21(a), all cross symbols in green is below the green line, which indicates the content of Fe in the clusters is lower than the one in the matrix. Fig. 3.21(b) gives a better view to

compare the content of Cr, Al and O in the clusters and in the matrix. The contents of Al and O in all the clusters are significantly higher than those in the matrix, whereas only 70% of the clusters have a higher content of Cr than the matrix.

The enrichment of Al, Cr and O combining with the depletion of Fe shown in Fig. 3.21 are consistent with the results obtained by Energy-Filtered TEM in the as-implanted samples. In addition, the evolution of atomic compositions in the clusters seems to be independent of the depth since no significant increase/decrease of elemental contents as a function of the depth coordinate was observed from Fig. 3.21.

The level of Fe measured in the clusters varies from 75% to 87%. While it is possible that clusters contain some Fe, it is thought this high level is mainly the result of trajectory aberrations known to occur with oxide particles (see Chapter 2, paragraph 4.5). Trajectory aberrations arise from precipitates that require different fields for evaporation. The oxide particles have been shown to image darkly during field ion evaporation [Marquis, 2008], so the field required to evaporate the oxide particles is lower than that required for the matrix. These oxide particles are thus referred to as low-field precipitates. The variation in the evaporation field leads to a flattening of the surface in the case of low-field precipitates, resulting in a lower field region that deflect the ion trajectories inwards, which causes an apparent increase in the density of hits [Gault, 2012]. This artifact was also reported in [Williams, 2010], which demonstrated that a reduced local magnification of precipitates in ODS steels compared to the surrounding matrix, leading to trajectory overlaps up to a few nanometers near the particle/matrix interface. Indeed, distortions induced by trajectory aberrations can lead to atoms as part of the matrix being reconstructed within a particle. In order to compare datasets, the amount of Fe was artificially set to zero and the matrix contribution was then corrected by calculating the likely proportion of alloying elements present together with Fe in the matrix, and removing this number of atoms from the raw cluster compositions. The corrected element content x_i^{Corr} is given by:

$$x_i^{Corr} = x_i - \left(\frac{x_{Fe} \cdot X_i'}{X_{Fe}'} \right)$$

where x_i and x_{Fe} are the uncorrected contents in the cluster, respectively; X_i' and X_{Fe}' are the elemental contents in the matrix, respectively. The resulting compositions are quoted as matrix-corrected compositions.

Compositions (at.%) in the matrix as well as uncorrected compositions (at.%) in the clusters are shown in Table 3.1(a-b). The standard deviation (σ) of each content value was calculated based on the equation described in the section 4.4 of Chapter 2.

Element	Fe	Cr	Al	O
at.%	86.78	10.06	0.47	2.69
σ	0.01	0.03	0.03	0.03

Table 3.1 (a) Matrix compositions (at.%) and standard deviation (σ) in the sub-volume of the as-implanted tip (R30_03984).

Element	Fe	Cr	Al	O	Al/Cr	(Al+Cr)/O
at.%	82.64	10.25	2.10	5.01	0.21	2.43
σ	0.11	0.24	0.25	0.25		

(b) Nanocluster uncorrected composition (at.%) and standard deviation (σ) in the sub-volume of the as-implanted tip ((R30_03984).

Element	Fe	Cr	Al	O	Al/Cr	(Al+Cr)/O
at.%	-	22.52	34.5	42.98	1.53	1.20
σ	-	0.35	0.57	0.59		

(c) Nanocluster matrix-corrected composition (at.%) and standard deviation (σ) in the sub-volume of the as-implanted tip (R30_03984).

The overall elemental content in the matrix was found to correspond to 86.78 ± 0.03 at.% Fe, 10.06 ± 0.09 at.% Cr, 0.47 ± 0.09 at.% Al and 2.69 ± 0.09 at.% O, whereas the overall uncorrected content in the 151 clusters was found to correspond to 82.64 ± 0.33 at.% Fe, 10.25 ± 0.72 at.% Cr, 2.10 ± 0.75 at.% Al and 5.01 ± 0.75 at.% O. The concentrations of core elements Al and O are 4.5 and 1.9 times higher compared to that measured from the matrix, respectively. The concentration of Cr in the clusters is slightly higher than that measured from the matrix. These results confirm again that the clusters are rich in Al, Cr and O.

Matrix-corrected compositions and the standard deviation (σ) in the clusters are listed in Table 3.1(c). The overall elemental content in the clusters was found to correspond to 22.52 ± 1.05 at.% Cr, 34.5 ± 1.71 at.% Al and 42.98 ± 1.77 at.% O after the normalization.

The clusters in the as-implanted tip were sorted by ascending order of the Guinier radius in the range of 0.8 to 2.2 nm with the bin width as 0.1 nm. The histograms of uncorrected and matrix-corrected elemental contents in the clusters are shown in Fig. 3.22(a)-(b) as a function of their Guinier radius. In these Fig.s, the cross signs with red color represent the average ratio of Al/Cr in each bin, and the dash line indicates the average ratio of Al/Cr based on all bins. Uncorrected compositions (Fig. 3.22(a)) show the total average ratio of Al/Cr and (Al+Cr)/O are approximately 0.21 and 2.43 in the clusters, respectively. With applying data correction, the ratios have evolved, showing Al/Cr = 1.53 and (Al+Cr)/O = 1.2. The ratio of Al/Cr is size independent before and after applying data correction.

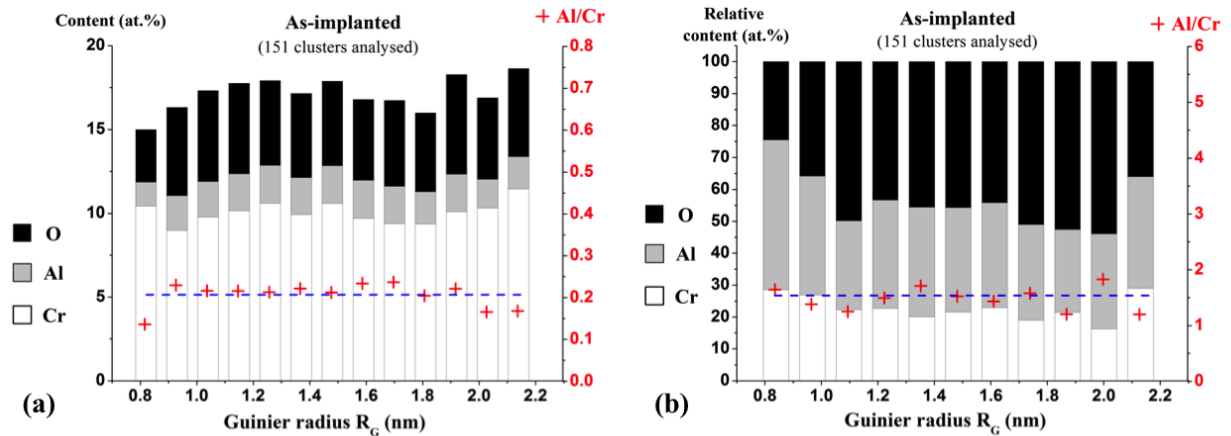


Fig. 3.22 Comparison of the elemental content in 151 clusters (a) before and (b) after applying data correction. Histograms of elemental contents in the clusters were drawn as a function of the Guinier radius with taking the bin width as 0.1 nm. The cross signs with red color represent the average ratio of Al/Cr in each bin. And the dash line with blue color represents the average ratio of Al/Cr based on all bins.

The APT-measured compositions deviates from the expected ratios of known stoichiometric (Al, Cr, O) oxides. Furthermore, the APT measurements show that these particles are still rich in Cr after applying a correction for the trajectory aberrations effect. The clusters are thus more likely to be Al-Cr-rich oxide.

N° of cluster analysis	CA15	CA16	CA17	CA18
$d_{\max}(\text{nm})$	1	1	1	1
L (nm)	0.7	1	1	0.9
N_{\min}	20	30	20	20
d_{erosion} (nm)	0.5	1	0.5	0.6
Cluster count	151	48	151	151

Table 3.2 List of analysis parameters (N_{\min} , L , d_{erosion}) used in each of the cluster analysis test CA15-18. The variation of parameters is highlighted.

The variation of the flexible analysis parameters (L , N_{\min} , d_{erosion}) within reasonable limits has provided additional information about the (Al, O) enriched zones (see Table 3.2). The distance L is used to add the atoms in a cluster if they are positioned within a surround distance L of a core atom defining the cluster. In particular, the decrease of the distance L makes it possible to decrease the cluster surface shell that consists of non-solute atoms. Comparing the cluster analysis CA15 ($L = 0.7 d_{\max}$) and CA17 ($L = d_{\max}$), the resulting decrease of the average Guinier radius (down from 1.4 nm for $L = d_{\max}$ to 1.2 nm for $L = 0.7 d_{\max}$) is accompanied with the increase of the average uncorrected content of Al and O in clusters (up from 2.1 and 5.01 at.% for $L = d_{\max}$ to 11.3 and 9.14 at.% for $L = 0.7 d_{\max}$). On the other hand, the strengthening of restrictions on the cluster identification in the cluster analysis

CA16 ($N_{\min} = 30$ and $d_{\text{erosion}} = d_{\max}$ rather than $N_{\min} = 20$ and $d_{\text{erosion}} = 0.5d_{\max}$ in CA17, respectively) results in the decrease of the cluster number density down to $\sim 3 \times 10^{23} \text{ m}^{-3}$ and the average Guinier radius down to ~ 1.2 nm. The relative contents of Al and O in the identified clusters increase up to 17.46 and 16.69 at.%, respectively, mostly at the expense of iron, whose relative part falls down to 58.11 at.%. The Cr content in the clusters also decreases, but much less pronounced (down to 7.75 at.%). As can be seen, the adjustment of cluster analysis parameters changes the nature (size, density, compositions...) of identified clusters in the sub-volume.

In conclusion, the APT analysis suggests that the clusters found in the as-implanted tip are more likely to be Al-Cr-rich oxides. Furthermore, the size of these clusters is too small (the Guinier radius ranges from 0.8 to 2.2 nm centered on 1.4 nm) to be observed easily by TEM techniques. Nonetheless, the results about chemical compositions of the nano-clusters obtained by APT are consistent with those obtained by Energy-filtered TEM.

3.3. APT analyses of annealed samples

3.3.1 Compositional measurements

Thermal annealing was carried out inside the TEM microscope at 500 °C with 3 hours. Then the annealed APT tips were produced by the *in-situ* lift-out techniques as described in Annexe A.

Fig. 3.23(a) shows the 3-D reconstruction of the APT data obtained from the annealed tip (R30_03984). The mass spectrum of sputtered atoms measured on the annealed tip demonstrated numerous peaks corresponding not only to single elements (Fe, Cr, Al and O) but also to small metal-oxygen fragments M_xO_y (FeO, Fe₂O, CrO, CrO₂, AlO, AlO₂) as well. The metal-oxygen fragments M_xO_y appearing on the top region close to the surface of the tip (Fig. 3.23(a)) arise from the oxidation in this region.

The profile of O in the range of 0 to 100 nm as shown in Fig. 3.23(b) confirmed also that the oxidation occurred. The overall elemental content of the studied volume was found to correspond to 87.41 ± 0.06 at.% Fe, 10.37 ± 0.09 at.% Cr, 0.59 ± 0.06 at.% Al and 1.49 ± 0.09 at.% O. The overall contents of Al and O are only 31% and 54% of that implanted, as estimated using SRIM code, respectively. No significant content of Ni was detected on the top of the annealed tip, which indicates the protective layer of Ni had been eliminated during the APT tip preparation. Therefore, the origin of the profiles obtained by the APT analysis starts directly at the surface of the annealed tip.

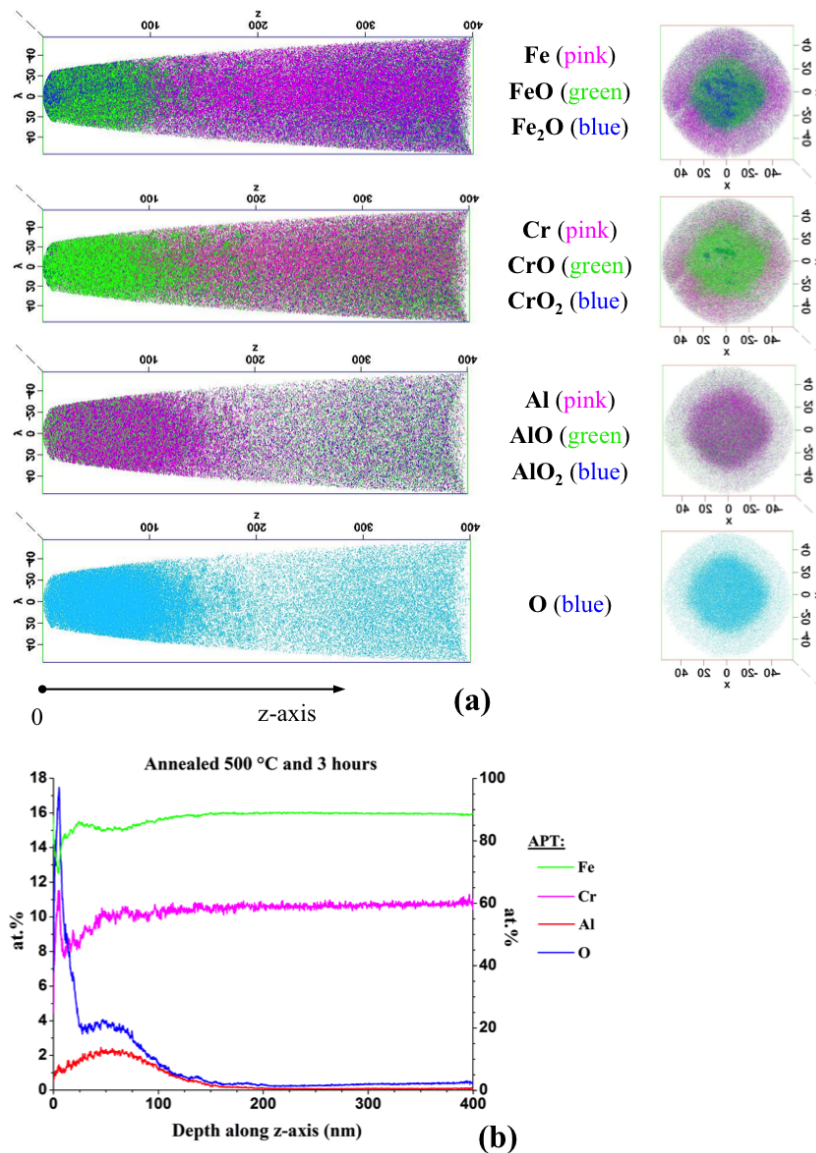


Fig. 3.23 (a) 3-D reconstruction of the APT data obtained from the annealed tip (R30_05514): the reconstructed volume is described by single elements (Fe, Cr, Al, O) and associated metal-oxygen fragments M_xO_y (FeO, Fe₂O, CrO, CrO₂, AlO, AlO₂); (b) 1-D elemental atomic concentration profiles along the z-axis of the reconstructed volume: The origin of the z-axis corresponds to the annealed sample surface. The left y-axis (0-18 at.%) is for profiles of Cr, Al and O, and the right one (0-100 at.%) is only for the profile of Fe.

The comparison between 1-D concentration profiles of Al and O obtained by the APT analysis and those estimated using SRIM code is shown in Fig. 3.24. The real profiles are obviously broader than that estimated using SRIM code. The depth corresponding to the maximum contents of Al and O is the same for both real and simulated profiles. However, the maximum values of the real profiles are lower than that of the simulated profiles.

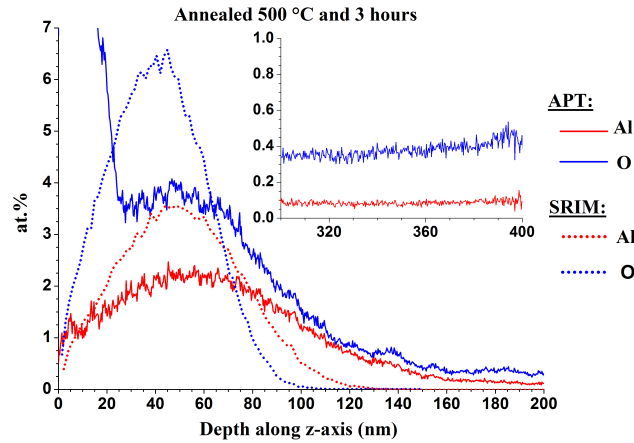


Fig. 3.24 Comparison of 1-D elemental atomic concentration profiles obtained by the APT analysis of the annealed tip (R30_05514) and the SRIM simulation of projected ions. The inset shows the profiles of Al and O in the range of 300 to 400 nm

According to the SRIM simulation, the contents of Al and O become to be negligible if the depth is more than 150 nm. On the contrary, the real contents of Al and O are still ~ 0.08 and 0.35 at.% in the range of 300 to 400 nm, respectively. The broader profiles of Al and O with low concentration peaks indicate that thermal annealing may enhance the diffusion of implanted Al and O atoms, which induced the implanted atoms to be diffused to much deeper region.

at.%	R30_05508 (z = 50-55 nm)	R30_05509 (z = 50-55 nm)	R30_05511 (z = 50-55 nm)	R30_05514 (z = 40-46 nm)
Al	2.26	2.26	2.31	2.47
O	4.02	3.89	4.02	4.08
Fe	83.19	83.47	83.29	83.3
Cr	10.14	10.08	10.07	10.1

Table 3.3 Maximum compositions (at.%) and corresponding depths in four different annealed APT tips.

The maximum concentrations of Al and O obtained in different annealed APT tips by the APT analysis are listed in Table 3.3. The maximum concentrations in four different annealed APT tips were found to be similar: ~ 2.3 at.% for Al and 4 at.% for O. In addition, the depth where concentrations reach maximum values corresponds well to the depth obtained by the SRIM simulation.

A sub-volume (approximately $40 \times 40 \times 140 \text{ nm}^3$) was selected from the whole reconstructed volume of the annealed tip (R30_05514). The range of the z-axis for the sub-volume is between 90 and 230 nm. Therefore, the large metallic oxide fragments near the surface of the tip were excluded.

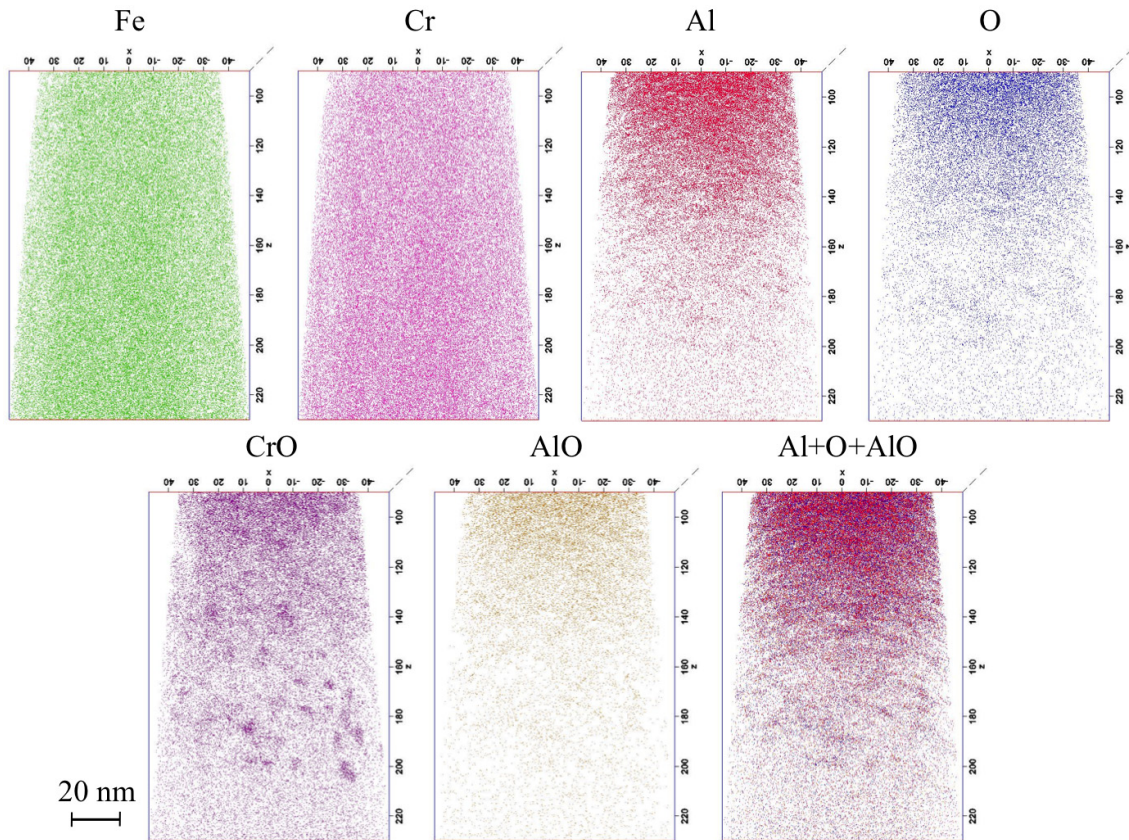


Fig. 3.25 3-D APT reconstruction from the annealed tip (R30_05514): the distributions of evaporated elements and molecular ions.

Fig. 3.25 shows the distributions of evaporated elemental species (Fe, Cr, Al, O) and molecular ions corresponding to oxides (CrO, AlO) in this sub-volume. The distributions of Fe and Cr in the sub-volume of the annealed tip are similar to the cases observed in the as-implanted tip, which are almost homogeneous. In contrast, the distributions of Al and O are evidently heterogeneous at this time. For molecular ions, the distributions of CrO and AlO are heterogeneous too. Precipitates can be observed clearly in the distribution of CrO as well as Al+O+AlO.

3.3.2 Cluster analysis

The cluster analysis algorithm was applied to the sub-volume (approximately $40 \times 40 \times 110 \text{ nm}^3$). Both elemental species (Al, O) and molecular species corresponding to aluminum oxide contribution (Al_2O , AlO and O_2) were selected to define the clusters. These species are called ‘core’ species. Core species were selected using a maximum separation distance $d_{\text{max}} = 1.25 \text{ nm}$. The value for d_{max} was determined from the nearest-neighbor distribution for all the selected species, which exhibits two distinct peaks, one at small distances for the clusters and one for the dilute matrix with larger average distances between the species. The local minimum between the two peaks was selected as a d_{max} value. Clusters were defined as a group of at least and $N_{\text{min}} = 30$ core atoms within d_{max} . In addition, clusters

smaller than a critical value of N_{\min} were considered as random clusters in the matrix solid solution and were removed from the analysis. The remaining atoms were included in a cluster if they are positioned within a surround distance $L = d_{\max} = 1.25$ nm of a core atom defining the cluster. The atoms at the interface were then eroded if they are within $d_{\text{erosion}} = 1$ nm from a matrix atom.

3.3.2.1 Number density, spatial distribution and size distribution of clusters

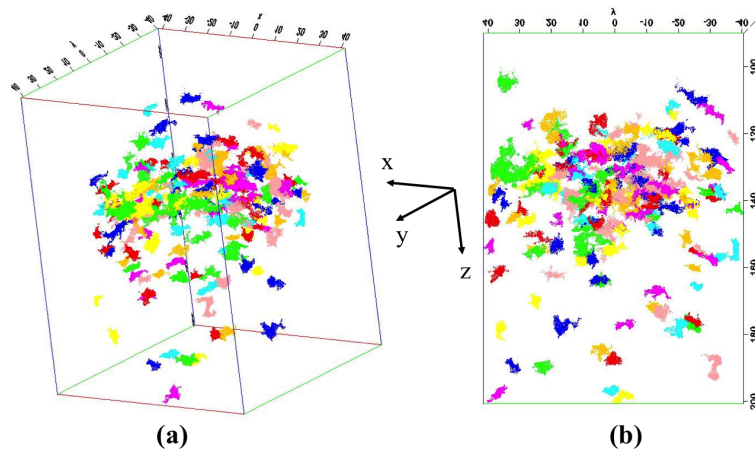


Fig. 3.26 (a) 3-D distribution of zones enriched in Al, O atoms and Al-O molecular ions in the selected sub-volume obtained by the application of cluster processing to the APT data. The depth direction is along the z-axis direction. (b) The projection of the sub-volume along the x-axis direction.

The obtained three-dimensional atom map of extracted clusters is shown in Fig. 3.26(a)-(b). 165 clusters were identified in the sub-volume, and the estimated density is $4.85 \times 10^{23} \text{ m}^{-3}$.

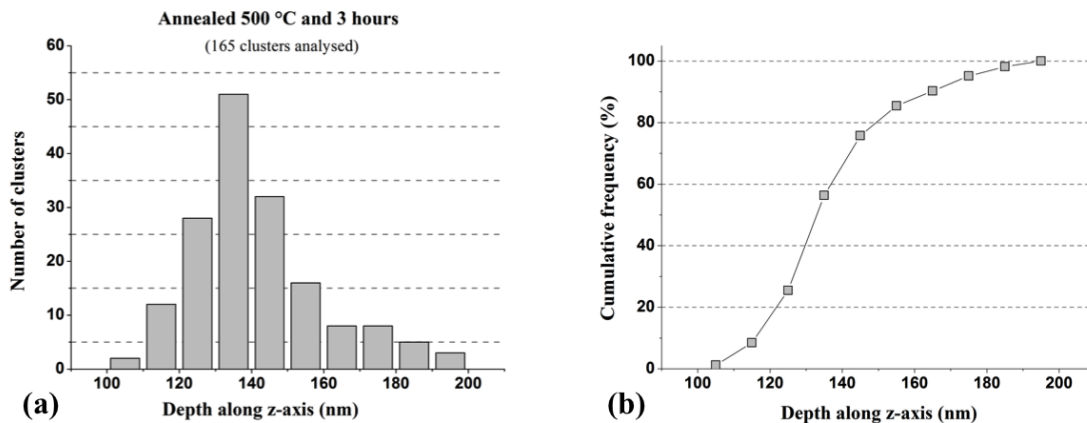


Fig. 3.27 (a) The depth distribution histogram of cluster centre positions with taking the bin width as 10 nm; (b) Cumulative frequency of the depth distribution histogram. The depth direction is along the z-axis.

The number of clusters with respect to the depth coordinate of clusters is shown in Fig. 3.27(a), and the cumulative frequency is shown in Fig. 3.27(b). The bin width of the histogram was set to 10 nm. The depth distribution of clusters is heterogeneous, and the number of clusters is much more intense at the depth of 130 nm.

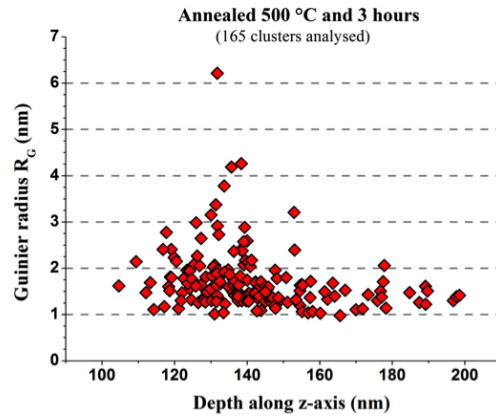


Fig. 3.28 The size distribution of clusters as a function of the depth coordinate of clusters: The Guinier radius R_G described in the section V.4 of Chapter II was adopted to represent the size of cluster.

An estimation of feature size is made from the Guinier radius R_G , which is related to the radius of gyration R_g by:

$$R_G = \sqrt{\frac{5}{3}} R_g$$

The size distribution was drawn as a function of the depth coordinate of clusters (see Fig. 3.28). It reveals that most of clusters are located in the depth between 110 and 180 nm, and the Guinier radius of these clusters ranges from 0.9 to 3 nm. In particular, we found that there is one cluster that is extremely bigger than others.

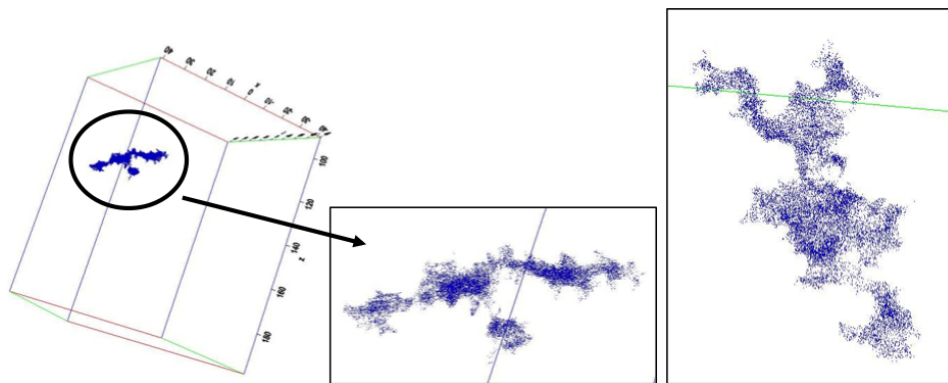


Fig. 3.29 Cluster n° 40: the biggest one in 165 clusters with the Guinier radius of 6.2 nm.

The cluster is illustrated in Fig. 3.29, and the its Guinier radius is ~ 6.2 nm. Such an unusual cluster is possibly the consequence of the agglomeration of several small clusters that are quite close to each other. Although the parameters are optimized for the cluster analysis algorithm, it is still difficult to distinguish them. So these small clusters are considered as a big cluster. Since the uncertainty of this cluster, such big cluster will not be considered for latter discussion.

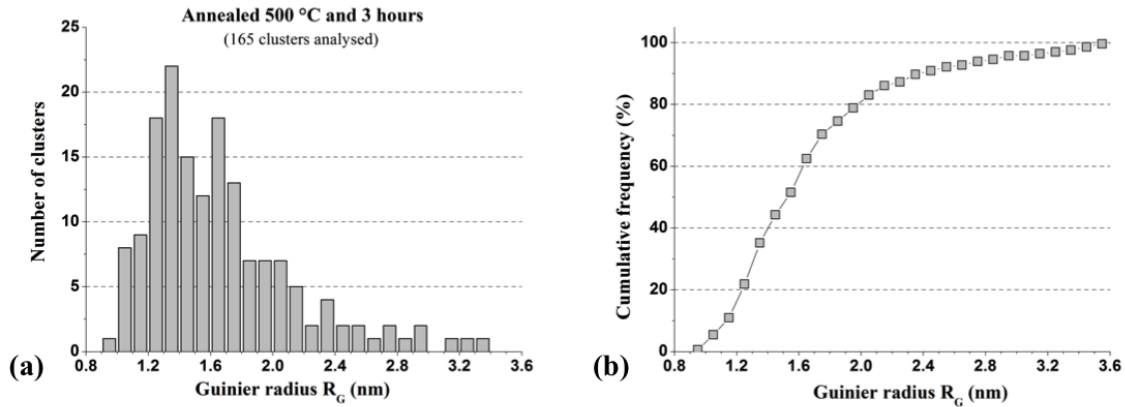


Fig. 3.30 (a) The size distribution histogram of clusters with taking the bin width as 0.1 nm; (b) Cumulative frequency of the size distribution histogram. The Guinier radius R_G was adopted to represent the size of cluster.

Fig. 3.30(a) shows the size distribution histogram of clusters as a function of the Guinier radius R_G . The bin width of the histogram was set to 0.1 nm. For 165 clusters, the Guinier radius varies ranges from 0.8 to 3.6 nm, centered on 1.7 nm. Furthermore, the curve of cumulative frequency shown in Fig. 3.30(b) reveals that 90% of clusters has the Guinier radius in the range of 1 to 3 nm.

The precipitate size and the number density of the clusters obtained by TEM characterizations and APT analyses are summarized in Table 3.4. The Guinier radius obtained by APT analyses are multiplied by two in order to compare with the equivalent diameters obtained by TEM characterizations.

	As-implanted		Annealed 500°C 3 hours	
	by TEM	by APT	by TEM	by APT
Size ranges (nm)	2-10.5	1.6-4.4	3.5-14	1.6-7.2
Centered on (nm)	4.3	2.8	7.7	3.4
Number density (m^{-3})	$(1 \pm 0.3) \times 10^{22}$	$(9.5 \pm 2) \times 10^{23}$	$(7 \pm 2) \times 10^{21}$	$(5.9 \pm 1) \times 10^{23}$

Table 3.4 The size in diameter (nm) and the number density of clusters in as-implanted and annealed samples measured by the TEM characterization and the APT analysis.

The average size measured by TEM is bigger than that measured by APT for both as-implanted and annealed samples. It is may due to a worse resolution of dark field (DF) TEM imaging comparing to APT cluster analysis, which makes it difficult to count really small particles in DF TEM micrographs. However, this case is not true for the number density. In fact, the average size increases, whereas the number density decreases before and

after thermal annealing. These results indicate that clusters tend to coarsen due to thermal annealing.

3.3.2.2 Chemical compositions of clusters

Elemental compositions in each of 165 clusters obtained from cluster analysis were drawn in Fig. 3.31. Cross symbols with different colors represent atomic compositions of Fe, Cr, Al and O in the clusters. Elemental compositions in the matrix were represented by colorful lines. In Fig. 3.31(a), all cross symbols in green is below the green line, which reveals the content of Fe in the clusters is lower than that in the matrix. Fig. 3.31(b) gives a better view to compare the content of Cr, Al and O in the clusters and in the matrix.

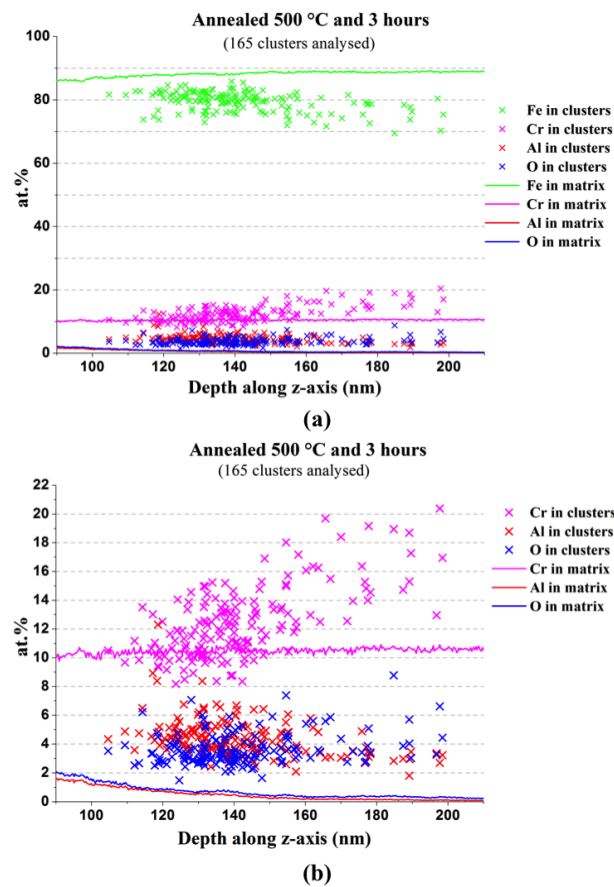


Fig. 3.31 (a) The evolution of elemental contents (including Fe) in the matrix and 151 clusters as a function of the depth coordinate of clusters; (b) The same evolution of elemental contents without Fe. The depth direction is along the z-axis direction. For the depth values written in black color, the origin of the depth corresponds to the surface of the protective layer of Ni. The depth values written in blue color were obtained by subtracting the thickness of the protective layer.

The contents of Al and O in all the clusters are significantly higher than those in the matrix. However, this is not the case for Cr content in the clusters. Only 90% of the clusters have a higher content of Cr than the matrix. The Cr content in the clusters seems to be dependent on the depth. The Cr content increases as a function of the depth. Finally, the Cr content can attain 20 at.% at the depth of 200 nm. In total, the results obtained from Fig. 3.31 reveal the

clusters are still rich in Al, Cr and O after thermal annealing. These results are consistent with the results obtained by Energy-Filtered TEM in annealed thin foils.

The level of Fe measured in the clusters varies from 70% to 87%. As we described in the section 3.2.2.2, a large portion of matrix elements observed in the oxide clusters can be attributed to trajectory aberrations associated with low evaporation field particles embedded in a higher-field matrix. Distortions induced by trajectory aberrations can lead to atoms as part of the matrix being reconstructed within a particle. In this work the exact quantity of Fe in the clusters was not addressed, the amount of Fe was artificially set to zero and used to subtract the other alloying elements introduced by trajectory aberrations. The corrected element content x_i^{Corr} is given by:

$$x_i^{Corr} = x_i - \left(\frac{x_{Fe} \cdot X_i'}{X_{Fe}'} \right)$$

where x_i and x_{Fe} are the uncorrected contents in the cluster, respectively; X_i' and X_{Fe}' are the elemental contents in the matrix, respectively.

Element	Fe	Cr	Al	O
at.%	88.94	10.51	0.17	0.38
σ	0.01	0.03	0.02	0.02

Table 3.5 (a) Matrix composition (at.%) and standard deviation (σ) in the sub-volume of the annealed sample (R30_05514-v03).

Element	Fe	Cr	Al	O	Al/Cr	(Al+Cr)/O
at.%	80.15	12.44	3.98	3.43		
σ	0.09	0.19	0.20	0.20	0.32	4.79

(b) Nanocluster uncorrected composition (at.%) and standard deviation (σ) in the sub-volume of the annealed sample (R30_05514-v03).

Element	Fe	Cr	Al	O	Al/Cr	(Al+Cr)/O
at.%	-	28.00	41.06	30.93		
σ	-	0.30	0.32	0.31	1.47	2.23

(c) Nanocluster matrix-corrected composition (at.%) and standard deviation (σ) in the sub-volume of the annealed sample (R30_05514-v03).

Compositions (at.%) in the matrix as well as uncorrected compositions (at.%) in the clusters are shown in Table 3.5(a-b). The stand deviation (σ) of each content value was calculated based on the equation described in the section 4.4 of Chapter 2. The overall elemental content in the matrix was found to correspond to 88.94 ± 0.03 at.% Fe, 10.51 ± 0.09 at.% Cr, 0.17 ± 0.06 at.% Al and 0.38 ± 0.06 at.% O, whereas the overall uncorrected content in the 165 clusters was found to correspond to 80.15 ± 0.27 at.% Fe, 12.44 ± 0.57 at.% Cr, 3.98 ± 0.6 at.% Al and 3.43 ± 0.6 at.% O. The concentrations of core elements Al and O are 23.5 and 9 times higher compared to that measured from the matrix, respectively. The

concentration of Cr in the clusters is 20% higher than that measured from the matrix. These results confirm that the clusters are rich in Al, Cr and O.

The clusters in the as-implanted tip were sorted by ascending order of the Guinier radius in the range of 0.8 to 2.2 nm with the bin width as 0.1 nm. For the same reason, the clusters in the annealed tip were sorted by ascending order of the Guinier radius in the range of 0.8 to 3.3 nm with the bin width as 0.1 nm.

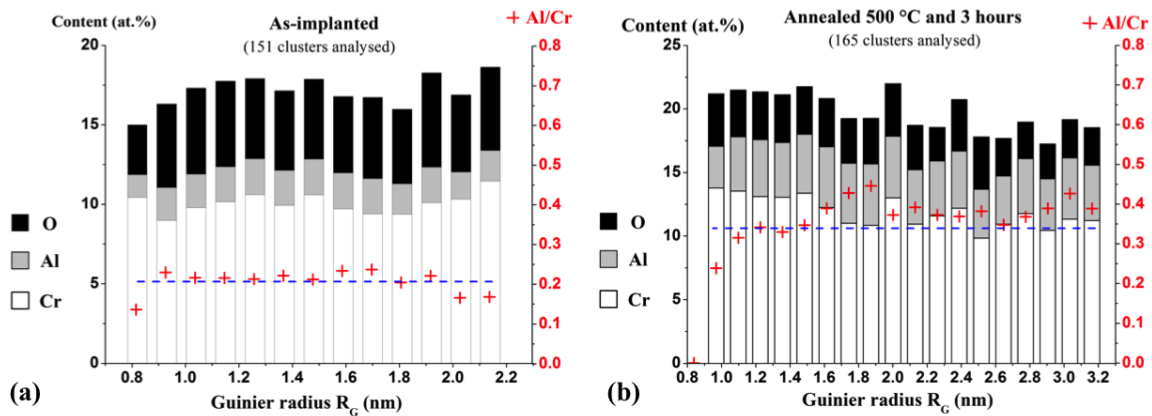


Fig. 3.32 Comparison of the uncorrected elemental contents in the clusters of the as-implanted tip (a) and the annealed tip (b). Histograms of elemental contents in the clusters were drawn as a function of the Guinier radius with taking the bin width as 0.1 nm. The cross signs with red color represent the average ratio of Al/Cr in each bin. And the dash line with blue color represents the average ratio of Al/Cr based on all bins.

The histograms of uncorrected elemental contents of the clusters in the as-implanted tip and the annealed tip are shown in Fig. 3.32 as a function of the Guinier radius. In both two histograms, the cross signs with red color represent the average ratio of Al/Cr in each bin, and the dash line indicates the average ratio of Al/Cr based on all bins. Fig. 3.32 compares the uncorrected Al/Cr and (Al+Cr)/Cr ratios before and after thermal annealing. The Al/Cr ratio is roughly size independent before and after thermal annealing. But the values of Al/Cr and (Al+Cr)/O ratios increase from 0.21 and 2.43 to 0.32 and 4.79, respectively.

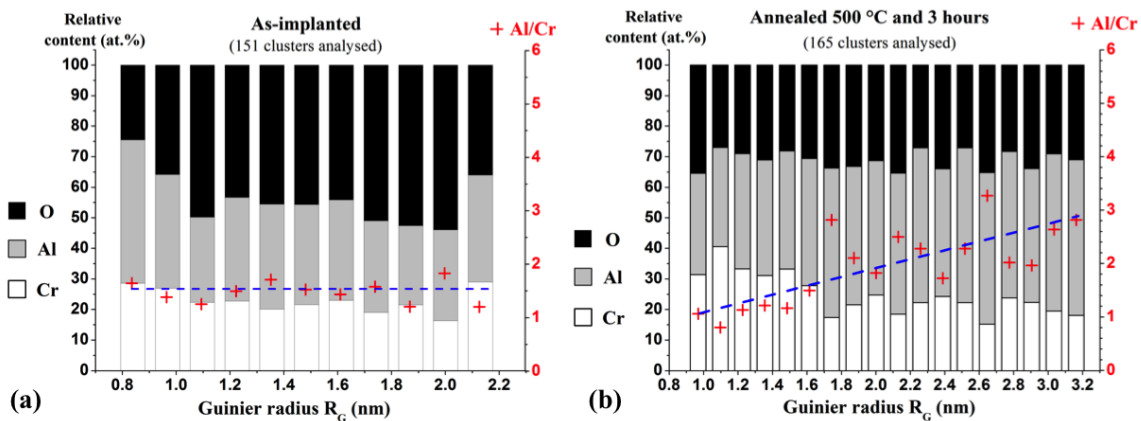


Fig. 3.33 Comparison of the matrix-corrected elemental contents in the clusters of the as-implanted tip (a) and the annealed tip (b). Histograms of elemental contents in the clusters were drawn as a function of the Guinier radius with taking the bin width as 0.1 nm. The cross signs with red color represent the average

ratio of Al/Cr in each bin. And the dash line with blue color represents the average ratio of Al/Cr based on all bins.

The histograms of matrix-corrected elemental contents of the clusters in the as-implanted tip and the annealed tip are shown in Fig. 3.33(a)-(b) as a function of the Guinier radius. Fig. 3.33 also compares the Al/Cr ratio before and after thermal annealing as a function of the cluster size. Prior to thermal annealing (Fig. 3.33(a)), the ratio of Al/Cr is size independent, showing the average ratio ~ 1.53 . While after thermal annealing (Fig. 3.33(b)), the larger the clusters, the higher the ratio of Al/Cr. The ratio of Al/Cr varies between 0.8 and 3.27. But the total average ratio of Al/Cr is ~ 1.47 , which is even slightly lower than the one obtained from the as-implanted tip. This unusual low value of Al/Cr is because the smaller clusters are predominant in the population of the clusters. The ratio of Al/Cr becomes to be size dependent after thermal annealing, suggesting that the large clusters have gathered preferentially Al with respect to Cr.

In conclusion, as suggested by comparing Fig. 3.19 and Fig. 3.30, the clusters tend to grow under thermal annealing. Further, a decrease in the number density is measured and summarized in Table 3.4. With comparing Fig. 3.33 (a)-(b), the clusters are still Al-Cr-rich oxides after thermal annealing. The ratio of Al/Cr is size independent prior to thermal annealing, whereas it becomes to be size dependent after thermal annealing. The larger the clusters, the higher the ratio, suggesting that the large clusters have gathered preferentially Al with respect to Cr.

4. Crystallographic structure of precipitates

4.1. Measurements of SAED and HRTEM obtained in as-implanted samples

Fig. 3.34(a) shows a bright field image on a region of the as-implanted thin foil. Precipitates are hard to see directly in Fig. 3.34(a) due to the presence of the low contrast difference between the matrix and the particles. Fig. 3.34(b) is the SAED pattern along the $\langle 111 \rangle$ zone axis of FeCr matrix corresponding to Fig. 3.34(a).

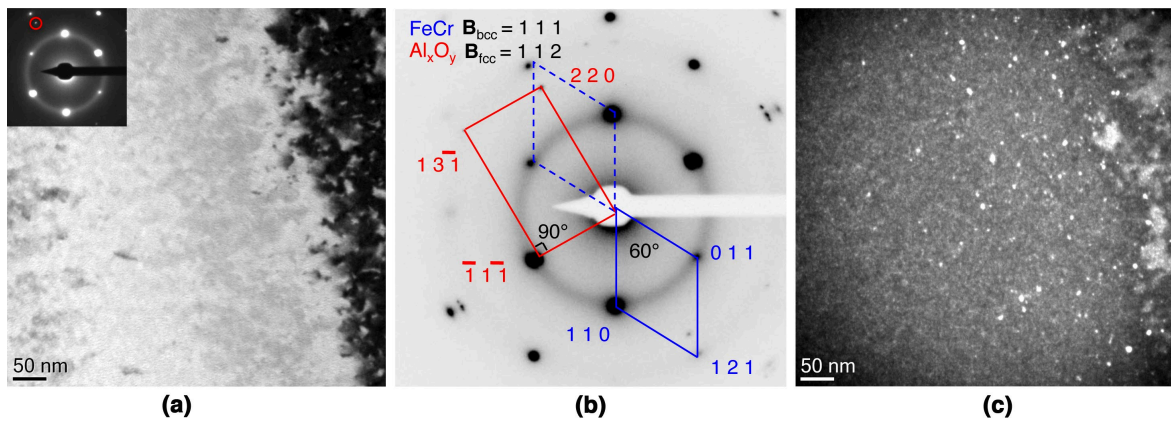


Fig. 3.34: Crystal structure analysis of as-implanted FeCr thin foil: (a) BF TEM image. (b) Diffraction pattern (negative level) for the region corresponding to Fig. 3.34(a). (c) DF TEM image corresponding to the selected spot (encircled by a red circle) on the diffraction pattern (normal level) inserted inside Fig. 3.34(a).

The diffraction pattern demonstrates the presence of two sets of diffraction spots. The spots corresponding to the body-centred-cubic (*bcc*) Fe-Cr matrix are marked in the Fig. 3.34 (b) with blue lines. The intersection angle of the matrix lattice (parallelogram) pattern is about 60° and the ratio of the lengths between adjacent sides is 1, as appropriate for the diffraction pattern of *bcc* structure viewed along $\langle 1\ 1\ 1 \rangle$ zone axis [Jouffrey, 1972]. The average lattice parameter of the matrix calculated using the Bragg equation is about $2.9\ \text{\AA}$, which is in agreement with the reference value of $2.876\ \text{\AA}$ for Fe-10Cr alloy [Villars, 1985].

Another set of spots (connected with red lines) does not belong to the matrix lattice and constitutes a rectangle pattern. These spots are due to precipitated particles created by the ion implantation. The rectangle pattern (with the intersection angle of 90° and the length ratio of 1.63) corresponds to face-centred cubic (*fcc*) lattice oriented along $\langle 112 \rangle$ zone axis [Jouffrey, 1972] and the average value of lattice parameter is $3.82 \pm 0.03\ \text{\AA}$.

Fig. 3.34(c) shows a dark field (DF) image corresponding to one selected diffracted spot, which is encircled by the red circle in the diffraction pattern inserted in Fig. 3.34(b). It shows exactly the same region of the as-implanted thin foil as in Fig. 3.34(a). The precipitated particles, having the bright contrast, are clearly visible in Fig. 3.34(c). Their diameter varies from 3 nm to 12 nm, and the mean size is 5 nm. Only a part of precipitates is bright in the selected spot, while others remain relatively dark, indicating that not all precipitates are oriented along the same direction with respect to the matrix orientation.

It should be kept in mind, however, that a single SAED pattern is insufficient to identify the lattice structure. Therefore, our identification of the particle lattice structure as *fcc* remains

preliminary until verified more rigorously.

With repeating the same processes, we have measured another diffraction pattern (Fig. 3.35(a)) along a different FeCr lattice direction ($\langle 110 \rangle$) on a region with significant number of visible precipitates (see Fig. 3.35(b)). Two sets of diffraction spots can be identified in Fig. 3.35(a). A set of peaks corresponding to the body-centered-cubic (bcc) FeCr matrix is marked in the Fig. with blue lines. As appropriate to the bcc diffraction pattern along $\langle 110 \rangle$ zone axis, the intersection angle of the rectangular lattice is about 90° and the ratio of the lengths between two sides is about 1.41. The lattice parameter determined from the diffraction pattern using the Bragg equation is about $a \approx 2.9 \text{ \AA}$, which agrees with the reference value for Fe-10Cr alloy (2.876 \AA [Villars, 1985]).

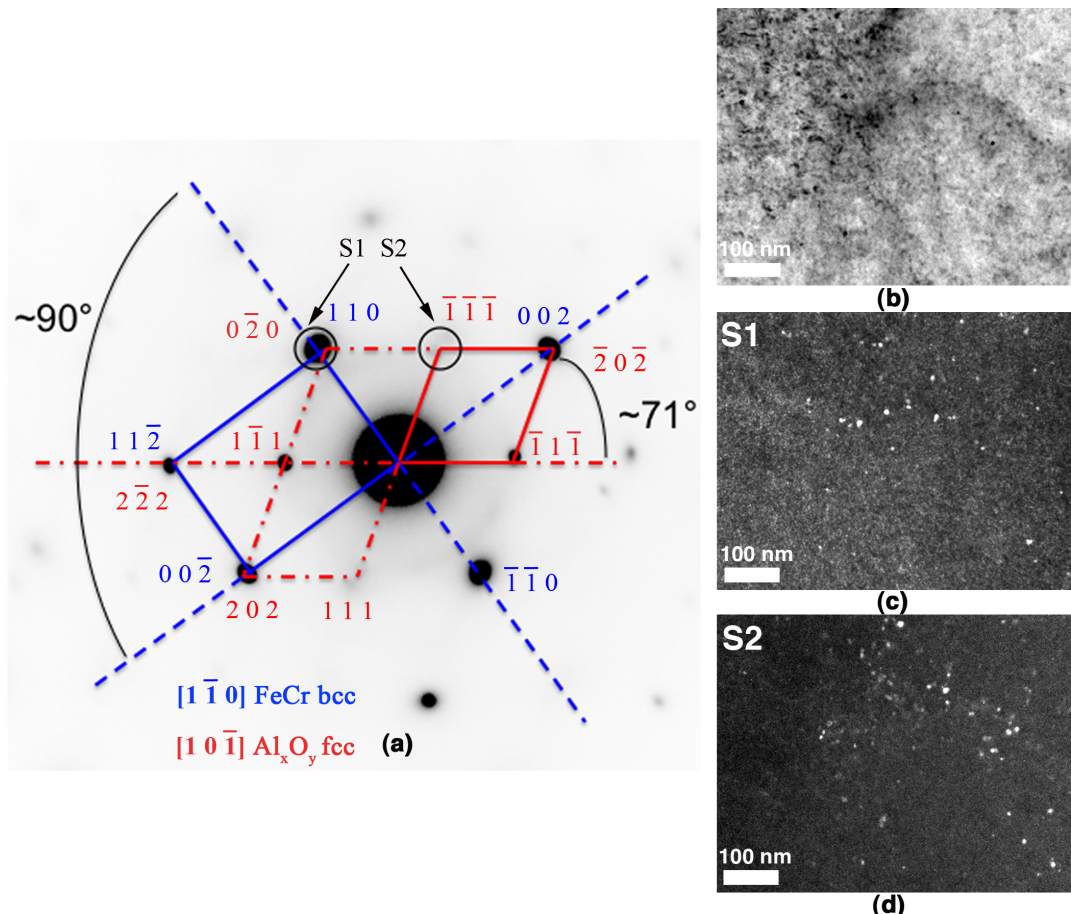


Fig. 3.35: Crystalline structure analysis showing the coexistence of the FeCr matrix and the precipitated particles in the as-implanted material. (a) Diffraction pattern (negative level) for the region corresponding to Fig. 35(b). The particular zone axis orientation adopted for indexing the diffraction spots is specified in the legend. (b) Bright field TEM image of the implanted material. (c) Dark field TEM image corresponding to spot S1 (common matrix-precipitate spot) in Fig. 35(a). (d) Dark field TEM image corresponding to spot S2 (single precipitate spot) in Fig. 35(a).

The second set of spots (connected with red lines in Fig. 3.35(a)) does not correspond to the FeCr matrix lattice and is interpreted as being due to the nano-precipitates created by Al and O ion implantation. Including into this set also the spots superimposed over the matrix ones, one easily recognizes the diffraction pattern corresponding to face-centered cubic (*fcc*) lattice oriented along $\langle 110 \rangle$ zone axis [Jouffrey, 1972]. As appropriate for the pattern, the lattice drawn in red in Fig. 3.35(a) has the line intersection angle of about 71° and the ratio of the lengths of adjacent sides of about 1. The estimated average value of the lattice parameter is $a = 4.29 \pm 0.22 \text{ \AA}$.

In order to confirm that the second set of diffraction spots is indeed related to the observed particles, the dark field (DF) images on two selected diffraction spots labeled S1 and S2 in Fig. 3.35(a) were obtained and can be seen in Figs. 3.35(c) and 3.35(d), respectively. Bright spots corresponding to precipitates can be observed in both micrographs. This confirms our assumption that S1 is a common diffraction spot to both the FeCr matrix and the *fcc* particles. The presence of common directions and spots for the matrix and the precipitates in the diffraction pattern implies the presence of orientation relationships between the particles and the matrix. In particular, $[001]_{bcc} \parallel [\bar{1}0\bar{1}]_{fcc}$, $[110]_{bcc} \parallel [0\bar{1}0]_{fcc}$ and $[11\bar{2}]_{bcc} \parallel [1\bar{1}1]_{fcc}$.

HRTEM images were taken on different particles in the as-implanted FIB lamina. We obtained tens of HRTEM images, which are adequate to identify the crystallographic structure of particles. And six of them are drawn in Fig. 3.36 (a-f). Statistically, most of particles observed in the HRTEM images present a cubic symmetry. The lattice structure of the particles is assumed to be *fcc* with a lattice parameter ranging from 3.8 to 4.2 \AA . In addition, the particle size ranges from 3 to 15 nm. In conclusion, these results relevant to particle structure are consistent with previous results reported by diffraction pattern analyses.

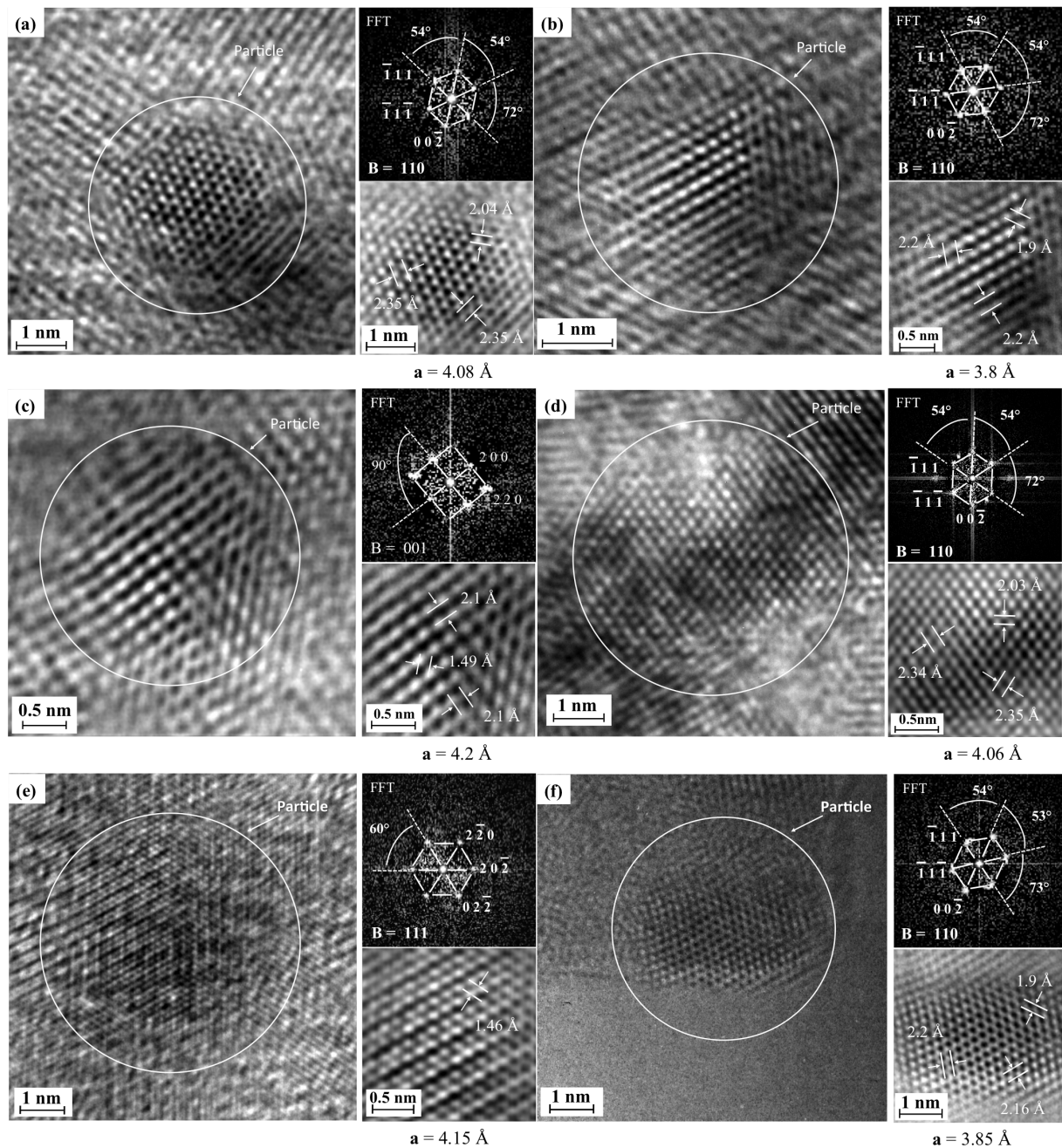


Fig. 3.36: High resolution TEM of six particles in the as-implanted FIB lamina: (a) oriented along $\langle 110 \rangle$; (b) oriented along $\langle 110 \rangle$; (c) oriented along $\langle 001 \rangle$; (d) oriented along $\langle 110 \rangle$; (e) oriented along $\langle 111 \rangle$ and (f) oriented along $\langle 110 \rangle$. The upper inset on the right shows the Fourier transform of the square selected on the image, and the lower inset shows a zoom of this part. The indicated values of distances and lattice parameters are measured from the images.

Fig. 3.37 shows HRTEM images taken on two different particles in as-implanted thin foils. Both of two particles present cubic symmetry. The HRTEM resolution being about 2 \AA , we can observe clearly a particle without seeing the matrix, even if there is a special orientation with the matrix. The lattice of the particle observed in Fig. 3.37(a) is oriented along $\langle 100 \rangle$ axis and, assuming it to be *fcc*, corresponds to the lattice parameter of 4.2 \AA (or a

multiple), very similar to the value suggested by the diffraction pattern (Fig. 3.35(a)). The particle in Fig 3.37(b), which has definitely fcc symmetry and is $\langle 110 \rangle$ -oriented, has its lattice parameter equal to only 3.83 Å (or a multiple), yet very similar to the value suggested by the diffraction pattern (Fig. 3.34 (b)).

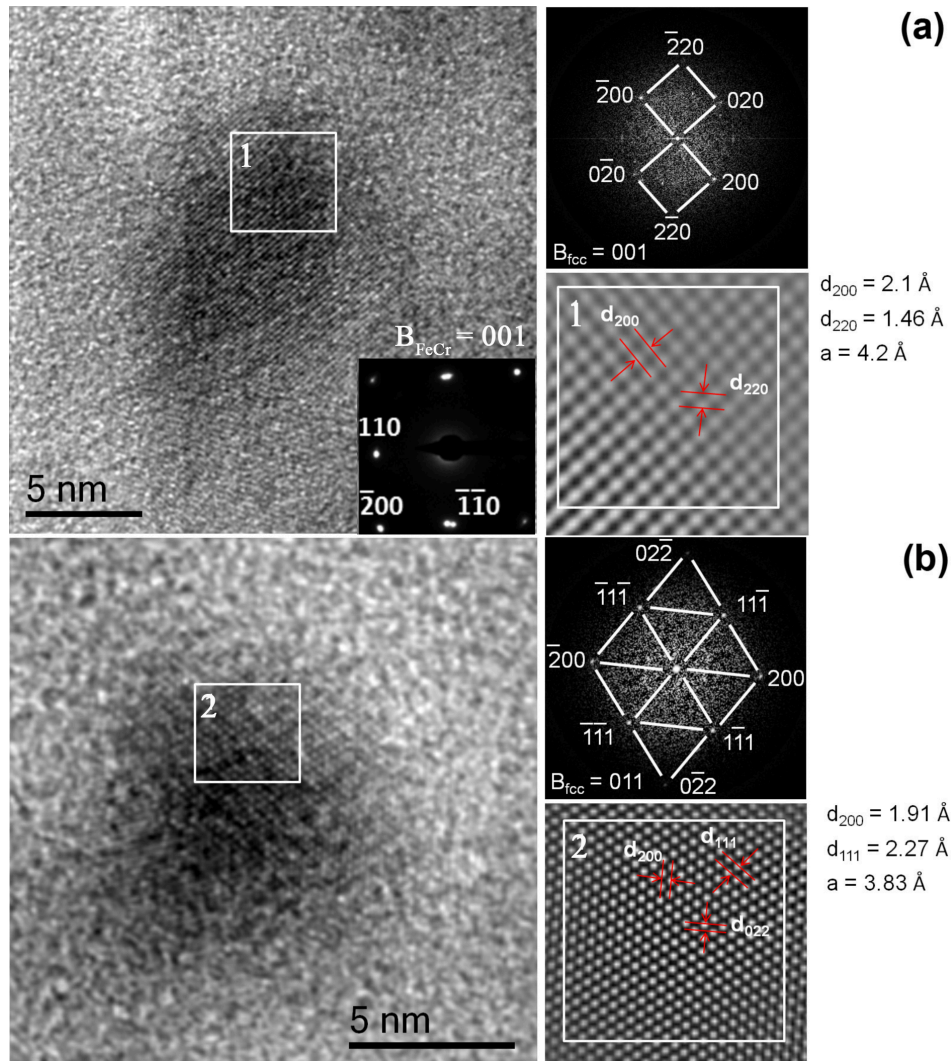


Fig. 3.37: High resolution TEM of two particles, (a) oriented along $\langle 100 \rangle$ and (b) oriented along $\langle 110 \rangle$. The upper inset on the right shows the Fourier transform of the square selected on the image, and the lower inset shows a zoom of this part. The indicated values of distances and lattice parameters are measured from the image.

According to EFTEM and APT measurements, the precipitates are enriched with Al, Cr and O. Furthermore, both diffraction pattern and HRTEM analyses revealed that the precipitates have a cubic symmetry, more precisely, a *fcc* structure with the lattice parameter ranging from 3.8 to 4.2 Å. There are few studies reported the observation of (Al, Cr)-rich oxides having such a *fcc* structure. Khatibi *et al.* [Khatibi, 2011] reported the discovery of a $(\text{Al}_{1-x}\text{Cr}_x)_2\text{O}_3$ solid solution ($0.6 < x < 0.7$) in films grown onto Si substrates using reactive radio frequency magnetron sputtering from Al and Cr targets at 400 °C. According to their X-ray diffraction

(XRD) and EDX in STEM mode measurements, the lattice parameter is about 4.04 Å and the stoichiometry ratio of Cr and Al is between 0.6 and 0.7. Therefore, they proposed a NaCl-like crystal structure in which the introduction of vacancies on the one third metal sites. Furthermore, the metal-oxygen ratio is set to the chemically preferred 2:3. A typical unit cell of the NaCl-like structure $(Al_{1-x}Cr_x)_2O_3$ ($0.6 < x < 0.7$) can be found in Fig. 3.38(e).

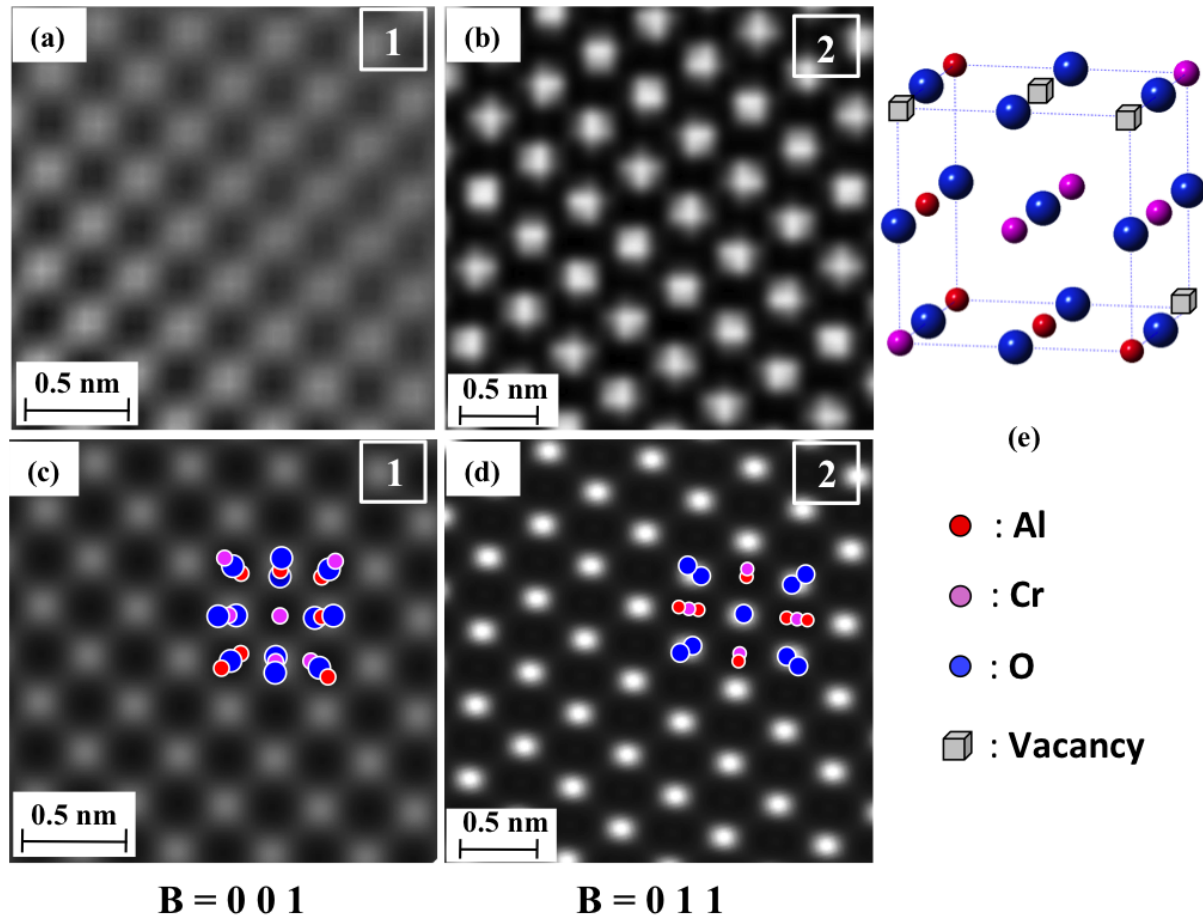


Fig. 3.38: (a) Zoom of the selected square from the particle shown in Fig. 37(a); (b) Zoom of the selected square from the particle shown in Fig. 37(b); (c) Simulated HRTEM image based on the crystallographic structure of NaCl-like structure $(Al_{1-x}Cr_x)_2O_3$ corresponding to (a); (d) Simulated HRTEM image based on the crystallographic structure of NaCl-like structure $(Al_{1-x}Cr_x)_2O_3$ corresponding to (b); (e) unit cell of *fcc* $(Al_{1-x}Cr_x)_2O_3$ reported by Khatibi *et al.* [Khatibi, 2011].

The simplest guess that particles are this NaCl-like structure $(Al_{1-x}Cr_x)_2O_3$ ($0.6 < x < 0.7$) does not seem improbable, at least for a part of the particles. In order to justify this assumption, Figs. 3.38(a)-(c) show the zoom of experimental HRTEM image of the particle shown in Fig. 3.37(a) and the simulated HRTEM image based on the crystallographic structure of NaCl-like structure $(Al_{1-x}Cr_x)_2O_3$ reported by Khatibi *et al.* [Khatibi, 2011]. There is an excellent match between the simulated and the experimental images in terms of spacing and angle of the same contrast patterns. On the other hand, the lattice parameter of 3.87 Å, as measured in Fig. 3.37(b), is too different from that of NaCl-like structure $(Al_{1-x}Cr_x)_2O_3$ reported by Khatibi *et al.* [Khatibi, 2011]. However, the zoom of experimental HRTEM

image for the particle shown in Fig. 3.37(b) and the simulated HRTEM image of NaCl-like structure ($\text{Al}_{1-x}\text{Cr}_x$) $_2\text{O}_3$ look very similar (see Figs. 3.38(b) and (d)).

Presumably, the observed particle contains in addition to Al some amount of Cr, which is known to easily replace Al in aluminum oxides. The HRTEM-based observation of lattice parameter variation in precipitated particles is thus indicative of the variability of elemental contents in precipitated particles, especially for the ratio of Al/Cr.

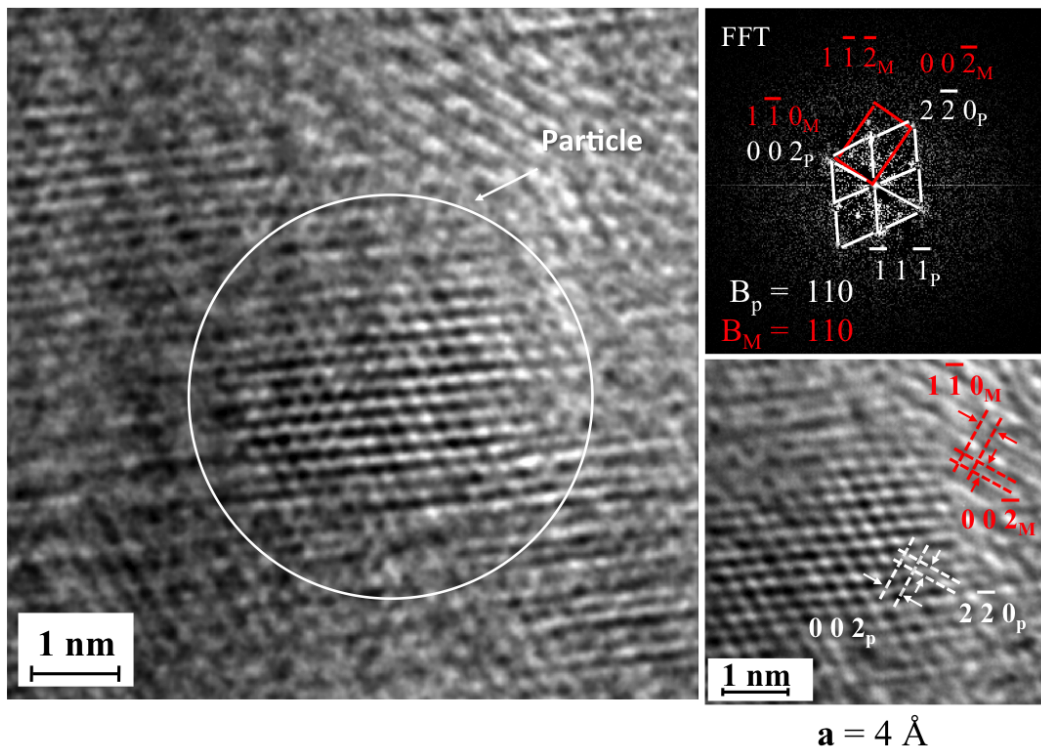


Fig. 3.39: High resolution TEM of the particle oriented along $\langle 110 \rangle$. The upper inset on the right shows the Fourier transform of the square selected on the image, and the lower inset shows a zoom of this part. The indicated values of distances and lattice parameters are measured from the image. Here, the spots corresponding to the matrix.

The orientation relationship between the particle and the matrix can be inferred from Fig. 3.36(a), which allows comparing FFT image from the particle with the diffraction pattern from the matrix. The matrix of the Fe-10Cr alloy is oriented along $\langle 0 0 1 \rangle$ direction, as identified from the SAED pattern. Both the particle and the matrix share zone axis $\langle 0 0 1 \rangle$ and appear to display a ‘cube on cube’ orientation relationship.

Fig. 3.39 shows the HRTEM image of the particle, which shares zone axis $\langle 1 1 0 \rangle$ with the matrix. The information of the zone axis of the matrix and the particle derived from the FFT pattern (the upper inset of Fig. 3.37). The values and directions of distances drawn in the lower inset of Fig. 3.39 indicate that $[002]_{fcc} \parallel [1\bar{1}0]_{bcc}$ and $[2\bar{2}0]_{fcc} \parallel [00\bar{2}]_{bcc}$. Furthermore, the interplanar distances of the particle lattice are equal to those of the matrix in these directions.

The orientation relationship implies that particle structure is strongly influenced by the surrounding host lattice. The fact that the particle ‘remembers’ the host lattice orientation suggests that the particle nucleation occurs through the correlated agglomeration of aluminum and oxygen atoms ‘on top’ of the existing iron lattice. In addition, the growing clusters should efficiently consume vacancies to free space for the oxide because the atomic density of oxides is notably less than that of the bulk iron (the latter is evidenced, in particular, by the strong iron depletion in the particle volume visible in Fe EFTEM elemental maps. Overall, the oxide lattice orientation with respect to the host lattice is very similar to that observed for yttrium oxide particles in ODS steels [Klimiankou, 2004; Ramar, 2009; Ribis, 2012], which are believed to precipitate by agglomeration of Y and O atoms dissolved in ferritic matrix [Ukai, 2012], and possibly suggests a qualitative similarity in the precipitation mechanisms.

4.2. Measurements of SAED obtained in annealed samples

Fig. 3.40(a) is the bright field image of the annealed thin foil, of which the matrix is oriented along the axis $\langle 110 \rangle$. Besides the spots belonging to the matrix, two sets of diffraction spots can be identified in the diffraction pattern (negative level) corresponding to Fig. 3.40(a) (see Fig. 3.40(b)).

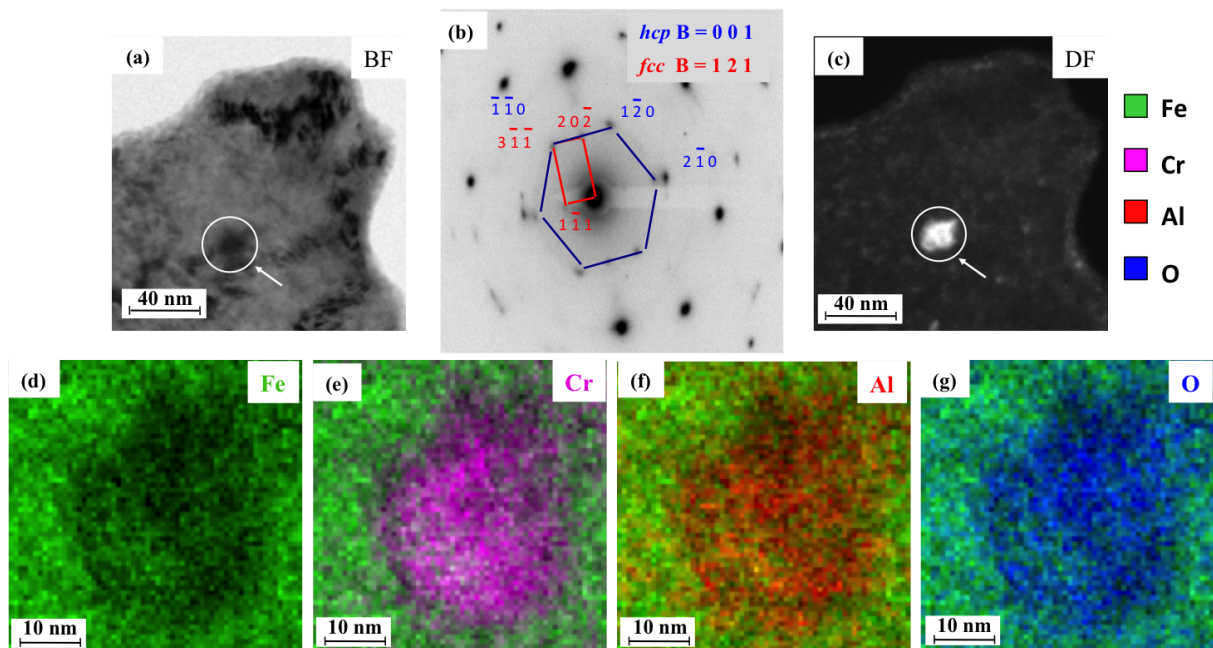


Fig. 3.40: Crystalline structure and EFTEM analyses showing the correlation between the crystallographic structure and chemical composition of the precipitated particle in the annealed thin foil: (a) Bright field TEM image of the annealed thin foil. A visible particle is encircled; (b) Diffraction pattern (negative level) for the region corresponding to (a); (c) Dark field TEM image corresponding to spot $[\bar{1}\bar{1}0]_{hcp}$; The panels show jump ratio EFTEM elemental maps of Fe-M_{2,3} edge (d), Cr-M_{2,3} edge (e), Al-L_{2,3} edge (f) and three-window EFTEM elemental map of O-K edge (g). The colors indicate the elements as marked in the legend.

The first set of spots (connected with red lines in Fig. 3.40(b)) shows a shape like the rectangle. This rectangle pattern (with the intersection angle of 90° and the length ratio of 1.64) corresponds to face-centred cubic (*fcc*) lattice oriented along $\langle 112 \rangle$ zone axis [Jouffrey, 1972] and the average value of lattice parameter is $8.35 \pm 0.05 \text{ \AA}$. Obviously, this measured value is larger than that of *fcc* (Al, Cr, O) particles (3.8-4.2 \AA) either suggested by A. Khatibi et al. [Khatibi, 2011] or measured in our as-implanted thin foils. In contrast, the measured lattice parameter is consistent with the reference value of stoichiometric *fcc*- FeCr_2O_4 . In conclusion, the *fcc* structure corresponds to FeCr_2O_4 , and is interpreted as being due to the oxidation occurring in the material (see Annex B).

The second set of spots (connected with blue lines in Fig. 3.40(b)) looks like a hexagon. Including into this set also the spots superimposed over the red ones, one easily recognizes the diffraction pattern corresponding to hexagonal (*hcp*) lattice oriented along $\langle 0001 \rangle$ zone axis [Jouffrey, 1972]. As appropriate for the pattern, the lattice drawn in blue in Fig. 3.40(b) has the line intersection angle of about 60° and the ratio of the lengths of adjacent sides of about 1. The estimated average value of the lattice parameter is $a = 4.87 \pm 0.05 \text{ \AA}$ and $c = 13.30 \pm 0.06 \text{ \AA}$.

The dark field image on the selected diffraction spot labeled $[\bar{1}\bar{1}0]_{hcp}$ was obtained and can be seen in Fig. 3.40(c). The particle encircled in the BF micrograph (Fig. 3.40(a)) shows the bright contrast and is clearly visible in the DF micrograph (Fig. 3.40(c)). The estimated particle size is about 28 nm. This confirms that the *hcp* structure corresponds to the particle. The EFTEM thickness map (not shown here) demonstrated the feasibility of the EFTEM investigation in the region shown in Fig. 3.40(a) since the estimated thickness is $\sim 36 \text{ nm}$ ($\frac{L}{\lambda} \sim 0.32$ and $\lambda \sim 110 \text{ nm}$). Considering the EFTEM elemental maps (Fig. 3.40 (d)-(g)) of Fe-M_{2,3}, Cr-M_{2,3}, Al-L_{2,3} and O-K, one can see evidently the Fe depletion matches with the accumulation of Al, Cr and O at the position of the particle encircled in both BF and DF micrographs. Combining the resulting EFTEM results with the diffraction pattern analysis, we can thus conclude that the particle observed in the annealed thin foil is (Al, Cr)-rich oxide having a *hcp* structure. Obviously, the crystallographic structure of precipitates is not the same before and after thermal annealing.

It is remarkable that *NaCl*-type-(Al_{1-x}Cr_x)₂O₃ solid solution is a thermodynamically metastable phase comparing to the well studied corundum-structure α -(Al_{1-x}Cr_x)₂O₃ solid solution since the reactive radio frequency magnetron is a thermodynamically non-equilibrium process as the same as ion implantation [Ramm, 2007; Diechle, 2010]. In addition, Khatibi *et al.* [Khatibi, 2012; Khatibi, 2013] reported the transformation of NaCl-like (Al_{1-x}Cr_x)₂O₃ metastable phase to corundum phase during annealing temperature of 900 degrees Celsius and above. The similar phase transition was also reported by Najafi *et al.* [Najafi, 2013], which claimed a synthesis of cubic (Al,Cr)₂O₃ films and its dynamic transition to corundum phase during the evaporation. It should be reminded that the diffraction pattern of the corundum structure along the <0001> direction has the same shape with that of the hexagonal structure. Furthermore, the lattice parameter reported in Najafi *et al.* [Najafi, 2013] is consistent with that measured in our study. These correlations indicate that the (Al, Cr)-rich oxide particles in annealed thin foils are probable to be corundum-(Al, Cr, O). In conclusion, we consider that a structure transformation from *fcc* to corundum occurred in (Al, Cr)-rich oxide particles due to thermal annealing.

5. Preferential precipitation in point defects sinks

5.1. Elements enrichment at grain boundaries

Point defect sinks (e.g. grain boundaries) in as-implanted specimens have been characterized by EFTEM. The resulting EFTEM elemental maps are presented in Fig. 3.41.

The dark contrast on Fe-L_{2,3} edge elemental maps (Fig. 3.41 (a) & (d)) show the local Fe deficiency at grain boundaries. Cr-L_{2,3} edge and Al-K edge elemental maps (Fig. 3.41(b-c)) reveal the enrichment of Cr and Al at the same grain boundary. Oxygen atoms are found to agglomerate at other grain boundary according to the O-K elemental map (Fig. 3.41(e)). Enrichment of implanted impurities (Al, O) and minor alloy component atoms (Cr) in point defect sinks (e.g. grain boundaries) are suggested to be radiation-induced segregation (RIS).

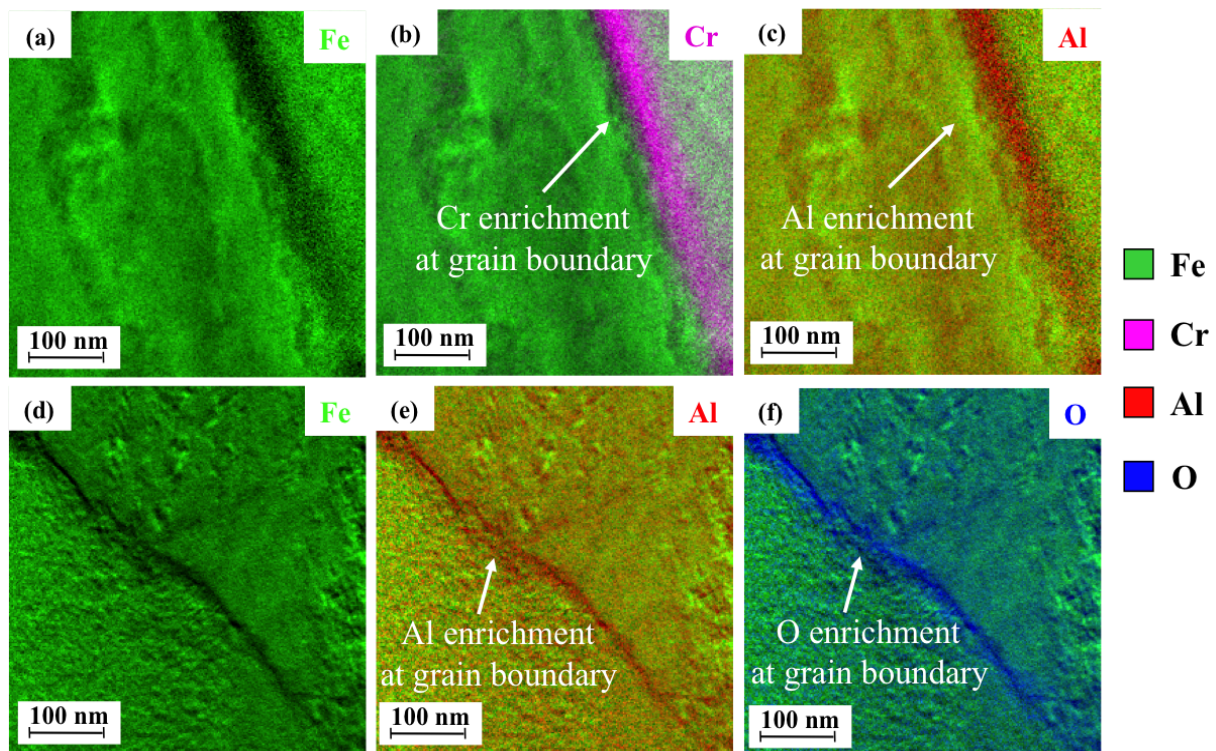


Fig. 3.41 Energy-filtered TEM series showing (Al, Cr, O) enrichment at grain boundaries in the as-implanted TEM thin foil: Fe- $L_{2,3}$ (a)-(d), Cr- $L_{2,3}$ edge (b), Al-K edge (c) and O-K (e) three-window EFTEM elemental maps. The colors indicate the elements as marked in the legend.

5.2. Precipitation on dislocation lines and loops

Conventional TEM observations were applied to point defect sinks (e.g. dislocation lines and loops) in as-implanted specimens. Fig. 3.42(a) shows a BF TEM micrograph where large portion of dislocation lines are clearly visible.

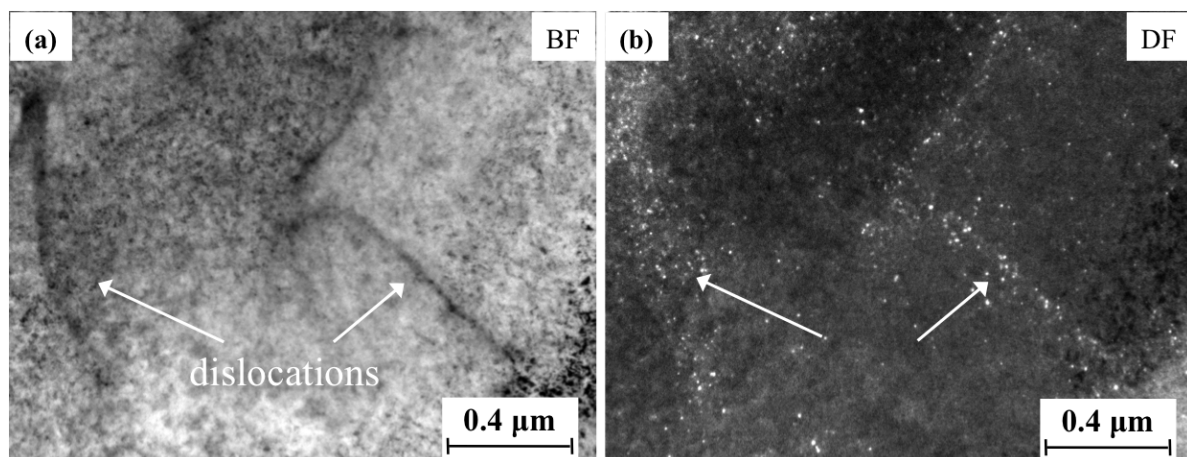


Fig. 3.42 TEM micrographs showing the precipitation on large portion of dislocation lines: (a) BF TEM micrograph: some of dislocations are clearly visible in this micrograph. (b) Corresponding DF TEM micrograph: precipitates agglomeration on the dislocations.

The corresponding DF TEM micrograph (Fig. 3.42(b)) shows exactly the same region of the as-implanted TEM thin foil as in Fig. 3.42(a). The precipitates, having the bright contrast, are clearly visible in Fig. 3.12(b). Their diameter varies from 3 nm to 15 nm, and the mean size is 5.5 nm. More interestingly, the precipitates are found to locate in or around the dislocation lines.

In order to obtain better contrast for dislocation loops, the specimen was tilted to satisfy two-beam condition.

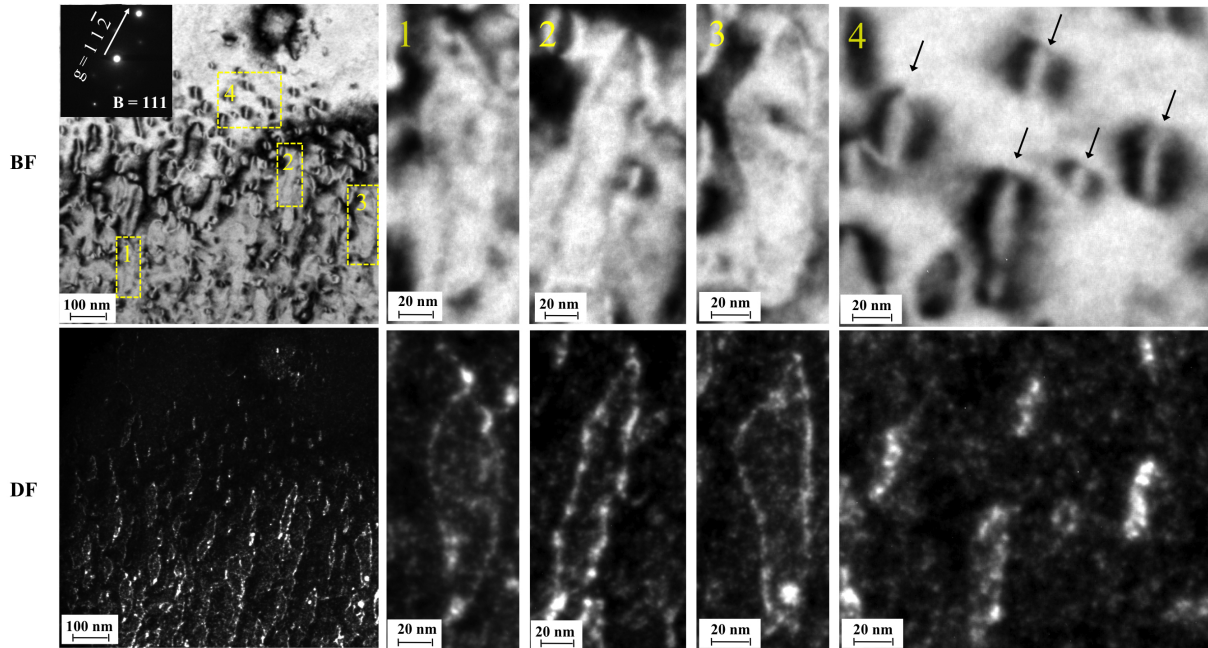


Fig. 3.43 TEM micrographs showing the precipitation on dislocation loops. The upper line from left to right: BF TEM micrographs of the whole region and zoom views of four different regions. The lower line from left to right: Corresponding DF TEM micrographs of the whole region and zoom views of four different regions. The diffraction pattern inserted in the BF TEM micrograph showing the TEM specimen was tilted to satisfy two beams condition ($s \approx 0$).

Fig. 3.43(a) shows a BF TEM micrograph in which numerous dislocation loops seem to be enriched. The inserted diffraction reveals the matrix is oriented along $\langle 111 \rangle$ direction, and two-beam condition is reached at this time. Thanks to two-beam condition, the white contrast shown in the corresponding DF TEM micrograph is clearly visible. Zoom views have been applied to four typical regions marked in the BF TEM micrograph. One clearly sees that the dislocation loops are decorated with very small precipitates (< 5 nm) with several slightly larger. The size of dislocation loops observed in these four regions is quite different. It can be as large as 150 nm (regions 1, 2 and 3), or as small as 20 nm (region 4).

The observation was achieved in as-implanted FIB lamina with using weak beam dark field (WBDF) method. The resulting BF and WBDF TEM micrographs are presented in Fig. 3.44.

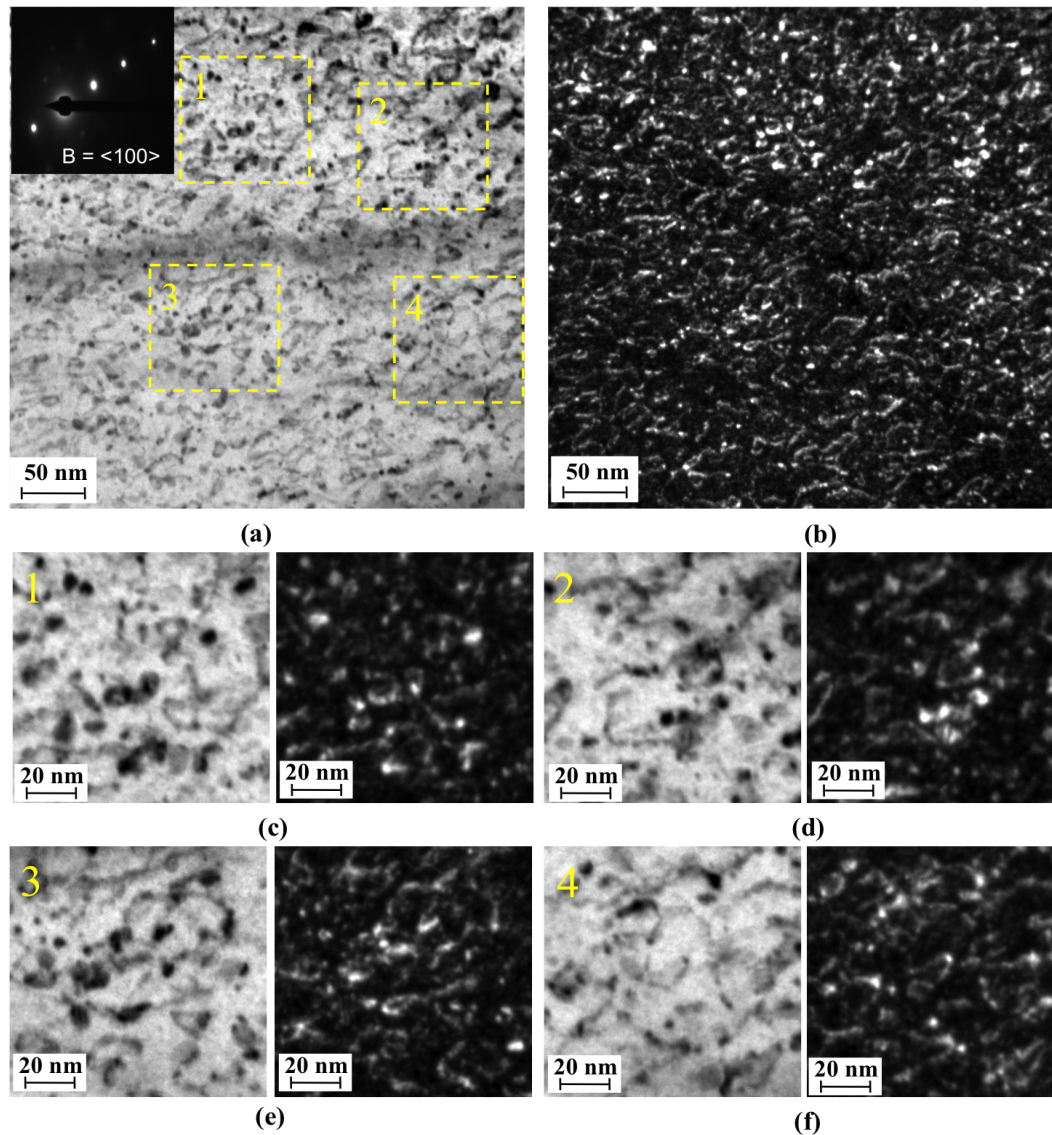


Fig. 3.44: TEM micrographs showing the precipitation on dislocation loops. (a) BF TEM micrograph of the whole region. (b) Corresponding weak beam dark field (WBDF) TEM micrograph. (c)-(f): Zoom views of BF and WBDF taken on 4 different regions as marked in (a). The diffraction inserted in (a) showing the sample was tilted to satisfy (g, 3g) weak beam condition.

In Fig. 3.44, we chosen also four typical regions to give zoom views for both BF and WBDF TEM micrographs. The specimen was tilted in order to reach weak beam condition. The inserted diffraction pattern indicates the matrix is oriented along $\langle 100 \rangle$ direction, and the (g, 3g) weak beam condition is reached. The precipitates, having the dark contrast in BF TEM micrographs, are already clearly visible. The bright contrast shown in DF micrographs reveals that precipitates accompany well with dislocation loops. The observed phenomenon is consistent with that observed under two-beam condition.

Similar results were also observed in annealed TEM thin foils. The detail of these results is given in Annexe C.

Chapter 4 Discussion

1. Room temperature material transport.....120
2. Physical mechanisms involved in precipitate synthesis.....124

The main result of this study shown in Chapter 3 is a clear demonstration of the feasibility of (Al, O) nano-size clusters precipitation in Fe-Cr alloy by introducing Al⁺ and O⁺ ions via ion implantation. The study provides also an ample body of information concerning the kinetics, crystal structure and chemical composition of cluster ensemble evolving as a result of ion beam synthesis, which included both room temperature ion implantation and subsequent high-temperature thermal annealing. In contrast to conventional ion beam synthesis technique, the post-implantation thermal treatment was not a prerequisite to start the precipitation. In this section we discuss some non-evident features of the experimental observations and demonstrate how they contribute to the physical understanding of the oxide precipitation kinetics. Room temperature material transport is discussed in the first section. Physical mechanisms involved in precipitate synthesis are proposed in the second section, based on the obtained experimental results.

1. Room temperature material transport

Temperature is a key parameter in the formation of precipitates by ion implantation. Implanted atoms are introduced in a statistically dispersed fashion and typically are immobile at room temperature. Thus, subsequent thermal annealing is usually required after ion implantation in order to promote the nucleation and growth of precipitates. Heating increases the mobility of implanted impurities so that they could agglomerate to form precipitates within reasonable time (minutes to hours) [Picraux, 1978]. Since in our case precipitation occurred without any subsequent annealing after implantation, we have to assume that the mass transfer of both Al and O atoms took place at room temperature.

An experimental proof of the high mobility of Al and O atoms results from the comparison of concentration profiles of Al and O measured by APT analysis and those simulated by SRIM (see Fig. 3.15 in Chapter 3). The difference of measured and simulated concentration profiles in the depth range of 100 to 125 nm indicates that both implanted Al and O impurities went farther than predicted by SRIM simulation.

According to experimental evidence, the implanted atoms were able to migrate for at least several tens of nanometers within the time of ion implantation (~ 1 to 3 hours). As a rough estimate, this gives us the lower estimate for the diffusion coefficient of $10^{-14} \text{ cm}^2 \cdot \text{s}^{-1}$. For purely thermally driven diffusion this value is far too high for either O, or Al. The estimated mobility of oxygen at 300 K is only $6 \times 10^{-19} \text{ cm}^2 \cdot \text{s}^{-1}$ [Takada, 1986], while that of aluminum is

virtually zero [Hirvonen, 1982].

On the other hand, it is known that irradiation is able to increase the mobility of solute atoms because the concentrations of point defects (vacancies and interstitials) under irradiation are much larger than the thermal ones [Was, 2007] for both oxygen [Lapuerta, 2006] and aluminium [Campbell, 1980]. Let us demonstrate that in our implantation conditions sufficient amounts of point defects were produced to provide the required diffusion mobility.

Let us start with aluminium, a substitutional impurity whose diffusion in iron-based alloys is mediated by available point defects. While during the high temperature annealing the transport of aluminium is mediated by thermal vacancies [Hirvonen, 1982], under irradiation both vacancies and interstitials produced by irradiation contribute to the aluminium diffusion coefficient, D_{Al} , that is

$$D_{Al} = D_V C_V + D_I C_I,$$

where D_V and D_I are diffusion coefficients of vacancies and interstitials and C_V , C_I - their concentrations.

In section V.4 of Chapter I, we introduced an approximation of non-equilibrium thermodynamics diffusion equations, that is $D_V C_V \approx D_I C_I$, which means that vacancies and interstitials contribute equally to atom mobility. A rough estimate for the average point defect concentrations created in a thin film by ion irradiation with the flux ϕ was given as [Fortuna, 2011]:

$$D_V C_V \approx D_I C_I = \gamma \Omega L \phi v_F$$

where γ is a numerical factor (of the order of unity) that takes into account the particular shape of the defect production profile, Ω is the matrix atomic volume ($\sim 12 \text{ \AA}^3$), L is the implanted foil thickness and v_F is the average number of Frenkel pairs produced by an incident ion. For the parameters of aluminium implantation ($\phi = 6.8 \times 10^{12} \text{ cm}^{-2} \cdot \text{s}^{-1}$, $v_F = 780$ vacancies per Al ion, and $L = 50 - 100 \text{ nm}$) this gives us $D_{Al} \sim 5 \times 10^{-13} \text{ cm}^2 \cdot \text{s}^{-1}$, a value well above the estimated mobility threshold of $10^{-14} \text{ cm}^2 \cdot \text{s}^{-1}$.

For oxygen the above estimate is inapplicable because oxygen in iron (as well as in Fe-10Cr) is an interstitial impurity. The experimental estimates of O migration energy give quite high values, 0.93 eV [Takada, 1986] or even 1.73 eV [Barlow, 1969]. However, these estimates are based on the interpretation of iron oxidation data at temperatures above 1000 K and are not necessarily applicable in the implantation conditions. According to the first-principles density

functional theory estimates [Fu, 2007], the migration energy of interstitial oxygen in pure iron is only ~ 0.6 eV. With this migration barrier, the oxygen diffusion coefficient at room temperature would be $\sim 10^{-10}$ $\text{cm}^2 \cdot \text{s}^{-1}$ (assuming the prefactor of $1 \text{ cm}^2 \cdot \text{s}^{-1}$), well above the required mobility threshold.

The origin for the difference between the simulation and experiment based values for oxygen mobility is not reliably ascertained. It seems reasonable, however, to ascribe it to the effect of oxygen capture by vacancies, which were abundant in both cited measurements (performed at ~ 1000 - 1100 K). According to Ref. [Fu, 2007], the vacancy-oxygen binding energy in iron is sensitive to the magnetic order of the lattice, being equal to 0.35 eV in non-magnetic and 1.45 eV in ferromagnetic iron state. This means that above the Curie point (1043 K for iron) the effective barrier for oxygen diffusion includes a contribution from oxygen-vacancy pair dissociation, being equal to ~ 0.95 eV. On the other hand, below the Curie temperature the thermal dissociation would cost prohibitively much energy; an oxygen-vacancy pair moves instead as an entity with the migration barrier of 1.55 eV [Fu, 2007]. The two values are very different, but suspiciously close to that or other experimental number.

While ion implantation also creates large numbers of vacancies capable to capture oxygen atoms, the concentration of free vacancies in the matrix is relatively low because of the presence of nearby free surface that is an efficient vacancy sink. Correspondingly, the efficiency of oxygen capture by vacancies should be noticeably lower than during the high temperature measurements. Moreover, high-energy recoils created by implanted ions are able to break vacancy-oxygen pairs, preventing complete oxygen immobilization. For these reasons, the concentration of mobile interstitial oxygen atoms in ion implantation conditions can be much larger than in the thermal equilibrium environment used for the determination of high temperature mobility of oxygen.

One more indication of the relatively high diffusion rate of Al and O atoms is their observed enrichment at extended structural defects, such as grain boundaries and dislocations. This enrichment was directly measured at grain boundaries. The accumulation of implanted atoms at dislocations is more indirect and follows from the fact that oxide precipitates after the implantation are observed preferentially at dislocations. Indeed, without Al segregation to dislocations it is hard to expect the precipitation because the concentration of implanted Al in the bulk is noticeably below the solubility of Al in Fe, which is relatively high (somewhat less than 20% , see the Fe-Al phase diagram in Fig. 4.1).

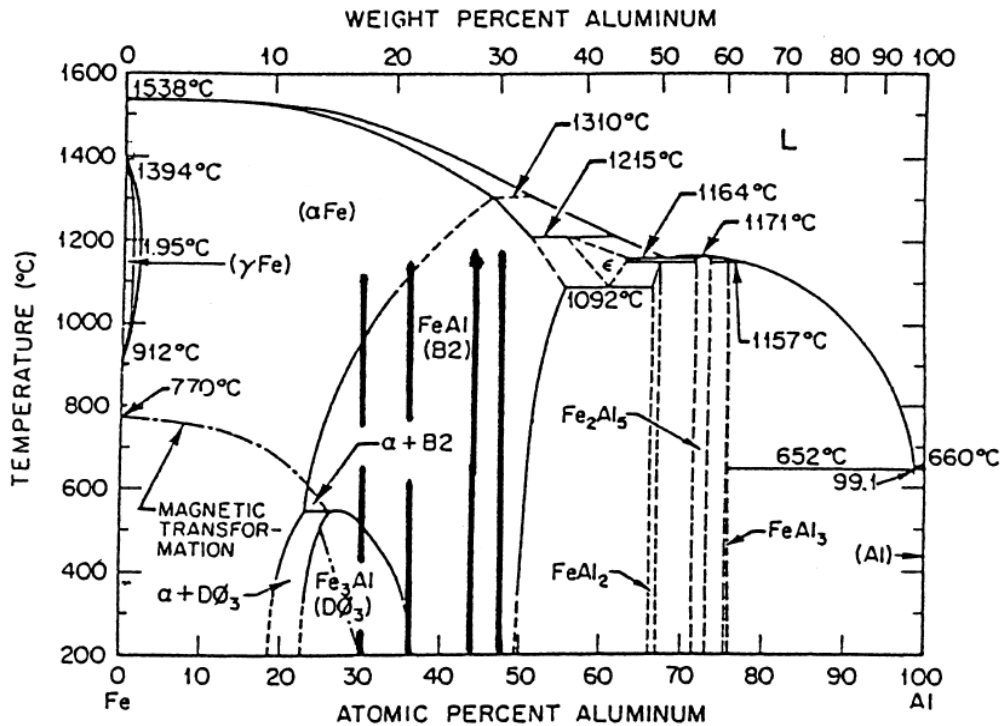


Fig. 4.1 The Fe-Al phase diagram [Massalski, 1986]

Radiation-induced segregation (RIS) and radiation-induced precipitation (RIP) are considered as a consequence of radiation-enhanced diffusion (RED). RIS and RIP mechanisms occur in materials in the presence of point defect (vacancy or interstitial) fluxes [Nastar, 2012]. The irradiation induces point defect fluxes towards point defect sinks: grain boundaries (GBs), dislocation lines, dislocation loops or free surfaces, where the recombination rate is higher than in the matrix [Cauvin, 1981]. The coupling between the point defect and the solute or impurity atoms fluxes toward point defect sinks leads to solute enrichment or depletion at these sinks. Therefore, RIS of implanted impurities (Al and O) and minor alloy component atoms (Cr) at grain boundaries in as-implanted samples (Fig. 3.41) may be due to these mechanisms.

In our experiments, oxide precipitation was observed on large portion of dislocation lines (Fig. 3.42) as well as dislocation loops (Fig. 3.43-3.44). One clearly sees that the dislocation lines and loops are decorated with very small precipitates (< 5 nm) with only several slightly larger. We suppose that this is a direct indication that both implanted Al and O (and possibly Cr) precipitate at the dislocation cores. Due to the increased concentration of solute atoms, dislocation lines and loops serve as nucleation place for oxide precipitates. Such effect of enhanced clustering on dislocation lines or loops is well known in irradiated metals and alloys.

2. Physical mechanisms involved in precipitate synthesis

In our study, Al and O atoms were introduced sequentially into high purity Fe-10Cr alloy by a two-stage ion implantation at room temperature. In order to understand at which implantation stage starts the precipitation, conventional and analytical TEM characterizations were carried out in TEM thin foils implanted by Al⁺ ions only. These TEM thin foils were prepared and implanted following the same processes as described in Chapter II. Since only Al⁺ ions were introduced, the TEM thin foils are referred below as single Al implanted samples. The full description of TEM characterization results can be found in Annexe E.

The most important result for these samples is the observation of Al-rich precipitates nucleated by the end of the implantation stage. It indicates that the precipitate nucleation requires no oxygen in order to start, at least at room temperature.

The second interesting feature revealed by the Al implantation experiment is that the formation of precipitates was observed to occur at grain boundaries. This observation correlates well with the results of two-stage experiment, where oxide particles were found to be associated with extended defects (grain boundaries and dislocations). It can thus be assumed that oxide particles are obtained via oxidation of Al-containing precipitates that nucleated already during the first implantation run.

Finally, the diffraction pattern analysis indicates that the Al-containing precipitates have a *fcc*-structure with the lattice parameter of $\sim 4.1 \pm 0.1 \text{ \AA}$ or $\sim 5.79 \pm 0.1 \text{ \AA}$. The simplest guess that precipitates are pure Al does not seem improbable. In fact, the pure Al has *fcc* lattice with the lattice parameter of 4.05 \AA [P. Villars, 1985], so the lattice structure of pure Al is consistent with the experimental observation. The reference lattice parameter (4.05 \AA) is also quite close to one of experimental values ($\sim 4.1 \pm 0.1 \text{ \AA}$). However, the EFTEM elemental maps reveal that Al and Fe matrix tend to form localized zones that are enriched in both Fe and Al, but depleted with Cr.

Based on the EFTEM observations, one might consider a possibility that the precipitation of Al starts in the form of intermetallic Fe₃Al phase, which is the most stable Fe-Al phase in the Al concentration region just above the solubility limit (see Fig. 4.1). Having in mind that precipitates tend to nucleate at extended defects that are able to accumulate solute atoms, one can assume that local Al content exceeds the solubility limit at room temperature. So these

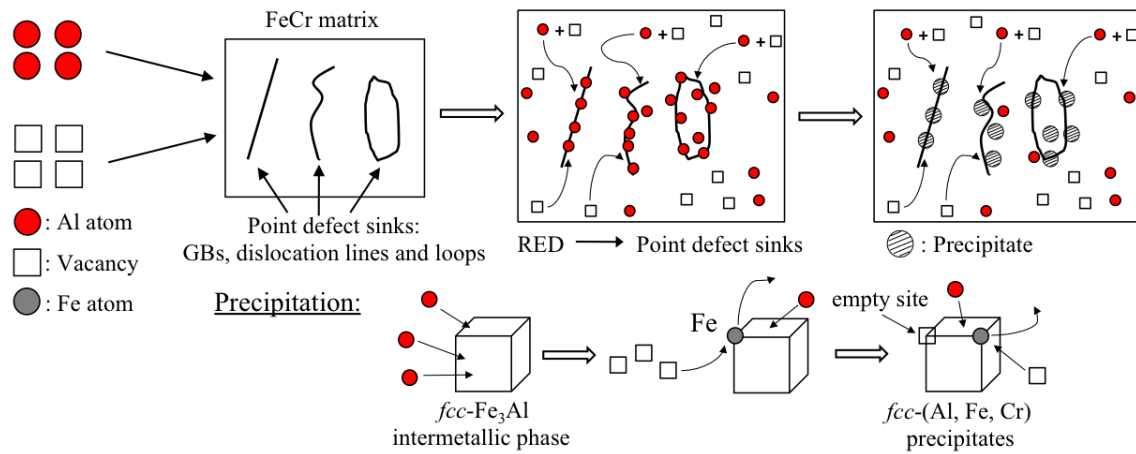
Al-rich zones transform into Al-rich clusters. Fe₃Al phase can give spots in the diffraction pattern, which are characteristic for *fcc* lattice, due to the fact that the Al sublattice in the D0₃ structure of Fe₃Al is *fcc*. In addition, the lattice parameter of this *fcc* sublattice is comparable to the double lattice parameter of iron, i.e. ~ 5.7 Å (cf. the lattice parameter 5.792 Å for unconstrained D0₃ structure of Fe₃Al [Villars, 1985]). The reference lattice parameter (~ 5.7 Å) is consistent with one of experimental values ($\sim 5.79 \pm 0.1$ Å). So it seems also probable that at least some experimentally observed particles are Fe₃Al. The most probable seems to be a hypothesis that the precipitation starts as Fe₃Al, but subsequently precipitates transform into a more Al-rich phase due to both the accumulation of more Al atoms and the capture of radiation produced vacancies that eliminate Fe from the precipitates.

Combining the results of single-beam and two-beam implantation experiments, the following sequence of events would give a consistent explanation of the Al₂O₃ particle synthesis in our experimental setup (see also Fig. 4.2 illustrating the physical mechanisms involved).

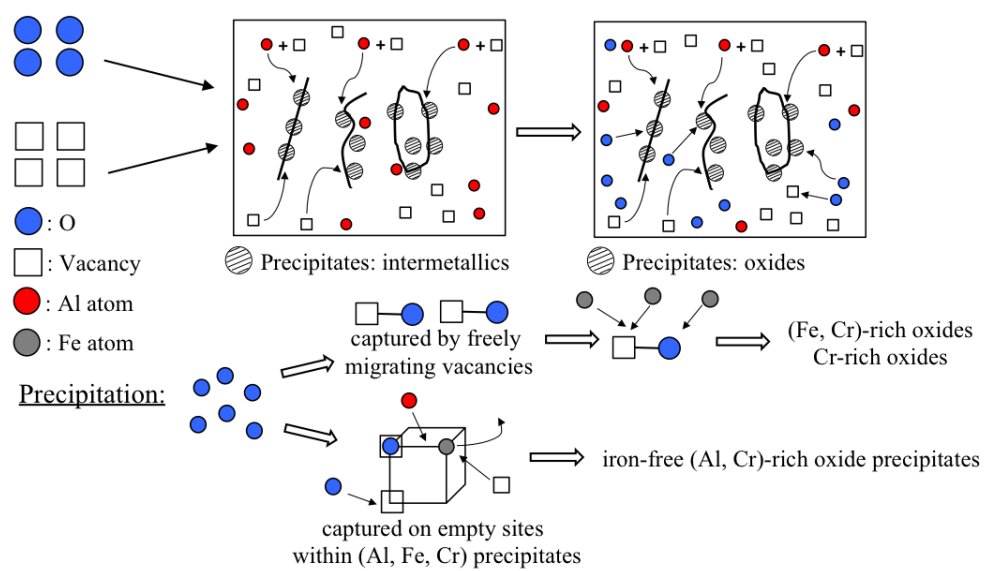
The first step is the Al precipitation during the Al implantation stage at room temperature. Thanks to radiation-enhanced diffusion, Al atoms can diffuse towards point defect sinks (ex: GBs, dislocation lines, dislocation loops...) and segregate in their vicinity. Due to the local increase of the Al content near point defect sinks, the concentration of Al seems to exceed locally the solubility limit and thus precipitation starts. The precipitates contain both Fe and Al and their diffraction pattern contains features appropriate for the *fcc*-structure.

Assuming that the precipitation starts in the form of Fe₃Al intermetallics, one can expect that these precipitates are attractive sinks for vacancies created during the implantation. Indeed, the formation energy of vacancies on the iron sublattices of Fe₃Al [Besson, 2008] is noticeably lower than that in the Fe bulk (~ 1.6 - 2 eV [Matter, 1979; de Schepper, 1983; Schaefer, 1987]). Vacancies are expected to replace preferably Fe atoms rather than Al atoms. As a consequence, Al atoms still stay within precipitates, whereas Fe atoms are removed from them into the surrounding lattice. In addition, the capture of vacancies in precipitates leads to the accumulation of empty sites within the precipitates. Cr atoms may also be removed by vacancies. However, it seems that they are removed slower than Fe atoms since both EFTEM and APT analyses indicate that the resulting precipitates after two-stages irradiation contain both Al and Cr in as-implanted state.

1st step: Al⁺ implantation at RT



2nd step: O⁺ implantation at RT



3rd step: thermal annealing at 500 °C and 3 hours

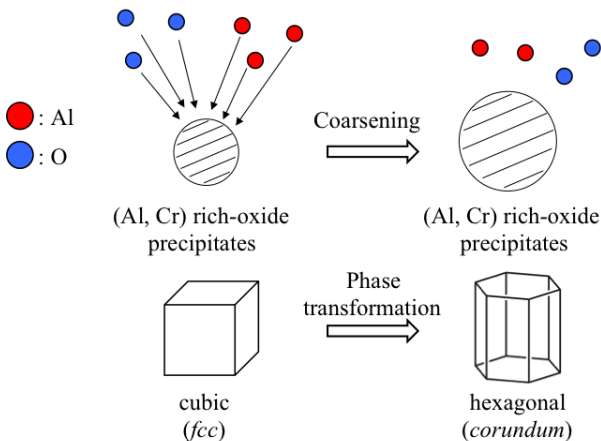


Fig. 4.2 A schema of physical mechanisms involved in precipitate synthesis

The second step takes place at the stage of O implantation at room temperature. Oxygen is an interstitial impurity, which requires no other point defects to assist the diffusion. But oxygen atoms can be captured by the lattice vacancies, including both freely migrating vacancies and those captured within precipitates. Oxidation occurs at each precipitate whatever metallic elements are enriched in, because of their good affinity to oxygen. As a result, oxygen atoms captured in free vacancies can serve as nucleation sites for such precipitates as (Fe, Cr)-rich or Cr-rich oxides. On the other hand, oxygen atoms captured on empty sites of Al-containing precipitates promotes the formation of (Al, Cr, Fe) oxides. Having in mind that vacancies in (Al, Cr, Fe) precipitates tend to eliminate preferentially iron atoms, the relative content of Al and Cr tends to increase, leading eventually to iron-free (Al, Cr) oxide particles. The increase of Al content in the oxide particles and particle growth can be due to the Al atoms that remain in the matrix after the Al implantation stage and continue to move during the O implantation stage and during the annealing stage.

The observation of the orientation relationship between the precipitate lattice and the lattice of the host alloy implies that particle structure is strongly influenced by the surrounding host lattice. The fact that the particle ‘remembers’ the host lattice orientation confirms our assumption that the particle nucleation occurs through the correlated agglomeration of aluminium and oxygen atoms ‘on top’ of the existing iron lattice. The coherency existing between particle and matrix lattices forces the formed (Al, Cr)-rich oxide particles to keep a cubic symmetry. Overall, the oxide lattice orientation with respect to the host lattice is very similar to that observed for yttrium oxide particles in ODS steels [Klimiankou, 2004; Ramar, 2009; Ribis, 2012], which are believed to precipitate by agglomeration of Y and O atoms dissolved in ferritic matrix [Ukai, 2012].

Finally, we observe that thermal annealing results in the noticeable particle coarsening. The particle size evolution obtained experimentally by TEM (see Fig. 3.7 in Chapter 3) confirms this suggestion. The Al and O contents in the matrix and in the identified clusters measured by APT (see Table 3.1 in Chapter 3) revealed that only a relatively small part of implanted Al and O atoms are involved in the precipitate nucleation during the implantation. This indicates thermal annealing at 500 °C strongly accelerates the diffusion of oxygen and aluminum atoms, which continue to be captured by oxide particles.

In addition to the particle growth, one observes that high temperature annealing promotes phase transformation within the particles. While at the early stages of particle growth they

have the cubic lattice structure, at high temperature the structure transforms into the hexagonal one, which is appropriate to the ground-state structure of Al-Cr oxide (corundum). This kind of high-temperature phase transformation is well known and is not unexpected. For example, Khatibi *et al.* [Khatibi, 2012; Khatibi, 2013] reported the phase transformation from cubic to corundum $(Al_{1-x}Cr_x)_2O_3$ in the temperature range of 900-1100 °C. Our observation is consistent also with the results of Najafi *et al.* [Najafi, 2011; Najafi, 2013] who used similar methods to synthesize $(Al_{1-x}Cr_x)_2O_3$ and applied thermal annealing to induce a phase transformation.

Conclusion and perspectives

Oxide Dispersed Strengthened (ODS) steels, which are reinforced with metal dispersions of nano-oxides (based on Y, Ti and O elements), are promising candidates for not only the application of fuel cladding of SFR but also the structural materials (e.g. first wall) of fusion reactors. The dispersoid serves as a block for mobile dislocation to improve the creep resistance at high-temperature and as a sink of point defects induced by radiation displacement to maintain superior radiation resistance. However, there are only few systematic studies that are dedicated to well understand the precipitation behavior of nano-oxide particles. The detailed understanding of the mechanisms involved in the precipitation of these nano-oxide particles would improve manufacturing and mechanical properties of these ODS steels, with a strong economic impact for their industrialization.

The main objective of this PhD study was to study experimentally the mechanisms involved in the precipitation of nano-oxide particles in high purity FeCr model alloys. An analytical approach by ion implantation and subsequent thermal annealing was used: high purity Fe-10Cr model alloys were implanted with Al and O ions at room temperature. Subsequent thermal annealing was effected in as-implanted samples at 500 °C and 3 hours. The morphology, crystal structure and chemical composition of precipitates before and after thermal annealing were characterized by conventional and analytical transmission electron microscopy (TEM) observations combining with atom probe tomography (APT) analyses.

- The main result of this study is a clear demonstration of the feasibility of (Al, Cr)-rich oxides precipitation in Fe-Cr alloy by introducing Al⁺ and O⁺ ions via ion implantation since TEM observations (Fig. 3.5) showed that the nano-oxides appear in the Fe-10Cr matrix upon ion implantation at room temperature without subsequent annealing.
- In contrast to conventional ion beam synthesis technique, the post-implantation thermal treatment was not a prerequisite to start the precipitation. The observed enrichment of implanted elements at extended structural defects, such as grain boundaries and dislocations (Fig. 3.41-3.44) indicated the relatively high diffusion rate of Al and O atoms in the high purity Fe10Cr alloy. The mobility estimation revealed that the diffusion of implanted Al and O atoms at room temperature was enhanced by

point defects created during ion implantation. Furthermore, the estimated mobility of implanted Al and O atoms was found to be well above the required mobility threshold.

- The results of single-beam implantation experiment (see Annexe E) showed that (Fe,Al)-rich precipitates nucleated by the end of the implantation stage. In addition, the formation of precipitates was observed to occur at grain boundaries. This observation correlates well with the results of two-beam implantation experiment, where oxide particles were found to be associated with extended defects (grain boundaries and dislocations). It indicates that the precipitate nucleation requires no oxygen in order to start, at least at room temperature. Al-rich precipitates are assumed to be formed during the Al implantation stage. The capture of vacancies in precipitates leads to the accumulation of empty sites within the precipitates.
- Combining the results of single-beam and two-beam implantation experiments, we assume that oxide particles are obtained via oxidation of Al-containing precipitates that nucleated already during the Al implantation run. Oxygen atoms can be captured by the lattice vacancies, including both freely migrating vacancies and those captured within precipitates. As a result, oxygen atoms captured in free vacancies can serve as nucleation sites for such precipitates as (Fe, Cr)-rich or Cr-rich oxides. On the other hand, oxygen atoms captured on empty sites of Al-containing precipitates promotes the formation of (Al, Cr) oxides.
- TEM observations after thermal annealing show the noticeable particle coarsening (Fig. 3.6-3.7). The resulting EFTEM elemental maps (Fig. 3.8-3.13) as well as APT cluster analyses (Fig. 3.33) revealed that precipitates are always (Al, Cr)-rich oxides before and after thermal annealing. The high-resolution TEM experiments and diffraction pattern analyses observed the high temperature annealing promotes phase transformation within the particles. While at the early stages of particle growth they have a cubic lattice structure, at high temperature the structure transforms into the hexagonal one, which is appropriate to the ground-state structure of Al-Cr oxide (corundum).

In conclusion, we studied experimentally the synthesis of nano-oxide precipitates in high purity FeCr model alloys by ion implantation and subsequent thermal annealing. A mechanism involved in the precipitation of nano-oxide particles in FeCr model alloys is

proposed in this manuscript, based on the obtained experimental results and the existing literature. The results obtained on high purity FeCr model alloys are fully applicable to industrial materials: indeed ion implantation reproduces the conditions of milling and heat treatments are at equivalent temperatures to those of thermo-mechanical treatments.

Several researches can be proposed for the continuity of this study:

- The high-resolution TEM observations were carried out in annealed conventional TEM thin foils. However, the hexagonal phase crystal structure was hard to be identified and further precise characterizations are required. An annealed FIB lamina is thus expected to facilitate the high-resolution TEM observations.
- The results obtained in single-beam Al ion implantation experiment are preliminary. Further TEM observations and other analyses need to undertake in order to obtain more information about chemical compositions and crystal structure of Al-rich precipitates formed at this implantation stage.
- A new (Y, Ti, O) system in high purity FeCr model alloys is proposed to be studied in order to match perfectly industrial materials' elements and understand the appearance of these nano-particles during grinding, based on the same experimental approach as shown in this manuscript.
- A tight coupling between experimental and modeling studies will help to understand better the first early stages of the nano-oxide precipitation in ODS alloys.

Annexes

Annexe A: APT and TEM sample preparation by Focused Ion Beam	135
Annexe B: (Fe,Cr)- and Cr-rich oxides	139
Annexe C: Precipitation in dislocation loops in annealed specimens	143
Annexe D: The effect of sample thickness on particle precipitation.....	145
Annexe E: TEM characterizations of single Al implanted samples.....	151
Annexe F: Scientific communications.....	157
Annexe G: Résumé en français de la thèse.....	159

Annexe A: APT and TEM sample preparation by Focused Ion Beam

A.1 APT specimen preparation by FIB

APT specimen preparation was carried out at IM2NP in Marseille, France in close collaboration with the group “Réactivité et Diffusion aux Interfaces” (staff: Dr Marion Descoins and Dr Dominique Mangelinck). Both as-implanted and annealed dimpled discs were firstly prepared at CSNSM/JANNuS Orsay, France, and then sent to IM2NP, Marseille for further as-implanted and annealed APT specimen fabrication.

In most case, APT specimens are needle-shaped tips, which are suitable to APT analysis since: (1) they are sharp enough to allow field evaporation; (2) they are robust enough to allow for significant evaporation events to occur.

While electrolytic polishing has been widely used for fabricating needle-shaped tips, it is still difficult to fabricate the tip from a highly specific site, which may contains interesting features of the materials. Moreover, not all materials have sufficient electrical conductivity to enable electropolishing. Recently, scanning electron microscope-focused ion beam (SEM-FIB) instruments have been well developed so that it enables specimens to be fabricated from any solid material with a local precision of approximately 10 nm. Different FIB-based methods were summarized in [Gault, 2012]. Among these FIB-based methods, we chose in-situ lift-out method to fabricate APT tips with using a FEI Helio 600 NanoLab 2-30 kV focused ion beam (FIB).

A lift-out method published by Thompson *et al.* [Thompson, 2007] has been widely adopted by the atom probe community. Prior to inserting the specimen in the FIB, a thin capping layer of sputter-coated nickel was applied to protect the top edge of the specimen from ion-beam damage. Once that was done, the specimen was mounted on the stage and inserted into the FIB. The in-situ lift-out process started.

Fig. A.1 illustrates the general steps of the lift-out procedure. A region of interest (ROI) was firstly selected. Secondly, a FIB-deposited platinum (Pt) strip was added to protect the surface and to mark the region to be extracted (arrowed in Fig. A.1(a)). The platinum layer is typically 2-3 μm wide and ~ 100 nm thick.

A triangle-shaped bar of the material, often referred to as a wedge, was then prepared by milling trenches from normal to the surface. Ga^+ ions beam was used as a tool to achieve milling and cutting. In this case, trench 1 (arrow 1 in Fig. A.1(b)) was created by tilting the stage to 22° (with respect to the electron beam) and milling with ion current in a rectangular pattern. The ion beam is scanned parallel to the long axis of the wedge starting far from the platinum strip and proceeding to the near edge. Trench 2 (arrow 2 in Fig. A.2(b)) was then created using the same procedure after rotating the stage through 180° . Milling was completed when trenches 1 and 2 meet beneath the ROI. Once the angled cuts were complete, a cut (arrow 3 in Fig. A.1(b)) was made at one end of the bar to release it from the specimen. The cut used a long rectangular pattern to cut across the entire wedge leaving behind a cantilevered wedge.

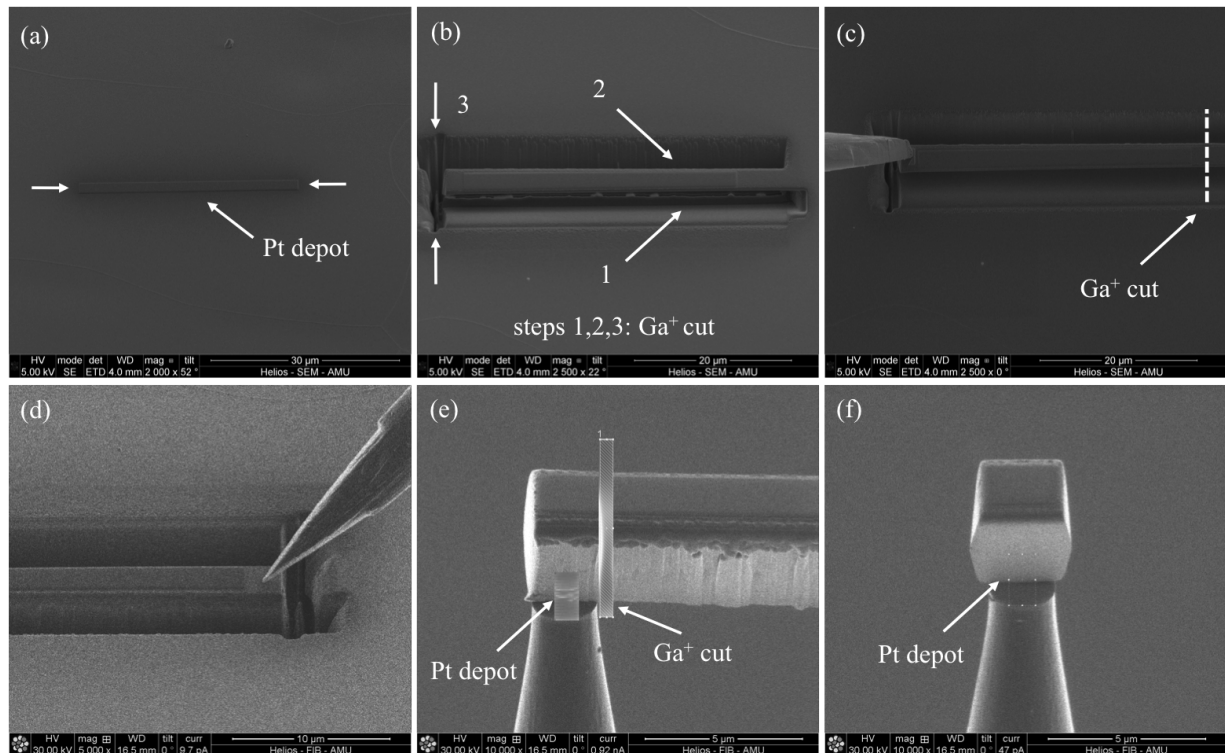


Fig. A.1 Images showing the initial steps of the in-situ lift-out process: (a) After depositing a protective strip over the region of interest (ROI) by FIB. (b) After the two angled cuts (arrows 1 and 2), and one end of the bar has been cut free (arrow 3). (c-d) Wedge cut-free and lifted out from the sample. (e) The wedge is positioned above the carrier microtip. The wedge is attached to the carrier tip with FIB-deposited platinum (left arrow) and then cut free from the carrier tip (right arrow). (f) Wedge is welded by depositing platinum on the opposite side of the carrier tip.

After returning the FIB stage to 0° tilt, an in-situ micromanipulator was then positioned adjacent to the free end of the bar. Pt deposition was used to attach the needle to the free end of the bar (Fig. A.1(c-d)). The Ga^+ ions were then used to cut free the other end of the specimen (Fig. A.1(c)), so that the bar was no longer attached to the original specimen.

The wedge was then removed from the original specimen by carefully lowering the FIB stage, and the micromanipulator was used to transfer the specimen onto the pre-fabricated arrays or coupons (Microtip coupons [Larson, 2001]). The presence of many microtips per coupon makes it easier to collect a significant number of specimens in a short amount of time under very similar processing conditions. The end of the wedge was welded to the microtip with Pt and the slice was cut free by using Ga^+ ions (Fig. A.1(e)). Another side of the wedge was also welded to the microtip with Pt (Fig. A.1(f)). The last two steps were repeated several times until the wedge was exhausted. As a result, we obtained a series of small wedge pieces.

The process of converting a lift-out wedge into a sub-20 nm diameter sharp needle is accomplished through a series of annular milling steps [Larson, 1999] followed by a low-energy FIB cleanup step [Thompson, 2007].

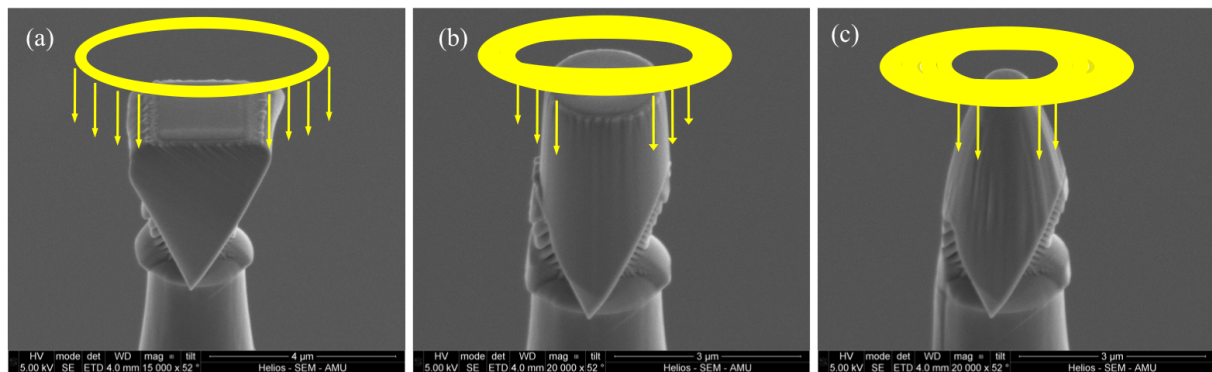


Fig. A.2 Milling of a tip by using annular milling pattern in a FIB. The inner annulus is progressively decreased in size from (a) to (c), while the beam current is decreased in order to improve resolution.

Tip shaping was accomplished by applying an annular milling pattern with constant outer diameter and a decreasing inner diameter (Fig. A. 2(a-c)). The milling proceeded from the outer diameter of the pattern to the inner diameter of the pattern to best control any potential for redeposition of removed material. Each pattern was applied for a length of time sufficient to achieve the desired tip diameter. The final tip shaping was accomplished with the low-energy (2-5 keV) FIB cleanup step. The goal of the low-energy milling step is to remove the damaged region created by high-energy milling.

A.2 TEM specimen preparation by FIB

TEM specimen preparation by FIB has been performed at CEA/DEN/DANS/DMN/SRMA by Benoît Arnal. The FIB-based lift-out procedure for TEM lamina preparation is quite similar to that for APT specimen preparation. In most case, the TEM lamina preparation consists of mill a thin slice of the material perpendicularly to the specimen surface, to glue it on a TEM

sample holder and to finish the thinning using low-voltage focused ion-beams [Giannuzzi, 1999; Jublot, 2014]. However, TEM FIB lamina should be transparent to electrons and the final size of the cross-section can be as large as $150\ \mu\text{m}^2$, to as small as $45\ \mu\text{m}^2$. This specialized requirement imposes to modify several steps in the lift-out procedure.

The first difference is that the FIB-deposited capping layer was a layer of tungsten instead of platinum and nickel. The second difference is that only two trenches were milled on either side of the tungsten that has been deposited above the ROI. The trenches have been milled so as to just touch the tungsten on either side, leaving a wall of material in the centre that is typically two microns thick.

The third difference is the shape of milling pattern applied during precise polishing. Instead of using annular milling in APT specimen preparation, rectangular milling pattern was applied directly to the surfaces of the membrane. The beam current reduced progressively when the thickness of membrane reduced. The low beam current would limit the creation of damage in the specimen. The last polishing step, again with reduced beam current, brought the membrane to a thickness of between 50 and 120 μm . At this thickness, the membrane is electron transparent, and will clearly display the cross-section of the ROI in a TEM.

The final step involves the use of micromanipulator, which is capable of moving the extremely thin membrane to the sample holder through exceptionally fine motions. With the use of this item, FIB lamina was attracted to the micromanipulator and adhered to it when they came into contact with it. Finally, the lamina was transported and welded to the sample holder.

Annexe B: (Fe,Cr)- and Cr-rich oxides

- *(Fe,Cr)-rich oxides*

The proxigram algorithms have been applied to cluster analysis during APT measurements. In the first step of this technique, a 50% Cr iso-concentration surface (green color) was applied to the reconstruction, as shown in Fig. B.1. A specific isosurface (pink color) identifying a precipitate was isolated, and the local atomic neighborhood adjacent to the interface was then examined. Atomic positions are correlated with respect to their distance to the local normal of the isosurface, making the algorithm independent of the interface geometry. As a result, a concentration distribution profile for any of the constituent elements can be generated characterizing the nature of the interface and its local environment.

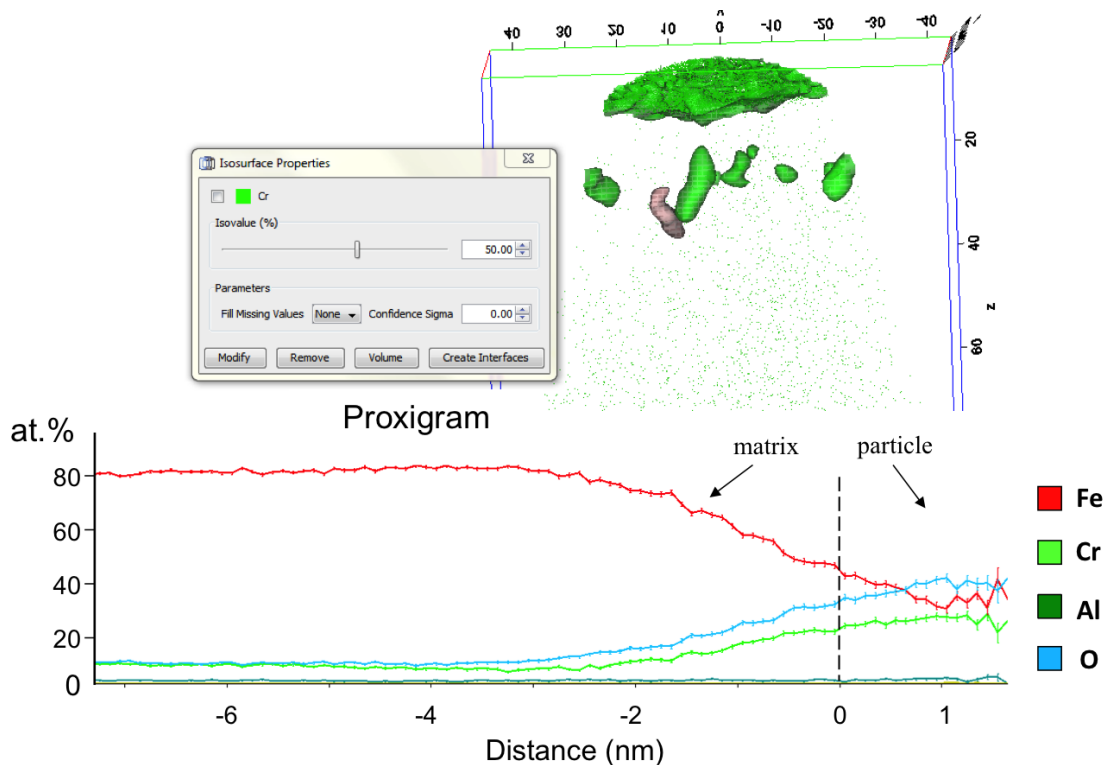


Fig. B.1 Proxigram analysis in annealed tip. Upper: A 50% Cr iso-concentration surface (green color). The surface selected for analysis is drawn in pink color. Lower: The resulting proxigram composition profiles.

As shown in Fig. B.1, the composition profiles of Fe, Cr and O pass through the interface between the matrix and the identified particle. The concentration of Fe decreases, whereas those of Cr and O increase from the matrix to the particle. The concentration of Al is negligible comparing to other elements. The resulting proxigram composition profiles indicate that the identified particle is (Fe, Cr)-rich oxides. This result confirms the synthesis of other oxide particles.

High resolution TEM observation was performed in (Fe, Cr)-rich oxide particles. The results are presented in Fig. B.2.

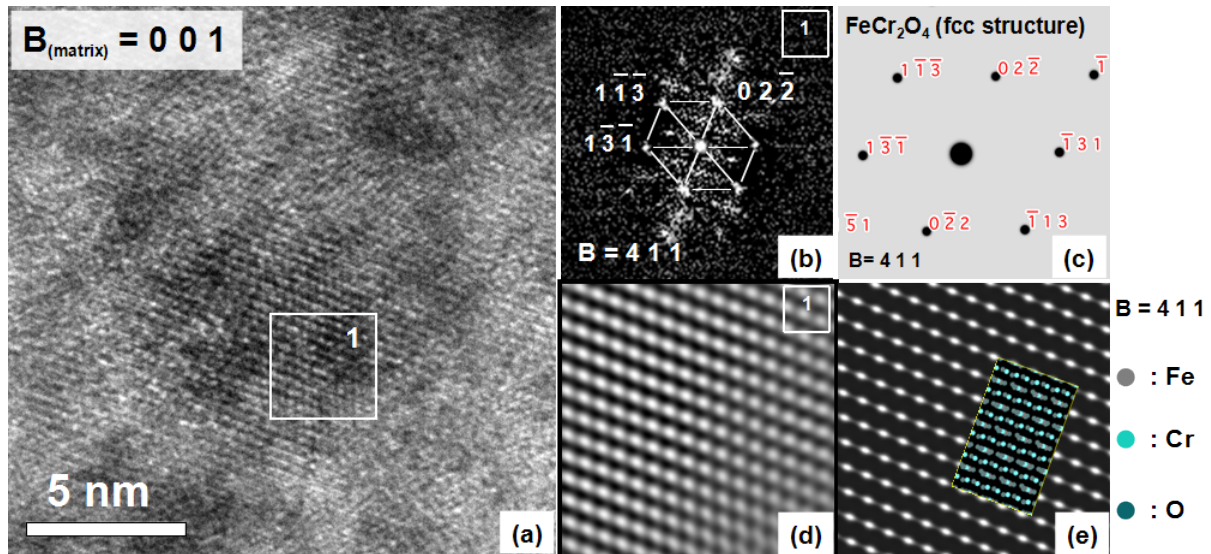


Fig. B.2 (a) High resolution TEM image of the particle oriented along $\langle 411 \rangle$; (b) The Fourier transform of the square marked in (a); (c) The simulated diffraction pattern of FeCr_2O_4 oriented along the $\langle 411 \rangle$ axis; (d) Detailed view of the square marked in (a); (e) Simulated HR-TEM image of FeCr_2O_4 oriented along the $\langle 411 \rangle$ axis.

The particle shown in Fig. B.2(a) presents cubic symmetry. The Fourier transform analysis (Fig. B.2(b)) shows that the particle lattice is oriented along $\langle 411 \rangle$ zone axis of presumably fcc structure and has the lattice parameter of $8.35 \pm 0.15 \text{ \AA}$, which correlates well with the reference lattice parameter of FeCr_2O_4 ($\sim 8.28 \text{ \AA}$ [Villars, 1985]). The simulated diffraction pattern of FeCr_2O_4 oriented along $\langle 411 \rangle$ is consistent with the Fourier transform pattern. In addition, the zoom view of the particle (Fig. B. 2(d)) is very similar with the HRTEM image (Fig. B.2(e)) simulated by JEMS software. However, the structure and chemical composition of oxide in nanometer-size particles should not necessarily coincide with those of any known large-scale mineral.

- *Cr-rich oxides*

The resulting energy-filtered images are presented in Fig. B.3. The dark contrast on the Fe- $\text{M}_{2,3}$ elemental map (Fig. B.3(b)) show the local Fe deficiency. The Fe elemental map gives a clear view of this precipitate in the matrix. The local Al deficiency is also observed in the Al elemental map (Figure B.3(d)). The other three elemental maps acquired by the filtering of the Cr- $\text{M}_{2,3}$ and O-K edges exhibit the same pattern of bright contrasts which correspond to the precipitate observed on Fe and Al elemental maps. This suggests that the precipitate are Cr-rich oxides.

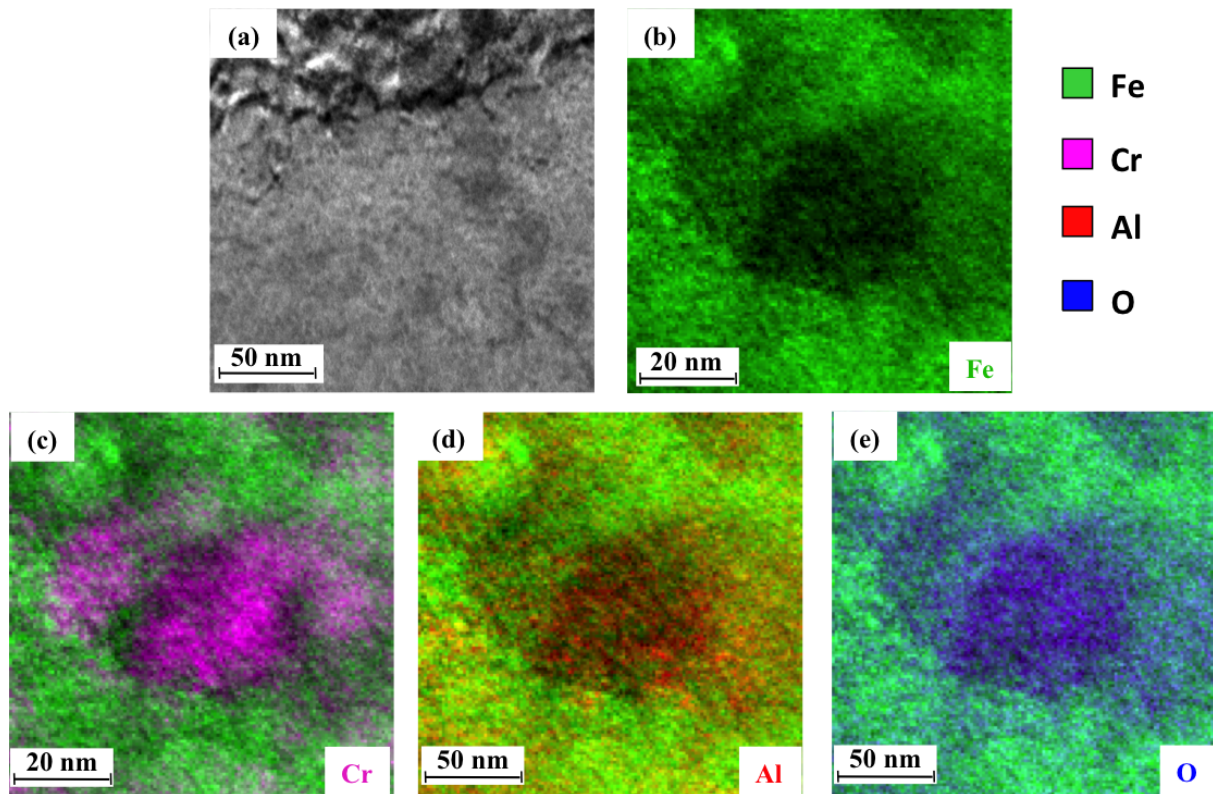


Fig. B.3 Energy-filtered TEM (EFTEM) characterization of typical precipitates in the annealed thin foil at 500 °C and 3 hours: (a) Bright Field (BF) TEM image of region of interest for EFTEM characterization. The panels show jump-ratio EFTEM elemental maps of Fe-M_{2,3} edge (b), Cr-M_{2,3} edge (c), Al-L_{2,3} edge (d) and three-window EFTEM elemental map of O-K edge (e). The colors indicate the elements as marked in the legend.

Fig. B.4 shows HRTEM images taken on two different particles in as-implanted thin foils. Both of two particles present hexagonal symmetry. The HRTEM resolution being about 2 Å, we can observe clearly a particle without seeing the matrix, even if there is a special orientation with the matrix. The lattice of the particle observed in Fig. B.4(a) is oriented along <0001>-axis and, assuming it to be *hcp*, corresponds to the lattice parameter of $a=4.96$ Å and $c=13$ Å, very similar to the reference value of Cr₂O₃ [Villars, 1985].

The lattice of the particle observed in Fig. B.4(b) is also oriented along <0001>-axis and corresponds to the lattice parameter of $a=4.97$ Å and $c=13.1$ Å. These results are consistent with that identified in the previous particle. However, the structure and chemical composition of oxide in nanometer-size particles should not necessarily coincide with those of any known large-scale mineral.

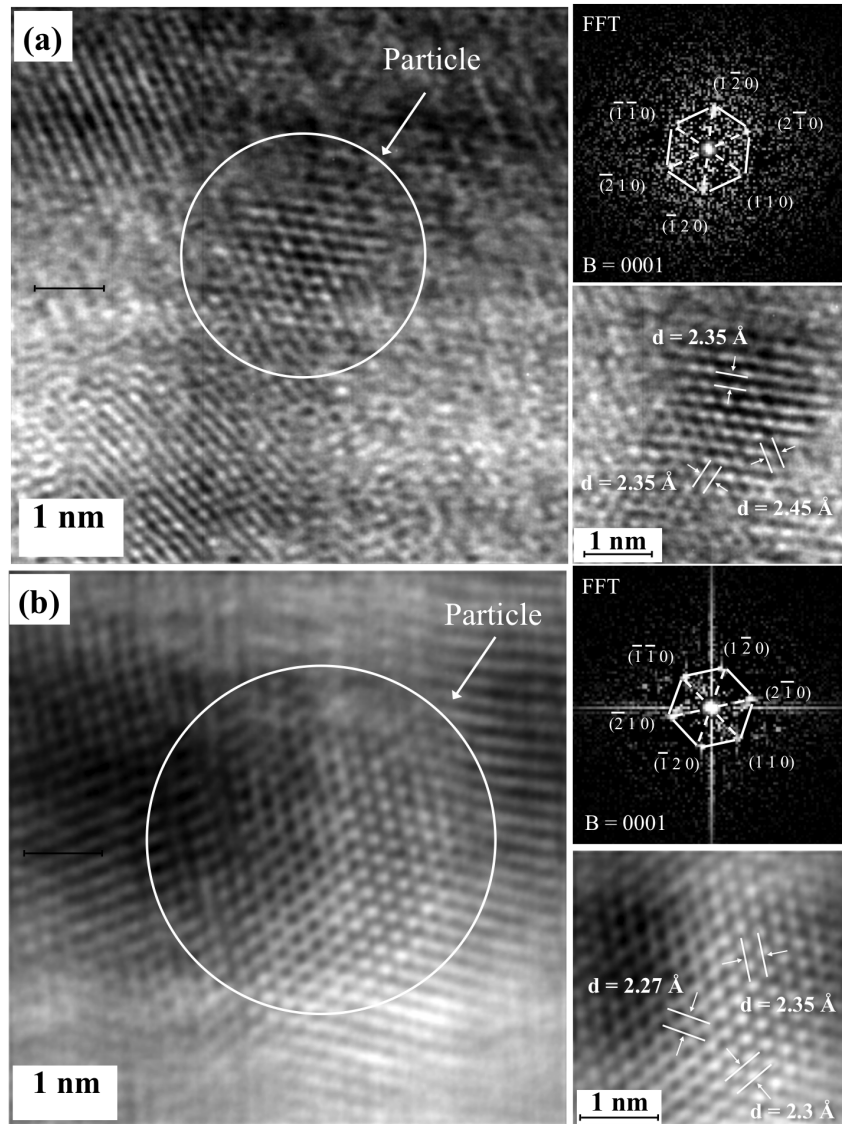


Fig. B.4 Energy-filtered TEM (EFTEM) characterization of typical precipitates in the annealed thin foil at 500 °C and 3 hours: (a) Bright Field (BF) TEM image of region of interest for EFTEM characterization. The panels show jump-ratio EFTEM elemental maps of Fe- $M_{2,3}$ edge (b), Cr- $M_{2,3}$ edge (c), Al- $L_{2,3}$ edge (d) and three-window EFTEM elemental map of O-K edge (e). The colors indicate the elements as marked in the legend.

Annexe C: Precipitation in dislocation loops in annealed specimens

Thermal annealing was carried out inside the microscope *FEI Tecnai G² 20 twin* with using the *FEI TEM* heating sample holder. The annealing temperature was set at 500 °C with a duration about 3 hours. The vacuum condition in the column of the TEM was 1.2×10^{-5} Pa. Annealed TEM thin foils were observed by conventional TEM methods as shown in Chapter 3. Here some pictures show the precipitation in dislocation loops in an annealed specimen.

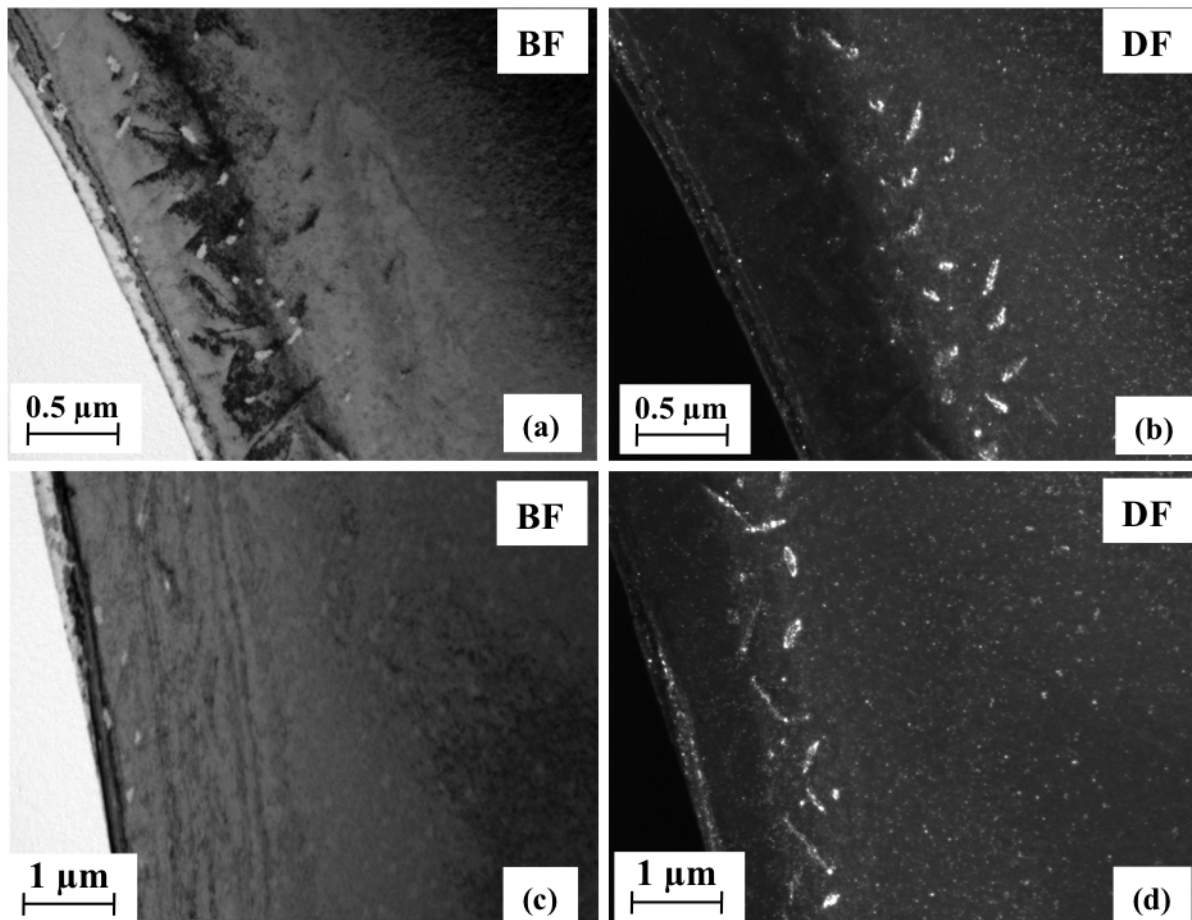


Fig. C.1 TEM micrographs showing the precipitation in dislocation loops after thermal annealing in two different regions: (a) BF TEM micrograph; (b) Corresponding DF TEM micrograph; (c) BF TEM micrograph; (d) Corresponding DF TEM micrograph.

Fig. C.1(a) & (c) shows BF TEM images taken in two regions near the hole. The corresponding DF TEM images (Fig. C.1(b) & (d)) indicate that dislocation loops are decorated with precipitates. The size of precipitates in dislocation loops increases significantly comparing to those in as-implanted specimens. Conventional TEM observation effected in annealed TEM thin foils confirms again the precipitation occurred in dislocation loops (see section 5, Chapter 3).

Annexe D: The effect of sample thickness on particle precipitation

A surprising effect observed in our study is the sensitivity of precipitation to the thickness of TEM samples.

Fig. D.1(a) is the bright field (BF) TEM image of the as-implanted TEM thin foil. The diffraction pattern inserted in Fig. D.1 shows the matrix is oriented along $\langle 111 \rangle$ direction. The corresponding dark field (DF) TEM image shown in Fig. D.1(b) indicates the distribution of precipitates is heterogeneous. More precisely, precipitates were only observed in the region which looks like a ribbon. Zoom views of the selected square marked in BF and DF TEM images are given in Fig. D.1 (c, d). The numerous bright spots observed in Fig. D.1(d) correspond to the precipitates synthesized due to ion implantation of Al and O.

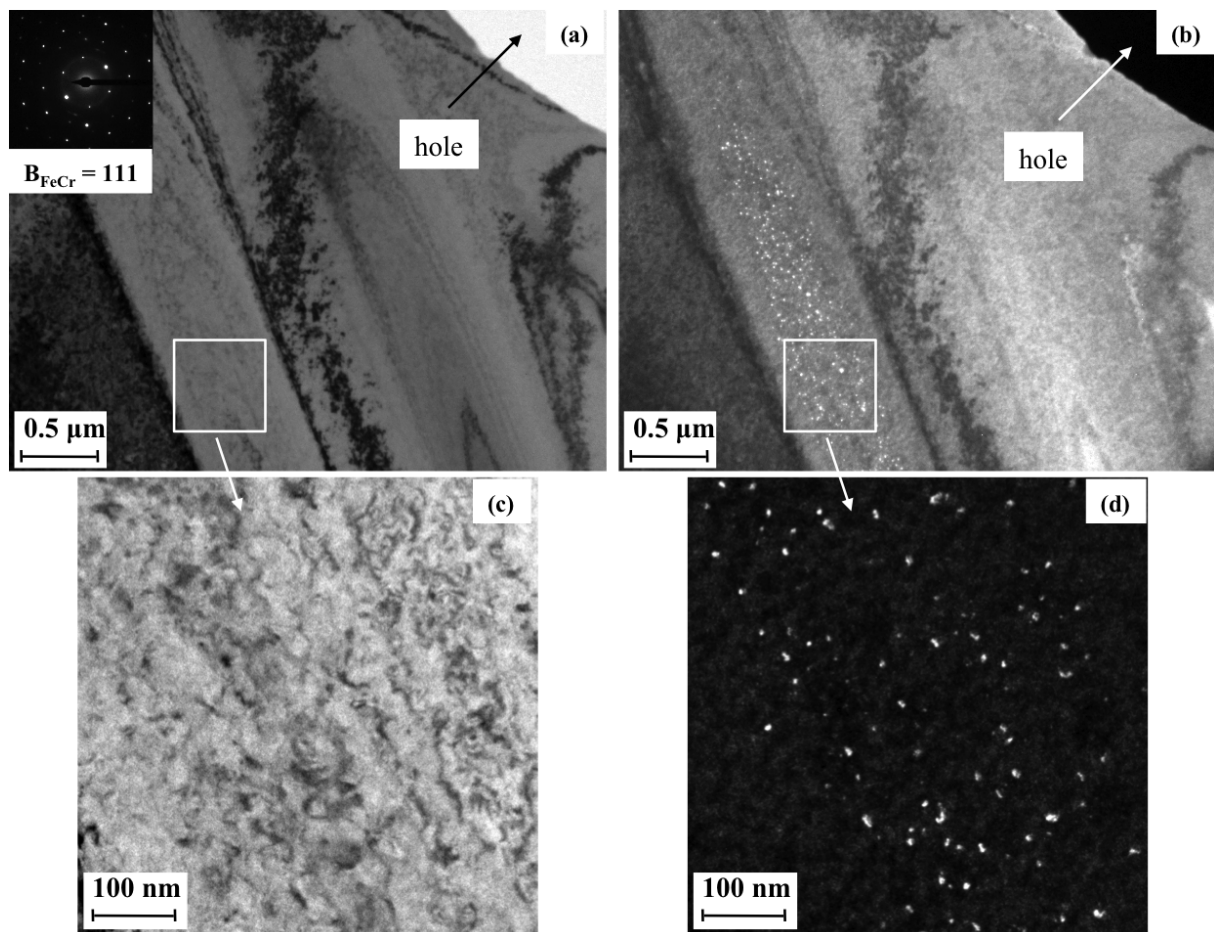


Fig. D.1 (a) BF TEM image of the as-implanted thin-foil sample oriented along $\langle 111 \rangle$ zone axis; (b) Corresponding DF TEM image showing the distribution of precipitates as a function of sample thickness; (c) Zoom view of the selected square marked in (a); (d) Zoom view of the selected square marked in (b).

In fact, the distribution of precipitates as a function of sample thickness is not observed occasionally. The same phenomenon was observed in the DF TEM image (Fig. D.2(a)) taken

from another as-implanted TEM thin foil. The local thickness in this region was estimated by energy-filtered TEM thickness map and added in Fig. D.2(a).

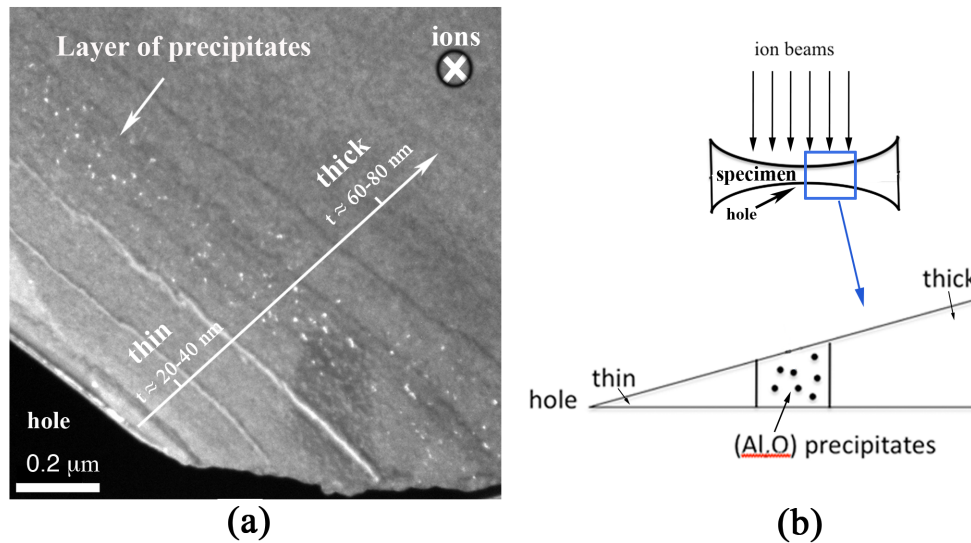


Fig. D.2 (a) DF TEM image showing the distribution of precipitates as a function of sample thickness. The direction of the ion beams with respect to the thin foil is perpendicular to the image; **(b)** A schema that illustrates the ion beam direction with respect to the TEM thin foil and the spatial distribution of precipitates inside the specimen.

A suppressed precipitation in thin sample parts, i.e. close to the hole (see Fig. 2(a)), is not unexpected; it was observed e.g. in [Ruault, 2008] and explained by the combined action of relatively low concentration of implanted ions (the majority being transmitted through the sample) and the proximity of free surfaces that act as efficient sinks of point defects and suppress defect-mediated diffusion of implanted impurity.

However, the absence of visible precipitates in the foil regions thicker than $\sim 60\text{-}80$ nm seems quite unusual and still requires an explanation. One possibility is that the sample in these regions is simply too thick to observe the precipitates. On the other hand, the results of APT measurements suggest that the precipitation in the thicker foil parts can be really delayed or suppressed because of a redistribution of Al atoms during ion implantation with the accompanying decrease of the average aluminum concentration. Indeed, as demonstrated in section 4.1 of Chapter 4, there are reasons to believe that aluminum atoms were able to move up to tens of nanometers at the oxygen implantation stage. This must be equally true for the Al^+ implantation run, where the displacement generation efficiency is more than twice higher. In order to demonstrate this in more quantitative terms, let us apply a simple rate theory model described in detail in Ref. [Fortuna, 2012].

The rate of redistribution of Al atoms is determined by the diffusion coefficient defined with

equation $D_{Al} = D_V C_V + D_I C_I$, which is sensitive to the local concentration of implantation-induced point defects in the foil. The spatial distribution of the product $w_\alpha = D_\alpha C_\alpha$ (where $\alpha=V$ or I for vacancies and interstitials, respectively) can be found from a standard diffusion equation

$$(1)$$

where G is the depth dependent rate of point defect generation (practically identical for vacancies and interstitials) and k_α^2 is the efficiency of α -type defect capture by internal sinks (first of all – dislocations). All parameters in the equation are assumed to vary as a function of only one coordinate - the depth from the sample surface, z . The depth dependence of the point-defect generation rate is described as

$$G(z) = \zeta \Omega \phi g(z), \quad (2)$$

where ζ is the cascade efficiency (a factor that accounts for the intra-cascade point defect annealing [Averback, 1978; Jung, 1983]) and the function $g(z)$, as determined by SRIM calculations, is shown in Fig. D.3(a). At the free sample surfaces ($z = 0$ and $z = L$) the point-defect concentrations are assumed vanishing.

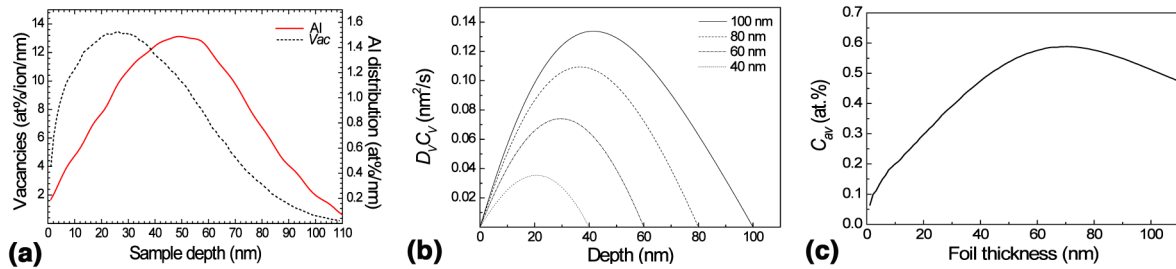


Fig. D.3 (a) Depth profiles of Al ion distribution and vacancy distribution due to 70 keV Al ion implantation into Fe-10Cr, as predicted by SRIM code. Curves are marked in the legend and are normalized per projectile; (b) Steady-state distribution of the product $D_V C_V$ over the foil depth for different foil thicknesses (as indicated in the legend); (c) The dependence of the average concentration C_{av} of Al atoms in a thin foil after the Al^+ implantation run as a function of the foil thickness.

In writing down equation (2) several reasonable simplifications are introduced. First of all, the time derivative of concentrations is omitted because the typical time of point defect equilibrium establishment, $\tau_\alpha \sim \frac{L^2}{D_\alpha}$, is much less than the typical implantation time. Indeed,

even for the slowest moving defect, vacancy, the diffusion coefficient at $\sim 50^\circ\text{C}$ is $D_V \sim 3 \times 10^{-9} \text{ cm}^2/\text{s}$ (assuming the vacancy migration energy of 0.55 eV [Vehanen, 1982] and the prefactor of $1 \text{ cm}^2/\text{s}$), giving $\tau_V \approx 3 \text{ } \mu\text{s}$ for $L \approx 100 \text{ nm}$. Second, the recombination of interstitials and vacancies is not included in equation (1) because point defect concentrations

in TEM films are very low due to the efficient loss at free sample surfaces and only the intra-cascade recombination of point defects is important [Fortuna, 2012]. Finally, we do not take into account the possible interaction of point defects with Al and other solute atoms, which affects point defect concentrations only marginally due to the low solute concentrations.

The solution of equation (1) is found numerically and is shown in Fig. D.3(b) for several relevant foil thicknesses. The curves are for the product $D_I C_V$ and are obtained assuming $k_V^2 \approx 10^{10} \text{ cm}^{-2}$ (a typical dislocation density in ferritic-martensitic steels) and $\xi = 0.2$, while other parameters are those used in the current experiment. The curves for $D_I C_I$ are similar because the sink strengths for vacancies and interstitials are usually nearly the same, while other parameters are insensitive to the point defect type. Hence, the Al diffusion coefficient is approximately twice the value shown in Fig. D.3(b).

Several conclusions can be drawn from Fig. D.3(b). First of all, the value of the diffusion coefficient is such that the mean free path for Al diffusion during the implantation time of 1 hour is $\sim 30 \text{ nm}$ or even more (up to 100 nm , when the dislocation density is below 10^9 cm^{-2} and the main point defect loss is at the foil boundaries). This justifies our statement above. Second, the profile of the Al diffusion coefficient is parabolic in shape, which means that in addition to the pure diffusion there is a drift of Al atoms, which is against the vacancy gradient. This means that the Al atoms should drift towards the position of point defect profile maximum. This is especially important for achieving Al distribution homogeneity in the thin foil parts (with $L < 60 \text{ nm}$), where the rate of Al deposition grows nearly linearly with the depth. Finally, the mobility of Al increases by nearly an order of magnitude when the foil thickness increases from 40 to 100 nm . It means that in the foil parts that have thickness of the order of 100 nm the implanted aluminum should be distributed relatively uniformly over the sample thickness by the end of the implantation run, in spite of the essentially Gaussian ion stopping range profile.

Fig. D.3(c) shows the averaged over the sample thickness concentration of implanted Al atoms, C_{av} , as a function of sample thickness; the dependence is calculated using the SRIM profile for the Al projected range (see Fig. D.3(a)) and the total fluence by the end of Al^+ implantation run. It can be noticed that C_{av} has a peak at sample thicknesses of $40\text{-}80 \text{ nm}$. In thinner regions a noticeable part of the incoming flux is transmitted through the sample, while in thicker parts the implanted ions are redistributed over larger sample volume. Due to the decreased aluminum concentration, the oxide particles formed during subsequent O^+

implantation can be too small to be visible in TEM, or possibly not form at all. However, further studies (e.g. depth profile TEM characterizations of as-implanted samples prepared as cross section shape) need to be done in order to justify this assumption.

Annexe E: TEM characterizations of single Al implanted samples

The TEM thin foils were prepared following conventional processes as described in Chapter 2. In contrast to two-stage ion implantation, the TEM thin foils were implanted by Al^+ ions only at room temperature in this case. The same setup (ion energy, fluence, temperature...) was maintained for this single Al^+ ion implantation. No subsequent thermal annealing was applied. Since only Al^+ ions were introduced, the TEM thin foils are referred in the following as single Al implanted samples. Both conventional and analytical TEM characterizations were carried out in these single Al implanted samples. The results are described below.

Fig. E.1(a) shows a bright field (BF) TEM micrograph of the single Al implanted sample, of which the matrix is oriented along $\langle 113 \rangle$. A grain boundary can be observed in this micrograph.

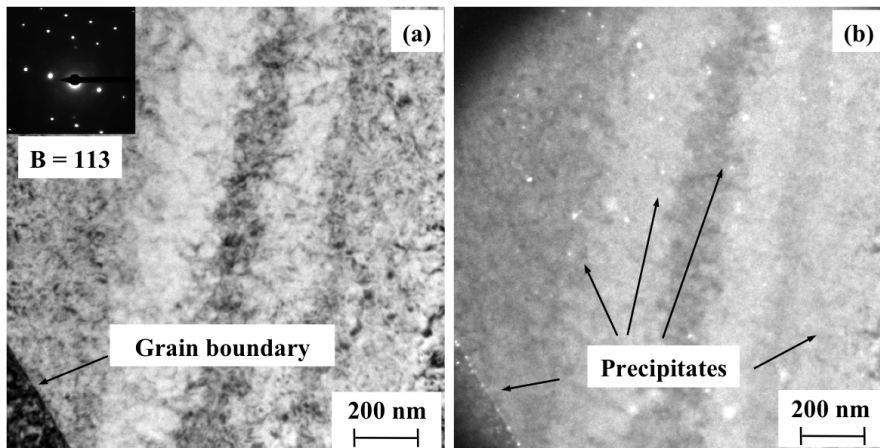


Fig. E.1 (a) Bright field (BF) TEM micrograph of the single Al implanted material oriented along $\langle 113 \rangle$; (b) Corresponding dark field (DF) TEM micrograph showing the presence of precipitates at the grain boundary.

The corresponding dark field (DF) TEM micrograph of this region is shown in Fig. E.1(b). The white spots observed in Fig. E.1 (b) correspond to precipitates. The distribution of precipitates is heterogeneous. The precipitate size ranges from 3 to 25 nm centered on 6 ± 1.5 nm. In addition, the segregation of precipitates was observed at the grain boundary. This observation correlates well with the results of two-stages experiment, where oxide precipitates were found to be associated with the extended defect sinks (grain boundaries and dislocations). The precipitate number density was found to be $(3.2 \pm 0.6) \times 10^7 \text{ m}^{-1}$ at grain boundary and $(3.74 \pm 0.8) \times 10^{20} \text{ m}^{-3}$ in the total volume. Comparing to the number density

measured in Al and O implanted samples ($(1 \pm 0.3) \times 10^{22} \text{ m}^{-3}$), the values measured in single Al implanted samples has a lower order of magnitude.

The crystallographic structure of precipitates was identified by the diffraction pattern analysis. We measured the diffraction pattern (Fig. E.2(a)) on the region where precipitates are hard to be seen directly (Fig. E.2(b)).

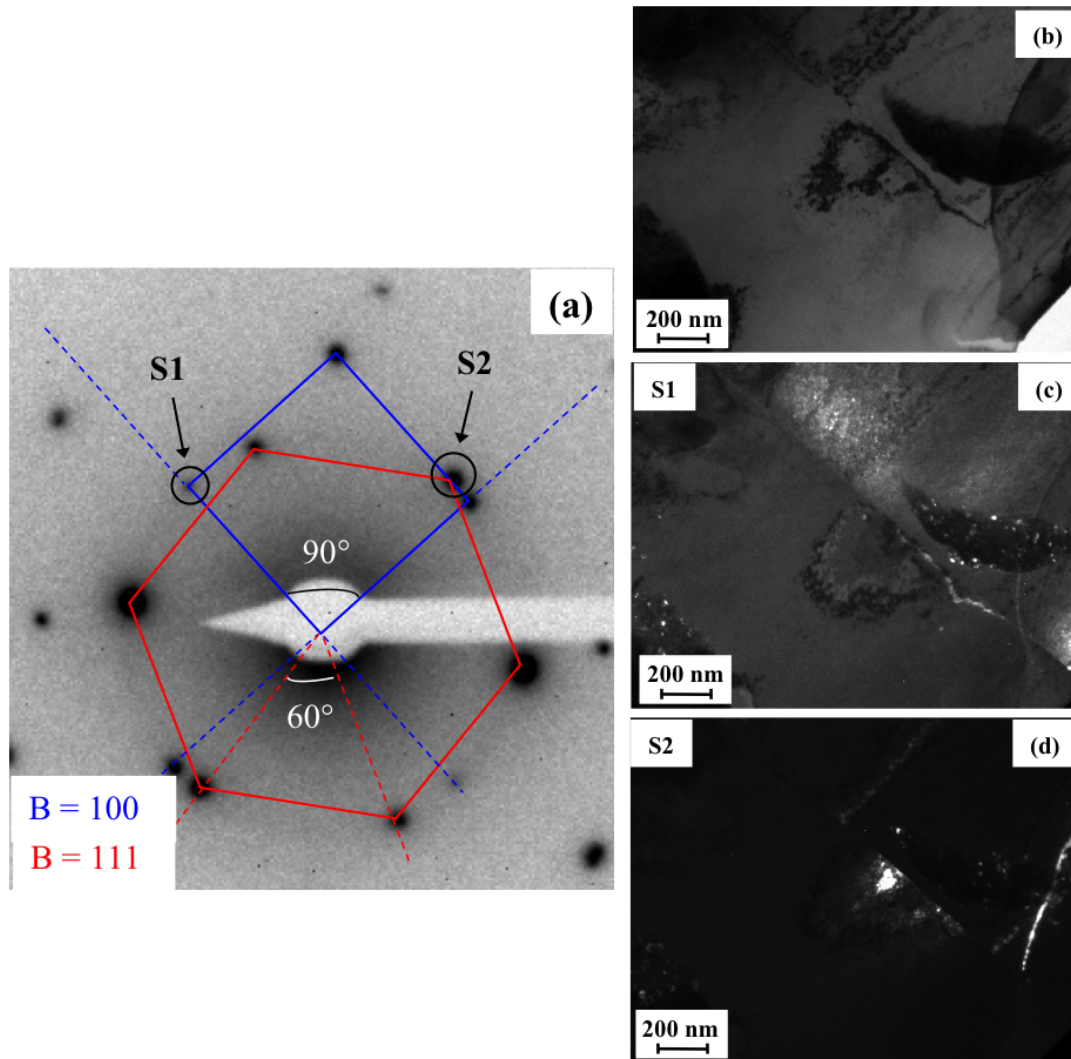


Fig. E.2 Crystalline structure analysis showing the coexistence of the FeCr matrix and the precipitated particles in the single Al implanted material. (a) Diffraction pattern (negative level) for the region corresponding to (b); (b) Bright field (BF) TEM micrograph of the single Al implanted material; (c) Dark field (DF) TEM micrograph corresponding to the spot S1 showing the presence of precipitates; (d) Dark field (DF) TEM micrograph corresponding to the spot S2 showing the presence of precipitates.

Two sets of diffraction spots can be identified in Fig. E.2(a). For the set of diffraction spots marked with blue lines, the intersection angle of the square pattern is $\sim 90^\circ$ and the ratio of the length between two sides is ~ 1 . This set of diffraction spots corresponds to the cubic lattice (either *bcc* or *fcc*) oriented along $\langle 100 \rangle$ zone axis. The lattice parameter determined from the diffraction pattern using the Bragg equation is about $a \approx 2.91 \pm 0.1 \text{ \AA}$ in the case of *bcc* structure and $a \approx 4.1 \pm 0.1 \text{ \AA}$ in the case of *fcc* structure, respectively. The lattice parameter obtained in the case of *bcc* structure agrees with the reference value for FeCr alloy (2.876 \AA

[P. Villars, 1985]). On the other hand, the precipitates, if they are related to this set of diffraction spots, are supposed to be *fcc* lattice with the determined lattice parameter of $a \approx 4.1 \pm 0.1 \text{ \AA}$.

In order to confirm the set of diffraction spots is related to the precipitates, the dark field (DF) TEM micrograph on the selected spot S1 in Fig. E.2(a) was obtained and can be seen in Fig. E.2(c). Bright spots corresponding to precipitates can be observed in the DF micrograph. This confirms our assumption that S1 is a common diffraction spot to both the *bcc* FeCr matrix and the *fcc* precipitates. The simplest guess that precipitates are pure Al ones does not seem improbable. In fact, the pure Al has *fcc* lattice with a lattice parameter of 4.05 \AA [Villars, 1985], so the lattice structure of pure Al is consistent with the experimental observation.

For the other set of diffraction spots, the lattice drawn in red in Fig. E.2(a) has the line intersection angle of $\sim 60^\circ$ and the ratio of the lengths of adjacent sides of ~ 1 . As a consequence, the set of diffraction spots corresponds also to the cubic lattice (either *bcc* or *fcc*) oriented along $\langle 111 \rangle$ zone axis. The estimated value of the lattice parameter is $a \approx 2.87 \pm 0.1 \text{ \AA}$ in the case of *bcc* structure and $a \approx 5.79 \pm 0.1 \text{ \AA}$ in the case of *fcc* structure, respectively. The lattice parameter obtained in the case of *bcc* structure still agrees with the reference value for FeCr alloy (2.876 \AA [P. Villars, 1985]). And we suppose again that the precipitates are *fcc* lattice with a lattice parameter of $a \approx 5.79 \pm 0.1 \text{ \AA}$ if they are related to this set of diffraction spots. For the same reason as the blue lattice set of diffraction spots, the dark field (DF) TEM micrograph on the selected spot S2 in Fig. E.2(a) was obtained and can be seen in Fig. E.2(d). Similarly, bright spots corresponding to precipitates can be observed in the DF micrograph. This confirms our assumption that S2 is also a common diffraction spot to both the *bcc* FeCr matrix and the *fcc* precipitates. In this time, with such a lattice parameter of 5.79 \AA , the precipitates are probably the intermetallic Fe_3Al phase, whose diffraction pattern is characteristic for *fcc* lattice and the lattice parameter $\sim 5.7 \text{ \AA}$ [P. Villars, 1985]. Evidently, the reference value of lattice parameter correlates with the experimental observation.

So, given this diffraction pattern analysis, the precipitates we observed are probably pure Al or the intermetallic Fe_3Al phase.

The EFTEM investigation was applied to single Al implanted TEM thin foils. The region selected for the investigation has the thickness found to be approximately 30 nm ($\frac{L}{\lambda} \sim 0.28$ and $\lambda \sim 110$ nm).

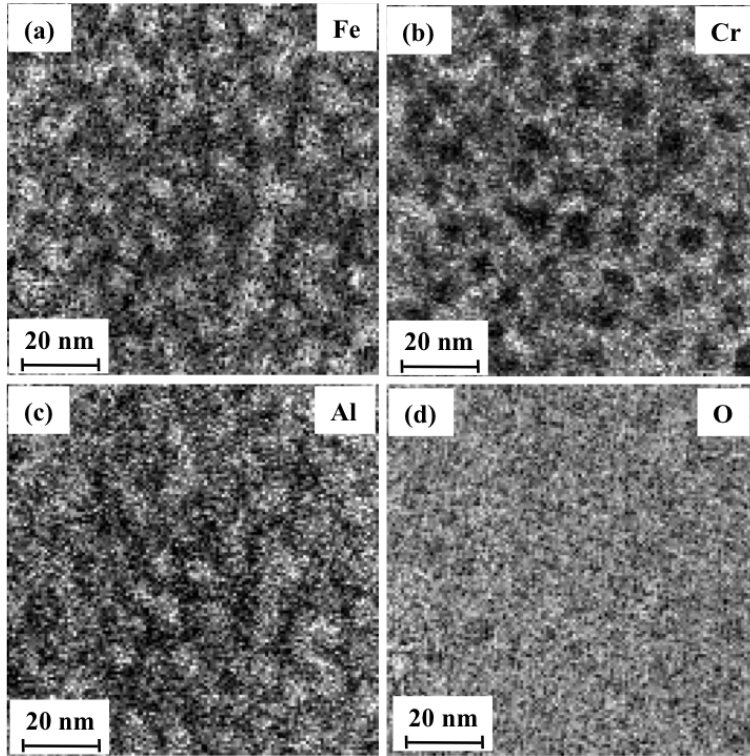


Fig. E.3 Energy-filtered TEM (EFTEM) characterization showing Al and Fe matrix tend to form localized zones that are enriched in both Fe and Al, but depleted with Cr: Three-window EFTEM elemental maps of Fe-L_{2,3} edge (a) and O-K edge (d). Jump ratio EFTEM elemental maps of Cr-M_{2,3} edge (b) and Al-L_{2,3} edge (c).

The resulting energy-filtered images are presented in Fig. E.3. White and dark contrasts seen on the EFTEM elemental maps represent enrichment and depletion of elements in these zones, respectively. The white contrast observed on the Fe-L_{2,3} elemental map (Fig. E.3(a)) correlates well with those on the Al-L_{2,3} elemental map (Fig. E.3(c)). On the contrary, the opposite contrast appears on the Cr-M_{2,3} elemental map (Fig. E.3(b)). The O-K elemental map (Fig. E.3(d)) seems to be homogeneous, which indicates no significant enrichment of oxygen in single Al implanted samples. The EFTEM elemental maps reveal that implanted Al atoms and Fe matrix tend to form localized zones that are enriched in both Fe and Al, but depleted with Cr.

In conclusion, ion implantation of Al⁺ ions only was performed in high purity FeCr at room temperature. Conventional and analytical TEM characterizations were performed in these single Al ion implanted TEM thin foils. The most important result revealed by this Al ion implantation experiment (without a subsequent O ion implantation) is the observation of

precipitates nucleated by the end of the implantation stage. In addition, the formation of precipitates was observed to occur at the grain boundary. These interesting features indicate that the precipitate nucleation requires no oxygen in order to start, at least at room temperature. Secondly, the diffraction pattern analysis indicates that the precipitates have a *fcc*-structure with the lattice parameter of $\sim 4.1 \pm 0.1 \text{ \AA}$ or $\sim 5.79 \pm 0.1 \text{ \AA}$. Comparing experimental values of the lattice parameter with the reference values, precipitates are suggested to be pure Al or intermetallic Fe_3Al phase. Finally, the EFTEM characterization reveals that Al and Fe matrix tend to form localized zones that are enriched in both Fe and Al, but depleted with Cr.

Annexe F: Scientific communications

Publications

- A manuscript in preparation
- **C. Zheng**, A. Gentils, J. Ribis, V. A. Borodin, L. Delauche, B. Arnal, Nano-size metallic oxide particle synthesis in FeCr alloys by ion implantation, Proceedings in IOP Conference Series: Materials Science and Engineering (MSE), submitted (2015)
- **Ce Zheng**, Aurélie Gentils, Joël Ribis, Vladimir A. Borodin, Nano-size oxide particle nucleation in high purity Fe-10%Cr alloy by ion implantation, Proceedings of the International Conference on Solid-Solid Phase Transformations in Inorganic Materials (PTM2015), edited by Matthias Militzer, Gianluigi Botton, Long-Qing Chen, James Howe, Chadwick Sinclair, Hatem Zurob, ISBN 978-0-692-43736-0 (TMS), 2015
- **C. Zheng**, A. Gentils, J. Ribis, V. A. Borodin, Odile Kaïtasov, Metal-Oxide nanoclusters in Fe-10%Cr alloy by Ion implantation, Proceedings of IBMM2014 conference, Nucl. Inst. Meth B **365** (2015) 319
- **C. Zheng**, A. Gentils, J. Ribis, Odile Kaïtasov, V. A. Borodin, M. Descoins, D. Mangelinck, The feasibility of Al-based oxide precipitation in Fe-10%Cr alloy by ion implantation, Philosophical Magazine **94** (2014) 2937

Attended Conferences

April 2015	Materials Research Society (MRS) 2015 Spring meeting, San Francisco, United States of America, Symposium XX: multiscale modeling and experiments on microstructural evolution in nuclear materials, Contributed oral presentation
September 2014	19 th International Conference on Ion Beam Modification of Materials (IBMM 2014), Leuven, Belgium, poster presentation
September 2014	XIVes Journées Nationales de Radiochimie et de Chimie Nucléaire (JNR 2014), Orsay, France, poster presentation
June 2013	3M workshop Materials for Nuclear Energy, INSTN, CEA, Saclay, France, poster presentation

Annexe G: Résumé en français de la thèse

Synthèse de nano-amas d'oxyde métallique par implantation ionique dans un alliage Fe10Cr de haute pureté

Le développement des centrales nucléaires du futur a pour objectif de répondre à un certain nombre de défis énergétiques soulevés par la demande mondiale croissante en énergie, la diminution des ressources en énergie fossile et la consommation durable des ressources en combustibles. Ces réacteurs du futur seront soit basés sur le phénomène de fission (réacteurs de génération IV¹), soit sur la fusion (réacteur ITER). Parmi les six concepts de réacteurs à fission retenus par le forum international de génération IV, la France a fait le choix de s'impliquer notamment sur les réacteurs à neutrons rapides refroidis au sodium (RNR-Na), et consacre une grande partie de ses efforts de recherche au développement de ce type de réacteur. Les conditions de fonctionnement envisagées pour les gainages combustibles appliqués dans les RNR-Na consistent en une température de 650 °C, un taux d'irradiation qui peut dépasser 200 dpa en fin de cycle². Les conditions envisagées pour la fusion nécessitent également des matériaux résistants à de fortes températures et taux d'endommagement. Malheureusement, aucun des matériaux actuellement utilisés dans l'industrie électronucléaire ne s'adapte parfaitement à ces conditions. C'est pourquoi il est nécessaire de développer de nouvelles gammes de matériaux.

Les aciers ODS (Oxide Dispersed Strengthened Steels), renforcés par des dispersions de nano-oxydes métalliques (à base d'éléments Y, Ti et O), sont des matériaux prometteurs pour les réacteurs nucléaires du futur. Ces aciers, élaborés par métallurgie de poudres, présentent en effet de bonnes propriétés mécaniques à haute température et une bonne résistance à l'irradiation sous flux neutronique. Le procédé de synthèse des aciers ODS se décompose en plusieurs étapes^{3,4}. Afin d'obtenir la fine précipitation désirée, l'oxyde d'yttrium est mis en solution solide dans la matrice métallique par une opération de broyage mécanique. La poudre est mise en gaine et ensuite consolidée. Pour finir, des traitements thermomécaniques sont réalisés afin de mettre le matériau en forme.

¹ https://www.gen-4.org/gif/jcms/c_9502/generation-iv-goals

² J. G. Marques, Energy Conversion and Management, **51** (2010) 1774

³ S. Ukai, S. Mizuta, T. Yoshitake, T. Okuda, M. Fujiwara, S. Hagi and T. Kobayashi, Journal of Nuclear Materials, **283** (2000) 702

⁴ G. R. Odette, M. J. Alinger and B. D. Wirth, Annual Review of Materials Research **38** (2008) 471

La compréhension fine des mécanismes mis en jeu lors de la précipitation de ces nano-oxydes permettrait d'améliorer la fabrication et les propriétés mécaniques de ces aciers ODS, avec un fort impact économique en vue de leur industrialisation.

Des résultats obtenus par différentes approches indiquent que la nature (taille, composition et structure) des nano-oxydes est très dépendante des conditions d'élaboration et de la composition des alliages^{5,6,7}. Fu et al.⁸ mettent en avant un mécanisme de germination des amas basé sur les lacunes. D'après des calculs ab initio dans le fer, l'oxygène en position interstitielle a une très forte affinité pour les lacunes, à tel point que, lorsque les lacunes pré-existent, l'énergie de formation d'une paire oxygène-lacune est quasiment nulle. De plus, il existe autour de cette paire oxygène-lacune des sites énergétiquement favorables aux atomes ayant une forte affinité pour O, tels que Ti ou Y. Lors du broyage, de nombreuses lacunes sont formées. Il y a donc formation de paires oxygène-lacune vers lesquels Ti et Y sont attirés, entraînant la germination d'amas enrichis en Ti, Y et O. Cette prédiction théorique a été vérifiée expérimentalement par analyse d'annihilation de positons⁹ et microscopie électronique en transmission¹⁰, confirmant l'importance des lacunes dans les mécanismes de formation des nano-amas.

Afin de déterminer le chemin cinétique de formation de ces nano-oxydes, nous proposons dans ce travail de thèse une alternative originale à la mécano-synthèse: l'implantation ionique, une technique qui reproduit parfaitement les conditions du broyage. En effet, cette technique permet d'introduire de façon contrôlée (température, concentration) les éléments dans la matrice métallique, formant ainsi une solution sursaturée hors-équilibre, tout en créant des lacunes comme le broyage. Un seul essai a été reporté dans la littérature par Sakuma et al.¹¹ dans lequel l'étape de broyage a été remplacée par une co-implantation d'ions Y⁺ et O⁺ dans un acier ferritique créant ainsi une solution solide sursaturée. Leurs observations par microscopie électronique en transmission montrent que la précipitation d'oxydes d'yttrium est induite à cause d'un recuit thermique à 1300 K après l'implantation, mais la nature des nano-précipités formés n'est pas détaillée.

Cette étude a permis de démontrer la faisabilité de cette méthode et d'étudier le comportement d'alliages modèles (à base d'oxyde d'aluminium) sous recuit thermique. Des alliages Fe-10Cr de haute pureté ont été implantés avec des ions Al et O à température ambiante.

⁵ M. Alinger, G. R. Odette and D. T. Hoelzer, *Acta Materialia*, **57** (2009) 392

⁶ E. A. Marquis, *Applied Physics Letter*, **93** (2008) 181904

⁷ M. Klimenkov, R. Lindau and A. Möslang, *Journal of Nuclear Materials*, **386** (2009) 553

⁸ C. L. Fu, M. Kremer, G. S. Painter and X. Q. Chen, *Physical Review Letters*, **99** (2007) 225502

⁹ J. Xu, C. T. Liu, M. K. Miller and H. M. Chen, *Physical Review B*, **79** (2009) 020204

¹⁰ A. Hirata, T. Fujita, Y.R. Wen, J.H. Schneibel, C.T. Liu, M.W. Chen, *Nature Materials*, **10** (2011) 922

¹¹ D. Sakuma, S. Yamashita, K. Oka, S. Ohnuki, L. E. Rehn and E. Wakai, *Journal of Nuclear Materials*, **329** (2004) 392

Les observations de microscopie électronique en transmission ont montré que des nano-oxydes apparaissent dans la matrice de Fe-10Cr dès l'implantation à température ambiante, sans recuit subséquent¹². Les défauts créés lors de l'implantation ionique sont à l'origine de la mobilité des éléments introduits, permettant la nucléation de ces nanoparticules, de quelques nm de diamètre. Ces nanoparticules sont composées d'aluminium et d'oxygène, et également de chrome. Les examens en haute résolution montrent que leur structure cristallographique correspond à celle d'un composé hors équilibre de l'oxyde d'aluminium (de type $\gamma\text{-Al}_2\text{O}_3$)¹³. Les traitements thermiques effectués après implantation induisent une croissance de la taille de ces nano-oxydes, et un changement de phase qui tend vers la structure d'équilibre (de type $\alpha\text{-Al}_2\text{O}_3$)¹⁴.

Ces résultats sur des alliages modèles s'appliquent entièrement aux matériaux industriels : en effet l'implantation ionique reproduit les conditions du broyage, et les traitements thermiques sont à des températures équivalentes à celles des traitements d'élaboration thermo-mécaniques. Ainsi des études récentes sur des matériaux industriels (à base Y, Ti, O) montrent les mêmes résultats que les nôtres, à savoir une apparition des nano-oxydes dès la phase de broyage^{15,16}. Il est montré également que ces nano-oxydes sont de structure hors équilibre¹⁷, et subissent un changement de phase lors du traitement thermo-mécanique¹⁸. Un mécanisme de la précipitation de nano-oxydes est proposé dans ce manuscrit de thèse.

¹² C. Zheng, A. Gentils, J. Ribis, O. Kaïtasov, V.A. Borodin, M. Descoins, D. Mangelinck, *Philosophical Magazine*, **94** (2014) 2937

¹³ C. Zheng, A. Gentils, J. Ribis, V.A. Borodin, O. Kaïtasov, F. Garrido, *Nucl. Instrum. Method. B*, **365** (2015) 319

¹⁴ C. Zheng *et al.*, en préparation

¹⁵ Thèse de Marie Loyer-Prost, CEA/DEN/DMN/SRMP, 2014

¹⁶ C.A. Williams, P. Unifantowicz, N. Baluc, G. D. W. Smith, E. A. Marquis, *Acta Materialia*, **61** (2013) 2219-2235

¹⁷ J. Ribis, E. Bordas *Nucl. Instrum. Method. B*, **365** (2015) 22

¹⁸ J. Ribis *et al.*, en préparation

References

- [**Ahn, 2006**] Channing C. Ahn, *Transmission Electron Energy Loss Spectrometry in Materials Science and the EELS Atlas*, John Wiley & Sons, 2006.
- [**Amara, 2010**] H. Amara, C. C. Fu, F. Soisson and P. Maugis, *Physical Review B* 81 (2010) 174101
- [**ammrf, website**] Australian microscopy & Microanalysis Research Facility, please see <http://www.ammrf.org.au/myscope/analysis/eds/xraygeneration/characteristic/>
- [**Alinger, 2004**] M. J. Alinger, G. R. Odette and D. T. Hoelzer, *Journal of Nuclear Materials* 329 (2004) 382
- [**Alinger, 2009**] M. Alinger, G. R. Odette and D. T. Hoelzer, *Acta Materialia* 57 (2009) 392
- [**Aust, 1968**] K. T. Aust, R. E. Hanneman, P. Niessen and J. H. Westbrook, *Acta Metallurgica* 16 (1968) 291
- [**Averback, 1978**] R. S. Averback, R. Benedek and K. L. Merkle, *Journal of Nuclear Materials* 69 (1978) 786
- [**Barlow, 1969**] R. Barlow, P. J. Grundy, *Journal of Materials Science* 4 (1969) 797
- [**Barouh, 2014**] C. Barouh, T. Schuler, C. C. Fu and M. Nastar, *Physical Review B* 90 (2014) 054112
- [**Benjamin, 1970**] J. S. Benjamin, *Metallurgical Transactions* 1 (1970) 2943
- [**Besson, 2008**] R. Besson, A. Legris, D. Connetable and P. Maugis, *Physical Review B* 78 (2008) 014204
- [**Bhattacharyya, 2012**] D. Bhattacharyya, P. Dickerson, G. R. Odette, S. A. Maloy, A. Misra and M. A. Nastasi, *Philosophical Magazine* 92 (2012) 2089
- [**Brandes, 2012**] M. C. Brandes, L. Kovarik, M. K. Miller and M. J. Mills, *Journal of Materials Science* 47 (2012) 3913
- [**Bremaecker, 2012**] A. D. Bremaecker, *Journal of Nuclear Materials* 428 (2012) 13
- [**Bruemmer, 1999**] S. M. Bruemmer, E. P. Simonen, P. M. Scott, P. L. Andresen, G. S. Was and J. L. Nelson, *Journal of Nuclear Materials* 274 (1999) 299
- [**Brydson, 2001**] R. Brydson, *Electron Energy Loss Spectroscopy*, Taylor & Francis, 1st edition, June 14, 2001
- [**Campbell, 1980**] A. B. Campbell, B. D. Sartwell and P. B. Needham, *Journal of Applied Physics* 51 (1980) 283
- [**Capus, 2007**] G. Capus, B. Bonin and F. Carré, “Comment les Systèmes nucléaires de 4^e generation se déploieront-ils?”, *Clefs CEA* (2007), N°55

- [**Carlan, 2009**] Y. de Carlan, J. L. Bechade, P. Dubuisson, J. L. Seran, P. Billot, A. Bougault, T. Cozzika, S. Doriot, D. Hamon, J. Henry, M. Ratti, N. Lochet, D. Nunes, P. Olier, T. Leblond and M. H. Mathon, *Journal of Nuclear Materials* 386 (2009) 430
- [**Cauvin, 1981**] R. Cauvin, G. Martin, *Physical Review B* 23 (1981) 3322
- [**Cayron, 2010**] C. Cayron, A. Montani, D. Venet and Y. de Carlan, *Journal of Nuclear Materials* 399 (2010) 219
- [**Chao, 1998**] J. Chao, *Materials Science and Engineering: A* 242 (1998) 248
- [**Cheon, 2009**] J. S. Cheon, C. B. Lee, B. O. Lee, J. P. Raison, T. Mizuno, F. Delage and J. Carmack, *Journal of Nuclear Materials* 392 (2009) 324
- [**Couvrat, 2011**] M. Couvrat, L. Chaffron, D. Nunes, P. Bonnaille, M. H. Mathon and M. Perrut, *Solid State Phenomena*, **172** (2011) 721
- [**CSNSM/TEM, website**] <http://www.csnsm.in2p3.fr/MET>
- [**Crozier, 1995**] P. A. Crozier, *Ultramicroscopy* 58 (1995) 157
- [**Diechle, 2010**] D. Diechle, M. Stueber, H. Leiste, S. Ulrich and V. Schier, *Surface and Coatings Technology* 204 (2010) 3258
- [**Dou, 2014**] P. Dou, A. Kimura, R. Kasada, T. Okuda, M. Inoue, S. Ukai, S. Ohnuki, T. Fujisawa and F. Abe, *Journal of Nuclear Materials* 444 (2014) 441
- [**Egerton, 1996**] R. F. Egerton, *Electron Energy Loss Spectroscopy in the electron microscope*, Plenum press, New York, 1996
- [**Egerton, 2009**] R. F. Egerton, *Reports on Progress in Physics* 72 (2009) 016502
- [**Fortuna, 2011**] F. Fortuna, V. A. Borodin, M. O. Ruault, E. Oliviero and M. A. Kirk, *Physical Review B* 84 (2011) 144118
- [**Fortuna, 2012**] F. Fortuna, M. A. Nguyen, M. O. Ruault, M. A. Kirk, V. A. Borodin and M. G. Ganchenkova, *Journal of Applied Physics* 112 (2012) 123504
- [**Fu, 2007**] C. L. Fu, M. Krcmar, G. S. Painter and X. Q. Chen, *Physical Review Letters* 99 (2007) 225502
- [**Garner, 2000**] F. A. Garner, M. B. Toloczko and B. H. Sencer, *Journal of Nuclear Materials* 276 (2000) 123
- [**Gault, 2011**] B. Gault, D. Haley, F. de Geuser, M. P. Moody, E. A. Marquis, D. J. Larson and B. P. Geiser, *Ultramicroscopy* 111 (2011) 448
- [**Gault, 2012**] (Springer Series in Materials Science 160) Baptiste Gault, Michael P. Moody, Julie M. Cairney, Simon P. Ringer, *Atom Probe Microscopy*, Springer New York (2012)
- [**Giannuzzi, 1999**] L. A. Giannuzzi, F. A. Stevie, *Micron* 30 (1999) 197
- [**GIF, website link**] https://www.gen-4.org/gif/jcms/c_9502/generation-iv-goals

- [He, 2014]** J. C. He, F. Wan, K. Sridharan, T. R. Allen, A. Certain, V. Shutthanandan and Y. Q. Wu, *Journal of Nuclear Materials* 455 (2014) 41
- [Hirata, 2011]** A. Hirata, T. Fujita, Y. R. Wen, J. H. Schneibel, C. T. Liu and M. W. Chen, *Nature Materials* 10 (2011) 922
- [Hirvonen, 1982]** J. Hirvonen, J. Räisänen, *Journal of Applied Physics* 53 (1982) 3314
- [Hoelzer, 2007]** D. T. Hoelzer, J. Bentley, M. A. Sokolov, M. K. Miller, G. R. Odette and M. J. Alinger, *Journal of Nuclear Materials* 367 (2007) 166
- [Hofer, 1995]** F. Hofer, P. Warbichler and W. Grogger, *Ultramicroscopy* 59 (1995) 15
- [Hofer, 1997]** F. Hofer, W. Grogger, G. Kothleitner and P. Warbichler, *Ultramicroscopy* 67 (1997) 83
- [Hsiung, 2011]** L. Hsiung, M. Fluss, S. Tumey, J. Kuntz, B. El-Dasher, M. Wall, B. Choi, A. Kimura, F. Willaime and Y. Serruys, *Journal of Nuclear Materials* 409 (2011) 72
- [IM2NP, website]** <http://www.im2np.fr/recherche/sat/index.html>
- [JANNuS Orsay, website]** <http://www.csns.in2p3.fr/Accelerateurs>
- [Jouffrey, 1972]** *Annexe "Coupes de l'espace réciproque, Structures CFC et CC"*, in: Bernard Jouffrey (ed.), *Méthodes et techniques nouvelles d'observation en métallurgie physique*, Société française de microscopie électronique, Paris, 1972, 525
- [Jublot, 2014]** M. Jublot, M. Texier, *Micron* 56 (2014) 63
- [Jung, 1983]** P. Jung, *Journal of Nuclear Materials* 117 (1983) 70
- [Juslin, 2007]** N. Juslin, K. Nordlund, J. Wallenius and L. Malerba, *Nuclear Instruments and Methods in Physics Research Section B: Beam Interactions with Materials and Atoms* 255 (2007) 75
- [Karlik]** *Etudes des métaux par microscopie électronique en transmission, "Analyse chimique locale"*, par M. Karlik et B. Jouffrey, *Techniques de l'ingénieur M4* 136, 1-8
- [Kasada, 2007]** R. Kasada, N. Toda, K. Yutani, H. S. Cho, H. Kishimoto and A. Kimura, *Journal of Nuclear Materials* 367 (2007) 222
- [Kasada, 2011]** R. Kasada, S. G. Lee, J. Isselin, J. H. Lee, T. Omura, A. Kimura, T. Okuda, M. Inoue, S. Ukai, S. Ohnuki, T. Fujisawa and F. Abe, *Journal of Nuclear Materials* 417 (2011) 180
- [Khatibi, 2011]** A. Khatibi, J. Palisaitis, C. Höglund, A. Eriksson, P. O. Å. Persson, J. Jensen, J. Birch, P. Eklund and L. Hultman, *Thin solid Films* 519 (2011) 2426
- [Khatibi, 2012]** A. Khatibi, J. Lu, J. Jensen, P. Eklund and L. Hultman, *Surface and Coatings Technology* 206 (2012) 3216
- [Khatibi, 2013]** A. Khatibi, A. Genvad, E. Göthelid, J. Jensen, P. Eklund and L. Hultman, *Acta Materialia* 61 (2013) 4811

- [Kelly, 2014]** J. E. Kelly, *Progress in Nuclear Energy* **77** (2014) 240
- [Kimura, 2009]** A. Kimura, R. Kasada and N. Iwata, In *Proceedings of ICAPP 09*, Tokyo, Japan, May 10-14, 2009, p. 9220
- [Kinchin, 1955]** G. H. Kinchin, R. S. Pease, *Reports on Progress in Physics*, RPPHA, **18** (1955) 1
- [Klimiankou, 2003]** M. Klimiankou, R. Lindau and A. Möslang, *Journal of Crystal Growth* **249** (2003) 381
- [Klimiankou, 2004]** M. Klimiankou, R. Lindau and A. Möslang, *Journal of Nuclear Materials* **329** (2004) 347
- [Klimiankou, 2007]** M. Klimiankou, R. Lindau and A. Möslang, *Journal of Nuclear Materials* **367** (2007) 173
- [Klimenkov, 2009]** M. Klimenkov, R. Lindau and A. Möslang, *Journal of Nuclear Materials* **386** (2009) 557
- [Klimenkov, 2009]** M. Klimenkov, R. Lindau and A. Möslang, *Journal of nuclear Materials* **386** (2009) 553
- [Klueh, 2005]** R. L. klueh, J. P. Shingledecker, R. W. Swindeman and D. T. Hoelzer, *Journal of Nuclear Materials* **341** (2005) 103
- [Lapuerta, 2006]** S. Lapuerta, N. Moncoffre, N. Millard-Pinard, H. Jaffrézic, N. Béreud and D. Crusset, *Journal of Nuclear Materials* **352** (2006) 174
- [Larson, 1999]** D. J. Larson, D. T. Foord, A. K. Petford-Long, H. Liew, M. G. Blamire, A. Cerezo and G. D. W. Smith, *Ultramicroscopy* **79** (1999) 287
- [Larson, 2001]** D. Larson, B. D. Wissman, R. Martens, R. J. Viellieux, T. F. Kelly, T. T. Gribb, H. F. Erskine and N. Tabat, *Microscopy and Microanalysis* **7** (2001) 24
- [Larson, 2001]** D. J. Larson, P. J. Maziasz, I-S Kim and K. Miyahara, *Scripta Materialia* **44** (2001) 359
- [Laurent-Brocq, 2010]** M. Laurent-Brocq, B. Radiguet, J.-M. Le Breton, F. Cuvilly, P. Pareige and F. Legendre, *Acta Materialia* **58** (2010) 1806
- [Laurent-Brocq, 2012]** M. Laurent-brocq, F. Legendre, M.-H. Mathon, A. Mascaro, S. Poissonnet, B. Radiguet, P. Pareige, M. Loyer and O. Leseigneur, *Acta Materialia* **60** (2012) 7150
- [Lee, 2007]** J. S. Lee, C. H. Jang, I. S. Kim and A. Kimura, *Journal of Nuclear Materials* **367** (2007) 229
- [Legendre, 2007]** F. Legendre, S. Poissonnet and P. Bonnaillie, *Journal of Alloys and Compounds* **434** (2007) 400
- [Li, 1993]** L. Li, Z. Xing, *Acta Metall Sinica* **29** (1993) 136

- [**Little, 1979**] E. A. Little, *Journal of Nuclear Materials* 87 (1979) 11
- [**Little, 2006**] E. A. Little, *Materials Science and Technology* 22 (2006) 491
- [**Liu, 1997**] C. L. Liu, G. R. Odette, B. D. Wirth and G. E. Lucas, *Materials Science and Engineering: A* 238 (1997) 202
- [**Liu, 2010**] Y. Liu, J. H. Fang, D. H. Liu, Z. Lu, F. Liu, S. Q. Chen and C.T. Liu, *Journal of Nuclear Materials* 396 (2010) 86
- [**Malis, 1988**] T. Malis, *Journal of Electron Microscopy Technique* 8 (1988) 193
- [**Mangelinck, 2014**] D. Mangelinck, F. Panciera, K. Hoummada, M. El Kousseifi, C. Perrin, M. Descoins and A. Portavoce, *Microelectronic Engineering* 120 (2014) 19
- [**Marques, 2010**] J. G. Marques, *Energy Conversion and Management* 51 (2010) 1774
- [**Marquis, 2008**] E. A. Marquis, *Applied Physics Letter* 93 (2008) 181904
- [**Marquis, 2010**] E. A. Marquis, *Materials Science and Engineering: R: Reports* 69 (2010)37
- [**Marwick, 1978**] A. Marwick, *Journal of Physics F: Metal Physics* 8 (1978) 1849
- [**Massalski, 1986**] T. B. Massalski, editor, *Binary alloy phase diagrams*. Metals Park, USA: ASM International, 1986, p.111
- [**Matter, 1979**] H. Matter, J. Winter and W. Triftshäuser, *Applied Physics A: Materials Science & Processing* 20 (1979) 135
- [**Maydet, 1977**] S. I. Maydet, K. C. Russell, *Journal of Nuclear Materials* 64 (1977) 101
- [**McClintock, 2009**] D. A. McClintock, M. A. Sokolov, D. T. Hoelzer and R. K. Nanstad, *Journal of Nuclear Materials* 392 (2009) 353
- [**Miller, 2003**] M. K. Miller, E. A. Kenik, K. F. Russell, L. Heatherly, D. T. Hoelzer and P. J. Maziasz, *Materials Science and Engineering: A* 353 (2003) 140
- [**Miller, 2004**] M. K. Miller, D. T. Hoelzer, E. A. Kenik and K. F. Russell, *Journal of Nuclear Materials* 329 (2004) 338
- [**Miller, 2005**] M. K. Miller, D. T. Hoelzer, E. A. Kenik and K. F. Russell, *Intermetallics* 13 (2005) 387
- [**Miller, 2006**] M. K. Miller, K. F. Russell and D. T. Hoelzer, *Journal of Nuclear Materials* 351 (2006) 261
- [**Miller, 2011**] M. K. Miller, D. T. Hoelzer, *Journal of Nuclear Materials* 418 (2011) 307
- [**Miller, 2014**] Michael K. Miller, Richard G. Forbes, *Atom Probe Tomography: Analysis at the Atomic level*, Springer US (2014)
- [**Monnet, 2004**] I. Monnet, P. Dubuisson, Y. Serruys, M. O. Ruault, O. Kaïtasov and B. Jouffrey, *Journal of Nuclear Materials* 335 (2004) 311
- [**Mrowec, 1980**] S. Mrowec, *Defects and Diffusion in Solids, an Introduction*. Elsevier, New York, 1980

- [**Murali, 2010**] D. Murali, B. K. Panigrahi, M. C. Valsakumar, S. Chandra, C. S. Sundar and B. Raj, *Journal of Nuclear Materials* 403 (2010) 113
- [**Najafi, 2011**] H. Najafi, A. Karimi, P. Dessarzin and M. Morstein, *Thin Solid Films* 520 (2011) 1597
- [**Najafi, 2013**] H. Najafi, A. Karimi, P. Dessarzin and M. Morstein, *Surface Coatings Technology* 214 (2013) 46
- [**Nastar, 2012**] M. Nastar, F. Soisson, Radiation induced segregation. In: R. Konings *et al.*, editors. *Comprehensive nuclear materials*. Amsterdam: Elsevier, 2012
- [**Odette, 2008**] G. R. Odette, M. J. Alinger and B. D. Wirth, *Annual Review of Materials Research* 38 (2008) 471
- [**Ohnuma, 2009**] M. Ohnuma, J. Suzuki, S. Ohtsuka, S. W. Kim, T. Kaito, M. Inoue and H. Kitazawa, *Acta Materialia* 57 (2009) 5571
- [**Ohtsuka, 2004**] S. Ohtsuka, S. Ukai, M. Fujiwara, T. Kaito and T. Narita, *Journal of Nuclear Materials* 329 (2004) 372
- [**Ohtsuka, 2006**] S. Ohtsuka, S. Ukai and M. Fujiwara, *Journal of Nuclear Materials* 351 (2006) 241
- [**Okamoto, 1973**] P. R. Okamoto, S. D. Harkness, and J. J. Laidler, *Transactions of the American Nuclear Society* 16 (1973) 70
- [**Okamoto, 1979**] P. R. Okamoto, L. E. Rehn, *Journal of Nuclear Materials* 83 (1979) 2
- [**Okuda, 1995**] T. Okuda, M. Fujiwara, *Journal of Materials Science Letters* 14 (1995) 1600
- [**Olier, 2012**] P. Olier, J. Malaplate, M. H. Mathon, D. Nunes, D. Hamon, L. Toualbi, Y. de Carlan and L. Chaffron, *Journal of Nuclear Materials* 428 (2012) 40
- [**Picraux, 1978**] S.T. Picraux, Chapter “*Equilibrium phase formation by ion implantation*”, part 3, p. 307-323, in: A. Perez A, Coussemont R (eds). *Site Characterization and Aggregation of Implanted Atoms in Materials*. NATO Advanced Study Institutes Series, series B: Physics, Vol. 47, Plenum Press, 1978
- [**Ramar, 2009**] A. Ramar, N. Baluc and R. Schäublin, *Journal of Nuclear Materials* 386 (2009) 515
- [**Ramm, 2007**] J. Ramm, M. Ante, T. Bachmann and B. Widrig, H. Brändle and M. Döbeli, *Surface and Coating Technology* 202 (2007) 876
- [**Ratti, 2009**] M. Ratti, D. Leuvrey, M. H. Mathon and Y. de Carlan, *Journal of Nuclear Materials* 386 (2009) 540
- [**Rose, 1956**] D. J. Rose, *Journal of Applied Physics* 27 (1956) 215
- [**Rehn, 1979**] L. Rehn, P. R. Okamoto and H. Wiedersich, *Journal of Nuclear Materials* 80 (1979) 172

- [Ribis, 2010]** J. Ribis, Premiers elements sur la mise en place de l'EFTEM au SRMA, application à la caractérisation fine des matériaux ODS avant et après irradiation, document technique DEN/DANS/DMN/SRMA/LA2M/NT/2010-3115/A (2010)
- [Ribis, 2012]** J. Ribis, Y. de Carlan, *Acta Materialia* 60 (2012) 238
- [Ribis, 2014]** J. Ribis, M. L. Lescoat, Y. Chen, E. A. Marquis, E. Bordas, P. Trocellier, Y. Serruys, A. Gentils, O. Kaïtasov, Y. de Carlan and A. Legris, *Acta Materialia* 78 (2014) 328
- [Ruault, 2008]** M. O. Ruault, F. Fortuna, V. A. Borodin, M. G. Ganchenkova and M. A. Kirk, *Journal of Applied Physics* 104 (2008) 033527
- [Russel, 1979]** K. C. Russell, *Journal of Nuclear Materials* 83 (1979) 176
- [Sakasegawa, 2009]** H. Sakasegawa, L. Chaffron, F. Legendre, L. Boulanger, T. Cozzika, M. Brocq and Y. de Carlan, *Journal of Nuclear Materials* 384 (2009) 115
- [Sakuma, 2004]** D. Sakuma, S. Yamashita, K. Oka, S. Ohnuki, L. E. Rehn and E. Wakai, *Journal of Nuclear Materials* 329 (2004) 392
- [Schaefer, 1987]** H. E. Schaefer, *Physica Status Solidi A* 102 (1987) 47
- [Schaublin, 2002]** R. Schaublin, T. Leguey, P. Spätig, N. Baluc and M. Victoria, *Journal of Nuclear Materials* 307 (2002) 778
- [Schepper, 1983]** L. De Schepper, D. Segers, L. Dorikens-Vanpraet, M. Dorikens, G. Knuyt, L. M. Stals and P. Moser, *Physical Review B* 27 (1983) 5257
- [Schneibel, 2008]** J. H. Schneibel, S. Shim, *Materials Science and Engineering: A* 488 (2008) 134
- [Shibahara, 1994]** I. Shibahara, N. Akasaka, S. Onose, H. Okada and S. Ukai, *Journal of Nuclear Materials* 212 (1994) 487
- [Smithells Metals Reference Book, 2004]** *Smithells Metals Reference Book*, 2004
- [Sporer, 1992]** D. Sporer, *Metal Powder Report* 47 (1992) 51
- [Stadelmann, 1987]** P. A. Stadelmann, *Ultramicroscopy* 21 (1987) 131
- [Steckmeyer, 2010]** A. Steckmeyer, M. Praud, B. Fournier, J. Malaplate, J. Garnier, J. L. Béchade, I. Tournié, A. Tancray, A. Bougault and P. Bonnaille, *Journal of Nuclear Materials* 405 (2010) 95
- [Subramanian, 2011]** S. Subramanian, G. Clark, K. Ly and T. Chrasteky, *Electronic Device Failure Analysis* 13 (2011) 20
- [Surgyanarayana, 2001]** C. Surgyanarayana, *Progress in Materials Science* 46 (2001) 1
- [Takada, 1986]** J. Takada, S. Yamamoto, S. Kikuchi and M. Adachi, *Oxidation of Metals* 25 (1986) 93

- [**Thompson, 2007**] K. Thompson, D. Lawrence, D. J. Larson, J. D. Olson, T. F. Kelly and B. Gorman, *Ultramicroscopy* 107 (2007) 131
- [**Ukai, 1993**] S. Ukai, M. Harada, H. Okada, M. Inoue, S. Nomura, S. Shikakura, K. Asabe, T. Nishida and M. Fujiwara, *Journal of Nuclear Materials* 204 (1993) 65
- [**Ukai, 1997**] S. Ukai, T. Nishida, H. Okada, T. Okuda, M. Fujiwara and K. Asabe, *Journal of Nuclear Science and Technology* 34 (1997) 256
- [**Ukai, 2000**] S. Ukai, S. Mizuta, T. Yoshitake, T. Okuda, M. Fujiwara, S. Hagi and T. Kobayashi, *Journal of Nuclear Materials* 283 (2000) 702
- [**Ukai, 2002**] S. Ukai, S. Mizuta, M. Fujiwara, T. Okuda and T. Kobayashi, *Journal of Nuclear Science and Technology* 39 (2002) 778
- [**Ukai, 2002**] S. Ukai, T. Okuda, M. Fujiwara, T. Kobayashi, S. Mizuta and H. Nakashima, *Journal of Nuclear Science and Technology* 39 (2002) 872
- [**Ukai, 2002**] S. Ukai, T. Kaito, S. Ohtsuka, T. Narita, M. Fujiwara and T. Kobayashi, *ISIJ international* 43 (2002) 2038
- [**Ukai, 2002**] S. Ukai, M. Fujiwara, *Journal of Nuclear Materials* 307 (2002) 749
- [**Ukai, 2012**] S. Ukai, *Oxide Dispersion Strengthened Steels*, in: *Comprehensive Nuclear Materials*, vol. 4, Konings R.J.M. (ed.), Elsevier, Amsterdam, 2012, p. 241
- [**Ullmaier, 1980**] H. Ullmaier, W. Schilling, *Radiation damage in metallic reactor materials*. In: *Physics of Modern Materials*, vol. I. IAEA, Vienna, 1980
- [**Unifantowicz, 2011**] P. Unifantowicz, *Fusion Engineering and Design* In Press (2011)
- [**Vehanen, 1982**] A. Vehanen, P. Hautojärvi, J. Johansson, J. Yli-Kaupilla and P. Moser, *Physical Review B* 25 (1982) 762
- [**Villars, 1985**] P. Villars, L. D. Calvert, *Pearson's Handbook of Crystallographic Data for Intermetallic Phases*, vol. 3, American Society for Metals, Metals Park, Oh 44073, 1985
- [**Was, 2007**] G. Was, *Fundamentals of Radiation Materials Science*, Springer, 2007
- [**Wharry, 2014**] J. P. Wharry, G. Was, *Acta Materialia* 65 (2014) 42
- [**Williams, 1996**] D. B. Williams, C. B. Carter, *Transmission Electron Microscopy*, Plenum Press, New York (1996), p.678
- [**Williams, 2009**] D. B. Williams and C. B. Carter, *Transmission Electron Microscopy*, 2nd ed., Springer, 2009
- [**Williams, 2010**] C. A. Williams, E. A. Marquis, A. Cerezo and G. D. W. Smith, *Journal of Nuclear Materials* 400 (2010) 37
- [**World energy outlook, 2012**] *World Energy Outlook 2012* International Energy Agency, IEA/OECD (2012)

- [**Xu, 2009**] J. Xu, C. T. Liu, M. K. Miller and H. M. Chen, *Physical Review B* 79 (2009) 020204
- [**Yamashita, 2004**] S. Yamashita, N. Akasaka and S. Ohnuki, *Journal of Nuclear Materials* 329 (2004) 377
- [**Yamamoto, 2010**] M. Yamamoto, S. Ukai, S. Hayashi, T. Kaito and S. Ohtsuka, *Materials Science and Engineering: A* 527 (2010) 4418
- [**Yamamoto, 2011**] M. Yamamoto, S. Ukai, S. Hayashi, T. Kaito and S. Ohtsuka, *Journal of Nuclear Materials* 417 (2011) 237
- [**Yamashita, 2002**] S. Yamashita, K. Oka, S. Ohnuki, N. Akasaka and S. Ukai, *Journal of Nuclear Materials* 307 (2002) 283
- [**Yazawa, 2004**] Y. Yazawa, T. Furuhashi and T. Maki, *Acta Materialia* 52 (2004) 3727
- [**Yutani, 2007**] K. Yutani, H. Kishimoto, R. Kasada and A. Kimura, *Journal of Nuclear Materials* 367 (2007) 423
- [**Yvon, 2009**] P. Yvon, F. Carré, *Journal of Nuclear Materials* 385 (2009) 217
- [**Ziegler, 1996**] J. F. Ziegler, J. P. Biersack, U. Littmark, *The Stopping and Range of Ions in Solids*, New York, Pergamon, 1996. See also <http://www.srim.org> for code description

Titre : Synthèse de nano-amas d'oxyde métallique par implantation ionique dans un alliage Fe10Cr de haute pureté

Mots clés : Implantation ionique, Recuit thermique, Précipitation, Sonde atomique tomographique, Microscopie électronique en transmission, Oxyde d'aluminium, Alliage métallique

Résumé : Les aciers ODS (Oxide Dispersed Strengthened Steels), renforcés par des dispersions de nano-oxydes métalliques (à base d'éléments Y, Ti et O), sont des matériaux prometteurs pour les réacteurs nucléaires de génération IV. La compréhension fine des mécanismes mis en jeu lors de la précipitation de ces nano-oxydes permettrait d'améliorer la fabrication et les propriétés mécaniques de ces aciers ODS, avec un fort impact économique en vue de leur industrialisation. Pour étudier expérimentalement ces mécanismes, une approche analytique par implantation ionique est utilisée dans cette étude, permettant de contrôler différents paramètres de synthèse de ces précipités comme la température et leur concentration. Ce projet a permis de démontrer la faisabilité de cette méthode et d'étudier le comportement d'alliages modèles (à base d'oxyde d'aluminium) sous recuit thermique. Des alliages Fe-10Cr de haute pureté ont été implantés avec des ions Al et O à température ambiante. Les observations de microscopie électronique en transmission ont montré que des nano-oxydes apparaissent dans la matrice de

Fe-10Cr dès l'implantation à température ambiante, sans recuit subséquent. Les défauts créés lors de l'implantation ionique sont à l'origine de la mobilité des éléments introduits, permettant la nucléation de ces nanoparticules, de quelques nm de diamètre. Ces nanoparticules sont composées d'aluminium et d'oxygène, et également de chrome. Les examens en haute résolution montrent que leur structure cristallographique correspond à celle d'un composé hors équilibre de l'oxyde d'aluminium (de type γ -Al₂O₃). Les traitements thermiques effectués après implantation induisent une croissance de la taille de ces nano-oxydes, et un changement de phase qui tend vers la structure d'équilibre (de type α -Al₂O₃). Ces résultats sur des alliages modèles s'appliquent entièrement aux matériaux industriels : en effet l'implantation ionique reproduit les conditions du broyage, et les traitements thermiques sont à des températures équivalentes à celles des traitements d'élaboration thermo-mécaniques. Un mécanisme de la précipitation de nano-oxydes dispersés dans des alliages ODS est proposé dans ce manuscrit.

Title: Metallic nano-oxide clusters synthesis by ion implantation in high purity Fe10Cr alloy

Keywords: Ion implantation, Thermal annealing, Precipitation, Atom probe tomography, Transmission electron microscopy, Aluminum oxide, Metallic alloy

Abstract: ODS (Oxide Dispersed Strengthened) steels, which are reinforced with metal dispersions of nano-oxides (based on Y, Ti and O elements), are promising materials for future nuclear reactors. The detailed understanding of the mechanisms involved in the precipitation of these nano-oxides would improve manufacturing and mechanical properties of these ODS steels, with a strong economic impact for their industrialization. To experimentally study these mechanisms, an analytical approach by ion implantation is used, to control various parameters of synthesis of these precipitates as the temperature and concentration. This study demonstrated the feasibility of this method and concerned the behavior of alloys models (based on aluminum oxide) under thermal annealing. High purity Fe-10Cr alloys were implanted with Al and O ions at room temperature. Transmission electron microscopy observations showed that the nano-oxides appear in the Fe-10Cr matrix upon ion implantation at room temperature without subsequent annealing.

The mobility of implanted elements is caused by the defects created during ion implantation, allowing the nucleation of these nanoparticles, of a few nm in diameter. These nanoparticles are composed of aluminum and oxygen, and also chromium. The high-resolution experiments show that their crystallographic structure is that of a non-equilibrium compound of aluminum oxide (cubic γ -Al₂O₃ type). The heat treatment performed after implantation induces the growth of the nano-sized oxides, and a phase change that tends to balance to the equilibrium structure (hexagonal α -Al₂O₃ type). These results on model alloys are fully applicable to industrial materials: indeed ion implantation reproduces the conditions of milling and heat treatments are at equivalent temperatures to those of thermo-mechanical treatments. A mechanism involving the precipitation of nano-oxide dispersed in ODS alloys is proposed in this manuscript based on the obtained experimental results, and the existing literature.